Acoustical Physics, Vol. 49, No. 5, 2003, pp. 487–490. Translated from Akusticheskiĭ Zhurnal, Vol. 49, No. 5, 2003, pp. 581–584.

Diffraction and Radiation of Flexural Waves by a Circular Aperture Loaded along the Edge

I. V. Andronov

St. Petersburg State University, ul. Ul'yanovskaya 1, Petrodvoretz, St. Petersburg, 198504 Russia
e-mail: iva@aa2628.spb.edu

Received August 26, 2002

Abstract—An inhomogeneous wave exponentially decaying in all directions may exist near the edge of a circular aperture if the mass and the moment of inertia are appropriately chosen (i.e., their values coincide with the critical ones) [1]. In this case, the solution to the diffraction problem is not unique. This paper inquires into the feasibility of the solution to the wave diffraction and radiation problem in the case of critical loading. The solution is constructed according to the procedure suggested in [2]. It is shown that the diffraction problem always has a solution while the radiation problem may have no solution. The effects related to the critical mass and the critical moment of inertia do not manifest themselves in the far field. © *2003 MAIK "Nauka/Interperiodica".*

1. PROBLEM FORMULATION AND SOLUTION

Stationary flexural vibrations of a thin elastic plate are described by the Kirchhoff model

$$(\Delta^2 - k^4)w(x, y) = 0, \tag{1}$$

where k is the wave number and w is the flexural displacement. We write the boundary conditions at a circular obstacle (at $r = R$) in the form

$$\mathbf{F}w = \omega^2 Mw, \quad \mathbf{M}w = \omega^2 I\frac{\partial w}{\partial r}, \tag{2}$$

where $\mathbf{F}$ and $\mathbf{M}$ are the differential operators of the force and the bending moment on the edge of the circular aperture; in polar coordinates (r, ϕ), they have the form

$$\mathbf{F} = D\left(\frac{\partial}{\partial r}\Delta + \frac{\nu}{r}\frac{\partial}{\partial r}\frac{1}{r}\frac{\partial^2}{\partial \phi^2}\right),$$

$$\mathbf{M} = D\left(\Delta - \frac{\nu}{r}\left(\frac{\partial}{\partial r} + \frac{1}{r}\frac{\partial^2}{\partial \phi^2}\right)\right).$$

Here, D is the flexural rigidity of the plate, $\nu = 1 - \sigma$, and σ is the Poisson ratio.

Conditions (2) describe the distributed mass load with a density M and the distributed load of the moment of inertia with a moment density I. As was found in [1] and as will be clear from the following, there are some special densities M and I that allow a nontrivial solution to problem (1), (2), this solution exponentially decaying in all directions.

We will simultaneously solve three problems with different excitation sources. In the first case, the field scattered by the aperture is excited by a plane flexural wave

$$w^{(i)} = e^{ikx} = e^{ikr\sin\phi}. \tag{3}$$

In the second case, a point force is applied to the edge of the aperture. In this case, the first boundary condition in Eqs. (2) is replaced by the inhomogeneous condition

$$\mathbf{F}w = \omega^2 Mw + \delta(\phi).$$

Finally, in the third problem, the field is excited by a point moment of force applied to the edge of the aperture. Here, the second condition in Eqs. (2) becomes inhomogeneous:

$$\mathbf{M}w = \omega^2 I\frac{\partial w}{\partial r} + \delta(\phi).$$

We search the scattered or radiated field $w(r, \phi)$ in the form

$$w(r, \phi) = \sum_{n=-\infty}^{+\infty} (\alpha_n H_n^{(1)}(kr) + \beta_n H_n^{(1)}(ikr))e^{in\phi}.$$

This form obeys the radiation conditions; hence, $H_n^{(1)}$ is the Hankel function of the first kind. The coefficients α_n and β_n are determined from the boundary conditions. Passing over the intermediate calculations, which are a replica of those in [2], we obtain the systems of equations

$$\begin{cases} F_n(kR)\alpha_n + F_n(ikR)\beta_n = f_n, \\ G_n(kR)\alpha_n + G_n(ikR)\beta_n = g_n, \end{cases} \tag{4}$$

1063-7710/03/4905-0487$24.00 © 2003 MAIK "Nauka/Interperiodica"

where

$$F_n(z) = -z(z^2 + \nu n^2)\dot{H}_n^{(1)}(z) + (\nu n^2 - mz^4)H_n^{(1)}(z),$$

$$G_n(z) = z(Jz^4 - \nu)\dot{H}_n^{(1)}(z) + (\nu n^2 - z^2)H_n^{(1)}(z).$$

The dimensionless mass m and moment of inertia J are determined by the formulas

$$m = \frac{M}{R\rho}, \quad J = \frac{I}{R^3\rho}.$$

Here, ρ is the surface density of the plate (the mass of a unit area of the plate) and the wave number is given by the expression

$$k^4 = \frac{\omega^2\rho}{D}.$$

The right-hand sides of systems (4) are different for the diffraction and radiation problems. In the diffraction problem, the incident plane wave generates the right-hand sides in the form

$$f_n = kR((kR)^2 + \nu n^2)\dot{J}_n(kR) - (\nu n^2 - m(kR)^4)J_n(kR), \quad (5)$$

$$g_n = kR(\nu - J(kR)^4)\dot{J}_n(kR) + ((kR)^2 - \nu n^2)J_n(kR),$$

where $J_n(kR)$ are the Bessel functions. A point force leads to the expressions

$$f_n = \frac{R^3}{2\pi}, \quad g_n = 0, \quad (6)$$

and a point moment of force, to

$$f_n = 0, \quad g_n = \frac{R^2}{2\pi}. \quad (7)$$

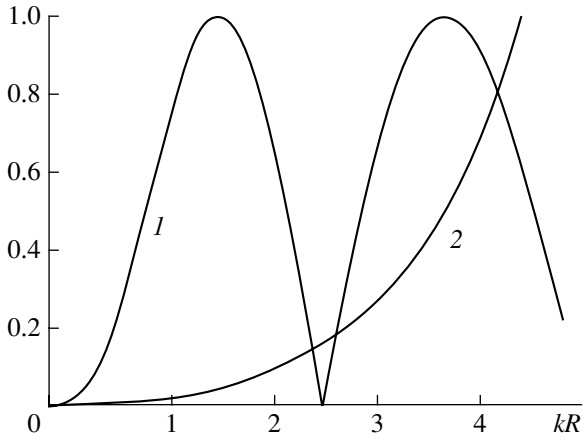

Fig. 1. Coefficients (*1*) α_0 and (*2*) β_0 for $m = m_0(2)$ and $J = I_0(2)$.

If the determinant of system (4)

$$Z = G_n(ikR)F_n(kR) - F_n(ikR)G_n(kR)$$

is nonzero, the solution is given by the formulas

$$\alpha_n = \frac{g_nF_n(ikR) - f_nG_n(ikR)}{Z}, \quad (8)$$

$$\beta_n = \frac{g_nF_n(kR) - f_nG_n(kR)}{Z}. \quad (9)$$

2. ANALYSIS OF THE SOLUTIONS

The quantities $i^{n+1}F_n(ikR)$ and $i^{n+1}G_n(ikR)$ are real-valued, and they vanish for certain values of m and J. Resolving equation $F_n(iz) = 0$ in m, we determine the functions $m_n(kR)$ such that the quantity $F_n(ikR)$ vanishes for $m = m_n(kR)$. From equations $G_n(iz) = 0$, we determine the functions $I_n(kR)$ such that the quantity $G_n(ikR)$ vanishes for $J = I_n(kR)$:

$$m_n(z) = \frac{(z^2 - \nu n^2)}{z^3}\frac{i\dot{H}_n^{(1)}(iz)}{H_n^{(1)}(iz)} + \frac{\nu n^2}{z^4},$$

$$I_n(z) = \frac{\nu}{z^4} + \frac{\nu n^2 + z^2}{z^5}\frac{iH_n^{(1)}(iz)}{\dot{H}_n^{(1)}(iz)}.$$

In our previous paper [1], other normalizing factors were used; in that paper, the plots of the functions $2m_n(z)$ and $12I_n(z)$ were presented. If we specify some index $n = n^*$ and some dimensionless frequency $z^* = k^*R$ and simultaneously set $m = m_n(z^*)$ and $J = I_n(z^*)$, the determinant Z will vanish at the critical frequency $k = k^* \equiv z^*/R$. In this case, formulas (8) and (9) lose significance in the general sense.

2.1. The Diffraction Problem

Consider first the problem of the diffraction of a plane wave. It is not difficult to show that, for $m = m_n(z^*)$ and $J = I_n(z^*)$, the right-hand sides of Eqs. (5) satisfy the identity

$$g_nF_n(k^*R) = f_nG_n(k^*R), \quad (10)$$

which can be easily verified by direct calculation. Consequently, system (4) for the right-hand sides of Eqs. (5) remains compatible at the critical frequency. Figure 1 shows the results of a numerical analysis of solution (8) for $n^* = 0$ and $z^* = 2$.

Consider now the case of parameters m and J that are close but not equal to their critical values. We first set $m = tm_0(2)$ and $J = I_0(2)$, where the mismatch t is close but not equal to unity. Figure 2 shows the curves $\alpha_0(kR)$ for $t = 0.95$, 0.98, 0.99, 1, 1.01, 1.02, and 1.05. For $t \neq 1$, every curve exhibits two resonance peaks, one

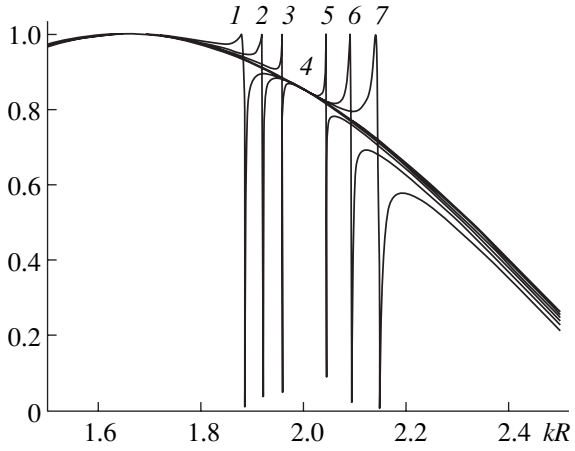

Fig. 2. Coefficient α_0 near the critical frequency for $m = tm_0(2)$ and $J = I_0(2)$, where t = (*1*) 0.95, (*2*) 0.98, (*3*) 0.99, (*4*) 1, (*5*) 1.01, (*6*) 1.02, and (*7*) 1.05.

to the left and another to the right from the critical frequency. As the mass tends to the critical value, the distance between these resonance peaks decreases, and, at $m = m_0(2)$, the peaks merge and cancel each other. A similar behavior occurs for the mismatch of the loading moment of inertia.

The scattering pattern Ψ and the effective scattering cross section Σ are important characteristics of the scattered field; these quantities are determined by the formulas

$$\Psi(\phi) = \frac{1}{\pi}\sum_{n=-\infty}^{+\infty}\alpha_n e^{ij\phi}, \quad \Sigma = \int_0^{2\pi}|\Psi(\phi)|^2 d\phi.$$

Figure 3 shows the frequency dependence of the scattering cross section (in decibels) for the critical mass and the critical moment at $kR = 2$ and $n^* = 0$. The prominent resonance behavior of this dependence can be explained by the fact that parameters m and J that are critical for $n = 0$ approximately coincide with the critical parameters corresponding to $n \neq 0$ but to greater values of the dimensionless radius of the obstacle. For this reason, the frequency dependences of the coefficients α_j for $j > 0$ exhibit a resonance behavior similar to that shown in Fig. 2. These resonance peaks appear in Fig. 3. It turned out that the summation of ten terms given by formula (8) is sufficient to calculate the efficient scattering cross section for the frequency range below $kR = 5$. The error of such an approximation does not exceed fractions of percent in the whole frequency range, excluding very narrow resonance regions for the series terms with numbers $j > 10$.

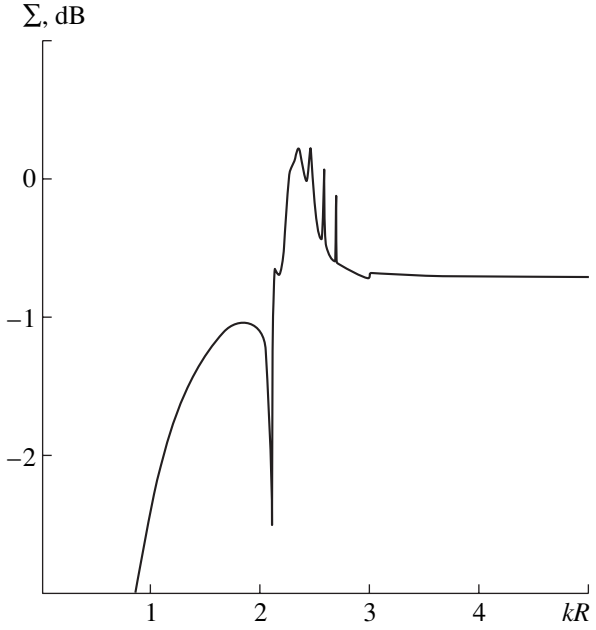

Fig. 3. Effective scattering cross section for $m = m_0(2)$ and $J = I_0(2)$.

2.2. Radiation Problems

Consider now the problems of wave radiation by a point force and a point moment of force. It is evident that identity (10) appears invalid in this case, and no solution to system (4) exists for a given $n = n^*$ at the critical frequency. Again, we choose the mass and the moment that are critical for $n = 0$ at $kR = 2$. Figures 4 and 5 show the results calculated by formulas (8) and (9). As the driving force or moment frequency approaches the critical value, the coefficient β_0 increases without limit. The coefficient α_0 remains finite and smoothly varies. This means that the critical frequency does not manifest itself in the frequency dependence of the effective scattering cross section,

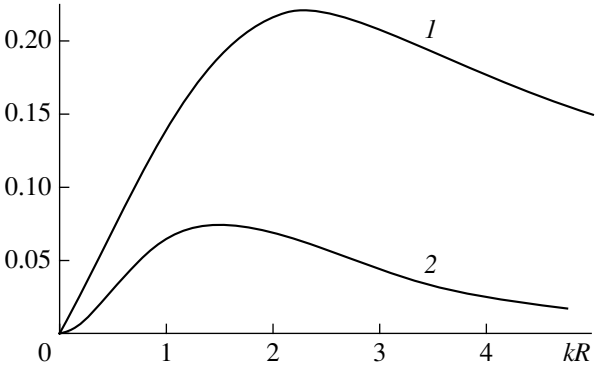

Fig. 4. Coefficients α_0 calculated by formula (8) in the context of the radiation problems for $m = m_0(2)$ and $J = I_0(2)$ (calculations for (*1*) a point force and (*2*) a point moment).

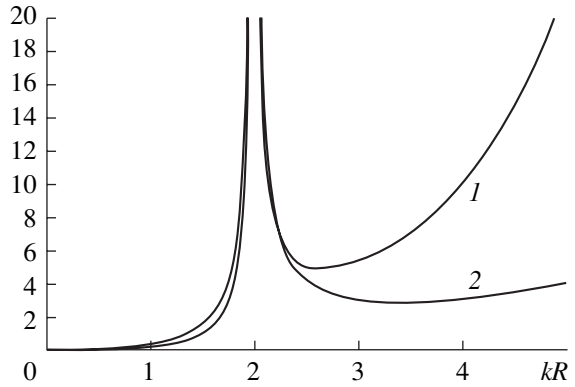

Fig. 5. Coefficients β_0 calculated by formula (8) in the context of the radiation problems for $m = m_0(2)$ and $J = I_0(2)$ (calculations for (*1*) a point force and (*2*) a point moment).

excluding the fact that no solution exists at the critical frequency.

3. CONCLUSIONS

In a plate with a circular obstacle, an inhomogeneous flexural wave may exist near the obstacle. This possibility is realized if the mass and the moment of inertia distributed along the edge are specially chosen. With such parameters, the diffraction problem has nonunique solutions, and the radiation problems have no solution in the general case. However, these effects do not manifest themselves in the far field.

REFERENCES

1. I. V. Andronov and B. P. Belinskiĭ, Akust. Zh. **47**, 7 (2001) [Acoust. Phys. **47**, 3 (2001)].
2. Yu. K. Konenkov, Akust. Zh. **10**, 186 (1964) [Sov. Phys. Acoust. **10**, 153 (1964)].

Translated by A. Vinogradov

Acoustical Physics, Vol. 49, No. 5, 2003, pp. 491–495. Translated from Akusticheskiĭ Zhurnal, Vol. 49, No. 5, 2003, pp. 585–589.

Reconstruction of a Complex-Shaped Defect from the Known Arrival Time of the Reflected Ultrasonic Wave

N. V. Boev, V. M. Zotov, and É. A. Troyan

Rostov State University, ul. Bol'shaya Sadovaya 105, Rostov-on-Don, 344006 Russia

Research Institute of Mechanics and Applied Mathematics of Rostov State University, pr. Stachki 200/1, Rostov-on-Don, 344090 Russia

e-mail: boyev@math.rsu.ru

Received August 28, 2002

Abstract—The problem of reconstructing the boundary of an arbitrarily shaped defect formed inside an elastic body from the measured time of arrival of the reflected ultrasonic wave in the echo method is considered. The characteristic size of the defect is assumed to be greater than the wavelength, and the defect is irradiated from the far-field zone, which means that the incident wave can be considered as plane. An algorithm is developed for reconstructing the convex envelope of a nonconvex defect from the arrival times of echo signals measured at different angles with the use of circular scanning. © *2003 MAIK "Nauka/Interperiodica".*

The problem of reconstructing the shape of a defect in ultrasonic nondestructive testing belongs to the class of inverse problems of short-wave diffraction in continuous media. For example, at operating frequencies of 2–5 MHz commonly used in ultrasonic nondestructive testing, the wavelengths in metals are within 0.5–3 mm; at the same time, the characteristic size of the most harmful defects is 3–20 mm, which is an order of magnitude greater than the wavelength. We will consider the class of problems in which the distance between the defect and the boundary of the solid containing it is large compared to the irradiation wavelength. In addition, we assume that the sample under test can be irradiated in a circle (i.e., from all directions in one plane). Such a model of ultrasonic nondestructive testing can be realized, for example, by the immersion method [1, 2]. In the model proposed here, we assume that the unknown boundary of the defect is irradiated by plane ultrasonic waves at different angles varying in a circle (or around a sphere in the three-dimensional case, i.e., from all directions in space), and the measured quantities are the arrival time and the amplitude of the reflected echo wave in the far-field zone. When the defect is irradiated by the existing ultrasonic transducers in the echo mode of operation, one of the two wave types (longitudinal or transverse) predominates [2]. In the case of a normal transducer, the predominant waves are longitudinal, and in the case of a tilted transducer, the transverse waves prevail.

In solving the problem of reconstructing the shape of a defect, the general approach is based on the use of the known amplitude of the reflected wave in the far-field zone [3–10]. For defects of convex shape, stable algorithms already exist [4]. However, for a defect of arbitrary shape, the problem is complicated by the presence of multiple wave reflections from the nonconvex parts of the defect. For the special case when the surface bounding the defect has no more than two points of mirror reflection, a numerical method of defect reconstruction was developed in [6]. This method provides a stable reconstruction of a wide range of defect boundaries at high frequencies. In other publications [7–10], inverse diffraction problems were treated using direct numerical nonlinear optimization techniques. However, the latter are effective only in the low-frequency range. In this paper, we describe a method that reconstructs a convex envelope of a nonconvex defect surface, i.e., the minimal convex surface enveloping the initial surface, from the known arrival times of the reflected sound wave. Knowledge of such a convex envelope, which can be reconstructed in real time in the process of scanning, provides important information on the characteristic size and position of the defect. In some cases, this information may be sufficient to draw definite conclusions about the strength of the structural element under test.

Let us assume that, in practice, the ultrasonic scanning of an elastic body is performed with the help of an ultrasonic transducer in such a way that the obstacle located inside this body and bounded by an unknown surface S can be irradiated from all directions (in a circle in the two-dimensional case) by ultrasonic pulses with a high-frequency sine carrier. This situation can be realized, for example, when a solid is insonified by the immersion method [1, 2]. In this case, for any given direction $\mathbf{q}$, the known quantities are the travel time of the echo pulse $t(\mathbf{q})$ and the real amplitude of the reflected wave $|A(\mathbf{q})|$. If the number of the sine carrier periods within a single pulse is sufficiently great, the problem can be studied using the approximation of

1063-7710/03/4905-0491$24.00

steady-state harmonic oscillations. We denote the convex parts of the surface S by S_e and the concave parts, by S_i. We restrict our consideration to the obstacles whose simply connected surfaces have smooth convex parts S_e and smooth junctions between the parts S_e and S_i.

We describe the surface S bounding the defect in a Cartesian coordinate system $OX_1X_2X_3$ whose origin of coordinates O lies inside the surface. The irradiation direction $\mathbf{q}$ and the direction of the outer normal to the surface S are characterized by the direction cosines $\cos\alpha_1$, $\cos\alpha_2$, and $\cos\alpha_3$. When the defect is irradiated with echo pulses along any arbitrary direction $\mathbf{q} = \{-\cos\alpha_1, -\cos\alpha_2, -\cos\alpha_3\}$, where $\cos^2\alpha_1 + \cos^2\alpha_2 + \cos^2\alpha_3 = 1$, one point of mirror reflection is always present on S_e. The diffraction pattern due to the surface parts S_i is more complicated because of possible multiple reflections.

A closed surface S irradiated along the direction $\mathbf{q}$ has a point of mirror reflection at which the outer normal $\mathbf{n} = \{\cos\alpha_1, \cos\alpha_2, \cos\alpha_3\}$ to the surface is parallel to the direction $\mathbf{q}$. Therefore, it is convenient to consider the reconstructed geometric characteristics of S as functions of $\mathbf{n}$.

The construction of the convex envelope S_0 of the boundary surface S of the defect is possible by knowing only the function $t(\mathbf{q})$. From this function, we determine the reference function $p(\mathbf{n})$ (directly dependent on the known arrival time $t(\mathbf{n})$, where $\mathbf{n} \parallel \mathbf{q}$) as the distance from the center O to the plane characterized by the normal $\mathbf{n}$ and passing through the point of the wave reflection from the surface. The equation of this tangent plane has the form

$$\begin{aligned} &Q(x_1, x_2, x_3, \alpha_1, \alpha_2) \\ &= x_1\cos\alpha_1 + x_2\cos\alpha_2 + x_3\cos\alpha_3 - p(\alpha_1, \alpha_2) = 0. \end{aligned} \tag{1}$$

The convex envelope S_0 is the envelope of the two-parameter family of such tangent planes.

According to the classical theory [11], the boundary points lying on the surface S_0 are determined from the system of equations

$$\begin{aligned} Q(x_1, x_2, x_3, \alpha_1, \alpha_2) &= 0, \\ \frac{\partial Q}{\partial\alpha_1}(x_1, x_2, x_3, \alpha_1, \alpha_2) &= 0, \\ \frac{\partial Q}{\partial\alpha_2}(x_1, x_2, x_3, \alpha_1, \alpha_2) &= 0. \end{aligned} \tag{2}$$

With allowance for the relations

$$\begin{aligned} \frac{\partial\alpha_3}{\partial\alpha_1}\sin\alpha_3 &= -\sin\alpha_1\cos\alpha_1/\cos\alpha_3, \\ \frac{\partial\alpha_3}{\partial\alpha_2}\sin\alpha_3 &= -\sin\alpha_2\cos\alpha_2/\cos\alpha_3, \end{aligned}$$

which follow from Eq. (1), system (2) takes the form

$$\begin{aligned} &x_1\cos\alpha_1 + x_2\cos\alpha_2 + x_3\cos\alpha_3 = p(\alpha_1, \alpha_2), \\ &-x_1\sin\alpha_1\cos\alpha_3 + x_3\cos\alpha_1\sin\alpha_1 = p'_{\alpha_1}(\alpha_1, \alpha_2)\cos\alpha_3, \\ &-x_2\sin\alpha_2\cos\alpha_3 + x_3\cos\alpha_2\sin\alpha_2 = p'_{\alpha_2}(\alpha_1, \alpha_2)\cos\alpha_3. \end{aligned}$$

We solve this system of linear algebraic equations for the unknown coordinates x_1, x_2, and x_3. For this purpose, we can use, for example, Cramer's rule. As a result, we obtain the Cartesian coordinates of the points of the convex envelope S_0:

$$\begin{aligned} x_1 &= [p(\alpha_1, \alpha_2) + p'_{\alpha_2}(\alpha_1, \alpha_2)\cot\alpha_2]\cos\alpha_1 \\ &\quad - p'_{\alpha_1}(\alpha_1, \alpha_2)\sin\alpha_1, \\ x_2 &= [p(\alpha_1, \alpha_2) + p'_{\alpha_1}(\alpha_1, \alpha_2)\cot\alpha_1]\cos\alpha_2 \\ &\quad - p'_{\alpha_2}(\alpha_1, \alpha_2)\sin\alpha_2, \\ x_3 &= [p(\alpha_1, \alpha_2) + p'_{\alpha_1}(\alpha_1, \alpha_2)\cot\alpha_1 \\ &\quad + p'_{\alpha_2}(\alpha_1, \alpha_2)\cot\alpha_2]\cos\alpha_3, \end{aligned} \tag{3}$$

where $p'_{\alpha_i} = \partial p/\partial\alpha_i$ $(i = 1, 2, 3)$.

In practice, the scanning is performed for a discrete set of directions, along which the measurements are taken with certain errors. Since the expressions for the coordinates x_1, x_2, x_3 of the surface S_0 involve the derivatives of the reference function $p(\alpha_1, \alpha_2)$, the calculation of the coordinates presents an ill-posed problem [12]. Hence, the direct application of Eqs. (3) in practice is impossible, first, because of the inaccuracy in the determination of $t(\mathbf{q})$ and, second, because of the presence of a finite step in the angular coordinate, which is not always sufficiently small to provide a correct calculation of the derivatives of the reference function. Even for convex parts of the defect surface, the resulting function $p(\mathbf{n})$ will be only piecewise smooth, and its first derivatives p'_{α_i} $(i = 1, 2)$ used in constructing S_0 may differ from the true values not only in magnitude but also in sign.

With allowance for these features, we construct an algorithm that provides the approximation of $p(\alpha_1, \alpha_2)$ by some smooth function, so that the values of this function and its derivatives are close to the actual ones. In practical measurements, when instead of the smooth function one obtains its approximate values at nodal points, the basic element of the algorithm is the approximation of the desired function by cubic splines [12].

Assume that we know the approximate values p_i of some smooth function (in our case, the reference function $p(n)$) at the points $n_1, \ldots, n_N$ and the estimate Δp_i of the rms deviation of p_i from the true values of the function, $p(n_i)$. The laboratory measurements and the numerical experiments on reconstructing the shape of model defects (these studies are described below) show

that the estimate Δp_i does not exceed 10%. Let us construct a function $f = f_\delta$, which, for the given parameter $\delta \in [0, 1]$ determined by the rms deviation, minimizes the functional [13]

$$\Pi(f) = \delta\sum_{i=1}^{N}\left[\frac{p_i - f_i}{\Delta p_i}\right]^2 + (1-\delta)\int_{n_1}^{n_N}[f''(t)]^2 dt \quad (4)$$

over all functions f with derivatives up to the second order.

The minimization of $\Pi(f)$ represents a compromise between two requirements: the closest approach to the preset values p_i and the smoothness of the resulting function. The necessary equilibrium between these requirements is achieved by fitting δ.

The function f_δ is known to be a second-order spline with simple nodes at the points $n_2, \ldots, n_{N-1}$, and this spline satisfies the condition $f''_\delta(n_1) = f''_\delta(n_N) = 0$. For simplicity, we assume that the step Δn in n is constant. Introducing the notations $a_i = f_\delta(n_i)$ and $c_i = f''_\delta(n_i)$, where $i = 1, \ldots, N$, we obtain the following continuity conditions for the first derivatives of f_δ in the case of a closed contour:

$$\begin{aligned}(c_{i-1} + 4c_i + c_{i+1})(\Delta n)^2 &= 6(a_{i-1} - 2a_i + a_{i+1}),\\ (c_{N-1} + 4c_N + c_1)(\Delta n)^2 &= 6(a_{N-1} - 2a_N + a_1),\\ (c_N + 4c_1 + c_2)(\Delta n)^2 &= 6(a_N - 2a_1 + a_2),\\ i &= 2, 3, \ldots, N-1.\end{aligned} \quad (5)$$

The corresponding expression for functional (4) has the form

$$\Pi(f) = \delta\sum_{i=1}^{N}\left[\frac{p_i - a_i}{\Delta p_i}\right]^2 + \frac{(1-\delta)}{3}\Delta n\sum_{i=1}^{N}(c_i^2 + c_i c_{i+1} + c_{i+1}^2).$$

Applying to Eq. (5) the approximation of the second derivatives of the function by its central differences in the values of the function itself at three nodes, we arrive at the condition of the minimum of functional (4) in vectorial form:

$$\begin{aligned}\frac{-2\delta}{(\Delta p)^2}(\mathbf{p} - \mathbf{a}) + \frac{1-\delta}{12\Delta n}\mathbf{X}\mathbf{c} &= 0,\\ \mathbf{p} &= \{p_1, p_2, \ldots, p_N\},\\ \mathbf{a} = \{a_1, a_2, \ldots, a_N\}, \quad \mathbf{c} &= \{c_1, c_2, \ldots, c_N\},\end{aligned} \quad (6)$$

where $\mathbf{X}$ is a very sparse matrix. The nonzero elements of this matrix form a diagonal band, whose width covers five elements and also two sets of three elements in the upper right and lower left corners of the matrix; Δp is the maximal error, which makes one tenth of the characteristic size of the defect.

Now, we change to the vectorial form of Eqs. (5):

$$(\Delta n)^2\mathbf{R}\mathbf{c} = 6\mathbf{Q}\mathbf{a}, \quad (7)$$

where $\mathbf{R}$ and $\mathbf{Q}$ are very sparse matrices. In terms of structure, these matrices are three-diagonal with two nonzero elements: one nonlinear element in the upper right corner and one in the lower left corner. Substituting Eq. (7) into Eq. (6), we obtain a system of linear algebraic equations for the determination of the vector $\mathbf{c}$ of the second derivatives:

$$\left(\frac{2\delta(\Delta n)^2}{(\Delta p)^2}\mathbf{R} + \frac{1-\delta}{2\Delta n}6\mathbf{Q}\mathbf{X}\right)\mathbf{c} = \frac{12\delta}{(\Delta p)^2}\mathbf{Q}\mathbf{p}. \quad (8)$$

To investigate the solution of this system of equations, it is convenient to use the parameter M given by the formula

$$M = \sum_{i=1}^{N}\left[\frac{p_i - a_i}{\Delta p}\right]^2 = \frac{(1-\delta)^2(\Delta p)^2}{(24\delta\Delta n)^2}\sum_{i=1}^{N}(\mathbf{X}\mathbf{c})_i^2.$$

With the parameter M, the search for the solution is reduced to the determination of such a minimal value of the parameter $\delta \in [0, 1]$ at which the value of M obtained for the vector of second derivatives found from system (8) is smaller than a certain preset value L.

After vector $\mathbf{c}$ is determined, from Eq. (6) we obtain vector $\mathbf{a}$ of the values of the function f_δ at the nodes:

$$\mathbf{a} = \mathbf{p} - \frac{(1-\delta)(\Delta p)^2}{24\delta\Delta n}\mathbf{X}\mathbf{c}$$

and the piecewise polynomial representation of the function f:

$$\begin{aligned}f_\delta(n_i) &= a_i,\\ f'_\delta(n_i) &= \frac{\Delta a_i}{\Delta n_i} - \frac{f''_\delta(n_i)}{2\Delta n_i} - \frac{f'''_\delta(n_i^+)}{6(\Delta n_i)^2},\\ f''_\delta(n_i) &= c_i,\\ f'''_\delta(n_i^+) &= \frac{f''_\delta(n_{i+1}) - f''_\delta(n_i)}{\Delta n_i}.\end{aligned}$$

The number L should be chosen between $\sqrt{2N}$ and N [13]. Such a choice allows us to obtain (with a small estimate of the rms deviation Δp_i) the function f_δ that yields a sufficiently close approximation of $p(n)$ together with its first and second derivatives at the points n_i.

It should be noted that, if the estimate of the rms deviation is wrong or if the way of choosing the number L is unknown, one should give up the choice and directly vary the smoothing parameter δ.

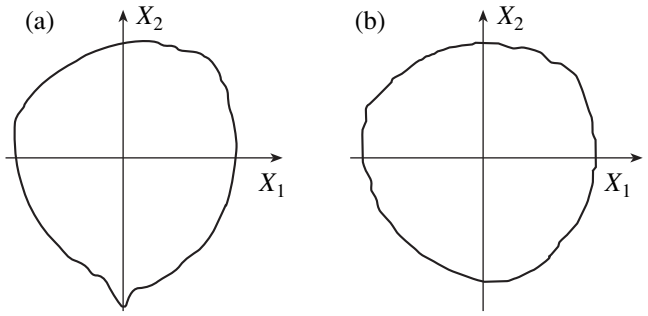

Fig. 1. Front of the reflected wave for different defects. Plots (a) and (b) correspond to the defects shaped as shown in Figs. 2a and 2b, respectively.

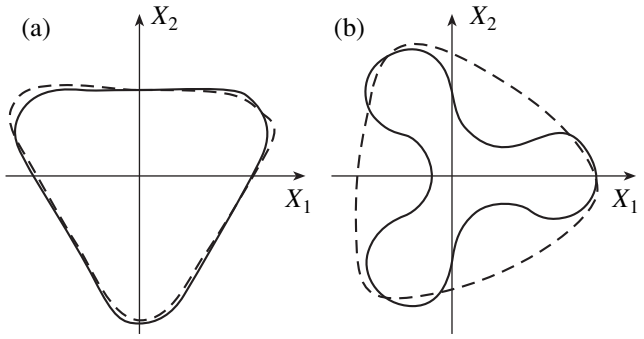

Fig. 2. Reconstruction of the defects of different shapes (the dashed lines). The solid lines show the actual shapes of the defects.

By substituting the resulting piecewise polynomial approximation of $p(n)$ into Eq. (1), we obtain the desired surface of the convex envelope S_0 of the defect under study.

The approach proposed above was tested in application to cylindrical defects of different cross sections, which were made at the centers of aluminum plates 65 mm in diameter and 25 mm in height. The characteristic size of the defect cross sections varied within 10–15 mm. The generatrix of a defect was parallel to the generatrix of the plate. To detect the defects, we used the immersion method of testing: the plate with the defect and an ultrasonic transducer were placed in a water bath at a distance of 30 mm from each other. The velocity of ultrasonic waves was 6100 m/s in aluminum (the wavelength $\lambda_l \sim 2.48$ mm) and 1490 m/s in water (the wavelength $\lambda \sim 0.6$ mm). The transducer was a standard normal one with a piezoelectric element 12 mm in diameter and with an operating frequency of 2.5 MHz. The arrival time of the reflected echo signal was measured using circular scanning with an angular step of 5° (the generatrix of the plate was parallel to the plane of the transducer). Figure 1 represents the measured travel time of the reflected signal between the defect and the generatrix of the plate versus the scanning angle. The plots shown in Figs. 1a and 2b were obtained for the defects shown by the solid lines in Figs. 2a and 2b, respectively.

With allowance made for the error in the time measurements, the inaccuracy in the fabrication of the model defects, and the relatively large step of the circular scanning, the total error Δp_i did not exceed 10% of the characteristic size of the defect cross section.

For the case under consideration, the Cartesian coordinates (1) of the convex envelope S_0 of the defect take the form [5]

$$x_1 = p(\alpha)\cos\alpha - p'_\alpha(\alpha)\sin\alpha,$$
$$x_2 = p(\alpha)\sin\alpha - p'_\alpha(\alpha)\cos\alpha,$$

where α is the angle between the normal to the defect boundary at the reflection point (x_1, x_2) and the positive direction of the OX_1 axis. In the realization of the proposed method of reconstructing S_0, the number L is $L \in [15, 25]$ at $N = 360°/5° = 72$, and the deviations Δp_i are about 10% of the characteristic size of the defect cross section. The cross sections of the convex and nonconvex defects made in the samples are shown by the solid lines in Figs. 2a and 2b, respectively. The dashed lines in the same plots represent the reconstruction of the defects with the use of the proposed method. The convex parts of the defect surfaces with weakly varying curvature (see Fig. 2) are reconstructed with a relative error of 0.5–2% (with respect to the characteristic size of the defect). As the curvature of the convex parts varies faster, the error increases up to 4%.

In conclusion, we summarize the results of the reconstruction as follows: the approach proposed in this paper provides the reconstruction of the convex envelope of an arbitrarily shaped defect on the basis of the values obtained experimentally for the time of arrival of the reflected ultrasonic wave from testing with a circular irradiation. The error in reconstructing the convex envelope of the defect with the use of circular scanning depends on the step in angle and on the error in measuring the arrival time of the reflected echo signal by present-day equipment.

ACKNOWLEDGMENTS

We are grateful to Prof. M.A. Sumbatyan for paying special attention to our work and for useful discussions.

This work was supported by the grant from the President of the Russian Federation in Support of Leading Scientific Schools no. NSh-2113.

REFERENCES

1. Yu. M. Shkarlet, *Contactless Methods of Ultrasonic Testing* (Mashinostroenie, Moscow, 1974).
2. I. N. Ermolov, *Theory and Practice of Ultrasonic Testing* (Mashinostroenie, Moscow, 1981).

3. M. A. Sumbatyan and N. V. Boev, Dokl. Akad. Nauk SSSR **318**, 880 (1991) [Sov. Phys. Dokl. **36**, 430 (1991)].
4. M. A. Sumbatyan and É. A. Troyan, Prikl. Mat. Mekh. **56** (3), 552 (1992).
5. N. V. Boev and M. A. Sumbatyan, Akust. Zh. **45**, 164 (1999) [Acoust. Phys. **45**, 133 (1999)].
6. I. I. Vorovich, N. V. Boyev, and M. A. Sumbatyan, Inverse Probl. Eng. **9** (4), 315 (2001).
7. M. Piana and M. Bertero, Inverse Probl. **13** (2), 441 (1997).
8. Monch Lars, Inverse Probl. **13** (5), 1379 (1997).
9. Kawamura Shoro, Ibuki Tatsuhiro, and Iwatsubo Takuzo, JSME Int. J., Ser. A **42** (3), 342 (1999).
10. V. A. Burov and I. P. Prudnikova, Akust. Zh. **45**, 759 (1999) [Acoust. Phys. **45**, 683 (1999)].
11. P. K. Rashevskiĭ, *Course of Differential Geometry*, 4th ed. (GITTL, Moscow, 1956).
12. A. N. Tikhonov and V. Ya. Arsenin, *Solutions of Ill-Posed Problems* (Nauka, Moscow, 1974; Halsted Press, New York, 1977).
13. C. de Boor, *A Practical Guide to Splines* (Springer, New York, 1978; Radio i Svyaz', Moscow, 1985).

Translated by E. Golyamina

Acoustical Physics, Vol. 49, No. 5, 2003, pp. 496–507. Translated from Akusticheskiĭ Zhurnal, Vol. 49, No. 5, 2003, pp. 590–603.

Uniqueness and Stability of the Solution to an Inverse Acoustic Scattering Problem

V. A. Burov and O. D. Rumyantseva

Faculty of Physics, Moscow State University, Vorob'evy gory, Moscow, 119992 Russia

e-mail: burov@phys.msu.su

Received October 17, 2002

Abstract—The uniqueness and stability of a discrete inverse scattering problem (functional description) is considered. The number of degrees of freedom, which determines the way of sampling for the functions of the scatterer and the secondary sources induced in it, may considerably vary from one problem to another, thus providing the adequacy of the discrete formulation of a specific problem. This number depends on the size of the scattering region in space and on the widths of the spatial spectra of both the scatterer and the secondary sources. Nonuniqueness of the solution occurs because of the configurations of secondary sources that exist in the scattering region and are not observable in any of the experiments. It is shown that precisely the number of degrees of freedom of the secondary sources determines the amount of discrete scattering data that is necessary to provide a unique solution. If this amount is collected in the experiments without exceeding a certain classical limiting resolution, the solution to the inverse problem is unique and stable. © *2003 MAIK "Nauka/Interperiodica".*

The inverse scattering problem, which is the problem of reconstructing the internal structure of an object sounded by wave fields, is a nonlinear ill-posed problem. This combination of properties makes analysis of the possible stability and uniqueness of its solution particularly complex and, at the same time, topical. In fact, the property of the problem of being ill-posed naturally leads to the instability of its solution. However, since the problem is nonlinear with respect to the scattering data measured experimentally, the nature of the uniqueness and stability of its solution may essentially change with increasing scatterer strength.

The purpose of this paper is to draw the reader's attention to the importance of the connection between the nonuniqueness and the instability of the solution of the inverse acoustic scattering problem for scatterers of an arbitrary strength and to the significance of the redundancy of experimental data, without claiming mathematical consistency and rigor in our presentation of the solution. This issue is nontrivial and allowance for these factors in solving applied problems is important, because the problem is nonlinear with respect to the characteristics of the scatterer. The analysis of this problem was started in [1], and this paper further elaborates upon it.

1. COMPARISON OF THE FUNCTIONAL DESCRIPTION OF THE SCATTERER WITH THE DESCRIPTION AS A SET OF POINT SCATTERERS: BROADENING OF THE SPATIAL SPECTRUM OF SECONDARY SOURCES

The acoustic scatterer created by irregularities of the acoustic phase velocity and by the attenuation factor and density of the medium is described by a function $\varepsilon(\mathbf{r})$. To reconstruct $\varepsilon(\mathbf{r})$, the scatterer is insonified by the incident field $U_0(\mathbf{r}, \alpha)$ whose parameters (including field configuration, incidence direction, and frequency) are characterized by a single index α. The interaction of U_0 and the scatterer induces secondary sources $I(\mathbf{r}, \alpha)$ in the scattering region $\Re$:

$$I(\mathbf{r}, \alpha) \equiv \varepsilon(\mathbf{r})U(\mathbf{r}, \alpha), \tag{1}$$

where $U(\mathbf{r}, \alpha)$ is the total field, which, in the single-frequency case, satisfies the Lippmann–Schwinger equation [2]

$$\begin{aligned} U(\mathbf{r}, \alpha) &= U_0(\mathbf{r}, \alpha) \\ &+ \int G(\mathbf{r} - \mathbf{r}', k_0)\varepsilon(\mathbf{r}')U(\mathbf{r}', \alpha)d\mathbf{r}' \quad \forall \mathbf{r}. \end{aligned} \tag{2}$$

Here, $G(\mathbf{r}, k_0)$ is the Green's function of the lossless infinite homogeneous medium with the wave number k_0 corresponding to the given α. As follows from formulas (1) and (2), the secondary sources produce the scattered field $u_{sc}(\mathbf{r}, \alpha) \equiv U(\mathbf{r}, \alpha) - U_0(\mathbf{r}, \alpha)$. Multiplying Eq. (2) by $\varepsilon(\mathbf{r})$ and performing the Fourier transformation in the $\mathbf{r}$ coordinate, we obtain the relationship that relates the spatial spectrum of the scatterer $\tilde{\varepsilon}(\boldsymbol{\xi}) \equiv \int \varepsilon(\mathbf{r})\exp(-i\boldsymbol{\xi}\mathbf{r})d\mathbf{r}$ to its secondary sources $\tilde{I}(\boldsymbol{\xi}, \alpha)$:

$$\begin{aligned} \tilde{I}(\boldsymbol{\xi}, \alpha) &= \tilde{I}_{\text{Born}}(\boldsymbol{\xi}, \alpha) \\ &+ \frac{1}{(2\pi)^p}\int \tilde{\varepsilon}(\boldsymbol{\xi} - \boldsymbol{\xi}')\tilde{G}(|\boldsymbol{\xi}'|, k_0)\tilde{I}(\boldsymbol{\xi}', \alpha)d\boldsymbol{\xi}', \end{aligned} \tag{3}$$

1063-7710/03/4905-0496$24.00 © 2003 MAIK "Nauka/Interperiodica"

where p is the number of dimensions of the space and $\tilde{G}(\boldsymbol{\xi}, k_0) = \tilde{G}(|\boldsymbol{\xi}|, k_0)$ is the spatial spectrum of the Green's function. The single-scattering approximation (Born approximation) assumes that $U(\mathbf{r}, \alpha) \approx U_0(\mathbf{r}, \alpha)$ for $\mathbf{r} \in \Re$; then $\tilde{I}(\boldsymbol{\xi}, \alpha) \approx \tilde{I}_{\text{Born}}(\boldsymbol{\xi}, \alpha)$, where

$$\tilde{I}_{\text{Born}}(\boldsymbol{\xi}, \alpha) = \frac{1}{(2\pi)^p}\int \tilde{\varepsilon}(\boldsymbol{\xi} - \boldsymbol{\xi}')\tilde{U}_0(\boldsymbol{\xi}', \alpha)d\boldsymbol{\xi}', \quad (4)$$

and $\tilde{U}_0(\boldsymbol{\xi}, \alpha)$ is the spatial spectrum of the incident field.

In the simplest case, a scatterer with a complicated structure is represented as a set S of point scatterers located at the points $\mathbf{r}_s$, $s = \overline{1, S}$:

$$\varepsilon(\mathbf{r}) = \sum_{s=1}^{S} \varepsilon_s \delta(\mathbf{r} - \mathbf{r}_s). \quad (5)$$

The scattering capability ε_s includes all internal processes of scattering by these infinitesimal scatterers. As a result, ε_s associated with each point scatterer characterizes the secondary source excited only by fields that are external with respect to the point scatterer, i.e., by the fields produced by primary field sources and by the fields scattered by the remaining point scatterers. In other words, ε_s is the renormalized coefficient of proportionality between the amplitude of the secondary source produced by the external field at the point $\mathbf{r}_s$ and the local value of this field, which excites the scatterer. The renormalization removes the singularity in the Lippmann–Schwinger equation (2) in the limiting case of point sources.

As follows from representation (5), secondary sources (1) appear only at the points $\mathbf{r}_s$. Therefore, the number of degrees of freedom that describe the scatterer and secondary sources is the same and is independent of the scatterer's strength. In the general case of a spatially distributed scatterer, it is defined by a function $\varepsilon(\mathbf{r})$, which must be reconstructed over the entire continuum of $\mathbf{r} \in \Re$. If the scatterer is strong enough (so that the multiple scattering processes inside $\Re$ are significant), the region in which the main portion of the spatial spectrum $\tilde{I}(\boldsymbol{\xi}, \alpha)$ of the secondary sources is localized proves to be broader than that for the scatterer spectrum $\tilde{\varepsilon}(\boldsymbol{\xi})$ [3–6]. The broadening effect is seen directly when expanding (3) into the Born–Neumann series [2, 6] in powers of $\tilde{\varepsilon}(\boldsymbol{\xi})$. The process is governed by two mechanisms. On the one hand, each new scattering event broadens the spectrum $\tilde{I}(\boldsymbol{\xi}, \alpha)$. On the other hand, the main portion of $\tilde{G}(|\boldsymbol{\xi}|, k_0)$ is concentrated near the Ewald surface ($|\boldsymbol{\xi}| = k_0$) and therefore exhibits a filtering effect [3]: the convolution in Eq. (3) restrains the broadening of the spectrum $\tilde{I}(\boldsymbol{\xi}, \alpha)$. As a result, if $\tilde{\varepsilon}(\boldsymbol{\xi})$ is sufficiently well localized in a certain domain of spatial frequencies, $\tilde{I}(\boldsymbol{\xi}, \alpha)$ may also appear to be well localized, although its support is not strictly finite. The stronger the scatterer is, the broader the localization region of $\tilde{I}(\boldsymbol{\xi}, \alpha)$ compared with that of $\tilde{\varepsilon}(\boldsymbol{\xi})$.

For the discrete mathematical description of the scattering process to be adequate, this circumstance should be taken into account. For instance, it is often convenient to represent the functions $\varepsilon(\mathbf{r})$ and $I(\mathbf{r}, \alpha)$ as expansions into the basis functions $\{\zeta_s(\mathbf{r})\}$ and $\{\Psi_k^\alpha(\mathbf{r})\}$:

$$\varepsilon(\mathbf{r}) = \sum_{s=1}^{S} \varepsilon_s \zeta_s(\mathbf{r}), \quad I(\mathbf{r}, \alpha) = \sum_{k=1}^{N_\alpha} \theta_k^\alpha \Psi_k^\alpha(\mathbf{r}), \quad (6)$$

where ε_s and θ_k^α are the expansion coefficients. Formulas (6) assume that the necessary accuracy is provided by a finite number of their terms. The basis functions $\{\zeta_s(\mathbf{r})\}$ and $\{\Psi_k^\alpha(\mathbf{r})\}$ and their dimensions S and N_α must be consistent with widths of the spatial spectra and overall sizes of the scatterer and secondary sources, respectively. These values can be estimated based on prior information about the statistical classification of the scatterers being reconstructed. Such an estimation method will be addressed in a separate paper.

These basis functions may be chosen in an economical or uneconomical manner. The economical manner takes the number of functions $\{\zeta_s(\mathbf{r})\}$ in Eqs. (6) equal to the number S of the scatterer's independent degrees of freedom. The number of the functions $\{\Psi_k^\alpha(\mathbf{r})\}$ is taken equal to the number N_α of the independent degrees of freedom that characterize $I(\mathbf{r}, \alpha)$ at a particular α. By "independent degrees of freedom" we understand such a combination of parameters (in this case, parameters that give a sufficiently full description of the scatterer or secondary sources) that, being averaged over a multitude of scatterers of a particular type, provide a cross-correlation coefficient that is much less than unity; then, none of these parameters can be reconstructed from the remaining ones. Consequently, the secondary sources must in the general case be described in terms of a fuller basis that is consistent with their broadened spatial spectrum. The uneconomical manner may use a common basis to describe both $\varepsilon(\mathbf{r})$ and $I(\mathbf{r}, \alpha)$ at all α [7]. The spatial sampling of the functions $\varepsilon(\mathbf{r})$ and $I(\mathbf{r}, \alpha)$ (or the internal fields) consistent with the sampling theorem can also be performed in two ways. The first way is to sample both functions in accordance with the total (in α) width of the spectra $\tilde{I}(\boldsymbol{\xi}, \alpha)$. The second way is to introduce two spatial grids with different spacings: one of them samples $\varepsilon(\mathbf{r})$; the other (a finer one) samples $I(\mathbf{r}, \alpha)$ [8]. The number of independent spatial samples in both cases however equals S for $\varepsilon(\mathbf{r})$ and N_α for $I(\mathbf{r}, \alpha)$ at each particular α.

For the point-scatterer representation given by Eq. (5), all bases in (6) are inherently the same, because they are represented by linear combinations of the functions $\{\delta(\mathbf{r} - \mathbf{r}_s)\}$; then, $N_\alpha = S$ at α.

2. THE POSSIBILITY OF A NONUNIQUE RECONSTRUCTION OF STRONG SCATTERERS: THE CONDITIONS FOR A UNIQUE AND STABLE RECONSTRUCTION

We say that a scatterer is weak if $|u_{sc}(\mathbf{r}, \alpha)| \ll |U_0(\mathbf{r}, \alpha)|$ for $\mathbf{r} \in \Re$; then $N_\alpha = S\ \forall\alpha$. For a scatterer of medium strength, at no point of the scattering region does the scattered field exceed the incident one: $|u_{sc}(\mathbf{r}, \alpha)| < |U_0(\mathbf{r}, \alpha)|\ \forall\mathbf{r} \in \Re$. Finally, for a strong scatterer, among the incident fields, a field can be found for which $|u_{sc}(\mathbf{r}, \alpha)| > |U_0(\mathbf{r}, \alpha)|$ at least at one point $\mathbf{r} \in \Re$. It is important that, for a scatterer consisting of a number of point scatterers, $u_{sc}(\mathbf{r}, \alpha)$ denotes the scattered field created at the points of their locations $\{\mathbf{r}_s\}$ by all the point sources, except for the scatterer located at the point of interest $\mathbf{r} = \mathbf{r}_s \in \Re$, where $\Re \equiv \bigcup_s \mathbf{r}_s$.

It is known that the reconstruction of a strong scatterer is nonunique, which is most simple to illustrate by the existence of invisible scatterers. Let a finite number A of experiments be performed and each of the experiments be associated with a particular incident sounding field $U_0(\mathbf{r}, \alpha)$, $\alpha = \overline{1, A}$ and with a finite number of different observations of the scattered field (scattering data). Each experiment records (outside $\Re$) B values $u_{sc}(\mathbf{y}_b, \alpha)$, where $\mathbf{y}_b \notin \Re$ and the index $b = \overline{1, B}$, b describes a fixed number of the receiver's parameters (for instance, its location). The total number of the scattering data collected in all the experiments is AB. The invisible scatterer is the scatterer for which all of the AB data (this number is finite) values are zero: $u_{sc}(\mathbf{y}_b, \alpha) = 0$ for $\alpha = \overline{1, A}$ and $b = \overline{1, B}$. It should be noted that, in this paper we consider a finite number (rather than a continuum) of zero data. Indeed, a scatterer in the form of a set of point scatterers cannot produce any field outside the region $\Re$ even for one particular $U_0(\mathbf{r}, \alpha)$ (by definition, a scatterer is called a nonradiative scatterer at a particular α if $u_{sc}(\mathbf{y}, \alpha) \equiv 0$ for $\mathbf{y} \notin \Re$). At the same time, a spatially distributed scatterer can be a nonradiative scatterer for one particular field $U_0(\mathbf{r}, \alpha)$ [9]. For a continuum of incident fields, only a scatterer whose $\varepsilon(\mathbf{r})$ decreases with distance no faster than a certain function may be a nonradiative scatterer [10].

The subsequent analysis relies on the general relationships for the observed scattered field, irrespective of the particular technique used for solving the inverse problem. To derive these relationships, it is convenient to represent the functions that enter into Eq. (2) in discrete form and, as in [3, 4], introduce the following operators: $\hat{\varepsilon}$ is the diagonal operator defined by the discrete values of $\varepsilon(\mathbf{r})$, U_0^α is the column vector of discrete values of $U_0(\mathbf{r}, \alpha)$, and $\hat{Q}_{out}$ and $\hat{Q}_{in}$ are the operators with the Green's function as the kernel ($\hat{Q}_{out}$ acts from $\Re$ to the observation region outside $\Re$ and $\hat{Q}_{in}$ acts inside $\Re$) defined as

$$\hat{Q}_{out}(\mathbf{y}_b, \mathbf{r}')(\bullet) \equiv \int G(\mathbf{y}_b - \mathbf{r}', k_0)(\bullet)d\mathbf{r}';$$

$$\hat{Q}_{in}(\mathbf{r}, \mathbf{r}')(\bullet) \equiv \int G(\mathbf{r} - \mathbf{r}', k_0)(\bullet)d\mathbf{r}';$$

$$\mathbf{y}_b \notin \Re; \quad \mathbf{r}, \mathbf{r}' \in \Re.$$

The variables in the parentheses of the operators are actually arguments of the related kernels. Equation (2) should be satisfied at the observation points inside $\Re$ and outside it as well:

$$U(\mathbf{r}, \alpha) = U_0(\mathbf{r}, \alpha) + \hat{Q}_{in}\hat{\varepsilon}U, \quad \mathbf{r} \in \Re; \tag{7}$$

$$U(\mathbf{y}_b, \alpha) = U_0(\mathbf{y}_b, \alpha) + \hat{Q}_{out}\hat{\varepsilon}U, \quad \mathbf{y}_b \notin \Re. \tag{8}$$

Relationship (7) multiplied by $\hat{\varepsilon}$ yields the function of secondary sources [4]

$$I(\mathbf{r}, \alpha) \equiv \hat{\varepsilon}U = [\hat{E} - \hat{\varepsilon}\hat{Q}_{in}]^{-1}\hat{\varepsilon}U_0^\alpha, \tag{9}$$

where $\hat{E}$ is the unit operator (for passive media, all eigenfunctions of the operator $\hat{E} - \hat{\varepsilon}\hat{Q}_{in}$ are complex-valued [11] and, therefore, the inverse operator always exists). Let us substitute relationship (9) into Eq. (8):

$$u_{sc}^\alpha = \hat{Q}_{out}[\hat{E} - \hat{\varepsilon}\hat{Q}_{in}]^{-1}\hat{\varepsilon}U_0^\alpha, \tag{10}$$

where u_{sc}^α is the column vector composed of discrete values $u_{sc}(\mathbf{y}_b, \alpha)$. Applying the Hermitian conjugate operator $\hat{Q}_{out}^+$ to Eq. (10), we obtain

$$\hat{Q}_{out}^+ u_{sc}^\alpha = \hat{Q}_{out}^+\hat{Q}_{out}[\hat{E} - \hat{\varepsilon}\hat{Q}_{in}]^{-1}\hat{\varepsilon}U_0^\alpha. \tag{11}$$

In the discrete representation, the operator $\hat{Q}_{out}^+\hat{Q}_{out}$, which acts on $I(\mathbf{r}', \alpha)$, is a square matrix independent of α. Therefore, the set of all eigenvectors of this operator (matrix), which at the same time are the Schmidt fundamental union elements of the pair of operators $\hat{Q}_{out}$ and $\hat{Q}_{out}^+$ [2], could be used as a basis for the secondary sources $I(\mathbf{r}, \alpha)$ for all α. However, when used to functionally describe a scatterer $I(\mathbf{r}, \alpha)$, this basis is not economical for each particular α. Therefore, below we will attempt to find an economical basis to describe the secondary sources at any U_0^α. To this end, we introduce the projection operator $\hat{P}^\alpha(\mathbf{r}', \mathbf{r}'')(\bullet) \equiv \int P(\mathbf{r}', \mathbf{r}'', \alpha)(\bullet)d\mathbf{r}''$, $(\mathbf{r}', \mathbf{r}'' \in \Re)$, which acts in the space of secondary sources, into Eqs. (2), (10), and (11). The space of secondary sources is the function space spanned by

functions that describe the secondary sources produced by scatterers of a particular type in response to incident fields with all permissible α. The operator $\hat{P}^{\alpha}$ extracts from all possible secondary sources only the sources that can be produced by the given particular U_0^{α}: $\int P(\mathbf{r}', \mathbf{r}'', \alpha) I(\mathbf{r}'', \alpha) d\mathbf{r}'' = I(\mathbf{r}', \alpha)$. For example, from the $\boldsymbol{\xi}$-representation, the projector $\hat{P}^{\alpha}$ extracts the spatial frequency domain that contains components of $\tilde{I}(\boldsymbol{\xi}, \alpha)$ for the given incident field, so that these components remain unaffected. Then, we have

$$u_{\mathrm{sc}}^{\alpha} = \hat{Q}_{\mathrm{out}}\hat{P}^{\alpha}[\hat{E} - \hat{\varepsilon}\hat{Q}_{\mathrm{in}}]^{-1}\hat{\varepsilon}U_0^{\alpha}; \tag{12}$$

$$\hat{P}^{\alpha}\hat{Q}_{\mathrm{out}}^{+}u_{\mathrm{sc}}^{\alpha} = \hat{P}^{\alpha}\hat{Q}_{\mathrm{out}}^{+}\hat{Q}_{\mathrm{out}}\hat{P}^{\alpha}[\hat{E} - \hat{\varepsilon}\hat{Q}_{\mathrm{in}}]^{-1}\hat{\varepsilon}U_0^{\alpha}. \tag{13}$$

Relationships (10) and (11) are equivalent to Eqs. (12) and (13). At the same time, the eigenvectors of the Hermitian operator $\hat{P}^{\alpha}\hat{Q}_{\mathrm{out}}^{+}\hat{Q}_{\mathrm{out}}\hat{P}^{\alpha}$ represented as an $N_{\alpha} \times N_{\alpha}$ square matrix that acts on the discrete vectors $I(\mathbf{r}_n, \alpha)$ ($n = \overline{1, N_{\alpha}}$; below, we assume for simplicity that $N_{\alpha} \approx N$ for α) form the desired economical basis for the secondary sources produced by a particular incident field. This operator is a degenerate operator. Its rank is B, because we assume that the tomographic experiment is arranged so that a weak scatterer ($N = S$) can be uniquely reconstructed from complete nonredundant ($AB = S$) scattering data. Such an arrangement can always be provided by appropriately choosing the primary fields and the characteristics of the receiving system. The rescattering processes increase the number of degrees of freedom that characterize the secondary sources and, hence, cannot reduce this rank. Therefore, among N linearly independent eigenvectors of the operator $\hat{P}^{\alpha}\hat{Q}_{\mathrm{out}}^{+}\hat{Q}_{\mathrm{out}}\hat{P}^{\alpha}$, B ($B < N$) eigenvectors $\{\eta_k^{\alpha}(\mathbf{r}_n)\}_{n=\overline{1,N}}^{k=\overline{1,B}}$ correspond to nonzero eigenvalues and describe the part of the secondary sources observed by the receivers. The remaining $N - B$ eigenvectors $\{\psi_k^{\alpha}(\mathbf{r}_n)\}_{n=\overline{1,N}}^{k=\overline{1,N-B}}$ correspond to zero eigenvalues and describe the part of the secondary sources not observed by the receiving system. It is convenient to choose these very N eigenvectors as the economical basis $\{\Psi_k^{\alpha}(\mathbf{r}_n)\}_{n=\overline{1,N}}^{k=\overline{1,N}}$ (see Eqs. (6)). Then, as follows from Eqs. (9) and (13), for a particular U_0^{α}, the secondary sources can be represented in terms of B observable configurations and $N - B$ nonobservable configurations:

$$I(\mathbf{r}_n, \alpha) = [\hat{E} - \hat{\varepsilon}\hat{Q}_{\mathrm{in}}]^{-1}\hat{\varepsilon}U_0^{\alpha} = \sum_{k=1}^{B} g_k^{\alpha}\eta_k^{\alpha}(\mathbf{r}_n) + \sum_{i=1}^{N-B} a_i^{\alpha}\psi_i^{\alpha}(\mathbf{r}_n), \quad \alpha = \overline{1, A},$$

where $\{g_k^{\alpha}\}$ and $\{a_i^{\alpha}\}$ are the appropriate expansion coefficients.

By definition, for the invisible scatterer $\varepsilon(\mathbf{r}) \equiv \varepsilon_{\mathrm{inv}}(\mathbf{r})$, we have $\{g_k^{\alpha}\} \equiv 0$ for $\alpha = \overline{1, A}$; i.e.,

$$I(\mathbf{r}_n, \alpha) = [\hat{E} - \hat{\varepsilon}_{\mathrm{inv}}\hat{Q}_{\mathrm{in}}]^{-1}\hat{\varepsilon}_{\mathrm{inv}}U_0^{\alpha} = \sum_{i=1}^{N-B} a_i^{\alpha}\psi_i^{\alpha}(\mathbf{r}_n), \quad \alpha = \overline{1, A}, \quad \text{which yields} \tag{14}$$

$$\hat{\varepsilon}_{\mathrm{inv}}\left[U_0^{\alpha} + \sum_{i=1}^{N-B} a_i^{\alpha}\Phi_i^{\alpha}\right] = \left[\sum_{i=1}^{N-B} a_i^{\alpha}\psi_i^{\alpha}\right], \quad \Phi_i^{\alpha} \equiv \hat{Q}_{\mathrm{in}}\psi_i^{\alpha}. \tag{15}$$

Because $\hat{\varepsilon}_{\mathrm{inv}}$ is a diagonal operator, at an arbitrary point $\mathbf{r}$, we have

$$\varepsilon_{\mathrm{inv}}(\mathbf{r}) = \left[\sum_{i=1}^{N-B} a_i^{\alpha}\psi_i^{\alpha}(\mathbf{r})\right] \Big/ \left[U_0(\mathbf{r}, \alpha) + \sum_{i=1}^{N-B} a_i^{\alpha}\Phi_i^{\alpha}(\mathbf{r})\right]. \tag{16}$$

The unknown coefficients $\{a_i^{\alpha}\}_{i=\overline{1,N-B}}^{\alpha=\overline{1,A}}$ satisfy the relationships

$$U(\mathbf{r}_n, \alpha_1)I(\mathbf{r}_n, \alpha_2) = U(\mathbf{r}_n, \alpha_2)I(\mathbf{r}_n, \alpha_1) \quad \left(\text{or } I(\mathbf{r}, \alpha_2) = I(\mathbf{r}, \alpha_1)\frac{U(\mathbf{r}, \alpha_2)}{U(\mathbf{r}, \alpha_1)}\ \forall \mathbf{r}\right), \tag{17}$$

which are valid for any pair ($\alpha = \alpha_1$, $\alpha = \alpha_2$) by virtue of relationship (1). Since, according to Eq. (7), $U = U_0 + \hat{Q}_{\mathrm{in}}I$ ($\mathbf{r} \in \Re$), the substitution of Eq. (14) into Eqs. (17), with α_1 alone fixed, gives

$$\sum_{i=1}^{N-B} Z_i^{\alpha_2\alpha_1}(\mathbf{r}_n)a_i^{\alpha_1} - \sum_{j=1}^{N-B} Z_j^{\alpha_1\alpha_2}(\mathbf{r}_n)a_j^{\alpha_2} + \sum_{i=1}^{N-B}\sum_{j=1}^{N-B} M_{ij}^{\alpha_1\alpha_2}(\mathbf{r}_n)a_i^{\alpha_1}a_j^{\alpha_2} = 0, \quad \alpha_2 = \overline{1, A}, \quad \alpha_2 \neq \alpha_1, \tag{18}$$

where $Z_j^{\alpha_1\alpha_2}(\mathbf{r}_n) \equiv U_0(\mathbf{r}_n, \alpha_1)\psi_j^{\alpha_2}(\mathbf{r}_n)$, $Z_i^{\alpha_2\alpha_1}(\mathbf{r}_n) \equiv U_0(\mathbf{r}_n, \alpha_2)\psi_i^{\alpha_1}(\mathbf{r}_n)$, and $M_{ij}^{\alpha_1\alpha_2}(\mathbf{r}_n) \equiv \psi_i^{\alpha_1}(\mathbf{r}_n)\Phi_j^{\alpha_2}(\mathbf{r}_n) - \psi_j^{\alpha_2}(\mathbf{r}_n)\Phi_i^{\alpha_1}(\mathbf{r}_n)$ are known. The number of unknowns $\{a_i^\alpha\}_{i=\overline{1, N-B}}^{\alpha=\overline{1, A}}$ in system (18) is $(N - B)A$, and it is necessary to find the number of independent equations in the system. (By independent equations, we mean such equations that, if any of them is excluded from the system, the set of admissible solutions becomes wider.) The number of different pairs (α_1, α_2) at a particular α_1 is $(A - 1)$. For any other pair (α', α''), equalities (17) are an evident consequence of the equalities considered above for the pairs $(\alpha_1; \alpha_2 = \alpha')$ and pairs $(\alpha_1; \alpha_2 = \alpha'')$, and, therefore, they do not produce new independent equations like Eqs. (18). For a particular pair (α_1, α_2), relationships (17) (and, hence, (18)) can be considered at N points $\{\mathbf{r}_n\}_{n=\overline{1, N}}$ where the secondary sources are statistically independent. We mean that, at a particular α, $I(\mathbf{r}_n, \alpha)$ at any point $\mathbf{r}_n$ cannot be expressed in terms of its values at the remaining points by a rule that is common for all scatterers of the class considered. Thus, the total number of independent equations in (18) is $N(A - 1)$. Each particular set $\{a_i^\alpha\}$ that is a solution vector of system (18) is associated with a type of invisible scatterer derived from Eq. (16).

Scatterers considered in [2, pp. 124–127] are indistinguishable (in terms of the discrete measurement scheme under study) from a given scatterer $\varepsilon_f(\mathbf{r})$; i.e., the scattered fields $u_{sc}(\mathbf{y}_b, \alpha)$ ($\alpha = \overline{1, A}$ and $b = \overline{1, B}$) observed in the given number of experiments with transmit–receive elements whose parameters are discrete are the same for $\varepsilon_f(\mathbf{r})$ and the corresponding indistinguishable scatterers. System (18) for invisible scatterers is a particular case of the system of equations for indistinguishable scatterers at $\varepsilon_f \equiv 0$. The number of indistinguishable scatterers (which certainly equals the number of solutions to the inverse scattering problem described by our discrete measurement scheme) is determined by the number of solutions to a system of equations analogous to Eqs. (18). This number (not known exactly), on the one hand, depends on the total number $N(A - 1)$ of independent equations in a system analogous to system (18) and the number $(N - B)A$ of unknowns $\{a_i^\alpha\}_{i=\overline{1, N-B}}^{\alpha=\overline{1, A}}$. On the other hand, when evaluating this number, one should impose the requirement that the passive scatterer be physically feasible: the sign of the imaginary part of the refractive index must correspond to a lossy medium. Information about the width of the scatterer's spatial spectrum may also impose certain constraints.

It should be emphasized once more that system (18) does not describe a method for solving the inverse scattering problem. It is only intended for analyzing the possibility that invisible and indistinguishable scatterers will occur; i.e., it serves to analyze the uniqueness of the solution. A zero solution $\{a_i^\alpha\} \equiv 0$ $(\forall i, \forall\alpha)$ to a system of equations analogous to system (18), which corresponds to the absence of scatterers or to a true scatterer $\varepsilon_f(\mathbf{r})$, is always present. If this solution is unique, the solution to the inverse problem is also unique. However, in the general case, if the number of equations in the system is equal to the number of unknowns, its solution is not unique, because the system is nonlinear due to the cross terms $a_i^{\alpha_1}a_j^{\alpha_2}$. Therefore, the necessary condition for the solution to the inverse scattering problem to be unique is that the amount of scattering data be increased so as to make system (18) overdetermined:

$$(N - B)A < N(A - 1), \quad \text{or} \quad AB > N. \tag{19}$$

The true solution automatically satisfies all equations of the overdetermined system because, being associated with the same scatterer, they have the same physical origin.

Condition (19) relates the amount AB of the experimental scattering data to the number N of degrees of freedom of the secondary sources. It is important that, first, A and B appear symmetrically, which agrees with the reciprocity theorem. Second, formula (19) contains the number N of independent parameters that describe the function $I(\mathbf{r}, \alpha)$ for only one incident field, because, if we know $I(\mathbf{r}, \alpha_1)$ at only one $\alpha = \alpha_1$, we can find $I(\mathbf{r}, \alpha)$ for any arbitrary α. Specifically, Eq. (7) yields $U(\mathbf{r}, \alpha_1) = U_0(\mathbf{r}, \alpha_1) + \hat{Q}_{in} I(\mathbf{r}', \alpha_1)$, $\mathbf{r} \in \Re$. Then, $\varepsilon(\mathbf{r}) = I(\mathbf{r}, \alpha_1)/U(\mathbf{r}, \alpha_1)$ and $I(\mathbf{r}, \alpha)$ can be found from Eq. (9) for α. Third, when we analyzed the number of invisible scatterers (or indistinguishable scatterers), i.e., the number of solutions to system (18), we assumed that the secondary sources associated with all these scatterers are described by the same number N of independent parameters and can be expanded in terms of the same basis for any particular incident field. At the same time, the characteristics of the scatterers (the number S of their independent parameters and the scatterer's basis functions) may be different. However, if the scattering problem is solved taking into account some prior information about the scatterer (which will be detailed below), condition (19) may be relaxed.

If the amount of scattering data required for the unique scatterer reconstruction can be collected in the set of experiments conducted and the scheme used to collect the discrete data is not required to go beyond the classical Rayleigh limit for the angular resolution, the solution to the inverse problem is unique and stable. Explicitly, to provide stability, the angular separation between adjacent transmit–receive elements of the antenna array (or between adjacent angles of both incident and scattered waves) must be no less than the Rayleigh angle $\Delta\varphi_{Rayl}$ in the two-dimensional problem or

$\Delta\Omega_{\text{Rayl}}$ in the three-dimensional problem ($\Delta\Omega_{\text{Rayl}}$ has the meaning of an average solid angle per one element):

$$\Delta\varphi_{\text{Rayl}} \cong \frac{\lambda_0/2}{L/2} = \frac{2\pi}{k_0 L};$$
$$\Delta\Omega_{\text{Rayl}} \cong \left(\frac{\lambda_0/2}{L/2}\right)^2 = \left(\frac{2\pi}{k_0 L}\right)^2, \quad (20)$$

where λ_0 is the wavelength and L is the linear dimension of the region $\Re$. Consequently, if the data collection scheme uses a circular array, the maximum number of the array elements that satisfies the stability condition is $M^{(2)}_{\text{Rayl}}$ for the two-dimensional arrangement and $M^{(3)}_{\text{Rayl}}$ for the three-dimensional arrangement:

$$M^{(2)}_{\text{Rayl}} \cong 2\pi/\Delta\varphi_{\text{Rayl}} \cong k_0 L;$$
$$M^{(3)}_{\text{Rayl}} \cong 4\pi/\Delta\Omega_{\text{Rayl}} \cong (k_0 L)^2/\pi. \quad (21)$$

Relationships (21) determine the maximum complication of the spatial structure of the secondary sources that allows a stable numerical solution to the inverse problem, so that small relative errors in the scattering data produce relatively small errors in the reconstructed scatterer function.

Thus, nonuniqueness occurs when nonobservable configurations of secondary sources (disturbances) exist in the region occupied by the scatterer, which produce no wave field outside this region in all the experiments. If the scatterers are spatially distributed, nonuniqueness appears due to the following mechanism. Multiple scattering (we consider the scattering process that cannot be described by the first term of the Born–Neumann series alone, the series itself even being capable of diverging) broadens the spatial spectrum of the secondary sources. This broadening increases the number of degrees of freedom that describe the secondary sources. In turn, this increase leads to the possibility that a sequence of configurations that are nonobservable in the entire set of the experiments will be generated.

3. RECONSTRUCTION OF A STRONG SCATTERER AS A SET OF POINT SCATTERERS

3.1. Nonredundant Scattering Data

In relationships (7), (8), and below, the operator $\hat{\varepsilon}$ for scatterer (5) consists of the amplitudes ε_s of the point scatterers. Then, in Eq. (16), $\varepsilon_{\text{inv}}(\mathbf{r})$ is replaced with $\varepsilon_s^{\text{inv}}$, and $\mathbf{r}$, with $\mathbf{r}_s$:

$$\varepsilon_s^{\text{inv}} = \left[\sum_{i=1}^{S-B} a_i^{\alpha}\psi_i^{\alpha}(\mathbf{r}_s)\right] \Big/ \left[U_0(\mathbf{r}_s, \alpha) + \sum_{i=1}^{S-B} a_i^{\alpha}\Phi_i^{\alpha}(\mathbf{r}_s)\right]. \quad (22)$$

The number of independent parameters that describe the scatterer is equal to that for the secondary sources ($N = S$). Therefore, when the scattering data are nonredundant ($AB = S$), the number of equations (18) is equal to the number of unknowns: $S(A - 1) = (S - B)A$. The reasoning presented below using point scatterers as an example allows us to understand the situation that is also generally typical of the inverse scattering problem for spatially distributed scatterers.

If the data set is nonredundant, a strong scatterer represented by point scatterers cannot be reconstructed uniquely [12]. The maximum number of indistinguishable scatterers or invisible scatterers can be evaluated as follows. Consider a space of parameters that describe all possible scatterers. In this space, physically feasible scatterers refer to the domain whose boundary is conventionally shown in Fig. 1 as a circle, while parameters of each invisible scatterer are indicated by a dot (the nonscattering homogeneous background medium is shown in Fig. 1 as state "0," which corresponds to the "zero" invisible scatterer with $\varepsilon_{\text{inv}} \equiv 0$). Each dot is surrounded by a subdomain of parameters that correspond to scatterers whose strength is medium relative to this invisible scatterer. The boundaries of these subdomains are shown in Fig. 1 as closed lines. The subdomains do not overlap, because, for scatterers of medium strength, the nonredundant problem has a unique solution. For example, an iterative process that starts with parameters of a particular invisible scatterer converges to a unique solution in the class of scatterers whose strength is medium relative to this invisible scatterer (lines with arrows in Fig. 1) [12]. Suppose that the volumes of these subdomains are approximately equal. Then, the number of invisible scatterers that are candidates to be a solution to the nonredundant inverse problem (without additional constraints on the scatterer strength) can be evaluated as the ratio of the volume of all physically feasible scatterer domains to the volume of one medium-strength scatterer subdomain. If the parameter space has a high number of dimensions (10^4–10^8), this ratio may be very large.

It should be noted once again that, in the nonredundant problem, the point scatterers whose strength is medium relative to the homogeneous nonscattering medium ($\varepsilon_{\text{inv}} \equiv 0$) can be reconstructed uniquely. Therefore, the rest of the invisible scatterers are strong scatterers relative to the homogeneous medium and relative to each other. They radically distort the incident field in the scattering region by introducing a phase shift comparable with or even exceeding 2π. The same conclusion follows from the analysis of expression (15). Since our experiment is designed so that weak scatterers are reconstructed uniquely, the Born's term $\hat{\varepsilon}_{\text{inv}} U_0^{\alpha}$ in the secondary source representation (15) must produce a nonzero scattered field outside the region $\Re$ (at least for one U_0^{α}). However, for an invisible scatterer, the scattered field observed is zero. Therefore, this nonzero

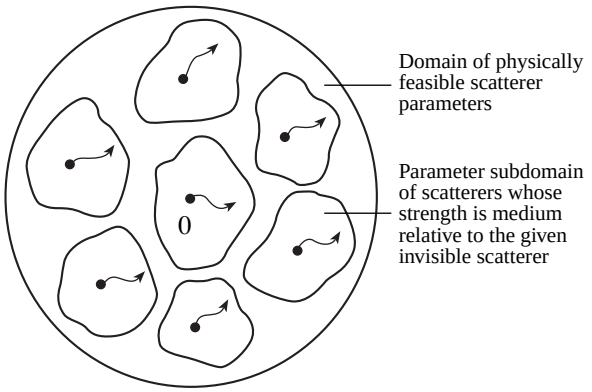

Fig. 1. Determination of the number of invisible scatterers in the nonredundant problem.

field component is compensated for by the scattered field created by multiple scattering. In turn, such a compensation can only occur if, inside the invisible scatterer, the scattered field $\sum_{i=1}^{N-B} a_i^{\alpha}\Phi_i^{\alpha}$ is comparable with the incident field U_0^{α}, which means that the invisible scatterer is a strong scatterer.

3.2. The Effect of Redundancy. Anomalous Errors

The situation with the uniqueness of the solution can be clearly illustrated using the notion of discrepancy $\mathrm{Dis} = \sum_{d,d'=1}^{\mathrm{AB}} (u_{\mathrm{sc}}^{d} - \bar{u}_{\mathrm{sc}}^{d})^{+} K_{dd'}^{-1} (u_{\mathrm{sc}}^{d'} - \bar{u}_{\mathrm{sc}}^{d'})$, where u_{sc}^{d} are the scattering data observed in the experiment, $\bar{u}_{\mathrm{sc}}^{d}$ are the scattering data for a given standard scatterer with variable parameters, and $K_{d'd}$ is the correlation matrix of the scattered field estimates. Let the horizontal axis symbolically represent the parameter space of all physically feasible scatterers, state "0" corresponding to a homogeneous nonscattering medium. The vertical axis represents the quantity $W = 1/(1 + \mathrm{Dis})$ with $W = 1$ at Dis = 0. Figure 2a illustrates the behavior of the discrepancy for a scatterer reconstructed in terms of the point scatterer representation from nonredundant data. For all scatterer solutions (a true solution and false ones, which correspond to indistinguishable scatterers that exactly satisfy the experimental data (Dis = 0), we have $W = 1$. Among the scatterers whose strength is medium relative to the homogeneous medium, there is only one such solution (the one closest to state "0").

For a scatterer represented in terms of point scatterers, the condition $AB > S$ for the scattering data to be redundant is equivalent to condition (19), because $N = S$. Therefore, the effect of redundancy of the scattering data is that the solution to the inverse problem becomes unique. However, it is very important in practice how the nonuniqueness is removed as data redundancy increases. In particular, adding extra measurements to nonredundant data makes system (18) overdetermined and guarantees that it will have a solution only for $\varepsilon_{\mathrm{inv}} \equiv 0$. Therefore, Dis = 0 is only guaranteed for the true scatterer. On the contrary, false scatterers that had Dis = 0 with the nonredundant data now acquire a nonzero discrepancy $\mathrm{Dis} \neq 0$ (the solid line in Fig. 2b or the dashed line for another set of redundant data). Consequently, the uniqueness of the solution is formally provided. However, if the scattering data are close to nonredundant data in their amount and nature, false peaks in W become only a little lower than the true peak. Therefore, even small errors in the experimental data may easily cause the solution to skip from being true to being false. Such a skip, which testifies to the strong instability of the solution, leads to the so-called anomalous errors in the reconstructed scatterer, i.e., actually, to nonuniqueness. A natural way to cope with nonuniqueness and instability is to increase the redundancy ratio of the scattering data. If this increase is achieved with the angular separation between the transmit–receive elements no smaller than Rayleigh angle (20), the false peaks in W become more and more uniformly distributed and their amplitudes decrease (Fig. 2b). Therefore, the true solution ($W = 1$) becomes increasingly contrasted against this background; i.e., the stability of the solution improves. However, as soon as the angular separation becomes smaller than the Rayleigh angle, a further increase in the amount of data does not improve the stability of the solution but leads to a decrease in the errors in the estimated characteristics of the true scatterer, if errors in the data are uncorrelated) and there are no skips.

Let us estimate the average distance Δx between the adjacent point scatterers at which the uniqueness (19) and stability (20) conditions can be satisfied simultaneously in a circular data-collection system. As follows from expressions (21), in the two-dimensional problem, the maximum amount of scattering data that satisfies the stability condition is $A = A_{\mathrm{Rayl}} \cong M_{\mathrm{Rayl}}^{(2)}$, $B = B_{\mathrm{Rayl}} \cong M_{\mathrm{Rayl}}^{(2)}/2$ (where B_{Rayl} is twice as small as A_{Rayl} due to the reciprocity theorem). Then, the condition $A_{\mathrm{Rayl}} B_{\mathrm{Rayl}} > S$, where $S \cong (L/\Delta x)^2$, yields the estimate $\Delta x > \lambda_0/(\sqrt{2}\pi) \approx \lambda_0/4$. The same estimate is obtained in the three-dimensional problem ($S \cong (L/\Delta x)^3$), if the amount of the scattering data is close to the nonredundant amount. But if the three-dimensional problem uses the whole redundant amount of data, we have $A = A_{\mathrm{Rayl}} \cong M_{\mathrm{Rayl}}^{(3)}$, $B = B_{\mathrm{Rayl}} \cong M_{\mathrm{Rayl}}^{(3)}/2$ and the estimate is $\Delta x > \frac{\lambda_0}{4}\sqrt[3]{\frac{\lambda_0}{L}}$.

It should also be noted that a scatterer represented as a set of point scatterers (5) must comply with additional constraints on the physical feasibility [13]. It has been

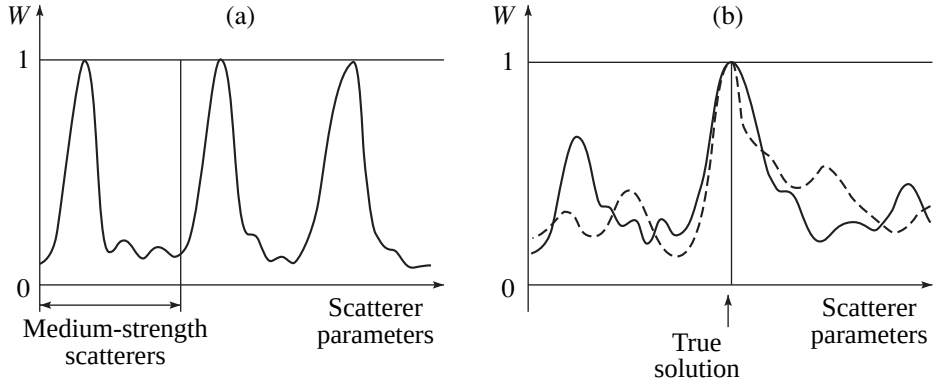

Fig. 2. Discrepancy behavior (a) when the scattering data are nonredundant and (b) for different sets of redundant scattering data.

found that the amplitude ε_s of each feasible point source must be a complex-valued number:

$$\varepsilon_s = |\varepsilon_s| \exp(i\phi_s), \tag{23}$$

whose phase and magnitude are uniquely related. For example, in the two-dimensional problem (an $\exp(i\omega t)$ time convention),

$$\sin(\phi_s) = |\varepsilon_s|/4; \tag{24}$$

and in the three-dimensional problem,

$$\sin(\phi_s) = |\varepsilon_s|/(4\pi/k_0).$$

A quantum-mechanical scattering by a singular δ-like potential was analyzed in [14] on the basis of the Schrodinger equation, and relationships were derived, from which a similar formula can be obtained for the three-dimensional problem. From Eq. (24), it follows that

$$|\varepsilon_s|^2 - 4\,\mathrm{Im}(\varepsilon_s) = 0, \tag{25}$$

because $\sin(\phi_s) = \mathrm{Im}(\varepsilon_s)/|\varepsilon_s|$. If an invisible scatterer is addressed, the substitution of Eq. (22) into Eq. (25) yields the following equations for $\{a_i^\alpha\}_{i=\overline{1,S-B}}^{\alpha=\overline{1,A}}$:

$$\left|\sum_{i=1}^{S-B} a_i^\alpha \psi_i^\alpha(\mathbf{r}_s)\right|^2 - 4\,\mathrm{Im}\left\{\left(\sum_{i=1}^{S-B} a_i^\alpha \psi_i^\alpha(\mathbf{r}_s)\right) \times \left(U_0(\mathbf{r}_s, \alpha) + \sum_{j=1}^{S-B} a_j^\alpha \Phi_j^\alpha(\mathbf{r}_s)\right)^*\right\} = 0. \tag{26}$$

The total number of equations (26) is AS (α and $\mathbf{r}_s$ are parameters); i.e., it is greater than that in system (18).

Thus, additional relationships (23)–(25) and equations (26) that follow from them are a kind of prior information about the scatterer. Therefore, in the case of nonredundant scattering data, solving the system of equations (18) (at $N = S$) together with Eqs. (26) or directly allowing for relationships (23)–(25) when reconstructing the scatterer can completely change the situation described above, so that the uniqueness of the reconstructed strong point scatterers will be provided for less redundant or even nonredundant data. However, this hypothesis must be thoroughly tested through numerical simulations.

4. INVERSE SCATTERING PROBLEM FOR SPATIALLY DISTRIBUTED SCATTERERS

As we discussed earlier (see Section 1), the functional description of the problem is not equivalent to the description in terms of point scatterers in its physical essence. The analysis of distributed scatterers allows us to relate the nonuniqueness and instability to the dimension of the problem, the scatterer's strength, and the complication of its spatial structure, which affects the width of its spatial spectrum. If it is known a priori that the spatially distributed scatterer belongs to the class of scatterers described by S independent parameters and the radius χ of localization region of its spatial spectrum $\tilde{\varepsilon}(\boldsymbol{\xi})$ is known, system of equations (18) can be supplemented by additional equations. These equations must describe the situation where, among N independent spatial samples $\{\mathbf{r}_n\}$ that enter into system (18), only S combinations of samples are independent in the description of the scatterer function itself. For example, these may be equations for $\tilde{\varepsilon}(\boldsymbol{\xi})$ ($\tilde{\varepsilon}(\boldsymbol{\xi}) \approx 0$) at $N - S$ independent $\boldsymbol{\xi}$ points that correspond to high spatial frequencies $|\boldsymbol{\xi}|$. Each of these equations relates (through the Fourier transform kernel) the values of $\varepsilon(\mathbf{r})$ at different spatial points and has the form of a quadratic equation for each unknown when all the remaining unknowns are fixed. These equations act as additional information about the scatterer. However, the question of how strong the influence of the additional equations is on the possibility of providing a unique solution to the inverse problem and on the possibility of relaxing requirement (19) imposed on the total amount of the scattering data still remains open (because the

equations are nonlinear), calling for numerical simulations.

In the functional description, the notion of scattering data redundancy is closely connected with the number of dimensions of the coordinate space in which the scatterer to be reconstructed is localized. For instance, the two-dimensional single-frequency problem is nonredundant in the functional (dimensionality) sense; i.e., the numbers of dimensions of the coordinate space and of the parameterized space of independent scattering data are the same and equal to two. On the contrary, the three-dimensional problem is dimensionally redundant (the number of dimensions of the parameterized space of the scattering data may equal four versus three for that of the scatterer's coordinate space). However, the number of discrete samples must be redundant in both the two-dimensional and three-dimensional problems. In particular, if there is no prior information about the scatterer, the minimum amount of independent sampled scattering data necessary for keeping the information about the scatterer from being lost is [6] $AB \cong N$, which agrees with condition (19). This amount is greater than that in the nonredundant case ($AB \cong S$) except for weak scatterers, for which $N = S$. The samples must be redundant because, when reconstructing the scatterer function, it is always necessary to reconstruct the secondary sources or internal fields, whose spatial spectrum is broader than the scatterer's spectrum.

Numerical estimates of the number of independent parameters for the scatterer and its secondary sources depend on the areas (at $p = 2$) or volumes (at $p = 3$) Γ_ε and Γ_I of the domains in the $\boldsymbol{\xi}$ space in which the components of $\tilde{\varepsilon}$ and $\tilde{I}$ are taken into account (for the required accuracy): $S \cong \dfrac{\Gamma_\varepsilon}{(2\pi/L)^p}$ and $N \cong \dfrac{\Gamma_I}{(2\pi/L)^p}$ (p = 2 or 3). Let l be the linear size of typical spatial features of the scatterer $\varepsilon(\mathbf{r})$ and χ be the radius of the region where $\tilde{\varepsilon}(\boldsymbol{\xi})$ is localized. If we approximately assume that the spectrum $\tilde{I}(\boldsymbol{\xi}, \alpha)$ broadens uniformly enough in all directions of the $\boldsymbol{\xi}$ space and is well localized in the domain with the half-width $m\chi$, we obtain

$$2\chi \cong 2\pi/l, \quad \Gamma_\varepsilon \cong (2\chi)^p, \quad S \cong (\chi L/\pi)^p;$$
$$\Gamma_I \cong (2m\chi)^p, \quad N \cong (m\chi L/\pi)^p \cong m^p S \quad (p = 2, 3). \tag{27}$$

(However, the number of terms that must be taken into account in the Born–Neumann expansions of Eqs. (2) and (3) may be significantly greater than m [2, 6]. For example, this situation occurs with scatterers that have a high contrast and are smooth.) But if the estimates allow for the filtering properties of the function $\tilde{G}(|\boldsymbol{\xi}|, k_0)$, the linear dimension of the domain where the spectrum $\tilde{I}(\boldsymbol{\xi}, \alpha)$ is localized increases mainly along the Ewald surface. Both approximate approaches, which assume that the spatial spectrum of the secondary sources broadens uniformly in either all directions or only along the Ewald surface, are fairly rough. A more detailed analysis shows that the spectrum broadens in a manner that is intermediate between these two cases.

4.1. Two-Dimensional Inverse Scattering Problem

A number of theorems proved for spatially distributed scatterers state that the two-dimensional single-frequency scattering problem allows a unique solution for weak and medium-strength scatterers [15]. For strong scatterers, the solution to this problem is not unique. Consequently, in the domain of medium-strength scatterers, a zero discrepancy occurs in only one case, and the behavior of W is similar to that with nonredundant data in the point scatterer representation (Fig. 2a). The similarity occurs because the two-dimensional single-frequency problem is nonredundant from the viewpoint of dimensionality.

Conditions (19) and (20) impose constraints (which are noticeably different for the two-dimensional and three-dimensional problems) on the admissible strength of the scatterer and on the complication of its spatial structure. Let us estimate the degree of broadening of the secondary source spectrum at which conditions (19) and (20) can be satisfied simultaneously in the two-dimensional problem with the circular data-collection scheme: $A = A_{\text{Rayl}} \cong M^{(2)}_{\text{Rayl}}$, $B = B_{\text{Rayl}} \cong M^{(2)}_{\text{Rayl}}/2$ (see (21)), and N is estimated from formulas (27) at $p = 2$; then condition $A_{\text{Rayl}}B_{\text{Rayl}} > N$ yields

$$m < 2k_0/\chi \quad \text{or} \quad l > m\lambda_0/4. \tag{28}$$

Estimate (28) means that, in the single-frequency two-dimensional inverse problem, the data sampling redundancy is in general efficient as long as the spatial spectrum of the secondary sources is well localized in a circle of radius $2k_0$; in particular, there must be no backscattering. (The center of localization of the secondary source spectrum, i.e., the center of the circle mentioned above, depends on the direction of the incident field.) When this requirement is violated, the solution becomes unstable. The more the spatial spectrum goes beyond the circle of radius $2k_0$, the more unstable the scatterer reconstruction is [5]. However, for weak scatterers with $\chi > 2k_0$, the stability of the solution will be provided if we limit the problem to the reconstruction of $\tilde{\varepsilon}(\boldsymbol{\xi})$ only for $|\boldsymbol{\xi}| < 2k_0$ by filtering out the higher spatial frequencies. It is the reconstruction of the high-frequency spectrum of the scatterer that is associated with the instability of such operations as analytical continuation. If multiple scattering is taken into account, the situation with instability becomes much more complicated, because the field in this case becomes dependent on the scatterer function. Therefore, as a result of the interaction with the internal field, each scatterer's spectral component associated with a particular spatial fre-

quency can produce spectral components of the secondary sources at spatial combination frequencies, both higher and lower. This effect, in turn, produces a small-scale structure of secondary sources and of the wave field inside the scattering region. It is precisely this small-scale structure that increases the instability of the reconstruction of the complicated structure of secondary sources and the internal wave field. The higher the order of multiple scattering that affects the process and the more complicated the spatial structure of the scatterer, the more complicated the structure of the secondary sources and internal field, and, consequently, the stronger the instability manifests itself. Therefore, the two-dimensional single-frequency problem provides stable reconstruction only for scatterers with a narrow spatial spectrum, and the constraints on the width of its spatial spectrum become more stringent with increasing scatterer strength. In addition, since as a result of the multiple scattering the secondary sources are formed through the nonlinear combination products of $\tilde{\varepsilon}$ at different spatial frequencies, the correct reconstruction at the cost of the spatial resolution (i.e., by filtering out the high-frequency components of $\tilde{\varepsilon}(\boldsymbol{\xi})$) becomes impossible. Now, unlike the case of weak scatterers, to correctly reconstruct a scatterer, the spectrum of secondary sources must be reconstructed at all spatial frequencies.

These conclusions may clearly be illustrated by the simplified Grinevich–Novikov algorithm, which is valid for medium-strength scatterers with a simple enough spatial structure [6, 16–18] and by the extension of this algorithm to scatterers of a complicated spatial structure (i.e., with a broad $\tilde{\varepsilon}(\boldsymbol{\xi})$) [19]. Both algorithms allow for multiple scattering in terms of the complex-valued **k**-space formulation. This situation, like the one typical of the two-dimensional single-frequency problem, can also be analyzed using the iterative solution technique as an example, which simultaneously or sequentially refines the reconstructed functions of the scatterer and its secondary sources. When the complete system consisting of the main equations (of the Lippmann–Schwinger type) for the scatterer function and the constraining equations (of the same type) for the secondary sources is solved simultaneously [3], the adequacy and uniqueness of the solution are only provided for a sufficiently large amount of scattering data determined by the width of the secondary source spectrum. This technique requires the full amount of the data as early as at the first iteration. If the subsystem of main equations for the scatterer is solved sequentially [5], which is computationally simpler, and the secondary sources belonging to a set of auxiliary subsystems are estimated subsequently, the first (Born's) iteration does not require a large amount of scattering data. However, the subsequent allowance for multiple scattering requires the amount of data determined by the width of the secondary source spectrum. Unlike the first approach, this one, however, does not always provide convergence of the overall iteration procedure. At the same time, in any iterative scheme, the stability is lost when the total number of equations exceeds the number $A_{\mathrm{Rayl}}B_{\mathrm{Rayl}}$ of essentially independent and experimentally obtained data; i.e., actually when the spatial spectrum of secondary sources goes beyond the circle of radius $2k_0$.

Constraint (28) yields numerical estimates typical of tomographic problems. In particular, at $\chi/k_0 \cong 1$–2, i.e., at $l \cong (1/4$–$1/2)\lambda_0$, we have $m \leq 1$–2, which is a tolerable broadening of the secondary sources' spatial spectrum. For scatterers with larger characteristic spatial features, the tolerable broadening is greater: at $\chi/k_0 \cong 0.1$–0.2, i.e., at $l \cong (2.5$–$5)\lambda_0$, we have $m \leq 10$–20.

Thus, the uniqueness of the solution to the two-dimensional single-frequency inverse problem is only guaranteed in the class of medium-strength scatterers. However, for both medium-strength and strong scatterers, whose spatial structure is so complicated that the secondary source spectrum goes beyond the circle of radius $2k_0$, the solution is unstable. (It should be noted that the scatterer may be strong but have a sufficiently narrow spatial spectrum. For example, this is typical of scatterers with a large wave dimension, whose characteristics smoothly vary in the coordinate space.) Therefore, in a two-dimensional single-frequency problem, two classes of scatterers are the best to reconstruct. The first class are weak scatterers, which may possess a broad enough spatial spectrum; the second class are medium-strength scatterers whose spectrum is predominantly localized in a narrow frequency band. Attempts to reconstruct other scatterers face nonuniqueness or instability problems. These problems can only be solved through the use of pulsed or multifrequency sounding, which is the only way to collect redundant (in terms of number of dimensions) data in the two-dimensional geometry.

4.2. Three-Dimensional Inverse Scattering Problem

In both the single-frequency and pulsed modes, the three-dimensional problem has a unique solution for spatially distributed scatterers of any strength if the set of parameters that specify the technique used for collecting dimensionally redundant scattering data has a nonzero measure [20–22]. The single-frequency three-dimensional problem already has a dimensional redundancy margin. In the pulsed mode, the possibility of collecting redundant data increases due to the frequency degree of freedom.

In the single-frequency three-dimensional problem, one can limit oneself to dimensionally nonredundant scattering data (three-dimensional parameterized data space and also three-dimensional scatterer coordinate space) that correspond, for example, to a two-dimensional manifold of all directions of the incident sounding wave combined with a one-dimensional manifold

of data on the scattered field collected on a certain arc or circumference. Then, the situation with the discrepancy is similar to that in the two-dimensional single-frequency problem (Fig. 2a). If the scattered field is measured on a different arc (or at a different sounding frequency) well separated from the first one, the new data produce false peaks in W at different scatterer parameters. To obtain dimensionally redundant scattering data, it is sufficient to replace the arc with a narrow strip in the vicinity of this arc or switch from the single-frequency mode to the pulsed mode, though with perhaps a very narrow relative bandwidth. The behavior of the discrepancy will be similar to that illustrated in Fig. 2b. The uniqueness of the solution is formally regained, although the probability of anomalous error is high. The noise robustness of the solution improves with increasing degree of redundancy of the independent data.

For dimensionally nonredundant scattering data, the same estimate (28) as for the two-dimensional problem is valid. According to Eqs. (21), the maximum attainable amount of dimensionally redundant scattering data that satisfy the solution stability condition is $A = A_{\text{Rayl}} \cong M^{(3)}_{\text{Rayl}}$, $B = B_{\text{Rayl}} \cong M^{(3)}_{\text{Rayl}}/2$. Then, condition $A_{\text{Rayl}} B_{\text{Rayl}} > N$ yields

$$m < \frac{2k_0 \sqrt[3]{k_0 L}}{\chi} \frac{2}{2} \quad \text{or} \quad l > m \frac{\lambda_0}{4} \frac{2}{\sqrt[3]{k_0 L}}. \tag{29}$$

Requirements (29) mean that, due to the dimensional redundancy of the data, the maximum admissible broadening of the spatial spectrum of secondary sources may be $\sqrt[3]{k_0 L}/2$ times as large as that in the two-dimensional problem (see expressions (28)). The larger the scatterer in terms of wavelength, the greater the available number of scattering data that satisfy the solution stability condition over the number of scatterer's independent parameters and, therefore, the higher the admissible broadening (29). The estimates typical of tomographic problems depend now not only on χ/k_0, but also on $k_0 L$. In particular, for scatterers that are small in terms of wavelength, the estimates are close to those of the two-dimensional problem. For example, let $\lambda_0 \cong 1$ mm and $L \cong 0.5$ cm $\cong 5\lambda_0$. Then, if $\chi/k_0 \cong 1$–2, i.e., $l \cong (1/4$–$1/2)\lambda_0$, we have $m \leq 1.6$–3.2; if $\chi/k_0 \cong 0.1$–0.2, i.e., $l \cong (2.5$–$5)\lambda_0$, we have $m \leq 16$–32. As the scatterer's dimensions in terms of wavelength increase, the estimates change. Let $\lambda_0 \cong 1$ mm and $L \cong 10$ cm $\cong 100\lambda_0$. Then, for $\chi/k_0 \cong 1$–2, we obtain $m \leq 4$–8; and for $\chi/k_0 \cong 0.1$–0.2, $m \leq 40$–80.

Thus, the dimensional redundancy of experimental data removes the limitation on the strength of the spatially distributed scatterer in the formulation of the uniqueness theorem. However, in each particular case, the values of the parameters that determine the stability of the solution to the inverse problem are different and should be analyzed separately. In this respect, the analysis of the role played by the additional characterization equations [23, 25] in the noise robustness problem is very important (though complicated). These equations relate the whole of the redundant scattering data as originating from one and the same scatterer. When the scattering data are complete, one can solve the three-dimensional problem by analytical methods. For example, in the single-frequency mode, the most promising model for studying the development of instability of the solution with increasing size, contrast, and degree of complicated of spatial structure of the scatterer may be the algorithm described in [24] and also considered in [25].

ACKNOWLEDGMENTS

This work was supported by the Russian Foundation for Basic Research, project no. 01-02-16282.

REFERENCES

1. V. A. Burov and O. D. Rumiantseva, Acoust. Imaging **22**, 107 (1996).
2. A. A. Goryunov and A. V. Saskovets, *Inverse Scattering Problems in Acoustics* (Mosk. Gos. Univ., Moscow, 1989).
3. V. A. Burov, A. A. Goryunov, A. V. Saskovets, and T. A. Tikhonova, Vopr. Sudostr., Ser. Akust. **20** (1), 32 (1985).
4. V. A. Burov, A. A. Goryunov, A. V. Saskovets, and T. A. Tikhonova, Akust. Zh. **32**, 433 (1986) [Sov. Phys. Acoust. **32**, 273 (1986)].
5. V. A. Burov and O. D. Rumiantseva, Proc. SPIE **1843**, 194 (1992).
6. V. A. Burov and O. D. Rumyantseva, Akust. Zh. **39**, 793 (1993) [Acoust. Phys. **39**, 419 (1993)].
7. S. A. Johnson, Y. Zhou, M. L. Tracy, *et al.*, Ultrason. Imaging **6** (4), 103 (1984).
8. Benli Gu and Dongyun Deng, Acoust. Imaging **20**, 111 (1993).
9. A. J. Devaney, J. Math. Phys. **19** (7), 1526 (1978).
10. P. G. Grinevich and R. G. Novikov, Commun. Math. Phys. **174**, 409 (1995).
11. N. N. Voĭtovich, B. Z. Katsenelenbaum, and A. N. Sivov, *Generalized Method of Natural Oscillations in the Diffraction Theory* (Nauka, Moscow, 1977).
12. V. A. Burov, M. N. Rychagov, and A. V. Saskovets, Acoust. Imaging **19**, 35 (1992).
13. V. A. Burov and S. A. Morozov, Akust. Zh. **47**, 751 (2001) [Acoust. Phys. **47**, 659 (2001)].
14. F. A. Berezin and L. D. Faddeev, Dokl. Akad. Nauk SSSR **137** (5), 1011 (1961).
15. R. G. Novikov, Funkts. Anal. Pril. **22** (4), 11 (1988) [Funct. Anal. Appl. **22**, 263 (1988)].

16. P. G. Grinevich and S. V. Manakov, Funkts. Anal. Pril. **20** (2), 14 (1986) [Funct. Anal. Appl. **20** (2), 94 (1986)].
17. R. G. Novikov, Teor. Mat. Fiz. **66** (2), 234 (1986) [Theor. Math. Phys. **66** (2), 154 (1986)].
18. V. A. Burov and O. D. Rumyantseva, Akust. Zh. **38**, 413 (1992) [Sov. Phys. Acoust. **38**, 226 (1992)].
19. V. A. Burov and O. D. Rumiantseva, in *Ill-Posed Problems in Natural Sciences* (TVP, Moscow, 1992), pp. 463–471.
20. Yu. M. Berezanskiĭ, Tr. Mosk. Mat. O–va **7**, 3 (1958).
21. A. G. Ramm, Inverse Probl. **3**, L77 (1987).
22. R. Weder, Inverse Probl. **7**, 927 (1991).
23. R. G. Newton, in *Proceedings of Conference on Inverse Scattering: Theory and Applications* (SIAM, Philadelphia, 1983), p. 1.
24. R. G. Novikov and G. M. Khenkin, Preprint No. 27M/1986 (Inst. of Physics, Siberian Division, Russian Academy of Sciences, Krasnoyarsk, 1986), p. 35.
25. A. I. Nachman, Ann. Math. **128** (3), 531 (1988).

Translated by A. Khzmalyan

Acoustical Physics, Vol. 49, No. 5, 2003, pp. 508–515. Translated from Akusticheskiĭ Zhurnal, Vol. 49, No. 5, 2003, pp. 604–612.

Two-Dimensional Phased Arrays for Surgical Applications: Multiple Focus Generation and Scanning

L. R. Gavrilov

Andreev Acoustics Institute, Russian Academy of Sciences, ul. Shvernika 4, Moscow, 117036 Russia

e-mail: gavrilov@akin.ru

Received September 17, 2002

Abstract—A numerical simulation and a comparative analysis of the acoustic fields produced by two-dimensional phased arrays intended for ultrasonic surgery are performed for the case of a multiple focus (in particular, 25 foci) generation. The calculations were conducted for arrays (with an operating frequency of 1.5 MHz) consisting of 256 elements 5 mm in diameter, which were positioned on the array surface both regularly and randomly. The array foci can be formed simultaneously, but, in this case, the intensity levels of the secondary peaks in the ultrasonic field can exceed the values that guarantee the safe application of this method in surgery. A much safer way is to synthesize many foci with the use of several configurations, each of which contains a smaller number of foci. The number of foci in individual configurations must be approximately the same. It is demonstrated that randomization of the element distribution over the array surface provides an opportunity to improve the array performance, to reduce the intensity levels of secondary peaks in the acoustic field, and to increase the array capability for multiple focus scanning off the array axis. © *2003 MAIK "Nauka/Interperiodica".*

One of the major advantages of ultrasonic phased arrays is their ability to synthesize several foci [1–8], which is important for surgical applications of such arrays, especially when the object intended for destruction is a deep-seated tissue of relatively large volume. The use of several foci provides an opportunity to substantially reduce the time needed for such a procedure in comparison with the case of scanning by a single focus [4]. In this case, the gain in time may exceed the number of synthesized foci.

A numerical simulation and a comparative analysis of the acoustic fields formed by two-dimensional phased arrays were conducted in [9–11] for the cases of the generation of and scanning by a single focus and several foci (specifically, nine foci). The calculation was performed for arrays with elements positioned on the surface both regularly (in square, annular, and hexagonal patterns) and randomly. The criteria for evaluating the quality of the intensity distributions in the field formed by an array were proposed for the case of scanning by several foci [9, 11]. The quality of intensity distributions for the arrays consisting of 255 and 256 elements 5 mm in diameter, which were positioned on the array surface regularly (in square, annular, or hexagonal patterns), was substantially lower than that for the arrays consisting of 256 randomly positioned elements.

Essentially, the approach proposed for designing two-dimensional arrays for surgical applications is based on the use of arrays with sparse elements randomly distributed over the array surface. The origin of such an approach is the fact that the level of side lobes in the field produced by the array depends on the regularity of the array structure. We demonstrated that, in the case of a random distribution of elements over the surface of a two-dimensional array and a certain ratio of the element diameter to the sound wavelength, it is possible to obtain a much higher quality of ultrasonic intensity distribution in the field produced by the array, as compared to regular arrays [9–11]. A similar approach is known, for example, in radar [12], but the effect of randomization of the element distribution does not manifest itself as noticeably as in the case of high-power ultrasonic arrays. Since the velocity of light is greater than that of sound, it is much simpler to manufacture electromagnetic arrays in which the distance between the element centers is smaller than the electromagnetic half-wavelength and thereby eliminate the side lobes associated with the array structure. Moreover, in radar, the common practice was to consider regular multielement arrays of which some active elements were chosen in a random way [12]. In our previous publications [9–11], we demonstrated that, with the help of randomization of the element distribution in a high-power two-dimensional array, it is possible to increase the element size up to five sound wavelengths while retaining an admissible level of side lobes and, thus, reduce severalfold the number of elements while retaining the same distribution quality.

It is of interest to clarify how much the utilization of phased arrays with a random distribution of elements over the surface can be useful in a situation where the array is used for the generation of a large number of foci. This paper presents a numerical simulation and a comparative analysis of the quality of the acoustic

1063-7710/03/4905-0508$24.00

Localization and relative phase values for 25 foci lying in one plane

$x-5, y+5, z$ ● $\pi/2$	$x-2.5, y+5, z$ ● $5\pi/8$	$x, y+5, z$ ● $3\pi/4$	$x+2.5, y+5, z$ ● $7\pi/8$	$x+5, y+5, z$ ● π
$x-5, y+2.5, z$ ● $3\pi/8$	$x-2.5, y+2.5, z$ ● $3\pi/2$	$x, y+2.5, z$ ● $7\pi/4$	$x+2.5, y+2.5, z$ ● 0	$x+5, y+2.5, z$ ● $9\pi/8$
$x-5, y, z$ ● $\pi/4$	$x-2.5, y, z$ ● $5\pi/4$	x, y, z ● 0	$x+2.5, y, z$ ● $\pi/4$	$x+5, y, z$ ● $5\pi/4$
$x-5, y-2.5, z$ ● $\pi/8$	$x-2.5, y-2.5, z$ ● π	$x, y-2.5, z$ ● $3\pi/4$	$x+2.5, y-2.5, z$ ● $\pi/2$	$x+5, y-2.5, z$ ● $11\pi/8$
$x-5, y-5, z$ ● 0	$x-2.5, y-5, z$ ● $15\pi/8$	$x, y-5, z$ ● $7\pi/4$	$x+2.5, y-5, z$ ● $13\pi/8$	$x+5, y-5, z$ ● $3\pi/2$

fields produced by the arrays with random and regular distributions of elements over the surface shaped as part of a sphere for the case of generation and scanning by 25 foci. As in [9, 11], the acoustic fields produced by two-dimensional phased arrays are calculated using the "pseudoinverse" approach proposed in [1, 2].

The values of the complex particle velocity u_n at the nth of N elements are connected with the complex sound pressure p_m at each of the M test points by an equation in matrix form [1, 2]:

$$\mathbf{u} = \mathbf{H}^{*t}(\mathbf{H}\mathbf{H}^{*t})^{-1}\mathbf{p}.$$

Here, $\mathbf{u} = [u_1, u_2, \ldots, u_n, \ldots u_N]^t$; $\mathbf{p} = [p_1, p_2, \ldots, p_m, \ldots p_M]^t$; $\mathbf{H}$ is an $M \times N$ matrix; the matrix elements have the form $h_{mn} = \dfrac{\exp(-jkr_{mn})}{r_{mn}}$, where r_{mn} is the distance from the mth test point to the center of the nth element of the array; and $\mathbf{H}^{*t}$ is the matrix conjugate to $\mathbf{H}$, where t means the matrix transposition. The M test points (corresponding to the focus localization) are positioned in the same focal plane, and their number is either 25 (for the case of a simultaneous generation of foci) or 4–5 (when several sequentially activated sets of foci are used; see below). To determine u_n ($n = 1, 2, \ldots N$), it is necessary to select the phases and amplitudes of the sound pressure at the test points p_m ($m = 1, 2, \ldots M$). To simplify the calculation, the amplitudes at the foci were assumed to be equal. The relative phase values at the test points and other characteristics of the foci are given in the table. The focus coordinates are given in millimeters (upper numbers) with respect to the central focus position (x, y, z). The relative phase values of the complex pressure at the foci are given by the lower numbers. As one can see, the phases uniformly rotate in a clockwise direction with respect to the axis of this set of foci.

The spatial distribution of acoustic fields was calculated in a region with the dimensions from 50 to 160 mm in the direction of the acoustic axis of the array and from 0 to ±30 mm in two other orthogonal directions. The grid step was 0.1 mm (1/10 of the wavelength), and in the case of qualitative estimations, no worse than 0.2 mm. A further increase in the grid step leads to substantial distortion of the field pattern.

Thus, as the result of calculation, we obtain a certain initial distribution of amplitudes and phases over all elements, at which the indicated M foci are formed. It is clear that many such combinations are possible with both large and small amplitudes at the elements. Since our aim is not only to produce a preset number of foci in a given place but also to provide the maximum power of the array, it is necessary to determine a phase distribution over the elements such that the desired M foci are formed at equal amplitudes at the elements. Therefore, in calculating the multiple focus ultrasonic fields, one has to use optimization techniques that provide an opportunity to obtain the preset number of foci at equal amplitudes at all elements and thereby attain the maximum acoustic power of the array. In our case, we use the optimization technique proposed in [1]. After a series of iterations, the number of which can reach several dozens for a large number of foci, a certain new phase distribution, at which the array efficiency (the ratio of the real power to the maximum possible power) is not less than 99%, is obtained. For a small number of foci (four to five), only one or several iterations are usually required. The technique that provides the summa-

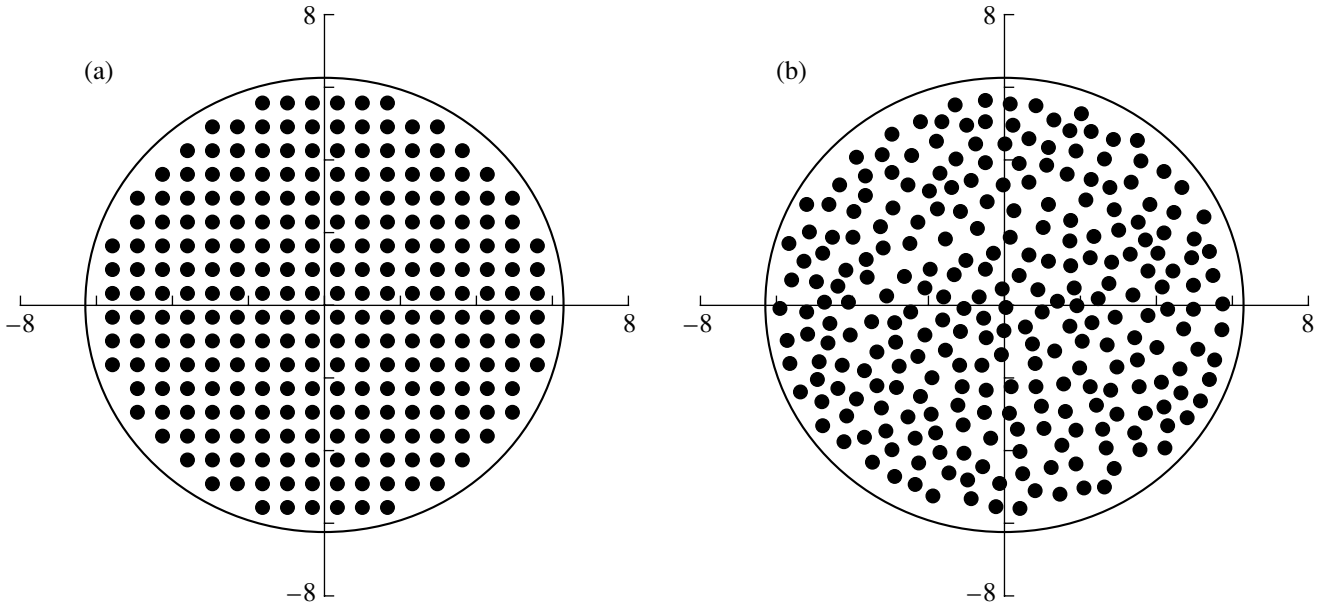

Fig. 1. Schematic representation of arrays consisting of 256 elements 5 mm in diameter that are positioned (a) in a square pattern and (b) randomly.

tion of acoustic fields from separate array elements with allowance for the phases obtained is described in [9, 11].

The calculation of the spatial distributions of acoustic fields was conducted for arrays whose surface was shaped as part of a spherical shell with a curvature radius of 120 mm. The array diameters were identical and equal to 130 mm. The arrays consisted of flat elements shaped like disks 5 mm in diameter. The intensity distributions in the field produced by arrays of the two following types were compared:

(1) an array of 256 elements positioned on the surface in a regular manner so as to form a square pattern; the minimum distance between the element centers was 6 mm;

(2) an array of 256 elements positioned on the surface randomly; in this case, the maximum distance between the element centers was 120 mm. The coordinates of the element centers (or more precisely, of their projections onto the horizontal plane) were randomly selected from a set of random numbers corresponding to the coordinates of tens of thousands of points within a circle with a diameter of 60 mm. The only limitation was that the minimum distance between the element centers should be no smaller than 5.5 mm.

The array types are schematically represented in Fig. 1. In both cases, the active area of an array (the total area of all elements) was 50.2 cm^2. The ultrasonic frequency was 1.5 MHz in all cases. The ultrasound was assumed to propagate through a biological tissue with a density of 1000 kg m^{-3}, a sound velocity of 1500 m s^{-1}, and an attenuation coefficient of 0.75 dB/cm (at this frequency). Since the design of real arrays includes a water-filled bole for establishing an acoustic contact with the object (see, e.g., [8]), it was assumed that, in the interval of z from 0 to 40 mm (z is the coordinate along the array axis), ultrasound propagates through water, and in the region $z > 40$ mm, it propagates through the tissue. Thus, the average attenuation at the given frequency along the whole path of ultrasound propagation was somewhat smaller than the value indicated above: for example, at $z = 120$ mm, it was equal to 0.5 dB/cm.

The computational means used for the calculation are described in [9, 10]. It is only necessary to add that the computer codes developed by us for calculating the spatial distributions of the acoustic fields produced by the arrays additionally provided an opportunity to calculate the maximum intensity at the foci and the position of the focus with the maximum intensity, to estimate the acoustic power of the array in the focal plane and in the vicinities of the foci, to determine the intensity gain factor, etc. The energy estimates were obtained on the assumption that the particle velocity is the same at all elements and distributed uniformly over their area, its value being 0.365 m/s. The latter corresponds to an intensity of 10 W/cm^2 at the elements. Thus, it was assumed that the maximum acoustic power obtained from the array surface was 502 W.

The quantitative analysis of the intensity distributions was performed using two-dimensional contour distributions in the focal plane (the *XY* plane) and in the plane perpendicular to it and passing through the acoustic axis of the array (the *XZ* plane). This approach proved to be more accurate in estimating the quality of the intensity distributions, as compared to the use of three-dimensional plots. Nine contours corresponding

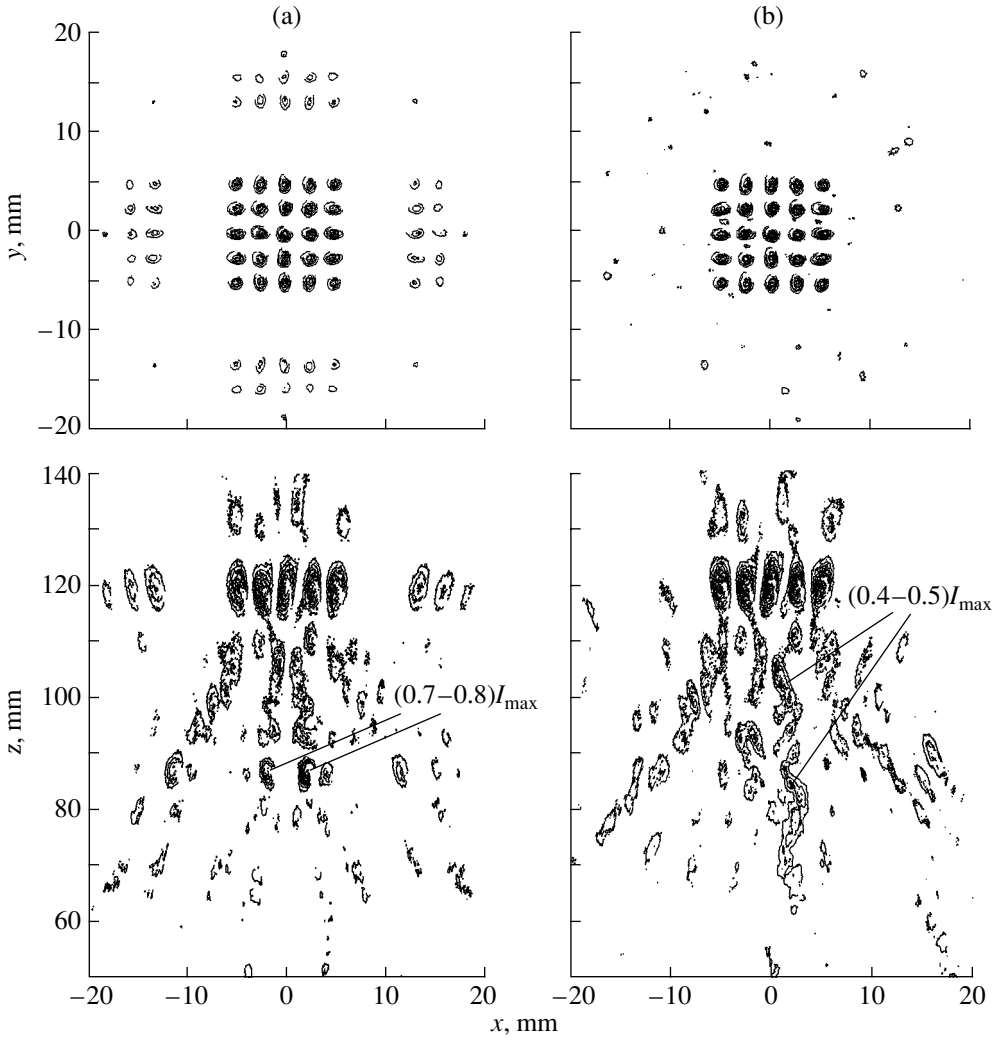

Fig. 2. Ultrasonic intensity distributions corresponding to a simultaneous generation of 25 foci in the *XY* plane (the upper plots) and in the *XZ* plane (the lower plots) for arrays with (a) regular and (b) random distributions of elements. The distance between the focus centers is 2.5 mm.

to the intensity values from 10 to 90% of I_{max} with a step of 10% of I_{max} are given in the following figures.

Figure 2 shows the distributions of ultrasonic intensity, which correspond to the simultaneous generation of 25 foci, for the arrays with a regular (Fig. 2a) and random (Fig. 2b) distribution of elements. The intensity distributions in the *XY* plane are given in the upper part of the plot, and the intensity distributions in the *XZ* plane, in the lower part. The distance between the centers of foci is 2.5 mm. The focal plane is at the distance z = 120 mm from the coordinate origin, which coincides with the deepest point on the array surface.

One can see that, for the regular array, clearly pronounced secondary peaks related to the array structure are observed in the focal plane. There are no such peaks for the randomized array: they seem to be spread in the focal plane. However, in both cases, the intensity values in the secondary peaks before the focal plane reach 0.4–0.8 of the maximum value I_{max}, which is unacceptable for using this technique in surgery according to the distribution quality criteria proposed earlier for the multiple focus case [9, 11]. The appearance of the points with elevated intensity is especially dangerous, because the radiation affects the tissue during the whole time of ultrasonic action on tissues. It is necessary to note that the distributions presented were obtained without using the iteration procedures described above, i.e., with a relatively low power and efficiency of arrays (approximately 25% for regular arrays and 30% for the randomized ones). In this case, the acoustic power summed over the *XY* plane for regular and randomized arrays is approximately 30 and 37.4 W, respectively, and the intensity at the foci is 75 and 85 W/cm^2. The use of the iteration procedures leads to an increase in the array efficiency up to 99%, but, at the same time, it also leads to a noticeable reduction of the quality of the intensity distributions, especially in the *XY* plane. A shift of the

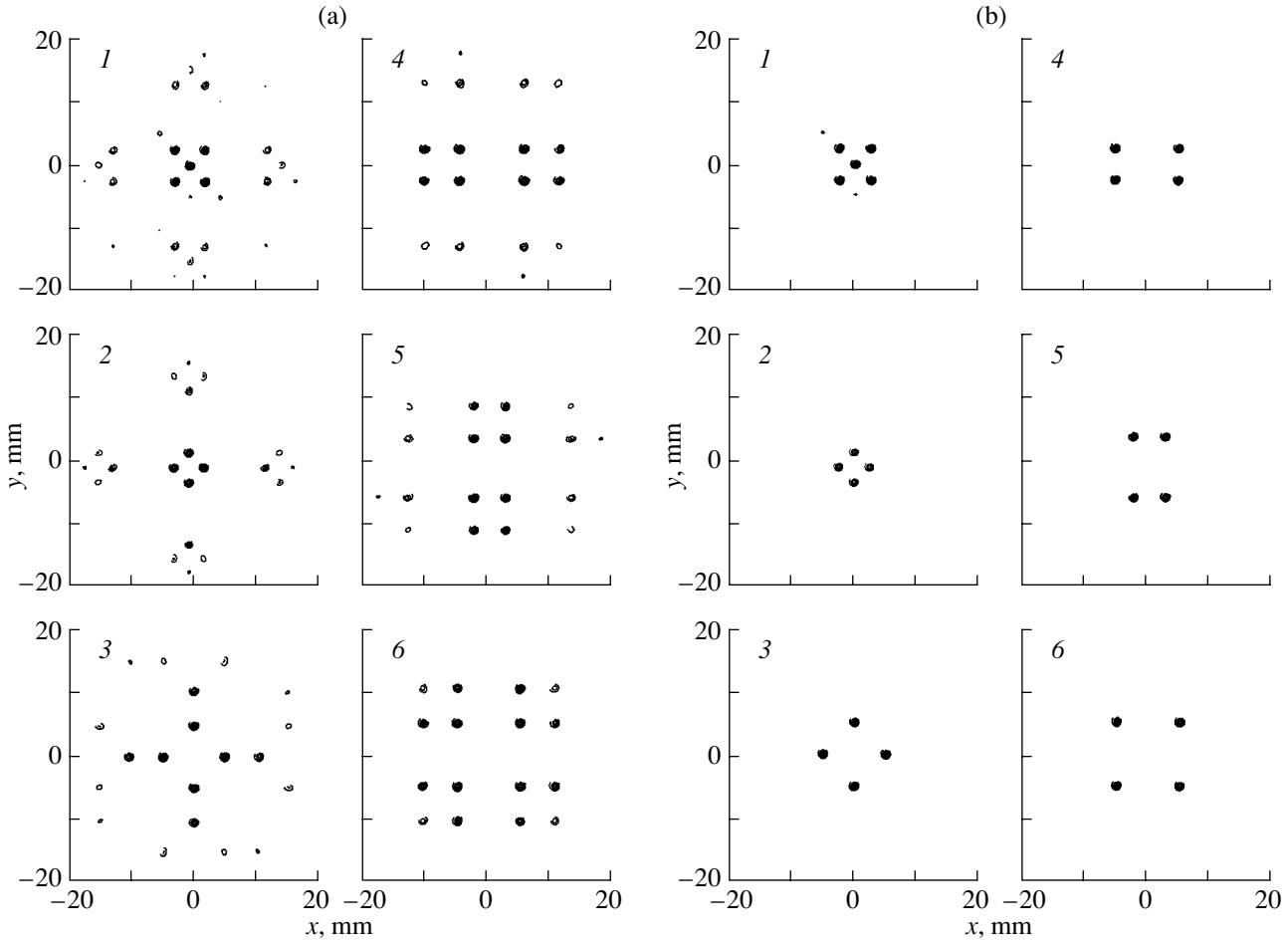

Fig. 3. Intensity distributions in the *XY* plane for six configurations of foci (5 + 4 + 4 + 4 + 4 + 4 foci), for (a) regular and (b) randomized arrays.

set of foci by 20–30 mm with respect to the axis towards the radiator, i.e., to z = 90–100 mm, leads to the same result (the corresponding distributions are not presented here to save space). It should be noted that such a shift of the foci along the z axis was not difficult in the case of the set of nine foci [9, 11]. Apparently, this method can be used in high-temperature hyperthermia, if the overheating in the hot points along the ultrasound propagation path does not yet cause necrotic changes in tissues.

From the data obtained, it follows that, in the case of using a large number of simultaneously produced foci in surgery (i.e., for the destruction of a preset tissue volume), it is necessary to find ways to reduce the levels of the secondary intensity peaks in the acoustic field before the focal plane. One such method was proposed for the first time in [3] and then developed by another team of researchers [6–8]. The basic idea is as follows: instead of a static field with a certain set of secondary peaks ("hot points"), one can use the fields of several configurations with a smaller number of foci, which are switched electrically with a frequency of 10–20 Hz. For example, the authors of [6–8] proposed using six such configurations consisting of 1 + 4 + 4 + 4 + 8 + 4 foci, respectively, to synthesize 25 foci. However, keeping in mind that one of the major requirements for high-power therapeutic arrays is sufficiently high intensity at the foci, the choice of the configurations cannot be approved. In one case, the acoustic power must be distributed among eight foci, and in the other, it must be released in only one of them. Since the intensities at all 25 foci must be approximately equal, the maximum intensity in the set of foci is finally determined by the intensity for the set of eight foci. Thus, the use of arrays with such a set of foci is inefficient.

It seems that, to raise the intensity at the foci, it is expedient to select the configurations consisting of approximately equal numbers of foci. For example, one can use a combination of 5 + 4 + 4 + 4 + 4 + 4 foci to generate a set of 25 foci. Figure 3 shows the intensity distributions in the *XZ* plane (z = 100 mm) for this configuration of foci for the cases of regular (Fig. 3a) and randomized (Fig. 3b) arrays. One can see that, in the case of a regular array (Fig. 3a), multiple secondary peaks with the intensity level up to 0.3 I_{max} are observed

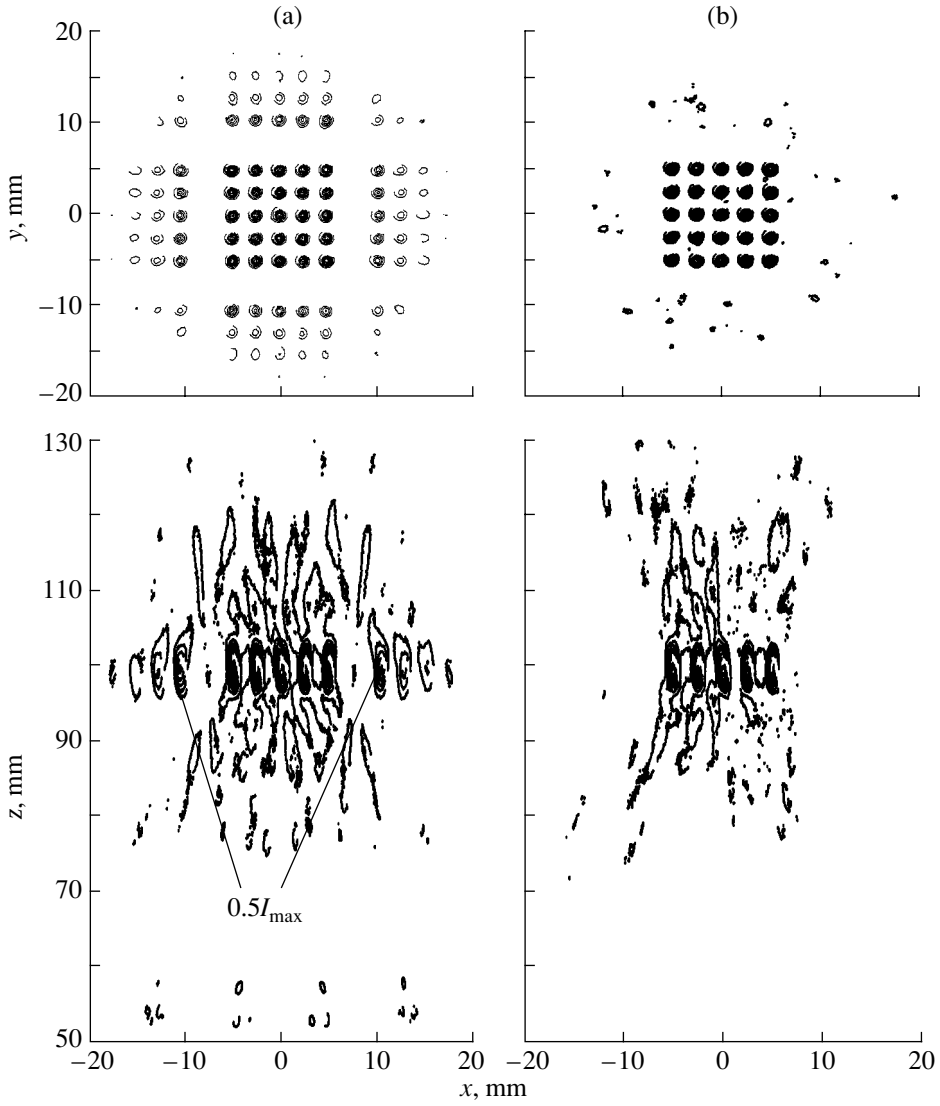

Fig. 4. Intensity distributions in the focal plane (the *XY* plane, $z = 100$ mm) and along the path of the ultrasonic beam (the *XZ* plane) for (a) regular and (b) randomized arrays in the case of 25 foci generated using six configurations of foci (Fig. 3). The distance between the focus centers is 2.5 mm. The central focus lies on the array axis.

in the focal plane, while in the case of a randomized array, no such peaks are present. The intensity values vary from 1100 W/cm^2 (a configuration of five foci) to 1500 W/cm^2 (a configuration of four foci) for a regular array and from 1070 W/cm^2 (five foci) to 1400 W/cm^2 (four foci) for a randomized array (the optimization of the array power was performed in both cases). The scatter of the intensity values can be minimized by hardware methods in such a way that the time-average intensity at the foci does not exceed 1100 W/cm^2.

Figure 4 shows how it is possible to generate a set of 25 foci with a distance between their centers of 2.5 mm with the help of the six configurations of foci shown in Fig. 3. The central focus is located on the array axis at the distance $z = 100$ mm. The time-average intensity at all foci is approximately equal to 180 W/cm^2, and the peak intensity, to 1100 W/cm^2. The power released in the *XY* plane with the generation of each set of foci is 155–160 W (taking into account the attenuation). One can see from Fig. 4 that, in the case of using several configurations of foci, the quality of the time-average intensity distributions along the path of the ultrasonic beam (in the *XZ* plane) is considerably improved in comparison with the distribution for 25 foci generated simultaneously (Fig. 2). One can also see that, in the field of a regular array, there are regions where the intensity of the secondary peaks reaches $0.5I_{max}$. There are no such potentially dangerous regions in the field of a randomized array.

In the case of the destruction of large-size tissue pieces (e.g., tumors), when it is necessary to affect the whole volume of tissue uniformly without any gaps,

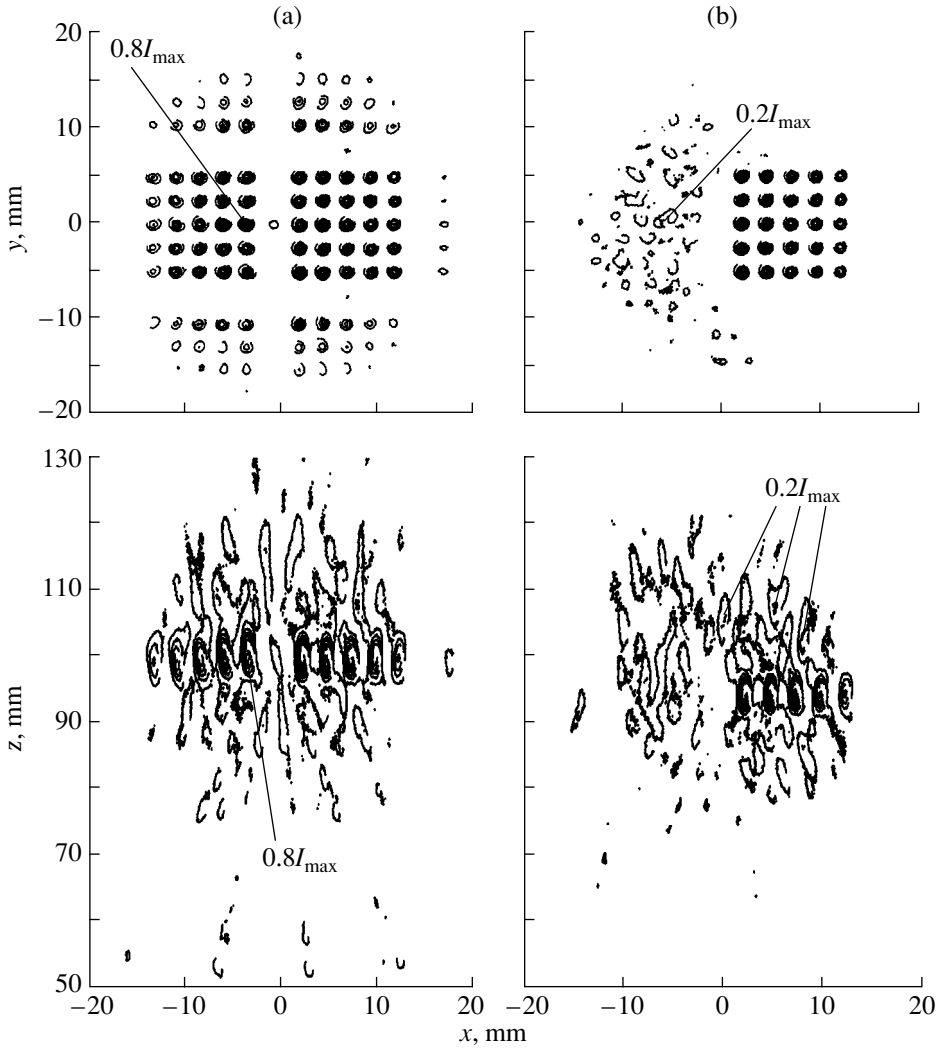

Fig. 5. Intensity distributions in the focal plane (the *XY* plane, $z = 100$ mm) and along the path of the ultrasonic beam (the *XZ* plane) for (a) regular and (b) randomized arrays in the case of 25 foci generated using six configurations of foci (Fig. 3). The set of foci is shifted 7 mm off the array axis in both cases.

one has to move the focusing system with a step of 1–2 mm. This can be accomplished either mechanically with the help of positioning systems or (which is more logical when using phased arrays) electronically. Therefore, it is of practical interest to evaluate the possibility of electronic scanning by a set of 25 foci with the help of regular and randomized arrays.

The comparison of intensity distributions in the focal plane (the *XY* plane, $z = 100$ mm) and along the path of the ultrasonic beam (the *XZ* plane) for regular (Fig. 5a) and randomized (Fig. 5b) arrays is given in Fig. 5 for the focus shifted by 7 mm off the axis in the case of 25 foci generated using six configurations of foci (Fig. 3). The array power was optimized. One can see that, with a regular array, a secondary set of foci is observed together with the main set, and this secondary set has almost the same intensity values (up to $0.8I_{max}$) as the main set. This may lead to unpredictable results of surgical or therapeutic action. In the case of a randomized array, there are only several points or regions with an intensity of $0.2I_{max}$ in the acoustic field, which is quite acceptable for practical purposes. Thus, the use of randomized arrays provides an opportunity to scan by the indicated set of foci in the plane through a distance of at least 15 mm. Such scanning is practically impossible using regular arrays.

Thus, in the case of using the above techniques, the randomized two-dimensional phased arrays allow one to generate a considerable number of foci in a preset volume and thereby considerably reduce the duration of the necessary surgical or therapeutic procedure. The capability of such arrays to move the set of foci in the focal plane (at least within the limits of ±7 mm) without the formation of potentially dangerous secondary intensity peaks is also useful from the practical point of view.

In conclusion, it should be noted that the results obtained from this study demonstrate that arrays with a random distribution of elements over the surface provide a better quality of intensity distributions in the case of multiple focus generation and scanning (for example, for 25 foci) compared to arrays with a regular distribution of elements (a square pattern). The advantages of randomized arrays were demonstrated in our previous papers [9–11] for the case of a single focus or a set of nine foci.

The major purpose of this study was to show that the utilization of randomized arrays instead of regular ones in many cases provides better spatial distributions of intensity in the field generated by an array. Apart from the paper by Goss *et al.* [13], we found nothing in the literature on phased arrays for surgical applications that discusses the possibility and expediency of using randomized arrays for these purposes. Furthermore, regular arrays with the elements positioned in square patterns were, and still are, the most popular designs discussed in the literature [2, 5–8, 14].

ACKNOWLEDGMENTS

This work was supported by the Russian Foundation for Basic Research, project no. 00-02-17855.

REFERENCES

1. E. S. Ebbini and C. A. Cain, IEEE Trans. Ultrason. Ferroelectr. Freq. Control **36** (5), 540 (1989).
2. E. S. Ebbini and C. A. Cain, IEEE Trans. Biomed. Eng. **38** (7), 634 (1991).
3. E. Ebbini and C. A. Cain, Int. J. Hyperthermia **7** (6), 951 (1991).
4. X. Fan and K. Hynynen, Ultrasound Med. Biol. **22** (4), 471 (1996).
5. H. Wan, P. VanBaren, E. S. Ebbini, and C. A. Cain, IEEE Trans. Ultrason. Ferroelectr. Freq. Control **43** (6), 1085 (1996).
6. D. R. Daum and K. Hynynen, IEEE Trans. Ultrason. Ferroelectr. Freq. Control **45** (1), 208 (1998).
7. X. Fan and K. Hynynen, Phys. Med. Biol. **41** (4), 591 (1996).
8. D. R. Daum and K. Hynynen, IEEE Trans. Ultrason. Ferroelectr. Freq. Control **46** (5), 1254 (1999).
9. L. R. Gavrilov and J. W. Hand, IEEE Trans. Ultrason. Ferroelectr. Freq. Control **47** (1), 125 (2000).
10. L. R. Gavrilov and J. W. Hand, Akust. Zh. **46**, 456 (2000) [Acoust. Phys. **46**, 390 (2000)].
11. L. R. Gavrilov, J. Hand, and I. G. Yushina, Akust. Zh. **46**, 632 (2000) [Acoust. Phys. **46**, 551 (2000)].
12. M. I. Skolnik, *Introduction to Radar Systems* (McGraw-Hill, New York, 1962; Mir, Moscow, 1965).
13. S. A. Goss, L. A. Frizell, J. T. Kouzmanoff, *et al.*, IEEE Trans. Ultrason. Ferroelectr. Freq. Control **43** (6), 1111 (1996).
14. R. J. McGough, M. L. Kessler, E. S. Ebbini, and C. A. Cain, IEEE Trans. Ultrason. Ferroelectr. Freq. Control **43** (6), 1074 (1996).

Translated by M. Lyamshev

Acoustical Physics, Vol. 49, No. 5, 2003, pp. 516–528. Translated in Akusticheskiĭ Zhurnal, Vol. 49, No. 5, 2003, pp. 613–625.

Rayleigh Wave and Detection of Low-Velocity Layers in a Stratified Half-Space[1]

Bixing Zhang and Laiyu Lu

Institute of Acoustics, Chinese Academy of Sciences, Beijing, 100080 People's Republic of China

e-mail: zhbx@mail.ioa.ac.cn

Received July 15, 2002

Abstract—The excitation and propagation of the guided waves in a stratified half-space and a Rayleigh wave exploration method in shallow engineering seismic exploration are studied in this paper. All the modes of the guided waves are calculated by the bisection method in the case where the low velocity layers are contained in a stratified half-space. Cases when the formation shear wave velocity gradually decreases from the top to the bottom layers are also studied. The dispersion curves obtained in actual Rayleigh wave exploration are usually noncontinual zigzag curves, but the dispersion curves given by the elastic theory for given modes of the guided waves are smooth and continual curves. In this paper, the mechanism of zigzag dispersion curves in Rayleigh wave exploration is investigated and analyzed thoroughly. The zigzag dispersion curves can give not only the possible positions of the low-velocity layers but also the other information on the formation structure (fractures, oil, gas, etc.). It is found that the zigzag dispersion curves of the Rayleigh wave are the result of the leap of the modes and the existence of low velocity layers in a stratified half-space. The effects of the compressional wave velocity, shear wave velocity, and density of each layer on zigzag dispersion curves and the relationship of the low velocity layers to zigzag dispersion curves are also investigated in detail. Finally, the exploration depth of the Rayleigh wave is discussed. The exploration depth of the Rayleigh wave is equal to the wavelength multiplied by a coefficient that is variable and usually given by the work experience and the formation properties of the local work area. *© 2003 MAIK "Nauka/Interperiodica".*

INTRODUCTION

Rayleigh Wave Exploration (RWE) is a shallow seismic exploration method that can be used to interpret geological information below the free surface. The Rayleigh wave is a guided wave propagated along a stratified half-space. It is characterized by low velocity, small attenuation, and strong interference immunity. The RWE method has high resolution, simple operation, and other characteristics. The Rayleigh wave with enriched frequencies can be excited by the source in practical exploration. The different wavelengths correspond to the different exploration depths. Rayleigh wave signals with different frequencies can give formation information on different depths. So, more and more researchers have focused on this topic [1–8].

The Rayleigh wave was discovered by Rayleigh in an elastic half-space [9]. The energy of the Rayleigh wave concentrates below the free surface and decays with distance from the free surface. In the homogeneous half-space, there is only one guided wave propagated along the surface. This guided wave is just the Rayleigh wave and is nondispersive. However, in a stratified half-space there are usually infinite dispersion guided waves that can propagate along the stratified direction. Which guided waves correspond to the received packet in practical RWE? It is difficult to find this corresponding relationship. However, the Rayleigh wave in a stratified half-space as a term usually means the received signal packet (no compressional and shear waves) in a practical situation and does not explain which modes of guided waves are corresponded to.

The guided waves in a stratified half-space can be classified into two categories [10, 11]: surface and trapped waves. The energy of the surface wave concentrates in a narrow range below the free surface. However, the trapped wave is fundamentally related to the interfaces under the free surface. The maximum of the energy flux density of a trapped wave is not at the free surface but at a certain depth. There is no strict borderline between the surface and trapped waves. Sometimes the energy density of a mode decays with distance from the free surface in one frequency. It looks like the surface wave. However, at another frequency, this mode concentrates its energy at a certain place instead of at the free surface. It looks like a trapped mode in this case. Surface and trapped waves are important for RWE. This should be studied thoroughly. In some frequency range for a special stratified half-space containing low-velocity layers, the surface waves cannot be excited by the source. However, the trapped waves can be excited. In this situation, the received guided waves may be the trapped waves, although the intensities of the trapped waves are not maximums at the free surface.

In RWE, the velocity–wavelength (V–λ) profile that is transformed by the velocity–frequency (V–f) disper-

[1] This article was submitted by the authors in English.

1063-7710/03/4905-0516$24.00 © 2003 MAIK "Nauka/Interperiodica"

sion curve is usually adopted and used to analyze the formation structure below the free surface. It is known that the effective exploration depth of the Rayleigh wave is related to its wavelength. So the V–λ curve is usually known as the velocity–depth (V–z) profile, which indicates the formation information along the depth direction. Generally speaking, the V–z profiles of the Rayleigh wave obtained in actual exploration are noncontinual zigzag curves for a stratified half-space containing low-velocity layers [7, 8, 12, 13]. The zigzag shapes can give the possible positions of the low-velocity structures. However, for a given mode of the guided wave, the dispersion curve given by the elastic theory is a smooth and continual curve without zigzag shapes. Why are the dispersion curves obtained in actual exploration noncontinual zigzag curves? Few authors have studied this problem. Figure 1 gives a typical example. It is an actual result of RWE in some place. It has been proved that the two zigzag shapes in Fig. 1 can display roughly the real structure of the formation. This figure will be analyzed in the following parts.

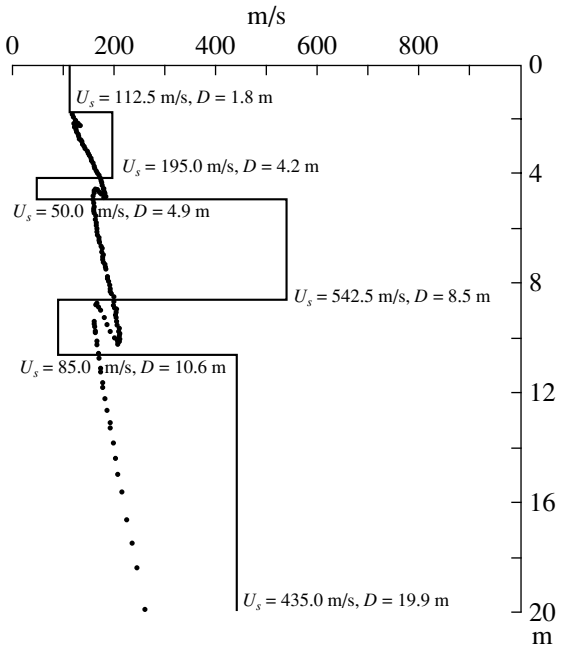

Fig. 1. An example of a zigzag dispersion curve obtained in RWE in some place.

Guided waves in a stratified half-space have been studied by many authors. Some methods were presented. The propagator matrix technique [14–16] is heuristic in many applications. However, the original propagator matrix [14] has the problem of loss of precision in the high frequency range. Abo-Zena [17] and Menke [18] presented a novel method to avoid the numerical problem that occurs in the high frequency range and this method perfected the elastic theory in multilayered media. In numerical simulation, the dispersion and excitation curves of the guided waves in the case where the compressional and shear wave velocities increase from the top to the bottom layers are studied by many researchers. However, when the low velocity layers are contained, especially when the shear wave velocity decreases from the top to the bottom layers, the guided waves in a stratified half-space have been numerically studied and analyzed by few authors.

Rayleigh wave exploration has also been focused on. McMechan *et al.* [4] demonstrated a wave field transformation method for analysis of dispersion wave trains. Yan [7, 8] analyzed the principle of RWE. Malagnini *et al.* [5] obtained the shear wave velocity and attenuation structure of the soft sediments by the Rayleigh wave for application in seismic engineering design in risky areas. Park *et al.* [6] developed a wavefield transformation method that provides images of dispersion curves directly from the recorded wavefields of multi-channels. H. Zhang *et al.* [19] proposed a coherent method to measure the dispersive curves of an elastic waveguide. B. Zhang *et al.* [10, 11, 20] investigated the propagation and energy distribution of the guided waves in multilayered media and presented two physical quantities of the Rayleigh wave that are sensitive to the material property of the medium and layered geometry. These works focused on the phase and group velocities, the characteristics, and the propagation mechanism. Few authors have studied the forming mechanism of the zigzag dispersion curves in RWE. Guan *et al.* [12, 13] analyzed the structure of the zigzag dispersion curves using a multilayered liquid model. B. Zhang *et al.* [21] analyzed all the modes of propagation along the multilayered media and studied the zigzag dispersion curves. However, some problems (such as the mechanism of the zigzag dispersion curves, relation of the zigzag dispersion curves to the formation parameters, and relation of the position of zigzag dispersion curves to the exploration depth) should be investigated further. These problems are very important to geophysics and engineering seismic explorations.

In this paper, the guided waves are studied in the B, P, C coordinate system [22] on the base of the propagator matrix developed by Thomson [23], Haskell [14], Abo-Zena [17], and Menke [18]. All the roots corresponding to the guided waves are obtained by the bisection method. At first, some mathematical formulations of the propagator matrix are reviewed. The excitation and propagation of the guided waves in a stratified half-space are analyzed. Then, the mechanism of the zigzag dispersion curves is studied and explained. The relation of the zigzag dispersion curves to the medium parameters of each layer is also studied. Finally, the dispersion curves with more than one zigzag shape are investigated and the relation of the position of zigzag dispersion curves to the exploration depth of the Rayleigh wave is analyzed.

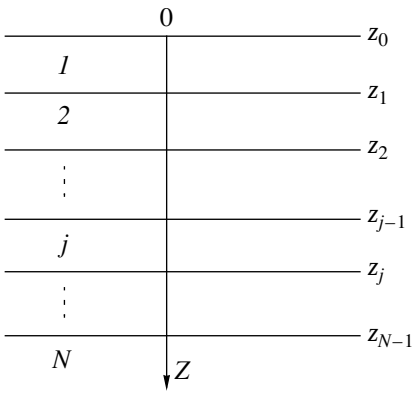

Fig. 2. Configuration of a stratified half-space.

FORMULATION

A semi-infinite medium made up of N parallel, homogeneous, isotropic layers are considered. All layers will be assumed to be elastic solid. The cylindrical coordinate system (r, θ, z) is adopted (Fig. 2). $Z = 0$ is the free surface of the first layer medium. It can be selected as the horizontal direction. The last layer medium extends to infinity along the z axis. The positive z axis is taken as the direction into the medium. The various layers and interfaces are numbered away from the free surface. For the jth layer, its properties are denoted by V_{pj} (P-wave velocity), V_{sj} (S-wave velocity), ρ_j (density), and h_j (thickness). The argument (j) will be omitted whenever it is possible without causing confusion.

It is convenient to introduce the B, P, C coordinate system [10, 21]

$$\begin{aligned} \mathbf{B} &= \mathbf{e_r}\frac{\partial}{\partial(kr)} + \mathbf{e}_\theta\frac{\partial}{kr\partial\theta}, \\ \mathbf{C} &= \mathbf{e_r}\frac{\partial}{kr\partial\theta} - \mathbf{e}_\theta\frac{\partial}{\partial(kr)}, \\ \mathbf{P} &= \mathbf{e_z}. \end{aligned} \tag{1}$$

Only the P–SV wave is considered in this paper. The displacement components in the B, P, C coordinate system and cylindrical coordinate system (r, θ, z) satisfy [10]

$$\begin{aligned} u_r &= \frac{1}{k}\frac{\partial u_B}{\partial r} + \frac{1}{kr}\frac{\partial u_C}{\partial\theta}, \\ u_\theta &= \frac{1}{kr}\frac{\partial u_B}{\partial\theta} - \frac{1}{k}\frac{\partial u_C}{\partial r}, \\ u_z &= u_P. \end{aligned} \tag{2}$$

Define the following vectors of S (motion stress) and ϕ (displacement potentials) [10, 17, 18, 20]

$$\begin{aligned} S &= (U_B/k, U_P/k, \tau_P/\omega^2, \tau_B/\omega^2)^T, \\ \phi(z) &= (Ae^{iaz}, Be^{-iaz}, Ce^{ibz}, De^{-ibz})^T \\ &= (\varphi^+, \varphi^-, \psi^+, \psi^-)^T. \end{aligned} \tag{3}$$

Then, the vectors S and ϕ satisfy [17, 18, 20]

$$\begin{aligned} S &= M\phi, \quad \phi(z_j) = \lambda\phi(z_{j-1}), \\ \lambda &= \mathrm{diag}(P, 1/P, Q, 1/Q), \\ M &= \begin{bmatrix} 1 & 1 & \gamma_s & -\gamma_s \\ \gamma_p & -\gamma_p & 1 & 1 \\ \rho(\gamma-1) & \rho(\gamma-1) & \rho\gamma\gamma_s & -\rho\gamma\gamma_s \\ \rho\gamma\gamma_p & -\rho\gamma\gamma_p & \rho(\gamma-1) & \rho(\gamma-1) \end{bmatrix}. \end{aligned} \tag{4}$$

The superscript T in Eq. (3) represents the transposed-matrix, $c = \omega/k$, $P = e^{\gamma_p kh}$, $Q = e^{\gamma_s kh}$, $\gamma = 2(V_s^2/c^2)$, $\gamma_p = -(1 - c^2/V_p^2)^{1/2}$, $\gamma_s = -(1 - c^2/V_s^2)^{1/2}$, $ia = k\gamma_p$, and $ib = k\gamma_s$. An implicit time dependence $e^{-i\omega t}$ of the field is assumed. $\varphi = \varphi^+ + \varphi^- = Ae^{iaz} + Be^{-iaz}$ and $\psi = \psi^+ + \psi^- = Ae^{ibz} + Be^{-ibz}$ are the displacement potentials of the P and SV waves in frequency wavenumber domain, respectively. φ^+ and ψ^+ represent waves propagating along the positive z axis, while φ^- and ψ^- represent waves propagating along the negative z axis. So the real parts of γ_p and γ_s should be smaller than (or equal to) zero.

By the boundary conditions of every interface, the vanishing of two stress components at the free surface and the potential at infinity, the dispersion equation can be obtained [18–20]:

$$E_6^{(1)} = 0. \tag{5}$$

It means that the sixth component of vector E at the free surface is vanishing, and it can be obtained by a propagator matrix using the relation [20]:

$$E^{(j-1)} = F^{(j)}E^{(j)}, \quad (j = 2, 3, \ldots, N), \tag{6}$$

where matrix F is a propagator matrix that can be decomposed into the following form [20]

$$F = \frac{1}{4\rho^2\gamma_p\gamma_s}U\lambda^*V. \tag{7}$$

The representations of matrices λ^*, U, and V can be referenced in the related literature [10, 17, 18, 20].

It is assumed that the source is located at $z = z_s$, $r = 0$ in the first layer medium. The components S_1 and S_2 of

the vector S at the free surface can be written as [20, 21]

$$S_1 = \frac{\Delta_1}{E_6^{(1)}} = \frac{(-T_{11}E_6^{(1)} + T_{31}E_3^{(1)} - T_{41}E_2^{(1)})A_{sn} + (-T_{12}E_6^{(1)} + T_{32}E_3^{(1)} - T_{42}E_2^{(1)})B_{sn}}{E_6^{(1)}},$$
$$S_2 = \frac{\Delta_2}{E_6^{(1)}} = \frac{(-T_{21}E_6^{(1)} + T_{31}E_5^{(1)} + T_{41}E_3^{(1)})A_{sn} + (-T_{22}E_6^{(1)} + T_{32}E_5^{(1)} + T_{42}E_3^{(1)})B_{sn}}{E_6^{(1)}}, \quad (8)$$

where A_{sn}, B_{sn}, and matrix T are the quantities related to the source [20].

The modes of the guided waves propagating in a stratified half-space are all given by the dispersion equation (5). It can be proved that the dispersion function is real for the real horizontal wavenumber. Only the modes of real horizontal wavenumber are considered in this paper. These modes can be obtained easily by the bisection method in numerical simulation, and their excitation amplitudes can be obtained by residues of the poles that are determined by Eq. (5). The displacement components of the guided waves can be written as

$$u_r(r, \theta, z; \omega) = i\pi\Delta_1\left[\frac{nH_n^{(1)}(kr)}{kr} - H_{n+1}^{(1)}(kr)\right]k^2\cos(n\theta)/\frac{\partial E_6^{(1)}}{\partial k},$$
$$u_z(r, \theta, z; \omega) = i\pi\Delta_2 H_n^{(1)}(kr)k^2\cos(n\theta)/\frac{\partial E_6^{(1)}}{\partial k}, \quad (9)$$
$$u_r(r, \theta, z; \omega) = -i\pi\Delta_1\frac{H_n^{(1)}(kr)}{kr}\sin(n\theta)/\frac{\partial E_6^{(1)}}{\partial k}.$$

The waveforms of time domain can be obtained by the Fourier transformation of Eq. (9).

GUIDED WAVES IN A STRATIFIED HALF-SPACE

It is indicated by numerical simulation that there exist many modes that correspond to guided waves propagated along the stratified direction in a stratified half-space. They are named as the first, second, third, etc., modes from the low frequency to high frequency. If the velocities of compressional and shear waves increase gradually from the first to the last media, the excitation intensity of the first mode is much greater than that of the other modes [24]. So the other modes are too small to be seen. Only the first mode can be received in practical RWE. This mode just corresponds to the Rayleigh wave. In this case, the dispersion curve obtained in RWE is a smooth curve. In fact, the zigzag dispersion curves of the Rayleigh wave obtained in RWE are the result of many modes generated by the low-velocity layers in a stratified half-space. So in what follows, we will pay more attention to the case where a low-velocity layer is contained in a stratified half-space. This formation model is important not only for natural resources exploration but also for the detection of fractures and faults.

At first, a three-layer model is chosen (model 1). The parameters of this model are shown in Table 1. In this model, the parameters of the third layer are the same as those of the first layer (similar results can be obtained if they are different).

Figure 3 gives the dispersion and excitation intensity curves of guided waves in model 1. It can be seen that there exist infinite guided waves. The first mode has no cutoff frequency (Fig. 3a), and the phase velocity when the frequency $f = 0$ is the Rayleigh wave velocity in the case where there is only the last layer. The other modes have cutoff frequencies at which the phase velocities are all equal to the velocity of the shear wave of the third layer. It can be found that the phase velocity of mode 4 is almost not related to frequency in the high frequency range, and it is equal to the velocity of the Rayleigh wave in the case where there is only the first layer. But the phase velocities of the other modes tend toward the shear wave velocity of the second layer as the frequency tends towards infinity.

It can be seen from Fig. 3b that the excitation intensities (displacement components u_z) of each mode are different and have different distribution ranges. In the low-frequency range the dominant guided wave is the first mode while in the high frequency range mode 4 is dominant. So in different frequency ranges, the modes which can be excited by the source are different. If the source frequency varies gradually, the received mode of guided waves will be skipped. Therefore, the received dispersion curves will be a noncontinual curve. It will be discussed in detail in the next section.

Then, another three-layer medium (model 2) is considered. Their parameters are also given in Table 1. In this model, the velocity of the compressional wave of the second layer is the minimum, and the velocity of the shear wave decreases gradually from the first to the third layers. It is easy to find that the velocity of the Rayleigh wave in the case where there is only the first layer is equal to 2884 m/s. We denote this velocity by $V_{1\infty}$, i.e., $V_{1\infty} = 2884$ m/s. It is easy to see that $V_{1\infty}$ is less than the shear wave velocity V_{s3} of the third layer. So the Rayleigh mode certainly exists at any value of the frequency. The dispersion curve in this model is depicted in Fig. 4. There is only one mode in this case. The phase velocity of this mode is less than the group velocity in the low frequency range, while it is greater

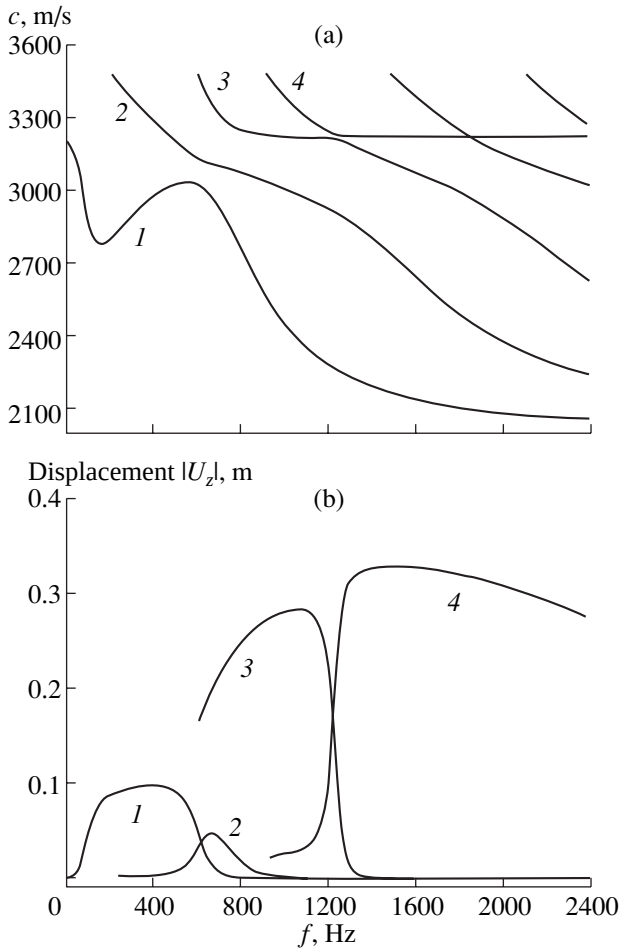

Fig. 3. The dispersion (a) and displacement intensities U_z (b) curves of modes in model 1.

than the group velocity in the high frequency range. If the formation parameters are similar to those in this case in RWE, the dispersion curves will be a continual and smooth curve.

Table 1. The values of the medium parameters in a stratified half-space

Model	*P*-wave velocity (m/s)	*S*-wave velocity (m/s)	Density (kg/m^3)	Thickness (m)
Model 1	6000	3500	3000	5
	3500	2000	2370	2
	6000	3500	3000	∞
Model 2	6000	3100	2200	5
	5000	3000	2800	2
	5990	2960	4540	∞
Model 3	6000	3500	3000	5
	5000	3000	2800	2
	4000	2500	2500	∞

Finally, model 3 is considered. The parameters are also given in Table 1. In this case, the velocities of the compressional and shear waves decrease gradually from the first to the third layers. It is easy to find $V_{1\infty}$ = 3213 m/s > V_{s3} = 2500 m/s. The dispersion curve in model 3 is displayed in Fig. 5. There is only one mode that can be excited when f < 200 Hz, and the phase velocity increases as the frequency increases. When the phase velocity is greater than the shear wave velocity V_{s3} (=2500 m/s) of the third layer, there is not any mode that can be excited by the source. This is because of the fact that the phase velocity of guided waves must be less than the shear wave velocity of the last layer in a stratified half-space. Otherwise, the energy of this guided wave will be infinite when the depth z tends towards infinity.

It should be pointed out that the first layer is a dominated layer when the frequency tends towards infinity. In this situation, a stratified half-space is equivalent to a homogeneous half-space that is composed of first layer medium. Therefore, the limit of the phase velocity of the guided waves is equal to $V_{1\infty}$ as the frequency tends towards infinity. In model 3, $V_{1\infty}$ = 3213 m/s is greater than V_{s3} = 2500 m/s. Although there is not any mode whose phase velocity is greater than 2500 m/s (V_{s3}) in the models, it should still be thought that the limit of the velocity of the guided wave is $V_{1\infty}$ = 3213 m/s in the high frequency.

ZIGZAG DISPERSION CURVES

In RWE, the velocity–wavelength (V–λ) curves of the Rayleigh wave that are transformed by the velocity–frequency (V–f) curves are usually adopted. The effective penetration depth (or exploration depth) of the Rayleigh wave is related to its wavelength. That is, the Rayleigh wave with the wavelength λ can reflect the formation information in the depth λ. So the V–λ curve is also named the velocity–depth (V–z) profile. In actual exploration, the V–z profile obtained is usually a non-continual zigzag curve. However, for a given mode of the guided wave, the dispersion curve is a continual curve. Why is it? Is the zigzag V–z curve obtained in the transformation course from V–f curve to V–λ curve? We found this idea to be wrong.

It is supposed the V–f curve of a mode is continual (Fig. 6). At a point B on the curve, $\lambda = V/f = \tan\alpha$. It is easy to find that the points B, C, and D on the curve have the same value of wavelength λ. This is why it is thought that the zigzag dispersion curve is possibly obtained in the transformation course. Now that point C is considered, it is easy to find that

$$\frac{dV}{df} > \frac{V}{f}. \tag{10}$$

And therefore, it can be proved at point C that the group

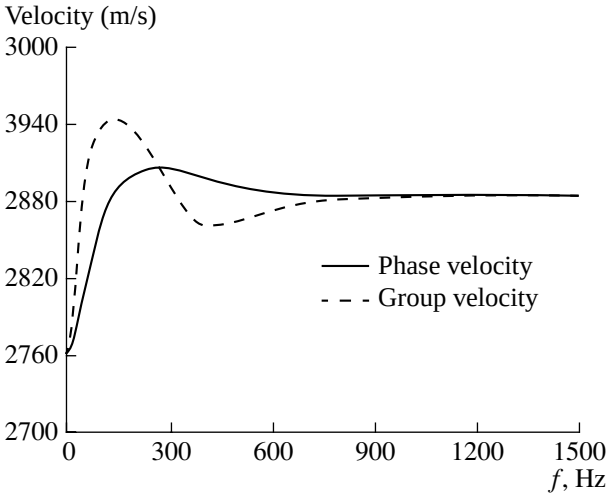

Fig. 4. Dispersion curve of the guided wave in model 2.

velocity satisfies

$$\frac{1}{V_g} = \frac{dk}{d\omega} = \frac{d}{d\omega}\left(\frac{\omega}{V}\right) = \frac{d}{df}\left(\frac{f}{V}\right) = \frac{f}{V^2}\left(\frac{V}{f} - \frac{dV}{df}\right) < 0. \quad (11)$$

This result is inconsistent with the actual case. The group velocity is the propagation velocity of the energy of the guided wave. The value of the group velocity must be greater than zero. So Eq. (11) is a wrong result, and point *C*, which satisfies Eq. (10), is nonexistent. This means that the tangent of any point on the dispersion curves does not pass through the origin of the coordinate system. That is, any straight line through the coordinate origin can intersect only once with the smooth *V*–*f* curve of a given mode. Hence, only one value of velocity for a given wavelength λ (or α) exists. The zigzag dispersion curve cannot be obtained in the transformation course for a given mode of guided wave.

Therefore, it can be thought that the zigzag dispersion curve in RWE is the result of many modes corresponding to the guided waves in a stratified half-space. As a typical example, model 1 is reconsidered. There exists more than one mode at a given frequency. The mode whose velocity is the highest will reach the receiver first. However, the mode with the highest velocity is not certainly received by the receiver. If the displacement intensity (or energy) of this mode is too small to be seen, this mode cannot be received by the receiver, although it has a higher velocity. On the contrary, if a mode has a slower velocity but a bigger intensity, this mode will be dominated and received. So it is important to consider the velocities and the excitation intensities of the guided waves. Not only the propagation velocities but also the intensities of the guided waves in RWE must be considered.

Figure 3a shows that there are many modes of guided waves, and Fig. 3b displays their excitation intensities in model 1. Mode 2 and the modes whose order are higher than 4 are relatively small. When the source frequency increases gradually, the received modes of the guided waves will be skipped from one mode to the higher mode. So the received guided waves may be skipped from mode 1 to mode 3, and to mode 4 when the source frequency increases from zero to infinity. The skip course can be represented by the thick lines in Fig. 3b. We connect the corresponding phase velocities and obtain Fig. 7a, which is composed piecewise of some modes of guided waves. Then, if this *V*–*f* curve is transformed further into the *V*–λ curve, the zigzag dispersion curve will be obtained. It is depicted in Fig. 7b. This structure of zigzag dispersion curves of the Rayleigh wave is very similar to that obtained in RWE.

In the case where the compressional and shear wave velocities increase gradually from top to bottom layers, only the first mode of the guided wave has the dominant intensity, and the other modes are too small to be seen. This is explained in the above section. If the velocity of

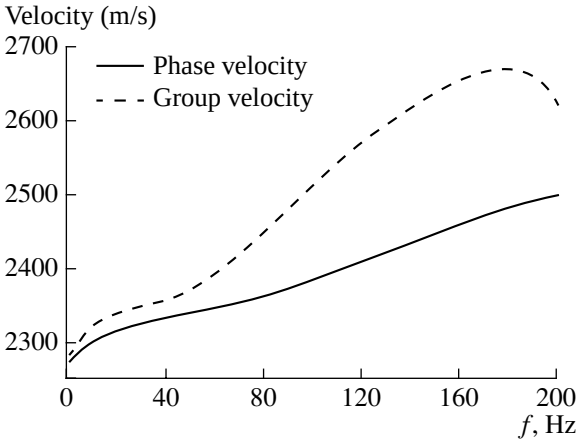

Fig. 5. Dispersion curve of the guided wave in model 3.

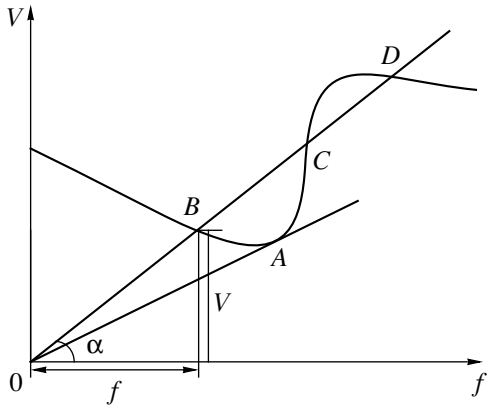

Fig. 6. Graph of dispersion curve.

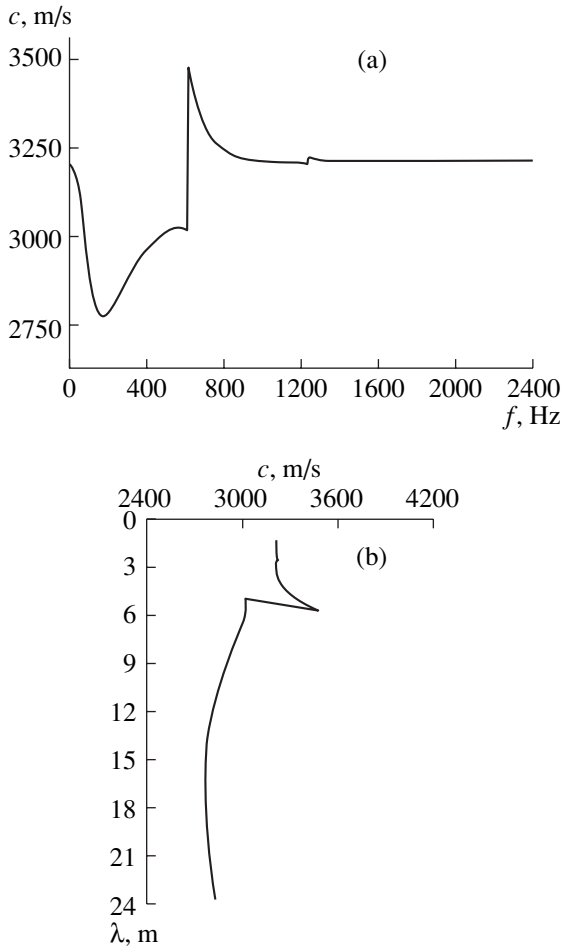

Fig. 7. (a) Velocity–frequency curve composed paragraphically by the modes in model 1. (b) Velocity–wavelength curve corresponding to (a).

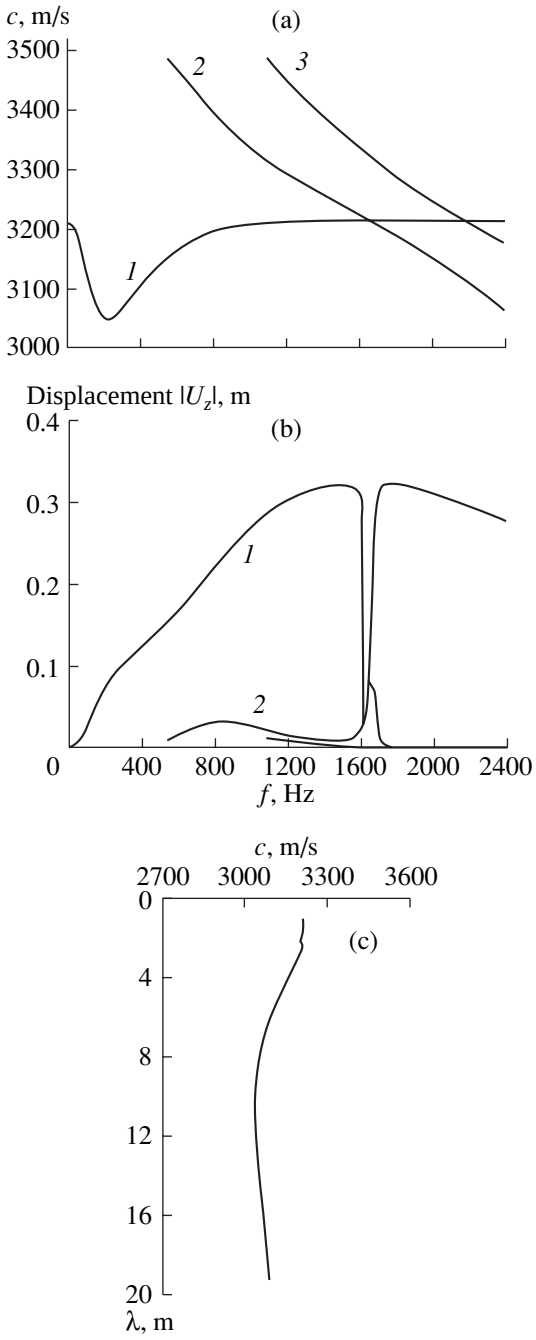

Fig. 8. Dispersion and excitation curves in model 1 with a thickness of the second layer of 0.5 m.

the shear wave decreases from top to bottom layers, the number of modes that can be excited is not greater than one. This characteristic can be also seen in Figs. 4 and 5. In these cases, the dispersion curves of the Rayleigh wave are smooth and continual curves. So the zigzag dispersion curve of the Rayleigh wave exists in the case where the low-velocity layers are contained in a stratified half-space. It is also indicated that there is an important relationship between the zigzag dispersion curve and the low-velocity layers.

Figure 8 gives another example of zigzag dispersion curves in model 1, but the thickness h_2 of the second layer is 0.5 m. All guided waves move to the high frequency range (Fig. 8a). It can be seen from Fig. 8b that the dominant mode is the first mode and the other modes are too small to be seen in this case. Figure 8c displays the corresponding V–z profile. It shows that the zigzag shape in the curve is very small. If the thickness h_2 of the second layer is less than 0.5 m, the zigzag structure cannot be seen. This also shows that a thinner low-velocity layer cannot produce a significant zigzag structure of the Rayleigh wave dispersion curves. This may be one of the reasons why it is difficult to detect the thinner low-velocity layers in RWE.

The above zigzag dispersion curves are obtained by the intensities, which are given by the residues of the poles, and phase velocity of the guided waves. We can also obtain the zigzag dispersion curves using the full-waveforms by the cross correlation method. In this method, at first, the total full-waveforms of the pure guided waves are obtained by eliminating the compres-

sional and shear waves. Then, the dispersion curves can be given by the cross correlation method using these full-waveforms of some channels. The dispersion curves obtained by the cross correlation method are almost equivalent to that by the above method in theory. In fact, it has been proved that the two methods are equivalent in our works by lot of numerical simulation.

Now, we can explain the zigzag shapes in Fig. 1. It is an actual exploration result in some place. It has been proved that two zigzag shapes can display the real structure of the formation. In fact, there basically exist six layers in the formation. Their shear wave velocities are 112.5, 195, 50, 542, 85, and 435 m/s, respectively. The thicknesses of each layer are 1.8, 2.4, 0.7, 3.6, 2.1 m, and infinity, respectively. The third and fifth layers are low-velocity layers. The theoretical simulation is conducted according to this model. The other parameters are known. But the compressional wave velocity of each layer can be concluded by the field soil and the Poisson's ratio of the rock, and the density of each layer can be concluded by the shear wave velocity and experience. The theoretical result of this model is depicted in Fig. 9. It is obtained by the cross correlation method from the time domain waveforms with no compressional and shear waves. It can be seen that the theoretical curve is very close to that of real data. There exist the inflection points of zigzag shapes near the two low velocity layers. It can also be found that there exists a definite difference between Fig. 1 and Fig. 9. This is because the model of the media is not the standard stratified media in an actual situation. And the compressional wave velocities and the densities of each layer are unknown and are given by the Poisson's ratio and experience. However, this difference is small; it basically shows that the method of this paper is reasonable.

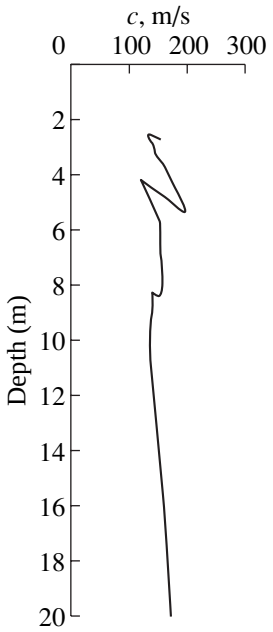

Fig. 9. Velocity–depth curve calculated by theoretical model after Fig. 1.

THE EFFECTS OF MEDIA PARAMETERS ON THE ZIGZAG DISPERSION CURVES

In this section, we analyze the effects of the medium parameters of each layer on the zigzag dispersion curves. The dispersion equation is a function of four parameters for each layer: *S*-wave velocity, *P*-wave velocity, density, and thickness. In this paper, the effects of *S*-wave velocities, *P*-wave velocities, and the densities of each layer on zigzag dispersion curves are studied in detail.

The Effects of S-Wave Velocities of Each Layer on Dispersion Curves

Model 1 is still considered in this section. The effects of *S*-wave velocities on zigzag dispersion curve are considered by changing the *S*-wave velocities of each layer while the other parameters are invariable. As a comparison, the dispersion curve of model 1 is given by the dashed line in Fig. 10.

Figure 10a gives the zigzag dispersion curves in model 1 by changing the *S*-wave velocity V_{s1} of the first layer from 3500 to 3000 m/s. It can be seen that the dispersion curve has a great change when V_{s1} is changed. The phase velocity of the Rayleigh wave is smaller when $V_{s1} = 3000$ than when $V_{s1} = 3500$ m/s. This shows that the effect of the shear wave velocity of the first layer on the Rayleigh wave is significant, especially in the range of short Rayleigh wave wavelength. However, the shift of the position of the zigzag shape in the depth direction is very small. This also shows that the position of the zigzag shape in the dispersion curves can really reflect the location of the low-velocity layer.

The dispersion curves in model 1 with the *S*-wave velocity 1500 m/s (V_{s2}) of the low-velocity (second) layer are shown in Fig. 10b. When the wavelength is greater than the thickness of the first layer, the Rayleigh wave velocity decreases as V_{s2} decreases. However, this change is small when the wavelength is less than the thickness of the first layer. The shift of the position of the zigzag shape in the depth direction is also small. The properties of zigzag dispersion curves near the free surface are determined by the parameters of the first layer. The effect of the velocity V_{s2} of the second layer on the Rayleigh wave velocity appears significantly in the range of wavelength that is more or less greater than the thickness of the first layer.

The solid line in Fig. 10c gives the zigzag dispersion curve obtained in model 1 with the *S*-wave velocity 4000 m/s (V_{s3}) of the third layer. As the shear wave velocity of the third layer increases, the zigzag shape in the dispersion curve has a slight shift towards the depth direction (wavelength). The zigzag shape can still reflect the location of the low-velocity layer. It can also

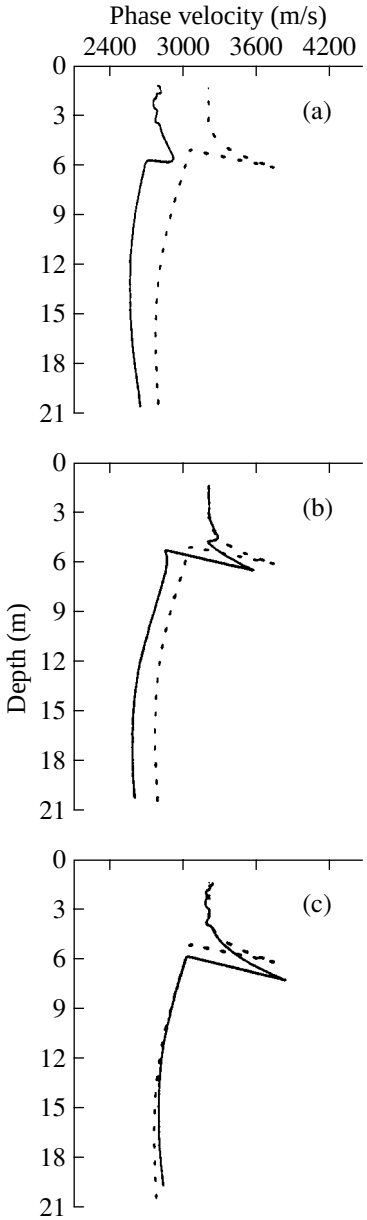

Fig. 10. Velocity–wavelength curves of the model with different shear wave velocity of the first (a), second (b), and third (c) layers.

be seen that the phase velocity in the long wavelength range increases slightly due to the increase in $V_{3\infty}$ (the Rayleigh wave velocity in the case where there is only the third layer).

From Figs. 10a–10c it can be found that the velocity of the Rayleigh wave increases (or decreases) as the shear wave velocities of each layer increases (or decreases). And the shift of the position of the zigzag shape in the depth direction is small. The change of the shear wave velocity of a layer mainly affects the velocity of the Rayleigh wave in the range of wavelength that is just about the depth of this layer, and the effect on the other wavelength range is relatively small.

The Effects of P-Wave Velocities of Each Layer on Dispersion Curves

Figure 11a is the dispersion curve in model 1 with the compressional wave velocity 5200 m/s (V_{p1}) of the first layer. Similar to Fig. 10a, the phase velocity becomes smaller when V_{p1} is decreased, but this change is apparent less than that in Fig. 10a. Not only the velocity of the Rayleigh wave but also the position of the zigzag shape is almost not changed when V_{p1} is changed.

Figure 11b gives the dispersion curve in model 1 with the compressional wave velocity 3000 m/s (V_{p2}) of the second layer, and Fig. 11c gives the dispersion curves in model 1 with the compressional wave velocity 5200 m/s (V_{p3}) of the third layer. In these cases, the velocity of the Rayleigh wave and the position of the zigzag shape are almost not changed.

It is indicated by Figs. 11a–11c that the Rayleigh wave velocity and the position of the zigzag shape in the depth direction are not sensitive to the compressional wave velocity of each layer. So, we do not consider the effect of the compressional wave velocity of the formation especially in the inversion study.

The Effects of Densities of Each Layer on Dispersion Curves

Figures 12a–12c give the dispersion curves in model 1 with the densities 2500 kg/m^3 (ρ_1) of the first layer, 1500 kg/m^3 (ρ_2) of the second layer, and 2500 kg/m^3 (ρ_3) of the third layer, respectively. It can be seen that the position of the zigzag shape has no changes, although the densities of each layer are changed. But phase velocity of the Rayleigh wave in the range of long wavelength has a definite change.

On the basis of the above analyses, it can be concluded that the effect of *S*-wave velocity on the dispersion curve of the Rayleigh wave is significant. The changes of the *S*-wave velocities of each layer affect not only the phase velocity of the Rayleigh wave but also the position of the zigzag shapes. However, the effect of the shear wave velocities of each layer on the position of zigzag shape in the depth direction is very small. The effects of *P*-wave velocities and the densities of each layer are relatively small. When the *P*-wave velocities and the densities of each layer are changed, the position of the zigzag shape in the depth direction is almost not changed.

It is also easy to see that when the parameters (compressional wave velocity, shear wave velocity, density) of each layer are changed, the value of the Rayleigh wave velocity is changed but the position of the zigzag shape of dispersion curve in the depth (wavelength)

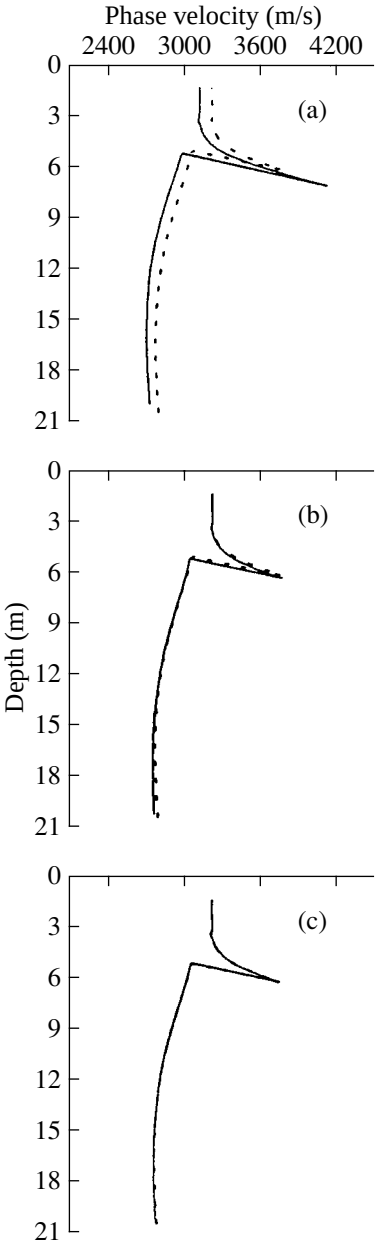

Fig. 11. Velocity–wavelength curves of the model with different compressional wave velocity of the first (a), second (b), and third (c) layers.

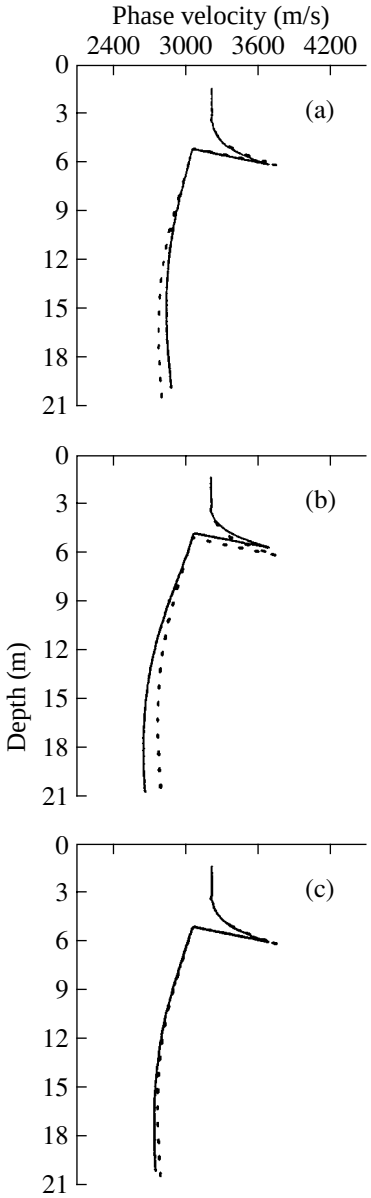

Fig. 12. Velocity–wavelength curves of the model with different density of the first (a), second (b), and third (c) layers.

direction is almost not changed. The change of the parameters of a layer mainly affects the velocity of the Rayleigh wave in the range of wavelength of the Rayleigh wave that is just about the depth of this layer, and the effect on the other wavelength range is relatively small.

ZIGZAG DISPERSION CURVES IN MORE THAN ONE LOW-VELOCITY LAYER

Only one low-velocity layer is considered in the above discussions. In this situation, the dispersion curve has only one zigzag shape whose location can indicate the position of the low-velocity layer. In this section, the formation models that contain more than one low-velocity layer are considered.

Firstly, a five-layer model (model 4) that contains two low-velocity layers is considered. The parameters of each layer are shown in Table 2. In this model, the second and fourth layers are low-velocity layers, and their top positions are at depths $z = 5$ and $z = 8.8$ m, respectively. The solid line in Fig. 13a gives the dispersion curves for this model. It can be seen that there are apparently two zigzag shapes that correspond to the two low-velocity layers, respectively. The position of

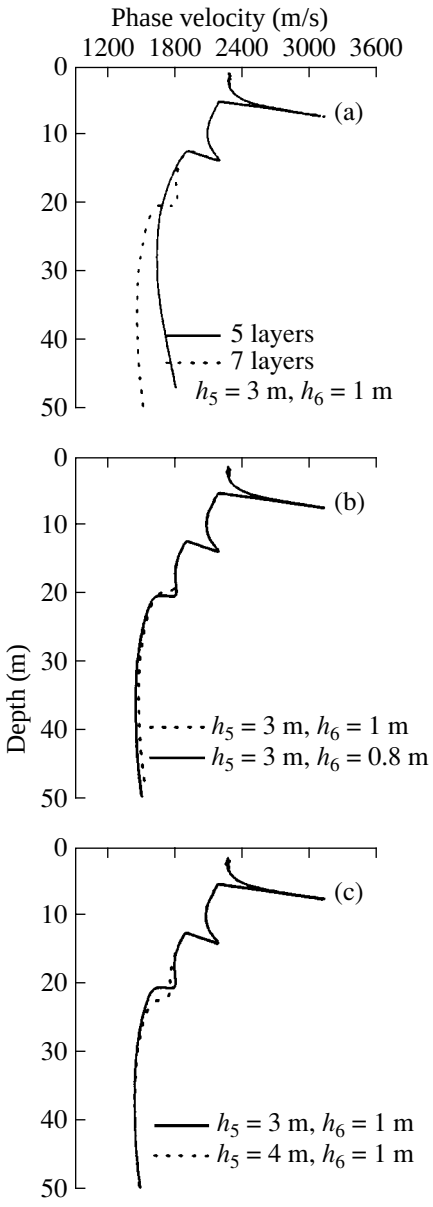

Fig. 13. (a) Velocity–wavelength curves for models 4 and 5. (b) Velocity–wavelength curves for model 5 with the thickness h_6 = 0.8 m of the sixth layer. (c) Velocity–wavelength curves for model 5 with the thickness h_5 = 4 m of the fifth layer.

the first zigzag shape is at about λ = 5 m. If we take the wavelength of the Rayleigh wave as the exploration depth. It can be seen that a good result can be obtained for the first low velocity layer. However, the position of the second zigzag shape is at about λ = 12 m, which is deeper than the real position (8.8–10.8 m) of the second low-velocity layer. This means that greater errors will be obtained in the location of the second low-velocity layer than in the first low-velocity layer if the wavelength of the Rayleigh wave is taken as the exploration depth.

Then, a seven-layer model (model 5) containing three low-velocity layers is considered. The parameters of each layer can be seen in Table 2. In this model, the first, second, third, fourth, and fifth layers are the same as that in model 4. The second, fourth, and sixth layers are low-velocity layers. The dashed line in Fig. 13a is the dispersion curve for this model. It is found that three zigzag shapes exist in dispersion curves. The first and second zigzag shapes near the free surface are coincident with that in the five-layer model (model 4), while the third zigzag shape is near 20 m. Similar to the second zigzag shape, the location of the third zigzag shape is deeper than the actual position.

The dispersion curves of the seven-layer model (model 5) with a different thickness h_6 of the third low-velocity layer are given in Fig. 13b. As we might expect, the locations of the first and second zigzag shapes when h_6 = 0.8 are coincident with that when h_6 = 1 m. The third zigzag shapes for two cases (h_6 = 0.8 and 1 m) have the same depth, but the zigzag shape when h_6 = 0.8 is smoother and vaguer than that when h_6 = 1 m. In practice, the third zigzag shape will vanish when the thickness of the third low-velocity layer decreases to a small value. This is the reason why thin low-velocity layers are difficult to find in Rayleigh wave exploration.

Figure 13c gives the dispersion curves in the seven-layer model (model 5) with different thickness h_5 of the fifth layer. It can be found that the position of the third zigzag shape when h_5 = 4 is deeper than that when h_5 = 3 m. It can be seen that only the third zigzag shape in the dispersion curve is changed when h_5 is changed. For a stratified half-space containing more than one low-velocity layer, it is more difficult to obtain information on the low velocity in a deeper place than that in a shallow place.

The penetration depth (or exploration depth) of the Rayleigh wave is a complicated problem. It can be seen that the exploration depth in the method of this paper is all about the wavelength for the first low-velocity layer (the top of the first low-velocity layer is at z = 5 m in all models in this paper). However, the exploration depth should be multiplied by a proper weight coefficient for the low velocity layer in the high depth. Generally speaking, this coefficient is less than 1 and is different for different depths. The deeper the low velocity is, the less the coefficient is. The compressional and shear wave velocities of the formation are relatively small in engineering seismic exploration, so the coefficient of the exploration depth is generally about 0.5. Hence, this method is usually known as the half wavelength method in engineering seismic exploration. However,

this coefficient is variable, and it is usually given by work experience and the local area. This coefficient is higher in the formations with higher velocities of compressional and shear waves.

CONCLUSIONS AND DISCUSSION

The mechanism of the zigzag dispersion curves that appear in RWE is studied on the basis of analyzing the guided waves in a stratified half-space. The characteristics of the zigzag dispersion curves and the effects of the formation parameters are analyzed. The relation of the shape and position of the zigzag dispersion curves to the exploration depth of the Rayleigh wave is also investigated.

There exist many modes in a stratified half-space. Different modes exist in different frequency ranges. If the source frequency increases (or decreases) gradually, the received modes of the guided waves should be skipped from one mode to another mode and the zigzag velocity–wavelength dispersion curves observed in RWE are formed. However, in the case where the compressional and shear wave velocities increase gradually from the top to the bottom layers, only the first mode of the guided wave has the dominant intensity, and the other modes are too small to be seen. So only one mode can be observed, and there is no zigzag shape in the dispersion curves in this case. Similarly, if the velocity of shear wave decreases from the top to the bottom layers, the number of modes that can be excited is not greater than one. This also shows that there is no zigzag shape in the dispersion curves. The zigzag dispersion curves of the Rayleigh wave exist certainly in the case where the low-velocity layers are contained in a stratified half-space.

If the parameters of each layer are changed, the value of the Rayleigh wave velocity should be changed significantly, but the position of the zigzag shape of the dispersion curve in the depth (wavelength) direction should be almost not changed. The change of the parameters of a layer mainly affects the velocity of the Rayleigh wave in the range of wavelength of the Rayleigh wave that is just about the depth of this layer, and the effect on the other wavelength range is relatively small.

The exploration depth of the Rayleigh wave is the wavelength multiplied by a proper weight coefficient. Generally speaking, this coefficient is less than 1 and is different for different depth. The deeper the low velocity layer is, the less the coefficient is. This coefficient is variable, and it is usually given by work experience and the soil properties of the local work area. The coefficient is generally about 0.5 in engineering seismic exploration, because the compressional and shear wave velocities are relatively small, while it is higher in the formation with higher velocities of compressional and shear waves.

Table 2. The medium parameters in a stratified half-space containing two and three low-velocity layers

Model	*P*-wave velocity (m/s)	*S*-wave velocity (m/s)	Density (kg/m^3)	Thickness (m)
Model 4	4000	2500	2500	5
	2350	1120	1060	0.8
	6000	3500	3000	3
	1500	800	1370	2
	5000	3000	2800	∞
Model 5	4000	2500	2500	5
	2350	1120	1060	0.8
	6000	3500	3000	3
	1500	800	1370	2
	5000	3000	2800	3
	1200	650	1000	1
	5000	3000	2800	∞

There exists an important relationship between the zigzag dispersion curves and the low velocity layers. It is necessary to study this relationship and explain the basis for RWE. This paper presents a trial investigation, although it is not perfect in some aspects. We hope that this paper will play an important role in a thorough study of the Rayleigh wave.

ACKNOWLEDGMENTS

This work was supported by the National Natural Science Foundation of China (19804019, 101340200) and the President Foundation of the Institute of Acoustics, Chinese Academy of Sciences.

REFERENCES

1. D. G. Harkrider, Bull. Seismol. Soc. Am. **54**, 627 (1964).
2. J. O. Parra, J. Acoust. Soc. Am. **90**, 2557 (1991).
3. J. O. Parra and P. C. Xu, J. Acoust. Soc. Am. **95**, 91 (1994).
4. G. A. McMechan and M. J. Yedlin, Geophysics **46**, 869 (1981).
5. L. Malagnini, R. B. Herrmann, A. Mercuri, *et al.*, Bull. Seismol. Soc. Am. **87**, 1413 (1997).
6. Choon Byong Park, R. D. Miller, and Jianghai Xia, in *SEG Expanded Abstracts* (1998), p. 1388.
7. Shoumin Yan, Prog. Geophys., No. 6, 21 (1991).
8. Shoumin Yan, Geophys. Geochem. Explor. **16**, 113 (1992).
9. Lord Rayleigh, Proc. London Math. Soc. **17**, 4 (1885).
10. Bixing Zhang, Ming Yu, Cong-Qing Lan, *et al.*, J. Acoust. Soc. Am. **103**, 125 (1998).

11. Bixing Zhang, Ming Yu, Wei Xiong, *et al.*, Chin. J. Nonferrous Met. **8**, 340 (1998).
12. Xiaoping Guan, Jiazheng Huang, and Hongqiu Zhou, Chin. J. Geophys. **36**, 96 (1993).
13. Jiazheng Huang, Hongqiu Zhou, and Xiaoping Guan, Geophys. Geochem. Explor. **15**, 268 (1991).
14. N. A. Haskell, Bull. Seismol. Soc. Am. **43**, 17 (1953).
15. Youming Li and Peiyi Shu, Chin. J. Geophys. **25**, 131 (1982).
16. Zhenxing Yao, Chin. J. Geophys. **22**, 181 (1979).
17. A. Abo-Zena, Geophys. J. R. Astron. Soc. **58**, 91 (1979).
18. W. Menke, Geophys. J. R. Astron. Soc. **59**, 315 (1979).
19. Hailan Zhang, Shuwu Dai, and Chengyn Zhang, Appl. Phys. Lett. **78**, 2846 (2001).
20. Bixing Zhang, Ming Yu, Cong-Qing Lan, *et al.*, J. Acoust. Soc. Am. **100**, 3527 (1996).
21. Bixing Zhang, Boxun Xiao, Wenjie Yang, *et al.*, Chin. J. Geophys. **43**, 591 (2000).
22. A. Ben-Menahem and S. J. Singh, Bull. Seismol. Soc. Am. **58**, 1519 (1968).
23. W. T. Thomson, J. Appl. Phys. **21**, 89 (1950).
24. Bixing Zhang and Laiyu Lu, Acta Acustica **27**, 295 (2002).

Acoustical Physics, Vol. 49, No. 5, 2003, pp. 529–534. Translated from Akusticheskiĭ Zhurnal, Vol. 49, No. 5, 2003, pp. 626–631.

A Helmholtz Resonator Buried in the Ground as a Source of Seismic Waves and Low-Frequency Sound in the Atmosphere

Yu. M. Zaslavskiĭ

Institute of Applied Physics, Russian Academy of Sciences, ul. Ul'yanova 46, Nizhni Novgorod, 603950 Russia
e-mail: zaslav@hydro.appl,sci-nnov.ru

Received October 15, 2002

Abstract—The procedure is given for calculating the total power of low-frequency sound and seismic waves produced by a Helmholtz resonator in the form of an air-filled spherical cavity buried in the ground and supplied with a hole through which it is connected with the atmosphere. The sound is generated by air oscillations in the resonator's neck section that is open to the atmosphere, while the compression and shear elastic waves are generated in the bulk of the ground by cyclic pressure fluctuations that act on the spherical walls of the cavity. Calculations show that the coincidence of the resonance frequencies (within approximately ten to hundred hertz), at which both the sound radiation to the atmosphere and the elastic seismic radiation in the form of longitudinal and transverse bulk waves are maximum, can occur only when the resonator is placed in a loose ground characterized by reduced elastic characteristics. In these conditions, the power of transverse waves exceeds the sound power by a factor of two and the power of longitudinal waves is smaller than the sound power by a factor of several tens. *© 2003 MAIK "Nauka/Interperiodica".*

INTRODUCTION

The development of new principles of constructing nonexplosive sources of acoustic waves in the atmosphere and seismic waves is rather topical, because it provides the basis for monitoring the atmosphere and for sounding the earth's depth by vibroseismic methods. For the air medium, high-quality acoustic sources have already been designed, including those operating in the low-frequency range. As for the seismic sources available on the market and even their new models under design, these sources are characterized by very low efficiency of elastic wave generation, which hampers the solution of multiple problems of seismic sounding. In this connection, some researchers have already proposed and discussed methods of generating seismic waves with the use of hydroacoustic sources [1–3]. This paper considers a source of vibrations that provides a combined generation of acoustic waves in the atmosphere and seismic waves with the use of a system that is well known in acoustics, namely, a Helmholtz resonator. An attractive feature of this source is that it requires no heavy (multiton) structures for providing a force action on the earth's surface, because it uses an air-driven source of pressure or airflow fluctuations: such a source can be realized using a routine compressor. The analysis presented in this paper deals with the quantitative estimates of the power of both seismic radiation and low-frequency sound in the atmosphere (in the range approximately from 20 to 100 Hz), which are excited by the oscillations of both air and the walls of the Helmholtz resonator completely buried in the ground. The object under consideration is an idealized system in which the resonator neck has a zero height; i.e., the resonator neck is simply a hole in the spherical cavity, and this hole opens flush with the ground surface, as shown in Fig. 1. In this configuration, the depth of the spherical cavity center coincides with the radius of the sphere. The calculation is aimed at evaluating the comparative energy characteristics of elastic seismic waves and sound waves in the atmosphere, both of which are generated by the same source: the sound in the atmosphere is generated by the acoustic oscillations of air in the neck section, and the elastic (or vibroseismic) waves are excited by the oscillating pressure which acts on the spherical walls of the resonator buried in the ground. The cavity in the surrounding medium represents one of the two coupled oscillators of the whole oscillating system, and it is necessary to determine the conditions at which these oscillators will have close resonance frequencies. The cavity is assumed to have no additional envelope, because such an envelope makes it necessary to introduce an additional stiffness, which complicates the problem. Since the Rayleigh surface waves are of little use in sounding and monitoring problems, the contribution of the surface waves excluded from the consideration and only the total energy of compression and shear bulk waves is evaluated, despite the fact that the contribution of surface waves is known to predominate at lower frequencies. It is obvious from general considerations that, in a resonator placed in a perfectly rigid medium, only acoustic oscillations that produce atmospheric sound

1063-7710/03/4905-0529$24.00

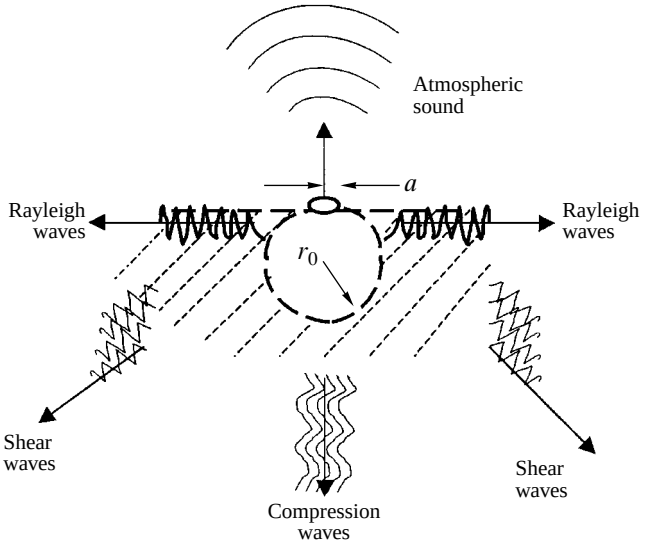

Fig. 1. Schematic diagram of seismic fields and atmospheric sound generated by the buried Helmholtz resonator.

will be excited. As the stiffness of the surrounding elastic medium is reduced to certain acceptable values, another oscillating system is formed: a spherical cavity in an elastic medium whose resonance frequency may be close or even coincident with the resonance frequency of the air oscillations in the Helmholtz resonator.

The presence of a free boundary and the hole connecting the cavity with the atmosphere violate the spherical symmetry, which is usually implied in calculating the resonance vibrations of a cavity. However, below, this factor is ignored in the calculations proceeding from the assumption that the resonance conditions vary only slightly when the hole radius is much smaller than the cavity radius. The problem under consideration includes the determination of the conditions under which the resonance frequency of the elastic cavity coincides with the resonance frequency of air oscillations in the Helmholtz resonator, as well as the evaluation of the sound power and the power of elastic waves in the ground under the aforementioned conditions. The comparison of these powers will show whether the source should be considered as a predominantly atmospheric or seismic source. It should be noted that the sound energy emitted into the atmosphere by a seismic vibrator located on the ground's surface was already considered in [4]. The calculation and the estimates showed that the sound power was negligible in comparison with the power of seismic radiation. The present paper considers another mechanism of sound generation in the atmosphere. The question arises as to whether the energy of acoustic oscillations predominates in this case. The answer requires some calculations. The analysis given below assumes the use of the solution that was obtained and analyzed in [5] for the elastic fields generated in the half-space by an oscillating sphere (a source of hydrostatic pressure) located at some depth below the free surface. This solution is appropriate for describing the seismic radiation from the oscillating walls of an almost spherical cavity. Thus, the desired comparative estimates can be obtained on the basis of the aforementioned information and the theory of sound radiation by a Helmholtz resonator [6].

THEORETICAL CALCULATION AND ESTIMATES

Let us assume that the Helmholtz resonator is excited by an external action producing oscillations of the air mass with a volume velocity amplitude V_0 and a frequency ω. In this case, one can easily calculate the power of the acoustic radiation generated in the atmosphere by the air oscillations in the section of the resonator's neck. It is known [6] that the generalized displacement of the air column in the resonator's neck u and the acoustic pressure p in the cavity satisfy the equations

$$\begin{aligned}\frac{\partial^2 u}{\partial t^2} + \alpha\frac{\partial u}{\partial t} + \omega_0^2 u &= -i\frac{\omega V_0}{\pi^3 a^2}e^{-i\omega t},\\ \frac{\partial^2 p}{\partial t^2} + \alpha\frac{\partial p}{\partial t} + \omega_0^2 p &= -i\frac{3\omega V_0 \rho c^2}{4\pi^3 r_0^3}e^{-i\omega t},\end{aligned} \tag{1}$$

where $\alpha = \dfrac{3}{8\pi^2}\dfrac{a^2 c}{r_0^3}$ is the attenuation factor, $\omega_0^2 = \dfrac{3}{2\pi}\dfrac{c^2 a}{r_0^3}$ is the squared frequency of natural oscillations without taking the attenuation into consideration, ρ is the air density, c is the sound velocity in air, a is the neck radius, and r_0 is the radius of the spherical cavity. The above expressions for the attenuation factor and the frequency are valid for a resonator whose neck has a zero height and whose geometric parameters satisfy the condition $a \ll r_0$.

It is not difficult to derive formulas describing the forced solutions of Eq. (1) in the coordinate u and the acoustic pressure p:

$$\begin{aligned}u &= \frac{V_0\omega}{\pi^3 a^2}\frac{\alpha\omega + i(\omega^2 - \omega_0^2)}{[(\omega^2 - \omega_0^2)^2 + (\omega\alpha)^2]}e^{-i\omega t},\\ p &= \frac{3V_0\omega\rho c^2}{4\pi^3 r_0^3}\frac{\alpha\omega + i(\omega^2 - \omega_0^2)}{[(\omega^2 - \omega_0^2)^2 + (\omega\alpha)^2]}e^{-i\omega t}.\end{aligned} \tag{2}$$

The total acoustic power emitted in a solid angle of 2π (the upper hemisphere, because we consider only the sound field in the atmosphere) can be calculated using Eq. (2) for the displacement u with consideration for the relationships between this displacement and the volume velocity amplitudes V_0, as well as the air oscil-

lations on the external side of the neck, which is the actual source of sound. This procedure gives the following result:

$$W^{ac} = \frac{\rho}{2c}\frac{V_0^2\omega^6}{\pi^5}\frac{1}{[(\omega^2-\omega_0^2)^2+(\omega\alpha)^2]}. \quad (3)$$

It turns out that the quantity $\frac{\rho V_0^2\omega^6}{2c\pi^5}$ is a common factor, which appears not only in expression (3) for the sound energy, but also in the expressions derived below for the powers of elastic waves of both types.

We estimate the power of the seismic radiation generated by a spherical source using the results obtained in [5, 6]. We start from the expression for wave displacements in the far field of the pressure wave generated by a harmonic monopole in the form of a spherical cavity of radius r_0 oscillating at a depth $H = r_0$ below the free boundary and producing the acoustic pressure amplitude p given by the second of Eqs. (2) at the cavity wall:

$$U_{ll} = \frac{ipr_0^3\omega}{\bar{\rho}c_l c_t^2(4+4ik_l^2r_0^2-k_t^2r_0^2)r}$$
$$\times\exp\left[i\omega\left(\frac{r-r_0}{c_l}-t\right)\right]\left\{(1+K_{ll})\cos\left(\frac{\omega r_0\cos\theta_l}{c_l}\right)\right. \quad (4)$$
$$\left.-i(1-K_{ll})\sin\left(\frac{\omega r_0\cos\theta_l}{c_l}\right)\right\},$$

where K_{ll} is the reflection coefficient (in the displacement amplitude) of the longitudinal wave in the case of its reflection from the free boundary with the transformation into a wave of the same type, r is the distance to the observation point, θ_l is the angle between the vertical and the beam propagating from the center of the resonator neck to the observation point, $\bar{\rho}$ is the density of the elastic medium, $k_{l,t} = \omega/c_{l,t}$ are the wave vectors of compression and shear waves, and $c_{l,t}$ are the velocities of these waves.

The field of elastic displacements in the shear wave formed a result of the transformation of the longitudinal wave incident on the plane boundary is given by the relationship

$$U_{lt} = \frac{ipr_0^3\omega}{\bar{\rho}c_l c_t^2(4+4ik_l^2r_0^2-k_t^2r_0^2)r}K_{lt}\frac{\tan\theta_l}{\tan\theta_t}$$
$$\times\exp i\omega\left[\frac{r}{c_t}-\frac{r_0(1-\cos\theta_l)}{c_l}\right]\exp(-i\omega t), \quad (5)$$

where θ_t is the angle of departure (measured from the vertical), at which the shear wave propagates from the boundary toward the bulk of medium, and K_{lt} is the coefficient of the longitudinal-to-transverse wave transformation (with respect to the displacement amplitude).

In the above formulas, the pressure p is given by Eq. (2), where the volume velocity amplitude V_0 takes a fixed value. However, this does not allow one to rigorously take into account the backpressure, which is of especial importance at resonance, and the effect of the added air mass that accompanies the motion of the rigid cavity walls. Consequently, our consideration of the mutual influence of two oscillatory processes is not exhaustive, and, hence, the above expressions cannot be considered as self-consistent, although they are quite appropriate for obtaining the amplitude relationships and energy estimates in the far zone. In particular, considering the denominators in Eqs. (4) and (5), one can easily see that the main resonance condition for the elastic cavity oscillation is formulated as the approximate equality $k_t^* r_0 \approx 2$, which yields an approximate expression for the resonance frequency:

$$f^* \approx \frac{c_t}{\pi r_0}. \quad (6)$$

The resonance frequency of forced acoustic oscillations of a Helmholtz resonator with a neck of zero height and with the losses and wall vibrations being neglected coincides with the frequency of natural oscillations and is determined by the formula

$$f_0 = \frac{c}{2\pi r_0}\sqrt{\frac{3a}{2\pi r_0}}. \quad (7)$$

Equating the resonance frequencies of the air cavity and the elastic medium, we obtain the condition that relates the cavity radius and the hole radius to the sound velocity in air and the shear wave velocity in the ground:

$$\frac{a}{8r_0} \approx \frac{c_t^2}{c^2}. \quad (8)$$

From formula (8) it follows that the resonance frequencies of the two oscillatory systems can coincide only when the velocity of shear waves is sufficiently low. This is possible in loose grounds that can be modeled as waterlike media with a shear modulus that is small in comparison with the compression modulus: $\mu \ll \lambda$. In particular, for peaty grounds, where the velocity $c_t \sim 70$–80 m/s, we find that the neck-to-cavity radius ratio is $a/r_0 \approx 0.3$–0.4. The Q factor of the Helmholtz resonator and the resonant oscillation of the elastic cavity remain sufficiently high in this case. For example, the Q factor of acoustic oscillations can be estimated as $Q^{ac} \approx 1.633(\pi r_0/a)^{3/2}$, so that $Q^{ac} \sim 35$–55. Additional dissipation mechanisms, such as turbulent phenomena in the region of the moving air column, may reduce the Q factor. Since the levels of sound and seismic waves depend on the particular value of the Q factor, the sound and seismic powers were calculated

Powers of the acoustic and seismic waves produced by the source

Q^{ac} \ f_0 (Hz)	25	50	100
	W^{ac} (W)		
	W^P (W)		
	W^S (W)		
10	0.5	2	7.5
	0.012	0.045	0.18
	1	4	15
25	3	12	48
	0.07	0.3	1.2
	7	24	95
37.5	7	27	110
	0.18	0.7	2.5
	14	60	220

for several values of the Q factor ($Q^{ac} \sim 10$, 25, and 37.5) and several resonance frequencies ($f_0 \sim 25$, 50, and 100 Hz).

In the table, the upper numbers in every cell represent the calculated estimates of the acoustic power W^{ac} emitted by the source at frequencies coinciding with all the above resonance frequencies for all the above values of the Q factor. The estimates were obtained with the use of Eq. (3) at the oscillating volume velocity amplitude $V_0 = 0.1$ m^3/s. Here, it was assumed that the resonance frequencies of acoustic and elastic vibrations coincide, and this assumption will be used below in estimating the power of pressure and shear waves.

The Q factor of the elastic cavity that is related to the radiation loss is determined by the relationship $Q^{Seis} = c_l/2c_t$. With the inclusion of the viscous loss, the values of the Q factor fall approximately within 3–5. The Q factor of the acoustic resonance appears to be much higher in comparison with this value. For this reason, the Q factor of air oscillations in the cavity will govern the common operating bandwidth of the seismic source under consideration. Remember that the resonance frequencies of two systems can be equalized with the use of coupling layers on the resonator walls. However, as was mentioned in the introduction to this paper, such an equalization makes the problem under consideration more complicated because of the inclusion of additional envelopes characterized by a different stiffness.

Now, let us consider the power characteristics of compression and shear waves in the elastic medium under the condition that the acoustic and elastic resonance frequencies of the source coincide. Using formulas (6) and (7), one can easily calculate the power of the emitted elastic waves. Omitting the intermediate rearrangements described in [5], we represent the power of the pressure waves produced in the ground by the formula

$$W^P = \frac{\rho V_0^2 \omega^6}{2c\pi^5}\frac{9\omega_0^4}{32\gamma}\left(\frac{\rho}{\bar{\rho}}\right)\left(\frac{c}{c_t}\right)^5 \times \frac{(F_1(\omega) + F_2(\omega))}{[(\omega^2 - \omega_0^2)^2 + \alpha^2\omega^2]\left[(\omega^2 - \omega_0^2)^2 + \frac{4}{\gamma^2}\omega^2\omega_0^2\right]}, \quad (9)$$

where

$$F_1(\omega) = \int_0^{\pi/2} \cos^2\left(\frac{2\omega}{\gamma\omega_0}\cos\theta\right) \times \frac{16\sin^4\theta\cos^2\theta(\gamma^2 - \sin^2\theta)\sin\theta d\theta}{[4\sin^2\theta\cos\theta\sqrt{\gamma^2 - \sin^2\theta} + (\gamma^2 - 2\sin^2\theta)^2]^2},$$

$$F_2(\omega) = \int_0^{\pi/2} \sin^2\left(\frac{2\omega}{\gamma\omega_0}\cos\theta\right) \times \frac{(\gamma^2 - 2\sin^2\theta)^4\sin\theta d\theta}{[4\sin^2\theta\cos\theta\sqrt{\gamma^2 - \sin^2\theta} + (\gamma^2 - 2\sin^2\theta)^2]^2},$$

$$\gamma = \frac{c_l}{c_t}, \quad \omega_0 = \frac{c}{r_0}\sqrt{\frac{3a}{2\pi r_0}}.$$

Using Eq. (9), we obtained the estimates of the power of compression (pressure) waves W^P. The table shows these estimates in the middle row of every cell. As before, these estimates were obtained for the source operating at frequencies coincident with the above resonance frequencies and for all three values of the Q factor. The calculations were performed using the following parameters: $\gamma = 6$, $c/c_t = 5$, $r_0 = 1$ m, $a = 0.3$ m, and other parameters mentioned earlier. As can be seen, the power of seismic compression waves is always below 2.5% of the acoustic power emitted to the atmosphere.

A similar procedure is used for determining the power of transverse waves excited in the ground by equivalent surface force sources originating from the oscillation of the buried monopole and producing an alternating effect on the boundary between the solid medium and the atmosphere. According to [5], we have

$$W^S = \frac{\rho V_0^2 \omega^6}{2c\pi^5}\frac{9\omega_0^4}{2}\left(\frac{\rho}{\bar{\rho}}\right)\left(\frac{c}{c_t}\right)^5 \times \frac{(G_1 + G_2(\omega))}{[(\omega^2 - \omega_0^2)^2 + \alpha^2\omega^2]\left[(\omega^2 - \omega_0^2)^2 + \frac{4}{\gamma^2}\omega^2\omega_0^2\right]},$$

where

$$G_1 = \int_0^{\arcsin(1/\gamma)} \frac{(1-2\sin^2\theta)^2 \sin^2\theta\cos^2\theta}{[(1-2\sin^2\theta)^2 + 4\sin^2\theta\cos\theta\sqrt{\gamma^{-2}-\sin^2\theta}]^2}\sin\theta d\theta,$$

$$G_2(\omega) = \int_{\arcsin(1/\gamma)}^{\pi/2} \frac{(1-2\sin^2\theta)^2 \sin^2\theta\cos^2\theta}{[(1-2\sin^2\theta)^4 + 16\sin^4\theta\cos^2\theta(\sin^2\theta-\gamma^{-2})]} e^{-\frac{4}{\gamma}\frac{\omega}{\omega_0}\sqrt{\sin^2\theta-\gamma^{-2}}} \sin\theta d\theta. \quad (10)$$

Using Eq. (10), we obtained the estimates of the power of transverse seismic waves in the ground W^S. These estimates are shown as the lower numbers in every cell of the table. They exceed the power of sound produced in the atmosphere by a factor of about 2. Such an appreciable power excess of the shear waves over the longitudinal waves is obviously a consequence of their lower velocity of propagation, which is characteristic of geologic materials of the type of loose grounds.

Figure 2 shows the sound power and powers of longitudinal and shear elastic waves, W^{ac}, W^P, and W^S, normalized by the factor $\frac{\rho V_0^2 \omega_0^2}{2c\pi^5}$ as functions of the relative frequency deviation ω/ω_0. The curves are given on a logarithmic scale and calculated for the acoustic Q factor Q^{ac} = 37.5 and the resonance frequency f_0 = 100 Hz.

The table summarizes all the calculated data representing the maximum powers produced by the Helmholtz resonator in the form of sound and seismic compression and shear waves for each of the three aforementioned values of the Q factor and each of the three resonance frequencies. With reference to the results obtained in [5], one can additionally infer that the power removed from the system by the Rayleigh surface waves can hardly exceed the total power of the two kinds of bulk waves even for the lowest frequency under consideration.

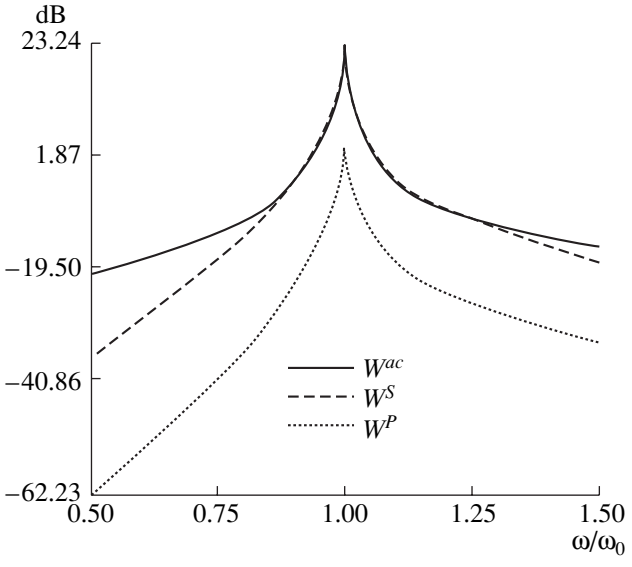

Fig. 2. Power of sound produced in the atmosphere and the powers of seismic waves as functions of the relative frequency deviation for Q^{ac} = 37.5 and f_0 = 100 Hz.

The data shown in the table suggest that such a source is relatively high frequency, because it generates seismic waves with power levels characteristic of seismic prospecting (100 W or more) only at frequencies exceeding 50 Hz. In order to produce these power levels, the Q factor of the acoustic component should be no lower than ~ 30. The fact that the power of transverse waves exceeds the power of longitudinal waves by two orders of magnitude and the coincidence of the power of transverse waves with the power of sound emitted to the atmosphere within an order of magnitude allow one to expect that such a source will efficiently generate both atmospheric acoustic waves and seismic shear waves under the condition that the source is located in a waterlike geologic medium and under the assumption that the value V_0 = 0.1 m^3/s used in the above calculations for the volume velocity amplitude is technically realizable.

CONCLUSIONS

From the results of the calculations described above, one can draw the following conclusions:

(1) An acoustic seismic resonator simultaneously operating as a source of shear seismic waves in an elastic medium and a source of acoustic radiation in the atmosphere can be implemented only in very soft or loose grounds. Narrowband atmospheric sound and mainly transverse seismic waves in the ground are generated as a result of the harmonic excitation of the Helmholtz resonator by an external source of fluctuating pressure or fluctuating airflow.

(2) The generation of shear seismic waves with an efficiency acceptable for practical applications is realized at frequencies above 50 Hz under the condition that the acoustic Q factor of the resonator is sufficiently high, $Q^{ac} \geq 30$.

(3) In the case of operation at a resonance frequency that is the same for both oscillating systems, the Helmholtz resonator considered in this paper cannot be unambiguously qualified as a predominantly acoustic or predominantly seismic source of vibration.

Presumably, such a source can be used in both seismic prospecting and low-frequency acoustic monitoring of the atmosphere, especially if a group of several in-phase sources is used. Since the resonator is located in the so-called low-velocity zone, where the velocity of wave propagation monotonically and rapidly increases with depth, a certain small portion of the seismic energy will be localized near the boundary. However, one should expect that most of the oscillation energy produced by the source will propagate into the bulk of the earth with the shear seismic waves, which are widely used for sounding the structure of the earth's interior.

ACKNOWLEDGMENTS

The paper was supported by the Russian Foundation for Basic Research, project no. 02-02-17089.

REFERENCES

1. V. S. Averbakh, B. N. Bogolyubov, Yu. A. Dubovoĭ, *et al.*, Akust. Zh. **48**, 149 (2002) [Acoust. Phys. **48**, 121 (2002)].
2. B. M. Glinsky, V. V. Kovalevsky, and M. S. Khairetdinov, in *Abstracts of 16th ISNA* (Moscow, 2002), p. 151.
3. V. I. Dobrinskiĭ, in *Proceedings of V Session of the Russian Acoustical Society on Geoacoustic Problems: Methods and Means* (Moscow, 1996), p. 169.
4. Yu. M. Zaslavskiĭ, Izv. Akad. Nauk SSSR, Fiz. Zemli, No. 9, 86 (1982).
5. V. S. Averbakh and Yu. M. Zaslavskiĭ, Fiz. Zemli, No. 1, 49 (1998).
6. M. A. Isakovich, *General Acoustics* (Nauka, Moscow, 1973).

Translated by A. Vinogradov

Acoustical Physics, Vol. 49, No. 5, 2003, pp. 535–539. Translated from Akusticheskiĭ Zhurnal, Vol. 49, No. 5, 2003, pp. 632–637.

Formation of Brillouin Waves in the Underwater Sound Channel

V. A. Zverev and G. K. Ivanova

Institute of Applied Physics, Russian Academy of Sciences,
ul. Ul'yanova 46, Nizhni Novgorod, 603950 Russia
e-mail: ivg@hydro.appl.sci-nnov.ru

Received May 20, 2002

Abstract—The mechanism of the vertical sound field structure formation in the underwater sound channel is considered. The calculations are performed by the ray method for the rays that have upper turning points at the ocean surface. It is shown that the vertical field structure is formed by the ray pairs producing opposing waves in the vertical. The rays belonging to one pair have the same sign of their departure angles at the source. The pairs are formed because of the presence of a minimum in the ray cycle length as a function of the departure angle. The resulting ray pairs are analogs of Brillouin waves. *© 2003 MAIK "Nauka/Interperiodica".*

In an ideal waveguide, the features of the sound field can be well interpreted in terms of Brillouin waves. Brillouin waves are defined as a pair of plane monochromatic waves that have the same absolute values of the wave vector and opposite signs of the wave vector projections on the plane normal to the waveguide axis x [1–3]. In the plane x = const, a pair of such waves produces an interference structure whose period is governed by the wavelength λ and the absolute value of the angle at which both plane waves propagate in the waveguide. With certain boundary conditions, Brillouin waves compose a so-called normal wave, which is a traveling wave in the x direction and a standing wave in the perpendicular direction [4]. Brillouin waves are a useful instrument for the physical interpretation of the sound field in a waveguide [3].

In ocean acoustics, in addition to the waves reflected by the waveguide boundaries, the waves refracted in the course of their propagation in the waveguide are considered. In ocean acoustics, a typical sound speed profile has a minimum at a certain depth, which leads to the formation of the so-called underwater sound channel (USC). An important feature of wave propagation in an ideal waveguide is that the rays are naturally separated into pairs. That is why the method of Brillouin waves is so efficient for the ideal waveguide. In the USC, such pairs have not yet been observed.

The objective of our paper is to demonstrate that, by analogy with the ideal waveguide, a natural separation of rays into pairs similar to Brillouin waves occurs in the USC, the rays in a pair producing opposing waves in the vertical. This fact makes it possible to universally describe the sound fields in both an ideal waveguide and the USC with the use of the generalized interpretation of Brillouin waves.

Let us illustrate the behavior of waves in the USC by considering a particular case with parameters taken from the hydrological data of the experiment performed in the Atlantic Ocean in 1989. These parameters are as follows: the ocean depth is 5000 m, the sound speed profile $c(z)$ has a near-surface maximum at a depth of 60 m and a minimum at the depth z = 1600 m, and the sound speed near the bottom is higher than in the near-surface maximum. Here, z is the vertical coordinate measured from the ocean surface and x is the horizontal coordinate at the depth of the sound source. An omnidirectional monochromatic transmitter is at the depth of the near-surface maximum in $c(z)$. We consider the water rays whose upper turning points lie at the ocean surface. Let us specify the distance to be x = 240 km, the frequency of the source to be 233.6 Hz, and the surface reflection coefficient to be –1.

Above all, note that, in contrast to an ideal waveguide, now the rays leaving the source at angles symmetric with respect to the x axis (i.e., towards the bottom and towards the surface) arrive at the reception plane x = 240 km only from below (from the bottom towards the surface). Even if the source is on the USC axis, where the shift of the symmetric ray trajectories is maximal, the major part of the rays are directed to the surface at x = 240 km (Fig. 1).

According to the calculations, the rays leaving the source at symmetric angles do not form Brillouin waves, as in an ideal waveguide. It is difficult to find a mechanism of wave separation into pairs and detect Brillouin-like waves by considering ray trajectories like those shown in Fig. 1. We suggest another way to solve this problem.

The procedure consists in calculating the coordinates of ray arrivals at the plane x = const as a function of the angle of departure from the source. In Fig. 2, the

1063-7710/03/4905-0535$24.00 © 2003 MAIK "Nauka/Interperiodica"

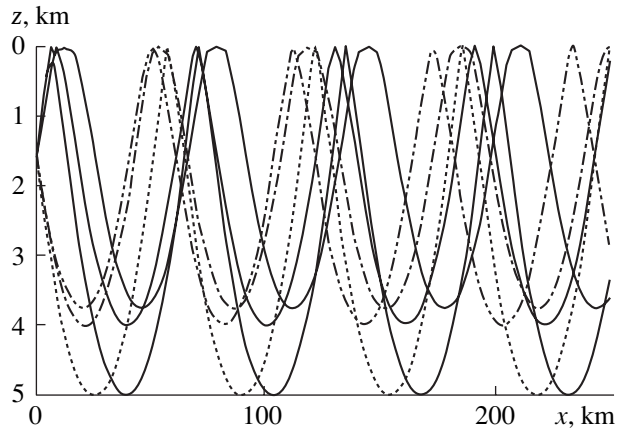

Fig. 1. Trajectories of rays leaving the source at symmetric angles. The source is at the USC axis, $z = 1600$ m.

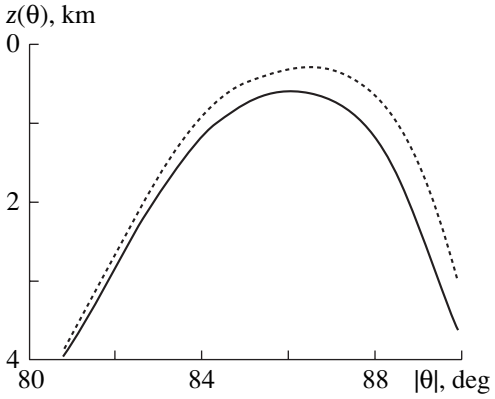

Fig. 2. Depth $z(\theta)$ of the ray arrivals at the distance $x = 240$ km with the source depth $z = 60$ m. The rays leave the source towards the surface (the solid curve) and towards the bottom (the dashed curve).

functions $z(\theta)$ are presented, where θ is the departure angle measured from the z axis. The absolute value of the angle θ is represented by the horizontal axis, and the waveguide depth measured from the surface, by the vertical axis. The solid curve indicates the coordinates of arrivals at the z axis for the rays leaving the source towards the surface ($\theta < 0$), and the dashed curve, towards the bottom ($\theta > 0$). Let us consider the specific features of the curves. One of these features consists in the fact that, at each point in depth, two rays arrive from a group of rays with the same signs of the departure angle. Another feature is that, as the departure angle changes, the depth $z(\theta)$ of ray arrivals first decreases and then increases for both positive and negative signs of the departure angle. In other words, the rays with departure angles of the same sign arrive at the same depths as the rays with previous values of the departure angles. From four rays arriving at a point z, two pairs can be formed that are analogous to Brillouin waves. Evidently, the pairs should be formed from the rays corresponding to a single curve, because it is precisely these rays that have an inverse change in the vertical coordinate, which is characteristic of Brillouin rays. Thus, the quartets of water rays are naturally separated into two pairs similar to Brillouin waves of the ideal waveguide. We can assume that, at the given distance x, the ray pairs are the plane waves that form a normal wave [4].

In addition to establishing the fact of the natural separation of waves into pairs in the USC, it is advantageous to reveal the mechanism of this phenomenon: what underlies the formation of the two opposing waves? The determination of this mechanism will allow us to generalize the result obtained by studying a particular case.

It was found that the reason for the opposite change in the ray depth of a pair (i.e., for the arrival of the rays with the same sign of the departure angle at a single point) consists in the presence of a minimum in the ray cycle length as a function of the departure angle θ. Figure 3 shows the dependence $D(\theta)$ of the ray cycle length on the absolute value of the departure angle. Although at first glance the existence of the minimum in the cycle length seems to be somewhat surprising, it can be easily explained. In fact, in an ideal waveguide, the cycle length (the distance between two reflections from the same surface) decreases as the angle between the z axis and the ray decreases and increases as the waveguide depth increases. These two statements hold for the USC in view of the fact that, for each ray, the waveguide depth is determined by the position of its turning point near the bottom. As a result, the following phenomenon takes place. A decrease in the departure angle (relative to its maximal value) has a stronger effect on the cycle length than that of the increase in the depth of the turning point (the waveguide depth). The cycle length decreases. After that, the effect of the second factor becomes stronger: the cycle length ceases decreasing, then becomes constant, and then begins to increase in spite of the decrease in the departure angle. Such minima in the cycle length were observed experimentally [5]. Note that the minima can exist only in waveguides with the USC. In channels with a monotonically changing speed of sound, no minima occur in the cycle length.

The formation of the opposing waves can be related to the change in the cycle length in the following way. As the cycle length decreases, the ray trajectories shrink, and the rays become displaced along the vertical at the chosen distance from the source. As the cycle length increases, the rays are displaced in the opposite direction, and they practically return to the previous positions. As a result of such a reciprocating motion of the trajectories, two opposite displacements of the ray occur, and opposing waves are formed along the z axis. In this counter motion of the rays, the sign of the wave vector does not change. The change in the sign occurs only at the surface reflections and at the turning points near the bottom. Returning to Fig. 2, one may notice

two features of the opposing waves. First, the formation of the opposing waves occurs with an arbitrary sign of the departure angle. This feature is confirmed by the existence of two curves produced by rays with departure angles of opposite signs. Second, the caustic forms at a point of extreme ray depth. The information on the coordinates of the caustic is a matter of practical significance. The curves shown in Fig. 2 are important in themselves, regardless of the problem at hand. These curves show the region of the sound field convergence in depth at the given distance, including the positions of caustics. To obtain these curves, it is sufficient to know the vertical distribution of the sound speed. The calculation of the function $z(\theta)$ for the channeled rays is described in [6].

Thus, we have shown that, in the natural waveguide with the USC, rays arriving at a single point at the plane x = const can form pairs similar to the Brillouin waves that exist in an ideal waveguide. Now let us consider the difference between the ray pairs in the USC and Brillouin waves.

The Brillouin waves in an ideal waveguide differ from their analog in the USC in that the spatial frequencies of Brillouin waves have different signs but do not change throughout the whole waveguide depth, while a similar pair in the USC has different frequencies, which, in addition, depend on the depth of their crossing the plane x = const. To reveal the consequences of this difference, let us consider the spatial frequency of the sound field throughout the waveguide depth.

Prior to proceeding with our particular case, let us obtain the dependence of the spatial frequency of the sound field produced by the rays along the z axis, regardless of the distance to the source. The vertical structure of the sound field is governed by the projection of the wave vector on the z axis. Let us denote this projection as $\gamma(z)$. Figure 4 shows the dependence $|\gamma(z)|$ for different absolute values of the ray departure angles with a step of 2°. The angle is measured from the z axis. In this and subsequent figures, the function $\gamma(z)$ is expressed in the 2π/m units. The lower curve corresponds to the largest departure angle, 89.95°. It is essential that Fig. 4 presents the full set of the spatial waveguide frequencies in the vertical. One can see that rays with different values of $|\gamma(z)|$ arrive at a single point in depth. Note an interesting feature of the curves: all of them exhibit maxima at the depth of the minimal sound speed.

Let us now consider the spatial structure of the sound speed along the z axis at the fixed distance x = 240 km. Figure 5 shows the function $\gamma(z)$ for the same rays as in Fig. 2., with the same notations. In Fig. 2, all the curves corresponding to the rays leaving the source upwards and downwards are rather distant from each other. In contrast, the curves $\gamma(z)$ nearly coincide, except for the region of caustics (the inflection points of the curves). In the case under consideration, the vertical field structures produced by rays with departure angles

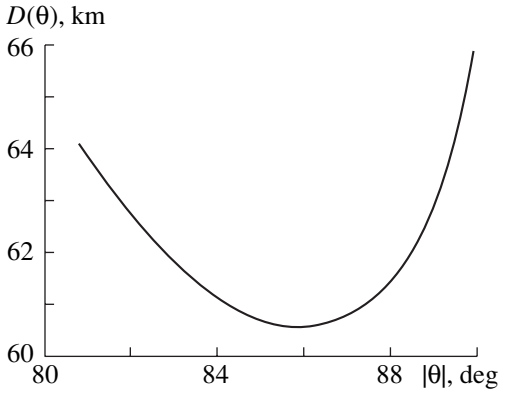

Fig. 3. Length $D(\theta)$ of ray cycles with the source depth z = 60 m.

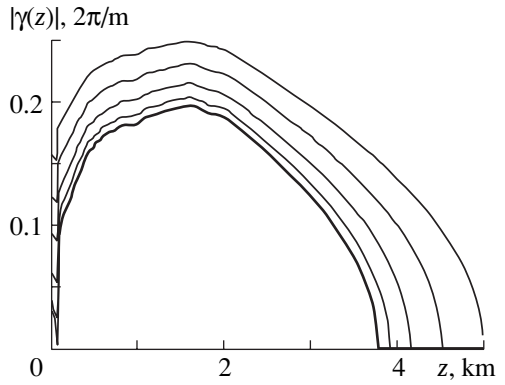

Fig. 4. Absolute value $|\gamma(z)|$ of the projection of the ray wave vector on the z axis. The step in departure angle is 2°. The lower curve corresponds to a departure angle of 89.95° with respect to the z axis.

of opposite signs little differ from each other. The essential feature consists in the fact that, on different sides of the caustic, the rays forming the Brillouin-like pair have different spatial frequencies. The lower parts of the curves correspond to greater angles θ and the upper parts, to smaller angles. Therefore, in contrast to an ideal waveguide, the ray pair of the USC does not form a standing wave in the vertical but rather leads to beating with the frequency equal to the difference in $\gamma(z)$ for the rays forming the pair. Note that the curves $\gamma(z)$ in Fig. 5 have maxima at the depth of the USC axis, as in Fig. 4.

Until now, we considered the vertical distribution of the sound field in the ray trajectory region where the rays can be approximated by plane waves. Let us now undertake the same consideration for the center of the convergence zone, x = 190 km, where such an approximation fails. In Figs. 6a–6c, the functions $z(\theta)$ and $\gamma(z)$ and the sound field spectrum along the z axis are shown. Similarly to Figs. 2 and 5, the sign of the ray departure angles does not matter. The difference is noticeable only in the region of caustics. The main group of rays,

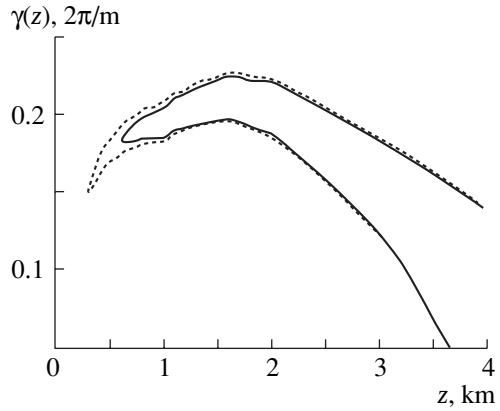

Fig. 5. Spatial frequency $\gamma(z)$ of the sound field along the vertical at the distance $x = 240$ km. Notations are the same as in Fig. 2.

between the points of surface reflection, propagates downwards, $\gamma(z) < 0$, and the rays reflected from the surface are added, $\gamma(z) > 0$. As a result, one to four rays arrive at each point with the same signs of the departure angle. Thus, at the chosen distance from the source, rays that are very close to the Brillouin waves of the ideal waveguide are present: the quantities $\gamma(z)$ are close in their values and opposite in signs. However, the number of rays with $\gamma(z) > 0$ is small, this feature being quite pronounced in the sound field spectrum along the z axis (Fig. 6c). According to the plots, most rays concentrate in the region of the caustic; it is precisely these rays that make the main contribution to the formation of the frequency structure of the sound field in depth. The calculation of the sound field in the vicinity of the near-bottom turning points shows that here, as in the two previous cases, the rays form pairs similar to Brillouin waves. The rays in the pairs have different spatial frequencies but the same sign.

Let us consider other situations. First of all, note that a change in the source depth leads to no significant consequences. A significantly new phenomenon arises at long distances x when the convergence zones overlap [7, 8]. Figures 7a and 7b show the functions $z(\theta)$ and $\gamma(z)$ calculated for an arbitrarily chosen distance x = 1500 km. The curves corresponding to rays with different signs of the departure angle are very close to each other. The spatial frequencies differ nowhere but at the caustic. Due to the overlapping of cycles, pairs of rays arriving at the reception plane from both above and below are formed, and these pairs fully correspond to the Brillouin waves of the ideal waveguide [9, 10]. According to Fig. 7a, the relative number of such rays is about 40% at the given distance. Hence, the contribution of the main weakly divergent beam decreases to 60%. Let us now consider the region of caustics in more detail.

In recent years, much attention has been paid to considering super-long-range sound propagation in a fluctuating ocean. In [11], a possible explanation is proposed for the conservation of the sound wave front at long distances from the source. The ray calculations described above offers the following explanation of this phenomenon. The conservation of an undistorted wave front in a fluctuating ocean can be observed when the signals are received in the vicinities of caustics. The rays producing the caustic have close departure angles and, hence, close ray trajectories. For x = 1500 km (Fig. 7), the total width of the beam is about 0.5° for these rays. The trajectories of other rays are more distant from each other, especially those of rays that

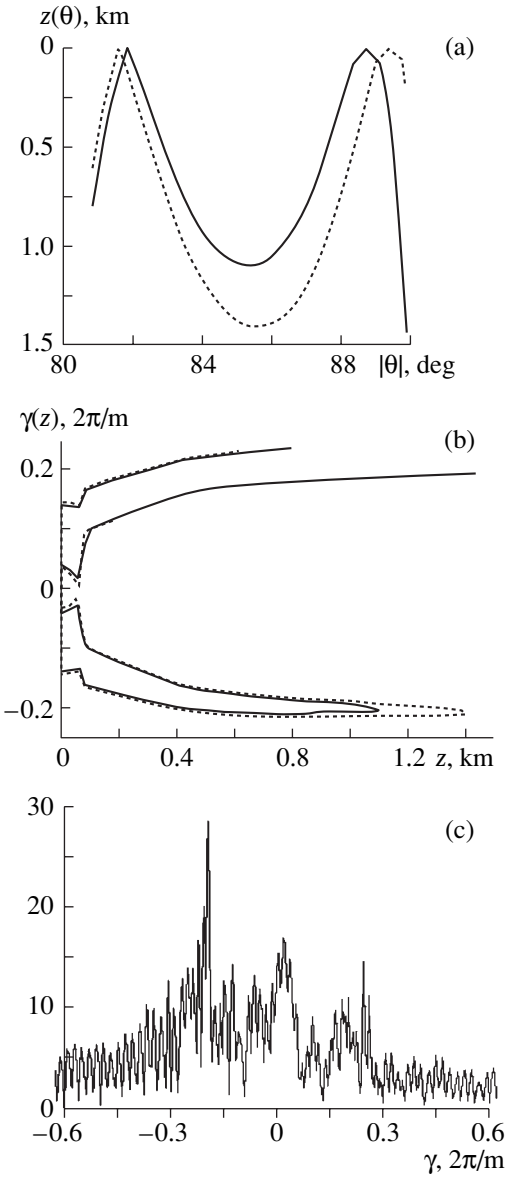

Fig. 6. Vertical structure of the sound field at the center of the convergence zone, $x = 190$ km: (a) the depth of ray arrivals $z(\theta)$; (b) the spatial frequency $\gamma(z)$ of the sound field along the vertical; and (c) the amplitude of the spatial spectrum of the sound field along the vertical.

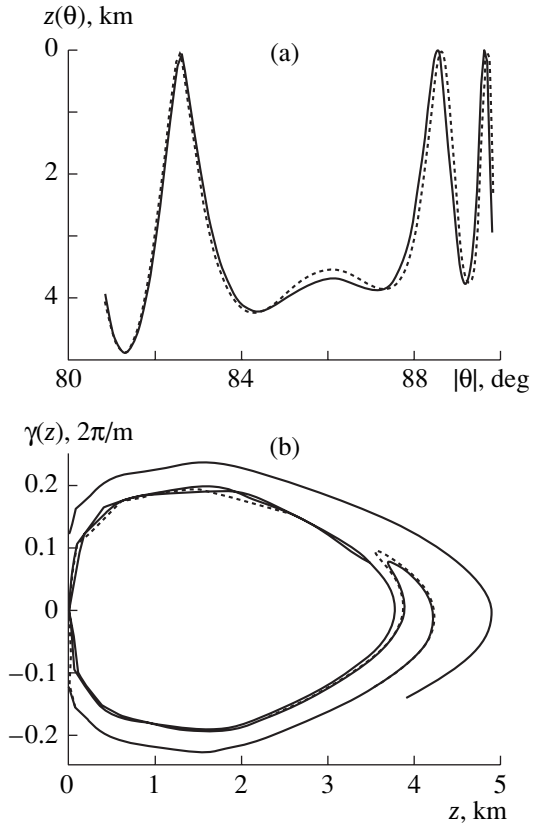

Fig. 7. Vertical structure of the sound field at the distance $x = 1500$ km: (a) the depth $z(\theta)$ of ray arrivals and (b) the spatial frequency $\gamma(z)$ of the sound field along the vertical.

appear due to the overlapping of convergence zones and form classical Brillouin waves. These rays travel through different ocean regions and undergo different distortions. The rays forming the caustic are distorted in the same way, and, therefore, the initial coherence of these rays is conserved. The latter fact explains the super-long-range propagation of such rays.

One more conclusion can be drawn from the calculations described above. Since the vertically opposing waves are obtained from the ray method, there is no need to use the mode technique to calculate the sound field in the waveguide with the USC, and all the more so because the main concept of the mode theory, i.e., the independence of the vertical field structure on distance, is not valid.

To conclude, the following remark should be made. For the chosen group of water rays, there exists a mechanism of pair formation from the rays arriving at a single point that allows one to draw an analogy between these pairs and the Brillouin waves of an ideal waveguide. The revealed mechanism of pair formation explains the rather weak divergence of the sound beam at long distances. Because of the presence of the minimal-length ray cycle in the USC, two rays of different spatial frequencies arrive at each point to form the main ray beam along the propagation axis. The amplitude dependence of the sound field along the waveguide is determined by the trajectory region that is intersected by the plane $x = \text{const}$. This phenomenon governs the width of the main beam, the caustic depth, and the spatial frequency in the caustic region.

A preliminary calculation of the sound field of channeled rays shows that part of the rays obey the aforementioned mechanism of pair formation, while the other part follows the classical description in terms of Brillouin waves.

REFERENCES

1. B. Z. Katsenelenbaum, *High-Frequency Electrodynamics: Fundamentals of Mathematical Methods* (Nauka, Moscow, 1966).
2. L. A. Vaĭnshteĭn, *Electromagnetic Waves*, 2nd ed. (Radio i Svyaz', Moscow, 1988).
3. R. P. Feynman, R. B. Leighton, and M. Sands, *The Feynman Lectures on Physics*, Vol. 6: *Electrodynamics* (Addison-Wesley, Reading, Mass., 1964; Mir, Moscow, 1966).
4. L. M. Brekhovskikh and Yu. P. Lysanov, *Fundamentals of Ocean Acoustics* (Gidrometeoizdat, Leningrad, 1982; Springer, New York, 1991).
5. L. M. Brekhovskikh, V. V. Goncharov, S. A. Dremuchev, *et al.*, Akust. Zh. **36**, 824 (1990) [Sov. Phys. Acoust. **36**, 461 (1990)].
6. V. V. Goncharov, V. Yu. Zaĭtsev, V. M. Kurtepov, A. G. Nechaev, and A. I. Khil'ko, *Acoustic Tomography of the Ocean* (Inst. Prikl. Fiz. Ross. Akad. Nauk, Nizhni Novgorod, 1997).
7. O. P. Galkin, A. M. Dymshits, E. A. Kharchenko, and L. V. Shvachko, Akust. Zh. **40**, 943 (1994) [Acoust. Phys. **40**, 835 (1994)].
8. O. P. Galkin and L. V. Shvachko, Akust. Zh. **44**, 192 (1998) [Acoust. Phys. **44**, 153 (1998)].
9. A. L. Virovlyansky, J. Acoust. Soc. Am. **108**, 84 (2000).
10. A. L. Virovlyanskiĭ, L. Ya. Lyubavin, and A. A. Stormkov, Akust. Zh. **47**, 597 (2001) [Acoust. Phys. **47**, 517 (2001)].
11. M. A. Wolfson and S. Tomsovic, J. Acoust. Soc. Am. **109**, 2693 (2001).

Translated by E. Kopyl

Acoustical Physics, Vol. 49, No. 5, 2003, pp. 540–544. Translated from Akusticheskiĭ Zhurnal, Vol. 49, No. 5, 2003, pp. 638–643.

Sound Radiation from a Joint of Plates of Different Thickness

V. Yu. Kirpichnikov and V. V. Romanova

Krylov Central Research Institute, Moskovskoe sh. 44, St. Petersburg, 196158 Russia

e-mail: albert@krylov.spb.su

Received April 5, 2002

Abstract—A method of solving the problem of sound radiation from a plate with elements of different thickness in its plane is proposed, and the results obtained with this method are presented. It is shown that the main sources of sound radiation are the inhomogeneous flexural fields formed in the elements on both sides of their joint. © *2003 MAIK "Nauka/Interperiodica".*

In some cases, vehicle bodies consist of plates of different thickness that are joined together. The problem of sound radiation from this kind of structure was considered in [1]. The solution obtained in the cited paper by the factorization method turned out to be rather cumbersome and of little use for practical implementation.

In the present paper, we propose a simpler approach to solving such problems. We determine the levels of sound radiation for the case of a joint of two and three plates of different thickness, whose outer surfaces lie in the same plane. We assume that, when a flexural wave propagates along the normal to the line of junction, the presence of the acoustic medium does not affect flexural vibrations and, therefore, the results obtained by us are applicable to plates located in low-density (gaseous) media. We consider thin plates satisfying the condition $h/\lambda_u < 6$ [2].

We consider the frequencies below the limiting frequency at which the sound wavelength in the medium is equal to the flexural wavelength in the structure. If the plate has a rib-type inhomogeneity, the sound radiation at these frequencies results from the effect of a shear force and a bending moment acting on the plate at the joint of the rib and the plate and determined as jumps of forces and bending moments in the plate cross sections before and after the rib [3]. In the case of a joint of plates of different thickness lying in one plane, the equalities of displacements, rotation angles, bending moments, and shear forces should be satisfied at the joint. There are no jumps of dynamic forces, unlike the case of a rib. The sound radiation occurs due to the lack of compensation of the contributions to the radiation from the flexural waves transmitted through the line of the plate junction and reflected from it.

Consider the sound radiation from two flexurally vibrating plates of different thickness when a rigid baffle is placed near the plates (the specific acoustic impedance of the baffle is much greater than the wave impedance of the medium); the baffle has an opening in the form of a strip of width $2a$ (Fig. 1). A flexural wave $\exp(ik_1x)$ (k_1 is the wave number of flexural waves in the plate in the region $x < 0$) propagates in the left part of the plate in the direction toward the line of junction.

The solution of this problem is determined by the Huygens integral [3], the integration being performed between $-a$ and a over the strip width:

$$P = \frac{\omega\rho}{2}\int_{-a}^{a}\dot{\xi}(x)H_0^{(1)}(kr)dx, \qquad (1)$$

where ω is the sound frequency, ρ is the density of the medium, k is the sound wave number in the medium, $r(x_0, z_0)$ is the distance from plate to the point of observation, and $\dot{\xi}(x)$ is the particle velocity of flexural vibrations of the plate.

In calculating the Huygens integral, we use the asymptotic representation of the Hankel function for $kr > 1$:

$$H_0^{(1)}(kr) = \sqrt{\frac{2}{\pi kr}}\exp\left(ikr - i\frac{\pi}{4}\right). \qquad (2)$$

Flexural waves in the plate are characterized by the

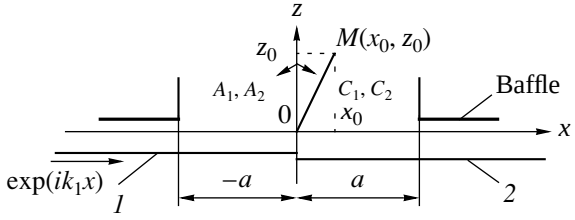

Fig. 1. Coordinate system for describing propagation of a flexural wave along the normal to the line of junction of two plates of different thickness; $M(x_0, z_0)$ is the point at which the level of sound radiation is calculated.

1063-7710/03/4905-0540$24.00 © 2003 MAIK "Nauka/Interperiodica"

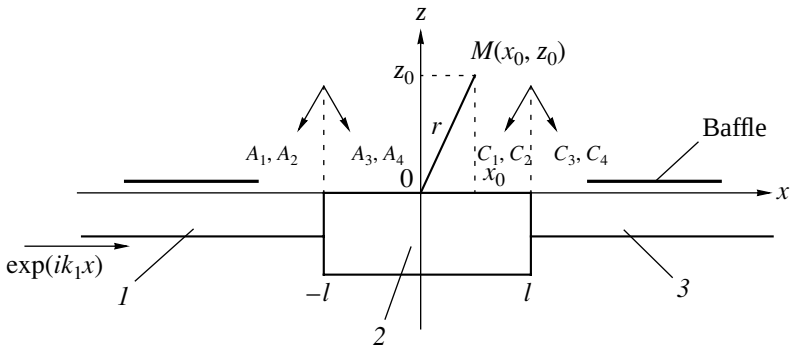

Fig. 2. Coordinate system for describing the propagation of a flexural wave along the normal to the line of junction of three plates of different thickness.

transverse displacement $\xi\exp(-i\omega t)$, where t is time. (The time factor $\exp(-i\omega t)$ is omitted below.)

In the regions $x < 0$ and $x > 0$, we have the following components:

$$\xi(x)_{x<0} = \exp(ik_1x) + A_1\exp(-ik_1x) + A_2\exp(k_1x), \quad (3)$$

$$\xi(x)_{x>0} = C_1\exp(ik_2x) + C_2\exp(-k_2x). \quad (4)$$

The terms $\exp(ik_1x)$, $A_1\exp(-ik_1x)$, and $C_1\exp(ik_2x)$ describe the traveling flexural waves propagating along the coordinate x, and the terms $A_2\exp(k_1x)$ and $C_2\exp(-k_2x)$ describe the inhomogeneous flexural waves that cause no energy transfer along the plate; here, k_2 is the wave number of flexural vibrations of the plate in the region $x > 0$.

To determine the four unknown quantities A_1, A_2, C_1, and C_2, we use the following boundary conditions at the plate joint (the continuity of displacements, rotation angles, bending moments, and shear forces) [1, 2]:

$$\lim_{\varepsilon\to 0}[\xi|_{x=0-\varepsilon} - \xi|_{x=0+\varepsilon}] = 0, \quad (5)$$

$$\lim_{\varepsilon\to 0}\left[\left.\frac{d\xi}{dx}\right|_{x=0-\varepsilon} - \left.\frac{d\xi}{dx}\right|_{x=0+\varepsilon}\right] = 0, \quad (6)$$

$$\lim_{\varepsilon\to 0}\left[B_1\left.\frac{d^2\xi}{dx^2}\right|_{x=0-\varepsilon} - B_2\left.\frac{d^2\xi}{dx^2}\right|_{x=0+\varepsilon}\right] = 0, \quad (7)$$

$$\lim_{\varepsilon\to 0}\left[B_1\left.\frac{d^3\xi}{dx^3}\right|_{x=0-\varepsilon} - B_2\left.\frac{d^3\xi}{dx^3}\right|_{x=0+\varepsilon}\right] = 0. \quad (8)$$

In the designation of the flexural rigidity B, the index 1 corresponds to the plate in the region $x < 0$, and the index 2, to the plate in the region $x > 0$.

For the case of three plates (Fig. 2), we have the following pattern of flexural waves:

in the region $x \le -l$,

$$\xi_1(x) = \exp(ik_1x) + A_1\exp(-ik_1(x-l)) + A_2\exp(k_1(x+l)), \quad (9)$$

within $l \ge x \ge -l$,

$$\xi_2(x) = A_3\exp(ik_2(x+l)) + A_4\exp(-k_2(x+l)) + C_1\exp(-ik_2(x-l)) + C_2\exp(k_2(x-l)), \quad (10)$$

and for $x \ge l$,

$$\xi_3(x) = C_3\exp(ik_3(x-l)) + C_4\exp(-k_4(x-l)). \quad (11)$$

We have eight unknown coefficients. To determine them, we use four boundary conditions at every line of plate junction (the continuity of displacements, rotation angles, bending moments, and shear forces), which are similar to conditions (5)–(8).

Using Eqs. (5)–(8) and relations (3), (4) to determine the unknown coefficients A_1, A_2, C_1, and C_2, we substitute them into Eqs. (3), (4). As a result, we obtain the solution to the problem of determining the flexural displacements of the elements of a two-plate structure. This solution allows one, by using Eqs. (1) and (2), to calculate the acoustic radiation from a plane structure consisting of two plates of different thickness. By using relations (9)–(11) as the boundary conditions, it is possible to obtain a similar solution for the case of a structure consisting of three plates of different thickness.

As seen from Fig. 3, for a joint of plates (a = 2 m) of the same thickness, the maxima of acoustic radiation occur near the edges of the baffle, where compensation of flexural waves propagating along the structure is lacking.

If the plates are of different thickness, an additional maximum of acoustic radiation arises against their joint, and the level of this maximum is almost equal to that of the maxima formed near the edges of the baffle.

In Fig. 4, on the exact solution for the case of the joint of the aforementioned plates of different thickness, an approximate solution is superimposed in which only the parameters of inhomogeneous flexural waves

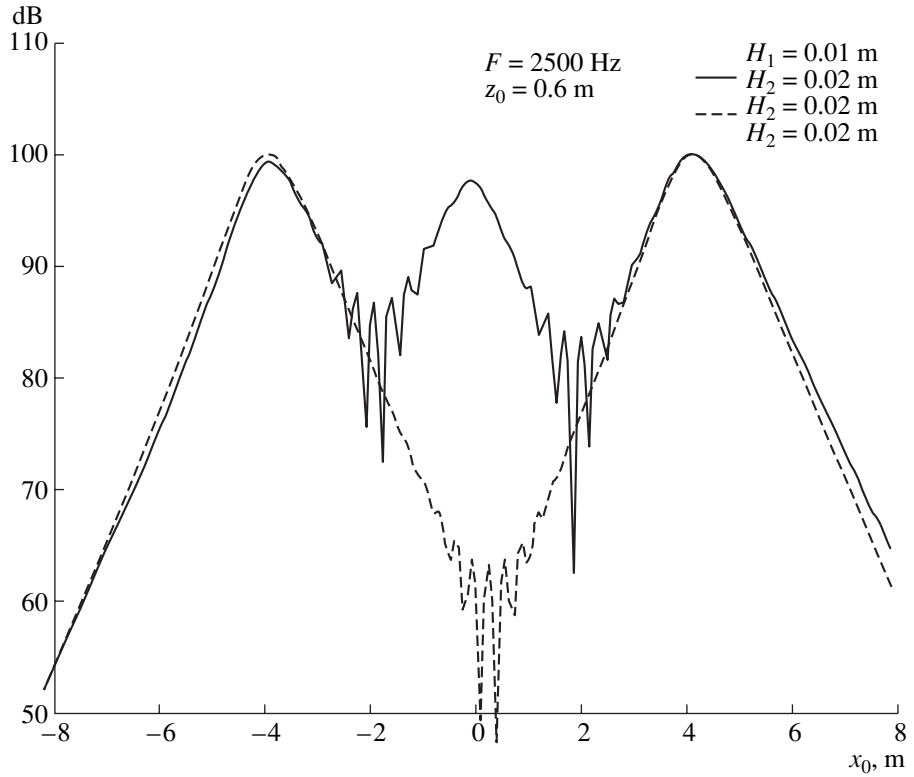

Fig. 3. Spatial distribution of the acoustic pressure levels for the case of a junction of two flexurally vibrating plates of the same thickness and of different thickness.

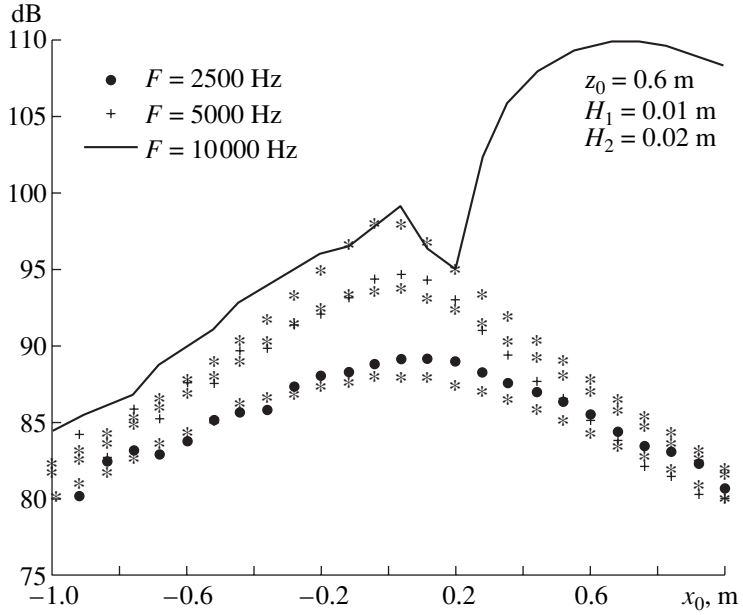

Fig. 4. Comparison of the exact (·, +, –) and approximate (*) solutions to the problem of sound radiation from two jointed plates of different thickness.

are substituted into the Huygens integral. In most cases, the solutions agree satisfactorily. (The disagreement observed against the thicker plate at a frequency of 10 000 Hz is related to its closeness to the limiting frequency of the plate at which sound is generated by the whole plate surface.)

This result testifies that the inhomogeneous flexural fields on each side of the plate joint play the main part

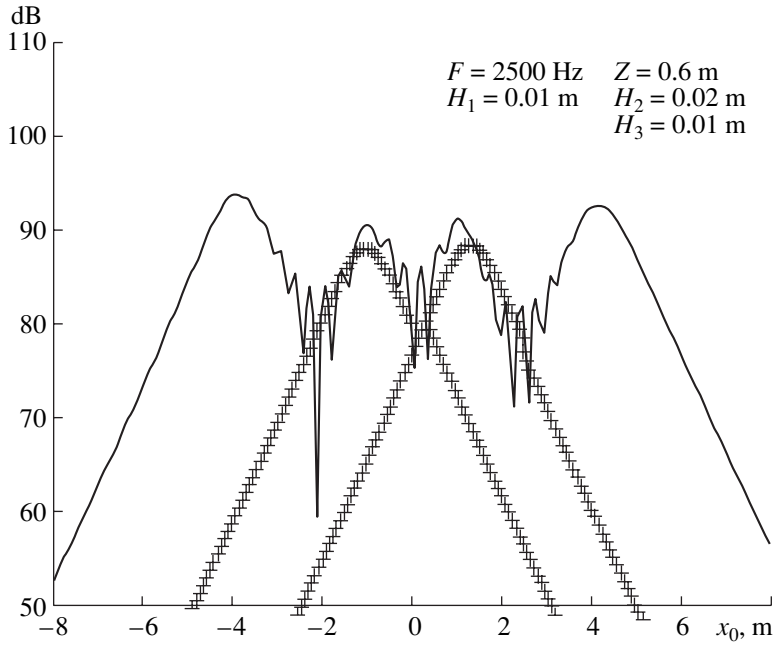

Fig. 5. Spatial distribution of the acoustic pressure levels with consideration for only inhomogeneous flexural fields and without the acoustic baffle.

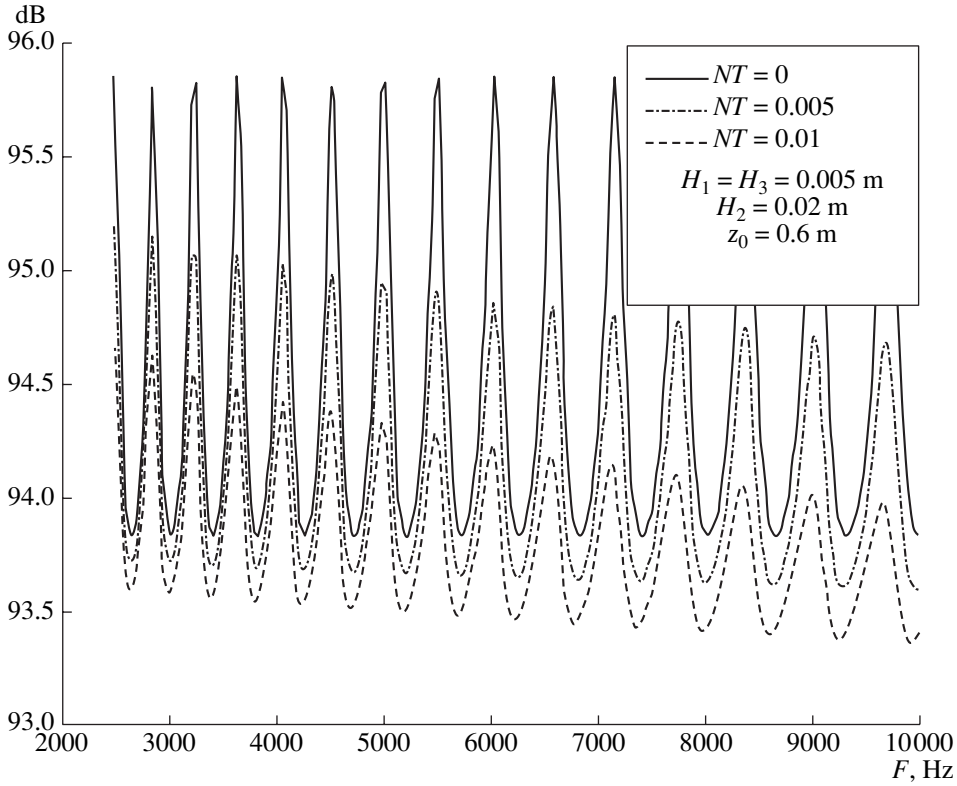

Fig. 6. Frequency dependences of the levels of sound radiation from a three-plate structure for various values of the loss factor.

in the formation of the acoustic field of a different-thickness structure. The indicated sources of the acoustic field can be replaced by piston radiators with equivalent particle velocities.

Thus, in solving the problem of sound radiation by a system of two plates of different thickness, one can determine the values of the displacements in inhomogeneous flexural fields on both sides of the plate joint, find

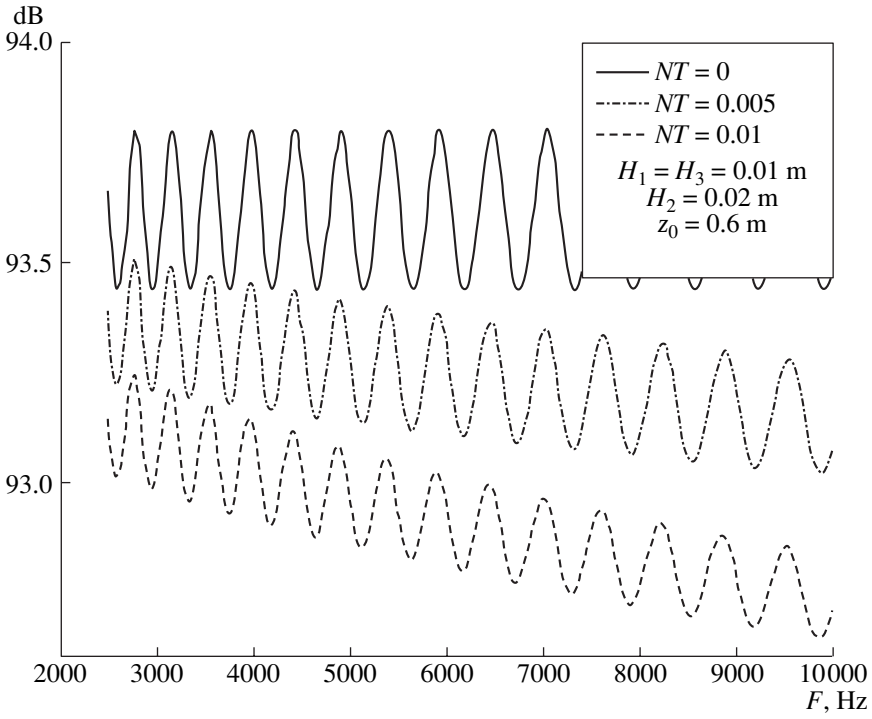

Fig. 7. Frequency dependences of the levels of sound radiation from a three-plate structure for various values of the loss factor.

the equivalent volume velocity of the sources by integrating these displacements with respect to the x coordinate, and use the known expressions for sound radiation by a linear source in a rigid baffle. This approach is also valid for determining the levels of sound radiation from a plate with a rib, along which a flexural wave is propagating. In this case, the main contribution to the formation of the acoustic field is also made by the inhomogeneous flexural fields arising on both sides of the rib [4].

Since the sources of acoustic radiation that were determined above proved to be concentrated near the joint of the plates of different thickness, the acoustic baffle can be eliminated by assuming that the plate itself plays its role. (When considering the sound radiation from plates in air, this assumption is valid for almost any plate thickness.)

Figure 5 shows the spatial distribution of the levels of acoustic pressure produced by a three-plate structure in an acoustic baffle opening (l = 1 m, a = 2 m).

When two plates of the same thickness ($H_1 = H_3$ = 0.01 m) are joined together by a thicker central insert (H_2 = 0.02 m), the sources of acoustic radiation (x_0 = ±1 m) also appear at the places of joints. Figure 5 displays the results of the exact (–) and approximate (+) calculations, which coincide accurate to 3 dB.

Figure 6 represents the frequency dependence of sound radiation from a structure consisting of peripheral plates of thickness $H_1 = H_3$ = 0.005 m and a central plate of thickness H_2 = 0.02 m for various values of the loss factor in the central plate (NT = 0, 0.005, and 0.01). As is seen from the figure, the levels of acoustic pressure strongly oscillate with frequency, and the amplitude of oscillations decreases with increasing loss factor of the central plate material because of the decrease in the levels of resonance vibrations of this plate. The oscillation amplitude also decreases with a decrease in the thickness difference between the elements of the structure, because in this case the energy flux from the central plate to peripheral ones increases, which, in its turn, suppresses the effect of the loss factor on the sound radiation (Fig. 7).

The proposed solution of the problem can be used for determining the acoustic pressure levels produced by flexurally vibrating different-thickness structures.

REFERENCES

1. S. F. Wu and J. Zhu, J. Acoust. Soc. Am. **97**, 2709 (1995).
2. A. S. Nikiforov and S. V. Budrin, *Propagation and Absorption of Sound Vibration in Ships* (Sudostroenie, Leningrad, 1993).
3. V. N. Romanov and V. S. Ivanov, *Sound Radiation from Elements of Ship Structures* (Sudostroenie, St. Petersburg, 1993).
4. E. L. Shenderov, *Wave Problems in Hydroacoustics* (Sudostroenie, Leningrad, 1972).

Translated by A. Svechnikov

Acoustical Physics, Vol. 49, No. 5, 2003, pp. 545–549. Translated from Akusticheskiĭ Zhurnal, Vol. 49, No. 5, 2003, pp. 644–649.

In memory of L.M. Lyamshev

Suppression of Acoustic Noise in the Measurements of Wall Pressure Fluctuations

E. B. Kudashev

Institute of Space Research, Russian Academy of Sciences, ul. Profsoyuznaya 84/32, Moscow, 117997 Russia
e-mail: eco@iki.rssi.ru

Received September 16, 2002

Abstract—It is shown that, in hydrodynamic noise measurements in the presence of acoustic noise acting upon the pressure fluctuation receiver, spatial filtering methods should provide the best results. Active methods are developed for suppressing the acoustic noise that affects a miniature receiver in the course of turbulent pressure fluctuation measurements. The methods are based on complicating the structure of the measuring transducer by introducing an extra compensating sensing element whose characteristics are identical with those of the main sensing element. The spatial filtering of small-scale turbulent pressure fluctuations by a finite-size electroacoustic transducer is used as the basis for the development of noise-compensated measuring systems, as well as methods of measuring the turbulent pressure fluctuations by receivers with noise compensation. A numerical study of the wave-number filtering of acoustic noise in wall pressure measurements by a noise-compensated receiver is performed. © *2003 MAIK "Nauka/Interperiodica".*

1. INTRODUCTION

The studies of hydrodynamic flow noise that were performed by L.M. Lyamshev at the boundary between acoustics and physical hydrodynamics received wide recognition in Russia and abroad. One of the most important fundamental results of these studies was the development of the theory of hydrodynamic flow noise. Lyamshev clarified the role of wall pressure fluctuations and viscous tangential stresses, which arise in a turbulent boundary layer, in flow noise formation. The studies concerned with the physics of hydrodynamic flow noise resulted in the appearance of a new area of research in acoustics: hydrodynamic acoustics.

The problem of reducing hydrodynamic flow noise attracted the attention of Lyamshev, and, in this connection, he performed a series of theoretical and experimental studies concerned with the methods of controlling the characteristics of turbulent pressure fluctuations. The problem of reducing the acoustic noise in the measurements of turbulent pressure fluctuations is closely related to these studies. The urgency of the problem is determined by the need to measure turbulent pressure fluctuations by miniature pressure receivers with the minimum possible receiving surface. However, this way of increasing the resolution in measuring the turbulent pressure field leads to an inevitable loss in the receiver sensitivity and, hence, to low signal levels generated by the measuring pressure transducers. In this case, the results of measurements are strongly affected by various external physical factors that accompany the experiment in actual conditions.

Among the sources of interference in acoustic hydrodynamic experimental studies, one should first consider noise and vibration [1–3, 5, 6]. It is well known that acoustic noise can be generated by both the flow and the equipment. Considerable interference is caused by acoustic noise originating from the experimental system or test bench. The effect of wall temperature fluctuations in a turbulent flow is also considerable [4, 6]. One should also take into account the vibrations of the sensing element of the pressure receiver due to the wall pressure fluctuations.

Present-day measurements of wall pressure fluctuations are performed not only in laboratory conditions but also in full-scale conditions, where the effect of interfering factors is greater. Over the last few years, in connection with the growing interest in the nonstationary aerodynamic processes that occur in power plants, it has often been necessary to perform measurements of wall pressure fluctuations near objects of complex shape in conditions close to full-scale ones. The interfering factors affect the experimental results to a certain extent, and the effect of interference often leads to discrepancies between the results obtained on different test benches or with different experimental systems.

This paper considers the problems of noise suppression in the measurements of wall pressure fluctuations when the possibilities of conventional methods of noise reduction are limited. In the experiments on an aerodynamic test bench, the signals from a turbulent pressure receiver also contain noise components associated with the compressor, the exhaust, and the pipeline elements.

1063-7710/03/4905-0545$24.00

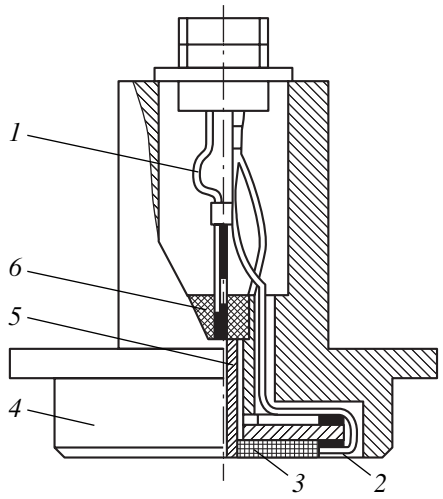

Fig. 1. Turbulent pressure receiver with acoustic noise compensation: (*1*) current leads, (*2*) compensating sensing element, (*3*) sealing element, (*4*) case of the receiver, (*5*) working sensing element, and (*6*) bushing.

It is also necessary to take into account the vibration of the test bench and the deformation of the sensing element of the receiver because of the nonstationary loading of its inactive surfaces, which do not directly perceive the pressure fluctuations. In this situation, the most promising methods of noise suppression are active methods based on the complication of the structure of the measuring transducer through the introduction of an extra compensating sensing element with characteristics identical to those of the main sensing element.

The essence of the general method is as follows. The compensating sensing element only responds to the field of the physical parameter interfering with the measurements and produces an electric signal proportional to the instantaneous value of this physical parameter. The function of the extra sensing element is to measure the noise field without distortions. Then, at any instant of time, the output signal of the compensating sensing element is identical with the noise component of the signal generated by the main sensing element. When the main and compensating elements are connected in opposition to each other, the noise component is electrically subtracted from the total signal.

When using active compensation methods in practice, one encounters a number of problems. They include the choice of the type and position of the compensating element with respect to the main element, the determination of the limits of applicability of the noiseproof measuring system, and the estimate of the efficiency of the active noise suppression method. Specific solutions to these problems largely depend on the characteristics of the noise field, as well as on the type of the receivers (sensing elements) used in the experiment and the properties of the pressure field under study.

Below, the problem of active noise suppression is considered in application to the measurements of wall pressure fluctuations in a turbulent boundary layer by miniature piezoelectric receivers.

2. A NOISE-COMPENSATED RECEIVER FOR TURBULENT PRESSURE FLUCTUATIONS

The spatial filtering of small-scale turbulent pressure fluctuations by a finite-size electroacoustic transducer lies at the basis of the development of noise-compensated measuring systems, as well as methods of measuring turbulent pressure fluctuations against the noise background.

The method of measuring the wall pressures in the presence of acoustic noise is based on the fact that the wall pressure fluctuations and the sound waves have noticeably different correlation scales (Fig. 3).

The active sensing element of a noise-compensated transducer is made of a miniature piezoelectric cylinder. The compensating sensing element is an electroacoustic transducer with an extended receiving surface; i.e., it is a pressure receiver with a much greater sensing area compared to the working sensing piezoelectric element. When the signal of the compensating sensing element is subtracted from the signal of the working (active) element, the resulting output signal is proportional to the turbulent pressure fluctuations alone.

Consider the structure of a noise-compensated receiver [2, 3] shown in Fig. 1.

The receiver has the form of two coaxial sensing elements, *2* and *5*, fixed in a case *4*. A sealing gasket *3* provides the leakproofness of the structure. The working sensing element *5* is a miniature piezoceramic cylinder 1.3 mm in diameter, which perceives the pressure fluctuations by a diaphragm mounted at the cylinder end. The compensating sensing element *2* is a bimorph piezoceramic transducer consisting of 30-mm-diameter disks cemented together. The piezoceramic cylinder *5* is mounted on a bushing *6* fixed inside the case by an epoxy compound. The electric signals are taken from the leads *1*, which are connected with the input of the subtracting device.

Figure 2 presents the noise-compensated transducers that were tested in the experimental measurements of wall pressure fluctuations [2].

A turbulent pressure fluctuation receiver with acoustic noise compensation is intended for operation in a turbulent pressure field formed by the models in aero- and hydrodynamic tunnels, as well as by structural elements in a turbulent flow, in the conditions close to the full-scale ones at low subsonic velocities.

The main principle of operation of a noise-compensated receiver is based on the fact that, owing to its considerable dimensions, the finite-size compensating sensing element is almost insensitive to the small-scale structure of turbulent pressure fluctuations because of the incoherent summation over the receiving surface. Therefore, this element perceives only the acoustic component of the turbulent pressure field (see Fig. 3).

As a result, the compensating sensing element produces an electric signal that is proportional or, in the case of an appropriate tuning, equal to the signal produced by the main working sensing element in response to the noise component of the field.

3. FILTERING PROPERTIES OF A NOISE-COMPENSATED RECEIVER

Specific estimates of the size ratio between the main and compensating sensing elements for the suppression of acoustic noise and the determination of the efficiency limits of the noise compensation method are based on spatial filtering methods.

By analogy with a signal on the background of vibration noise [1], the signal produced by a noise-compensated receiver can be represented in the form

$$S(t) = \int [K_1(\mathbf{x}) - K_2(\mathbf{x})]\, p(\mathbf{x}, t)\, d\mathbf{x}. \qquad (1)$$

Here, K_1 and K_2 are the amplitude distributions of the sensitivity to pressure fluctuations over the receiving surfaces of the main working sensing element and the compensating element of the transducer, respectively.

If the main working sensing element is made in the form of a miniature piezoceramic cylinder, the simplest model of the amplitude distribution over the aperture can be a uniform sensitivity distribution. The compensating sensing element is an extended receiver in the form of a bimorph piezoceramic transducer made of circular plates. It is well known that the spatial distribution of the sensitivity of a circular plate is proportional to the sag of the plate under a point force. The sag of a supported plate decreases when the distance from its center to the point of the force application increases. Hence, the sensitivity function of a bimorph receiver smoothly decreases from its center to the periphery. This statement is confirmed by the measurement [9] of the spatial distribution of the function $K(x)$ over the receiving surface of a bimorph flow noise receiver.

The simplest example of the amplitude distribution of sensitivity over the aperture corresponds to K_1 and K_2 in the form of step functions. After considering this model of the sensitivity function, it is possible to pass to related but more complicated descriptions.

For circular sensing elements of the receivers, we represent the distribution functions of their sensitivity to pressure, $K_1(x)$ and $K_2(x)$, in the form

$$K_1(x) = \begin{cases} \gamma/\pi R_1^2 & |\mathbf{x}| < R_1, \\ 0 & |\mathbf{x}| \geq R_1; \end{cases} \qquad (2)$$

$$K_2(x) = \begin{cases} \gamma/\pi R_2^2 & |\mathbf{x}| < R_2, \\ 0 & |\mathbf{x}| \geq R_2, \end{cases} \qquad (3)$$

where γ is the receiver sensitivity under a coherent action.

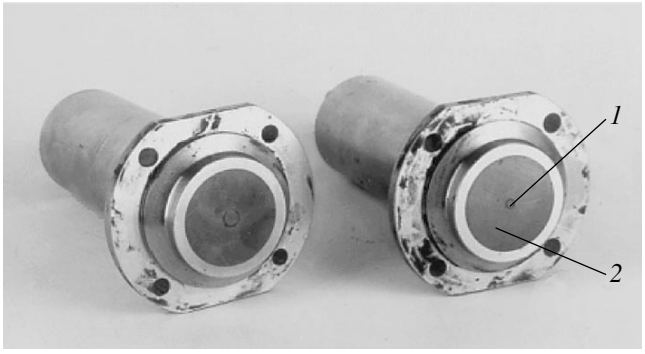

Fig. 2. Noise-compensated transducers of wall pressure fluctuations: (*1*) working sensing element and (*2*) compensating sensing element.

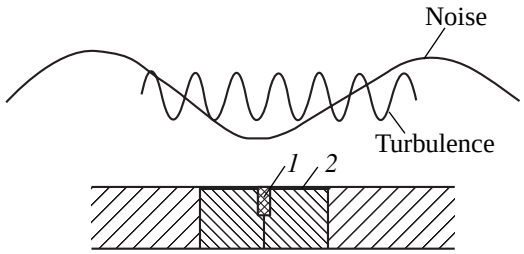

Fig. 3. Noise–signal situation in the measurements of wall pressure fluctuations: (*1*) working sensing element and (*2*) compensating sensing element.

The following analysis of the method of measuring pressure fluctuations against acoustic noise is performed on the assumption that the vibration noise is insignificant.

For a noise-compensated receiver, the Fourier transform $K(\kappa)$ of the amplitude distribution of the sensitivity to pressure fluctuations is determined by the formulas

$$K(\boldsymbol{\kappa}) = K_1(\boldsymbol{\kappa}) - K_2(\boldsymbol{\kappa}) = \gamma\left[\frac{J_1(\kappa R_1)}{\kappa R_1/2} - \frac{J_1(\kappa R_1)}{\kappa R_2/2}\right], \qquad (4)$$

where $J_1(\kappa R)$ is the Bessel function of the first kind.

Since the amplitude distribution of sensitivity has a center of symmetry, the wave-number characteristic of the noise-compensated receiver is determined by the equality $S(\kappa) = |K(\kappa)^2|$.

After some transformations, we obtain the expression for the wave-number characteristic that determines the spatial filtering of acoustic noise by the noise-compensated receiver for turbulent wall pressure measurements:

$$S(\kappa) = \gamma^2\left(\frac{2J_1(\bar{\kappa})}{\bar{\kappa}}\right)^2\left[1 - \frac{\alpha J_1(\bar{\kappa}/\alpha)}{J_1(\bar{\kappa})}\right]^2, \qquad (5)$$

where $\bar{\kappa} = \kappa/R$, $\kappa = |\bar{\kappa}|$, and $\alpha = R_1/R_2$ is the ratio of the diameters of the main and compensating sensing elements of the noise-compensated receiver.

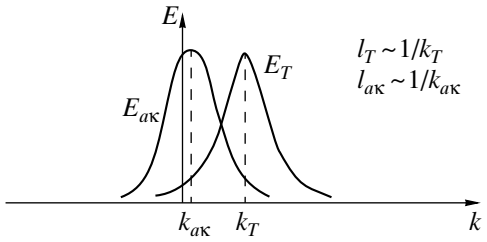

Fig. 4. Energy distributions of the turbulent pressure and the acoustic noise field.

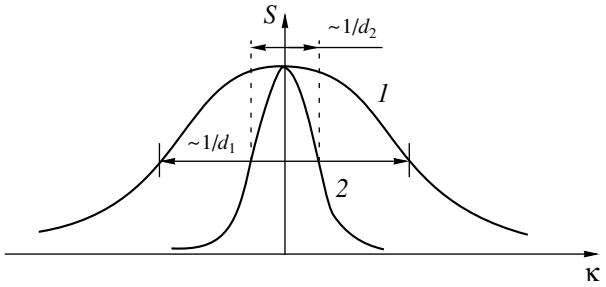

Fig. 5. Wave-number characteristics of the (*1*) main and (*2*) compensating sensing elements of a noise-compensated transducer.

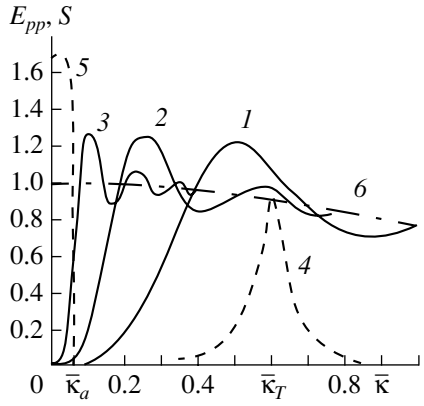

Fig. 6. Wave-number filtering of acoustic noise by a noise-compensated wall pressure receiver: (*1–3*) wave-number characteristics of the receiver for difference values of the diameter ratio of the main and compensating sensing elements α = 0.1, 0.05, and 0.02 (respectively); (*4*, *5*) wave-number spectra of turbulent pressure fluctuations and acoustic noise; and (*6*) wave-number characteristic of an uncompensated receiver.

Figure 6 presents the results of the numerical experiment that was carried out to study the filtering properties of turbulent pressure fluctuation transducers providing the compensation of acoustic noise. The modeling of noise-compensated receivers was performed with the following size ratios of the main and compensating sensing elements of the transducer: 1:10, 1:20, and 1:50.

If the wave-number characteristics of noise-compensated receivers are known, the general expression for spatial filtering

$$\Phi_{SS}(\omega) = \int_{\infty} S(\boldsymbol{\kappa}) E_{pp}(\boldsymbol{\kappa}, \omega) d\boldsymbol{\kappa}$$

can be used to determine the spectral densities of the signal measured by the turbulent pressure transducer under intense acoustic noise and to estimate the effect of noise suppression.

According to Fig. 4, we assume that the spatial spectrum of wall pressure fluctuations is a sum of the turbulent component E_{pp}^{T} and the acoustic noise $E_{pp}^{a\kappa}(\boldsymbol{\kappa}, \omega)$. Then, in the wall pressure fluctuation measurements, the frequency–wave-number spectrum $E_{pp}(\boldsymbol{\kappa}, \omega)$ has the form

$$E_{pp}(\boldsymbol{\kappa}, \omega) = E_{pp}^{T}(\boldsymbol{\kappa}, \omega) + E_{pp}^{a\kappa}(\boldsymbol{\kappa}, \omega). \qquad (6)$$

In analyzing the compensation of acoustic noise, it is important to take into account that the energy-carrying components of the turbulent pressure field are localized on the scales for which $x_\xi U/\omega \approx 1$ [7], where U is the average flow velocity, while the acoustic waves representing the noise manifest themselves only when $\kappa_x c_s/\omega \le 1$, where c_s is the velocity of sound. Hence, as one can see from Fig. 4, the components E_{pp}^{T} and $E_{pp}^{a\kappa}$ are separated in the κ space. The peak of the turbulent component of the frequency–wave-number spectrum of pressure fluctuations corresponds to the values of the spatial frequencies k_T, while the upper bound of the acoustic noise region corresponds to the values $k_{a\kappa}$.

The wave-number characteristics determining the filtering properties of the receiver for the main sensing element *1* and the extra compensating sensing element *2* are shown in Fig. 5.

4. WAVE-NUMBER FILTERING OF ACOUSTIC NOISE

In application to the noise-compensated transducers of wall pressure fluctuations tested in acoustic hydrodynamic experiments [12], a numerical experiment was performed with the aim of studying the efficiency of the wave-number filtering of acoustic noise in the wall pressure measurements by a noise-compensated receiver of turbulent pressures.

The results of modeling a noise-compensated receiver as a wave-number filter are presented in Fig. 6. Curve *4* in Fig. 6 shows the distribution of the energy E_{pp}^{T} of turbulent pressures in the flow direction according to the model field [8]. Curve *5* shows the wave-number component $E_{pp}^{a\kappa}(\boldsymbol{\kappa}, \omega)$ corresponding to the noise field for the Mach number M = 0.1.

The effect of the spatial filtering of acoustic noise is demonstrated by curves *1–3*, which represent the wave-

number characteristics of the noise-compensated receiver for $\alpha = 0.1$, 0.05, and 0.02, respectively.

The best suppression of acoustic noise with the minimum distortion of the pressure fluctuation spectrum is evidently achieved when the wave-number characteristic of the noise-compensated transducer $S(\boldsymbol{\kappa})$ has the form of a step function: $S(\kappa)$ is equal to zero in the noise region $\bar{\kappa} \le \bar{\kappa}_{a\kappa}$ and to a nonzero constant in the whole remaining region of spatial frequencies $\bar{\kappa} > \bar{\kappa}_{a\kappa}$. In this case, the efficiency of noise suppression increases with decreasing Mach number M.

The analysis of the curves shown in Fig. 6 and the estimate of the wave-number filtering show that the proposed noiseproof receiver of turbulent pressure fluctuations provides an efficient suppression of acoustic noise when the diameter ratio of the main operating and extra compensating sensing elements is 1 : 20 and the Mach number is $M \le 0.1$.

This result is obtained in the frequency range corresponding to the Strouhal numbers within $0.2 \le \frac{\omega R_1}{\nu} \le 0.8$, which, for standard conditions of an aerodynamic experiment, is approximately within 750–3000 Hz.

5. SUMMARY

The studies described above show that the methods of spatial filtering prove to be promising in analyzing the measurements of turbulent pressure fluctuations in the presence of acoustic noise.

Active methods are developed for suppressing the acoustic noise that affects a miniature receiver of turbulent pressure fluctuations. The methods are based on the complication of the structure of the measuring transducer, namely, on the introduction of an extra compensating sensing element whose characteristics are identical to those of the main sensing element. The spatial filtering of small-scale turbulent pressure fluctuations by a finite-size electroacoustic transducer is used as the basis for the development of noise-compensated measuring systems and methods for measuring turbulent pressure fluctuations in the presence of acoustic noise. The theory of a noise-compensated receiver as a wave-number filter of acoustic noise is developed.

It is important to note that the efficiency of the method of measuring the spectral components of turbulent pressure fields by suppressing the acoustic noise is limited. The limitation is related to the possibility of determining the actual wave-number characteristic of a turbulent pressure fluctuation receiver with the compensation of acoustic noise.

However, from the literature it follows that, as a rule, the wave properties $K(\boldsymbol{\kappa})$ of pressure fluctuation receivers are obtained by numerical integral transformations of the distribution of the local sensitivity to pressure fluctuations [7].

Within the framework of this approach, the field of the spatial distribution $K(x)$ over the aperture, in its turn, is determined experimentally: the existing methods use a mechanical excitation of individual points of the sensing surface of the turbulent pressure fluctuation receiver [9, 10].

It should be stressed that, for the determination of the filtering properties of a compensated receiver suppressing the acoustic noise, experimental methods of studying the wave-number characteristic $S(\boldsymbol{\kappa})$ are quite promising.

The author of this paper proposed a method that allows a direct measurement of the wave-number characteristic $S(\boldsymbol{\kappa})$ of an electroacoustic transducer [11]. As a result of calibration, the quantity $S(\boldsymbol{\kappa})$ proves to be directly related to the signal of the turbulent pressure fluctuation transducer.

ACKNOWLEDGMENTS

I am grateful to I.D. Vereb'evskii from the Mendeleev Institute of Metrology for taking part in the experiment and to L.R. Yablonik from the Polzunov Boiler and Turbine Institute for discussing the problems of spatial filtering of physical fields.

This work was supported by INTAS (project no. INF0-00-089) and the Russian Foundation for Basic Research (project no. 01-07-90008).

REFERENCES

1. E. B. Kudashev, Akust. Zh. **49**, 215 (2003) [Acoust. Phys. **49**, 176 (2003)].
2. E. B. Kudashev and I. D. Vereb'evskiĭ, Tr. Metrolog. Inst. SSSR, No. 157 (217), 101 (1975).
3. E. B. Kudashev, Izv. Vses. Nauchno-Issled. Inst. Gidrotekh. im. B.E. Vedeneeva **190**, 91 (1986).
4. E. B. Kudashev and L. R. Yablonik, Akust. Zh. **32**, 127 (1986) [Sov. Phys. Acoust. **32**, 78 (1986)].
5. E. B. Kudashev and L. R. Yablonik, Izv. Vyssh. Uchebn. Zaved., Energ., No. 2, 72 (1986).
6. E. B. Kudashev and L. R. Yablonik, Izv. Vyssh. Uchebn. Zaved., Energ., No. 8, 77 (1986).
7. I. Ya. Miniovich, A. D. Pernik, and V. S. Petrovskiĭi, *Hydrodynamic Sources of Sound* (Sudostroenie, Leningrad, 1972).
8. G. Corcos, J. Acoust. Soc. Am. **35**, 192 (1963).
9. A. A. Veĭp, E. B. Kudashev, V. S. Petrovskiĭ, and V. M. Tkachenko, in *Proceedings of III All-Union Convention on Theoretical and Applied Mechanics* (Nauka, Moscow, 1968), p. 65.
10. R. B. Gilchrist and W. A. Strawderman, J. Acoust. Soc. Am. **38**, 298 (1965).
11. E. B. Kudashev and L. R. Yablonik, USSR Inventor's Certificate No. 723418, Byull. Izobret., No. 11 (1980).
12. E. B. Kudashev, in *Proceedings of International Symposium on Nonlinear Acoustics ISNA-16* (Moscow, 2002).

Translated by E. Golyamina

Acoustical Physics, Vol. 49, No. 5, 2003, pp. 550–554. Translated from Akusticheskiĭ Zhurnal, Vol. 49, No. 5, 2003, pp. 650–655.

Excitation of Shear Waves Due to the Interband Absorption of Laser Radiation in a Piezoelectric Semiconductor–Dielectric Layered Structure

L. N. Makarova

Stepanov Institute of Physics, National Academy of Sciences of Belarus, pr. F. Skoriny 68, Minsk, 220072 Belarus
e-mail: Liudmila@imaph.bas-net.by

Received July 15, 2002

Abstract—Optical piezoelectric generation of shear bulk acoustic waves by volume-distributed electric fields in the vicinity of a hard planar interface between a piezoelectric semiconductor and a dielectric is described theoretically. Nonstationary and nonuniform electric fields are formed as a result of the spatial separation of electrons and holes photoexcited in the piezoelectric semiconductor due to the interband absorption of laser radiation. Frequency regions where the efficiency of the optical piezoelectric excitation of shear waves increases when the surface of the piezoelectric semiconductor is loaded by another piezoelectric with a high acoustic impedance are found. Numerical estimates of the applicability of the immobile hole model are presented. © *2003 MAIK "Nauka/Interperiodica".*

One of the methods of enhancing the amplitude of acoustic pulses generated in a solid by a thermoelastic mechanism consists in the modification of the boundary. For this purpose, the solid (usually, a metal) is covered by a layer of a liquid or an optically transparent dielectric, which is in acoustically hard contact with the solid. In this case, not only the longitudinal waves generated in the absorbing material are amplified [1], but also the directivity pattern is strongly modified [2]. Theoretical analysis of the thermooptical sound generation in such a layered system, which, in the simplest case, consists of two semi-infinite rigidly bound solids [3, 4], showed that the aforementioned changes depend not only on the ratio of the acoustic impedances of adjoining media, but also on the relation between the thermoelastic parameters of these media. In addition, if the elastic properties of one of the media forming the layer structure are anisotropic, a mode conversion of an acoustic pulse thermoexcited in the isotropic medium is possible at the reflection from the boundary of the anisotropic medium. This effect offers good possibilities for determining the elastic constants [5].

Recent experimental [6] and theoretical [7] studies revealed a much more efficient method of generating bulk and surface sound pulses in piezoelectric semiconductors by using the inverse piezoelectric effect. However, the studies were mainly concerned with the case of a free boundary of a piezoelectric semiconductor. At the same time, the case of an acoustically hard boundary of two materials, one of which (or both) has the properties of a piezoelectric semiconductor, is of great interest. In principle, such a system allows one to generate acoustic waves in the material adjoining the piezoelectric semiconductor. If one of the crystals forming the layered structure is a photoconductor and the other is a piezoelectric, the layered structure allows a piezogeneration of acoustic waves by the electric fields penetrating from the adjoining photoconductor and initiated as a result of the drift and diffusion of photoexcited nonequilibrium electrons and holes. Such a structure was used in the experimental study [8] of the piezogeneration of a surface acoustic wave (SAW) propagating along a piezoelectric crystal surface adjoining a photoconductor. On the other hand, one would expect that the sound generated in the piezoelectric semiconductor will be amplified owing to the modification of its boundary. This paper presents the first attempt to analyze the generation of bulk acoustic waves near a hard planar interface between a piezoelectric semiconductor and piezoelectric.

Let us consider the laser-induced excitation of bulk acoustic waves in a layered structure at the expense of only the inverse piezoelectric effect, i.e., neglecting the thermoelastic and deformation mechanisms, which act along with the piezoelectric mechanism in the process of optical generation of free carriers and partial thermalization of the absorbed energy. The piezoelectric excitation of sound generally prevails over the deformational and thermoelastic mechanisms, if the laser-induced electric fields are not strongly screened [9–11]. Moreover, as was shown in [10, 12, 13], the inverse piezoelectric effect can become the dominant mechanism of sound generation, even in the case of an ambipolar diffusion of the photoexcited quasi-neutral plasma (the sound generation by the Dember field).

In the analysis of the optical generation of bulk acoustic waves in a layered structure, we take into account only the anisotropy of the piezoelectric proper-

1063-7710/03/4905-0550$24.00 © 2003 MAIK "Nauka/Interperiodica"

ties of adjoining crystals. The importance of piezoelectric anisotropy is caused by the fact that, in some piezoactive directions and high-symmetry crystal planes, only certain types of acoustic waves can be excited (for example, Rayleigh waves [7] or Gulyaev–Bleustein waves [14, 15]). We consider the physical situation when bulk acoustic waves of a purely shear type are excited in a piezoelectric–photoconductor structure. To simplify the problem, we neglect the anisotropy of elastic and dielectric properties of adjoining crystals; i.e., we use the model of an elastically isotropic solid. We also neglect the processes of bulk and surface recombination of nonequilibrium photoexcited charge carriers. This means that the analysis of piezoelectric generation of shear waves is performed for the frequencies at which the process of recombination of nonequilibrium carriers is too slow ($\omega \geq \tau_R^{-1}$, where τ_R is the characteristic lifetime of electrons and holes).

Let us consider the excitation of acoustic waves in the layered structures that consist of a wide-band and a narrow-band piezoelectric crystal. In this case, the nonequilibrium charge carriers are generated in the narrow-band crystal as a result of interband absorption of light incident from the side of the wide-band crystal, while the wide-band piezoelectric crystal is transparent for laser radiation. The electric field that results from the spatial separation of nonequilibrium electrons and holes gives rise to acoustic waves in both crystals of the layered structure because of the inverse piezoelectric effect.

For definiteness, we consider the layered structures that consist of crystals of the 6mm class with an acoustic contact between them. An example of such structures is the ZnO–CdS system. Let the sixfold symmetry axes C_6 of both crystals be parallel and lie in the boundary plane between the crystals. Assume that the Z axis of the Cartesian coordinate system coincides with this direction and the X axis, with the normal to the boundary, so that it is directed towards the narrow-band piezoelectric crystal.

Consider the excitation of well-collimated acoustic beams, i.e., beams with plane phase fronts. Experimentally, this is achieved by focusing the laser beam into a strip whose length L is much greater than the width l ($L \gg l$). To simulate this situation, we assume that the laser radiation is focused into a strip parallel to the Z axis, and all physical quantities are independent of the z coordinate.

In the case of a wide laser beam, the consideration can be restricted to the one-dimensional problem. In the physical situation under study ($Z \parallel C_6$), only the transverse bulk acoustic waves can be excited through the inverse piezoelectric effect. The wave equation that describes the displacement $U_z \equiv U$ in the shear traveling wave in each of the two crystals of the layered structure has the form

$$\frac{\partial^2 U_i}{\partial t^2} - \nu_i^2 \frac{\partial^2 U_i}{\partial x^2} = \frac{e_i}{\rho_i}\frac{\partial^2 \varphi_i}{\partial t^2}, \tag{1}$$

where e denotes the nonzero piezoelectric moduli $e_{131} = e_{113} = e_{232}$ that are active in the chosen crystal configuration, ν is the velocity of transverse bulk acoustic waves, and ρ is the equilibrium density. The index $i = 1, 2$ characterizes the physical quantities for the first and second crystals, respectively.

The boundary conditions of equal displacements and mechanical stresses in two adjoining crystals at $x = 0$ define the system of equations relating U_1 and U_2:

$$\begin{gathered} U_1 = U_2, \\ \rho_1 \nu_1^2 \frac{\partial U_1}{\partial x} + e_1 \frac{\partial \varphi_1}{\partial x} = \rho_2 \nu_2^2 \frac{\partial U_2}{\partial x} + e_2 \frac{\partial \varphi_2}{\partial x}. \end{gathered} \tag{2}$$

In describing the induced electric fields, we neglect the direct piezoelectric effect, because the inverse effect of acoustic waves on the electric fields is of the second order of smallness. The potentials φ_i of quasistatic electric fields in each crystal of the layered structure are defined by the Poisson equations:

$$\varepsilon_i \varepsilon_0 \frac{\partial^2 \varphi_i}{\partial x^2} = Q_i^{(\nu)}, \quad i = 1, 2, \tag{3}$$

where ε_0 is the dielectric constant of vacuum, ε is the relative permittivity of the medium, and $Q^{(\nu)}$ is the volume charge density. In what follows, we assume that $Q_2^{(\nu)} = 0$, because the charge carriers photoexcited in the narrow-band photoconductor do not diffuse into the wide-band crystal. The potentials in both crystals of the layered structure are related to each other by the boundary conditions at the surface $x = 0$:

$$\varepsilon_1 \frac{\partial \varphi_1}{\partial x} = \varepsilon_2 \frac{\partial \varphi_2}{\partial x}, \quad \varphi_1 = \varphi_2. \tag{4}$$

The volume electric charge $Q_1^{(\nu)}$ in the narrow-band conductor arises as a result of the spatial separation of photoexcited electrons and holes. For a quasi-neutral crystal, we have

$$Q_1^{(\nu)} = -Q_0(n^e - n^h), \tag{5}$$

where n^m ($m = e, h$) is the nonequilibrium concentration of electrons and holes and Q_0 is the elementary charge. The dynamics of free carriers is described by the continuity equation

$$\partial n^m/\partial t + \operatorname{div} J^m = G, \tag{6}$$

where the electron and hole flux densities are determined by the drift and diffusion of the corresponding

carriers:

$$J^m = \pm \mu_m (n_0^m + n^m)\nabla\varphi - D_m \nabla n^m. \quad (7)$$

Here, μ_m, D_m, and n_0^m are the mobility, diffusion coefficient, and equilibrium concentration of carriers. The function $G \equiv G(x, y, t)$ describes the space–time distribution of the optical source of electrons and holes. Their fluxes (7) at the surface $x = 0$ should satisfy the condition $J_x^m = 0$. According to expression (7), the spatial separation of electrons and holes is caused by the difference in the mobilities of charge carriers of different sign ($\mu_e \neq \mu_h$ and, consequently, $D_e \neq D_h$) at their diffusion and drift in the induced electric field.

At the first stage, we linearize the equations for the carrier fluxes by neglecting the terms $n^m\nabla\varphi$ compared to $n_0^m\nabla\varphi$. The system of equations (1)–(7) fully describes the optical piezoelectric excitation of shear acoustic waves in the piezoelectric semiconductor–piezoelectric structure. Since it is a system of linear partial differential equations, it is natural to solve it by the method of integral transformations. We apply the Fourier transformation in time t and the Laplace transformation in the x coordinate [11, 13]:

$$\tilde{F}(\omega, x) \equiv \int_{-\infty}^{\infty} \exp(i\omega t) F(t, x)\, dt,$$
$$\hat{F}(\omega, p) \equiv \int_{0}^{\infty} \exp(-p|x|)\tilde{F}(\omega, x)\, dx, \quad (8)$$

where F is any of the physical variables of the problem under study. We also introduce the notation $F(0) = F(t, 0)$ for the function values at the boundary between the two crystals.

Using expressions (8) to transform the wave equation (1) with boundary condition (2) and using the radiation condition, we eliminate from Eq. (1) the spectral components of displacements $\tilde{U}_i(0)$ and their derivatives at the surface $x = 0$:

$$\rho_1 v_1^2 (p_1^2 + p^2)\hat{U}_1(\omega, p) + e_1 p^2 \hat{\varphi}_1(\omega, p)$$
$$= (\rho_1 v_1^2 p_1 + \rho_2 v_2^2 p_2)^{-1}$$
$$\times \{ e_1 p_1^2 (i\rho_1 v_1^2 p - \rho_2 v_2^2 p_2)\hat{\varphi}_1(\omega, ip_1) \quad (9)$$
$$+ e_1 \rho_2 v_2^2 p_2 (p - ip_1)\tilde{\varphi}_1(0)$$
$$- e_2 \rho_1 v_1^2 p_2 (p - ip_1)[\tilde{\varphi}_2(0) + ip_2 \hat{\varphi}_2(\omega, -ip_2)] \},$$

$$\rho_2 v_2^2 (p_2^2 + p^2)\hat{U}_2(\omega, p) + e_2 p^2 \hat{\varphi}_2(\omega, p)$$
$$= (\rho_1 v_1^2 p_1 + \rho_2 v_2^2 p_2)^{-1}$$
$$\times \{ e_2 p_2^2 (i\rho_2 v_2^2 p - \rho_1 v_1^2 p_1)\hat{\varphi}_2(\omega, -ip_2) \quad (10)$$
$$+ e_2 \rho_1 v_1^2 p_1 (p + ip_2)\tilde{\varphi}_2(0)$$
$$- e_1 \rho_2 v_2^2 p_1 (p + ip_2)[\tilde{\varphi}_1(0) - ip_1 \hat{\varphi}_1(\omega, ip_1)] \}.$$

Here, $p_{1,2} = \omega/v_{1,2}$ is the wave number of transverse bulk waves in the first and the second mediums. Transforming in a similar way Eqs. (3)–(7) for the potentials of electric field and nonequilibrium carriers, we determine the spectral components of the potentials of electric fields. Since the hole mobility is much smaller than that of electrons ($\mu_h \ll \mu_e$), we assume that holes are immobile ($D_h \sim \mu_h \longrightarrow 0$). Then, for the piezodielectric ($n_0^e = n_0^h = 0$), we obtain

$$\hat{\varphi}_1(\omega, p) = \frac{Q_0}{\varepsilon_0 \varepsilon_1 i\omega (p^2 - p_e^2)} \left\{ \hat{G}(p) - \frac{p}{p_e}\hat{G}(p_e) \right\};$$
$$\hat{\varphi}_2(\omega, p) = -\frac{Q_0}{\varepsilon_0 \varepsilon_1 i\omega p}\frac{\hat{G}(p_e)}{p_e}; \quad (11)$$
$$\hat{\varphi}_1(0) = \hat{\varphi}_2(0) = -\frac{Q_0}{\varepsilon_0 \varepsilon_1 i\omega p}\frac{\hat{G}(p_e)}{p_e}.$$

Here, $p_e \equiv \sqrt{-\frac{i\omega}{D_e}}$, $\mathrm{Re}\{p_e\} > 0$, and $\hat{G}(p) \equiv \hat{G}(\omega, p)$. The optical sources of nonequilibrium carriers generated as a result of the interband absorption of laser radiation are described by the following simple model:

$$G(t, x) = \frac{\alpha(1 - R)I_{\mathrm{in}}}{h\nu_L} f(t) \exp(-\alpha x), \quad (12)$$

where α and R are the light absorption and reflection coefficients, $h\nu_L$ is energy of the optical quantum, and I_{in} is the intensity of incident radiation. The function $f(t)$ describes the time distribution of intensity of the exciting radiation. Then, the spectrum of photoexcited sources has the form

$$\hat{G}(\omega, p) = \frac{(1 - R)I_{\mathrm{in}}}{h\nu_L}\hat{f}(\omega)\frac{\alpha}{\alpha + p}. \quad (13)$$

Using this spectrum and expressions (9)–(12), one can find the amplitudes of spectral components $\hat{U}_{1,2}(\omega, p)$ of the optically excited shear bulk waves in both crystals.

Let us consider the laser-induced generation of shear waves in the narrow-band piezoelectric semiconductor 1. The spectrum $\hat{U}_1(\omega, p)$ can be written as

$$\hat{U}_1(\omega, p) = \Phi(\omega, p)/(p - ip_1), \quad (14)$$

where $\Phi(\omega, p)$ is a function without poles, whose explicit form is too cumbersome to be presented here.

Performing the inverse Laplace transformation in p, we obtain the frequency spectrum of shear waves:

$$\tilde{U}_1(\omega, x) = \Phi(\omega, ip_1)\exp(ip_1 x). \quad (15)$$

Expression (15) can be represented as

$$\tilde{U}_1(\omega) \equiv H(\omega)\tilde{f}(\omega)\exp(ip_1 x). \quad (16)$$

Analysis of the optical piezoelectric generation of shear waves in the piezoelectric semiconductor is performed with the help of the spectral transfer function $H(\omega)$ [10], which describes the efficiency of the excitation of acoustic waves at a given frequency. In the physical situation under study, the optical piezoelectric generation of shear waves in a piezoelectric semiconductor without equilibrium electrons and holes ($n_0^e = n_0^h = 0$) is determined by the transfer function

$$H(\omega) = H_0\frac{-i\omega_{D1}}{(\omega - i\omega_{D1})}\frac{1}{(N+1)} \times\left\{\frac{\omega_{D1}\omega_{\alpha 1}}{\sqrt{-i\omega\omega_{D1}}(\omega_{\alpha 1} + \sqrt{-i\omega\omega_{D1}})} - \frac{N\omega_{\alpha 1} - i\omega}{\omega_{\alpha 1}^2 + \omega^2}\right\}. \quad (17)$$

Here, $N \equiv \dfrac{\rho_1 v_1}{\rho_2 v_2}$ is the ratio of acoustic impedances of the absorbing and transparent crystals. In addition, we introduced two characteristic frequencies: $\omega_{D1} = v_1^2/D_e$, at which the phase velocity of the diffusion wave $v_{\mathrm{Dif}} \equiv \sqrt{D_e\omega_{D1}}$ equals the phase velocity of the sound wave v_1, and the frequency $\omega_{\alpha 1} = \alpha v_1$ equal to the inverse travel time of sound through the region of light absorption, α^{-1}. The dimensionless parameter H_0 is characterized by the physical parameters of piezoelectric semiconductor 1 and laser radiation.

Let us consider the case of a strong absorption of laser radiation, when $\omega_{\alpha 1}/\omega_{D1} = m_D \equiv \alpha D_e/v_1 \gg 1$. We analyze the result of loading the absorbing piezoelectric crystal with another transparent piezoelectric crystal in this simplified physical situation. Then, we consider two limiting cases. If the acoustic impedance of the medium used to load the piezoelectric semiconductor is much higher than that of the piezoelectric semiconductor, the boundary is an acoustically hard one ($N \longrightarrow 0$). Otherwise, the boundary is free ($N \longrightarrow \infty$). The transfer functions for the hard H_h and free H_s boundaries have the form

$$H_h(\omega) = H_0\frac{-i\omega_{D1}}{(\omega - i\omega_{D1})} \times\left\{\frac{\omega_{\alpha 1}}{\sqrt{-i\omega}(\sqrt{\omega_{n1}} + \sqrt{-i\omega})} + \frac{i\omega\omega_{\alpha 1}}{\omega_{\alpha 1}^2 + \omega^2}\right\}, \quad (18)$$

$$H_s(\omega) = H_0\frac{-i\omega_{D1}}{(\omega - i\omega_{D1})}\frac{\omega_{\alpha 1}^2}{(\omega_{\alpha 1}^2 + \omega^2)}. \quad (19)$$

The frequency $\omega_{n1} = \alpha^2 D_e$ introduced in these expressions has a physical meaning of the inverse diffusion time of carriers within the region of photoexcitation.

At the frequencies $\omega < \omega_{D1}$, when the diffusion of photoexcited carriers is subsonic, the loading of the piezoelectric crystal surface with another piezoelectric with a higher acoustic impedance allows one to increase the efficiency of shear wave generation:

$$\left(\frac{H_h}{H_s}\right) \sim \sqrt{\frac{\omega_{D1}}{\omega}} > 1. \quad (20)$$

In the case of a subsonic diffusion of photoexcited electrons, the sound has enough time to follow their redistribution due to the diffusion, and, hence, the generation of shear waves occurs at the electric field gradients caused by the electron motion. Since the piezoelectrically excited sound pulse is reflected from the transparent medium in phase with the incident pulse in the case of an acoustically hard boundary and in antiphase in the case of an acoustically soft boundary, the efficiency of the piezogeneration of sound in the absorbing crystal increases in the case of a hard boundary, as compared to the case of a free boundary.

At the frequencies $\omega_{D1} < \omega < \omega_{\alpha 1}$, the diffusion of electrons becomes supersonic, but the light absorption region is still acoustically thin. The redistribution of electrons at these frequencies occurs faster than the sound propagation through their diffusion region. Therefore, the sound generation takes place at higher electric field gradients, which are caused by photogenerated immobile holes. As one can see from Eqs. (18) and (19), the increase in the elasticity modulus of the absorbing crystal leads to a decrease in the efficiency of transverse wave excitation:

$$\left|\frac{H_h}{H_s}\right| \sim \sqrt{\frac{\omega_{D1}}{\omega}} < 1. \quad (21)$$

This results from the fact that, in the case of the supersonic diffusion of electrons and the acoustically thin region of light absorption, the source of sound generation is a surface one, because the photoexcited holes are concentrated in the acoustically thin surface layer and their gradient is maximum near the boundary. According to the boundary conditions between the media, at the free boundary of the absorbing piezoelectric crystal, the mechanical deformation created by the electric field of photogenerated holes is compensated by the elastic stress of the crystal lattice:

$$e_1\left.\frac{\partial\varphi_1}{\partial x}\right|_{x=0} = -\rho_1 v_1^2\left.\frac{\partial U_1}{\partial x}\right|_{x=0}, \quad (22)$$

while at the hard boundary, by the difference in the elastic stresses in the transparent and absorbing crys-

tals, because the electric field on the side of the transparent crystal does not cause any mechanical deformation at the boundary owing to its equipotential nature:

$$e_1 \frac{\partial \varphi_1}{\partial x}\bigg|_{x=0} = \left(\rho_2 v_2^2 \frac{\partial U_2}{\partial x} - \rho_1 v_1^2 \frac{\partial U_1}{\partial x}\right)\bigg|_{x=0}. \quad (23)$$

Since at the hard boundary the acoustic impedance of the transparent medium $\rho_2 v_2$ is considerably greater than that of the absorbing medium $\rho_1 v_1$, the stress created by the electric field at the boundary is compensated mainly by the elastic stress produced in the transparent crystal. Therefore, at the frequencies $\omega_{D1} < \omega < \omega_{\alpha 1}$, the sound excitation is more efficient in the piezoelectric crystal with a free boundary than in the hard-boundary loaded piezoelectric crystal.

At the frequencies $\omega > \omega_{\alpha 1}$, when the carrier photoexcitation region is acoustically thick, the loading of the surface of the absorbing piezoelectric crystal with a more acoustically hard medium again leads to the higher efficiency of transverse sound generation compared to the free boundary case:

$$\left|\frac{H_h}{H_s}\right| \sim \frac{\omega}{\omega_{\alpha 1}} > 1. \quad (24)$$

At the frequencies under consideration, the diffusion of photoexcited electrons is supersonic, and, hence, as in the frequency region $\omega_{D1} < \omega < \omega_{\alpha 1}$, the sound generation occurs at the instantaneous turn-on of the electric field of immobile holes. However, with such small times their photoexcitation region becomes acoustically thick. Then, contrary to the case of an acoustically thin absorption region, the sound source is not a surface one, and it is necessary to take into account the piezoelectrically excited acoustic pulses reflected from the impedance boundary of the absorbing crystal. Due to their inphase nature, these pulses increase the efficiency of the piezoelectric generation at the hard boundary.

In conclusion, we assess the applicability limits of the model of immobile holes. The electrons formed in the process of interband absorption of laser radiation separate from the immobile holes and move independently within times less than the Maxwell electron relaxation time ω_M^{-1}. After this time elapses, one has to take into account the slower motion of holes and the combined ambipolar diffusion of carriers with different signs. Therefore, the model of immobile holes, as well as the approximation of the independent motion of electrons and holes, is valid at frequencies $\omega > \omega_M$.

Since in the present work the case of strong absorption of laser radiation is analyzed, the minimum characteristic frequency ω_{D1} should fall in the frequency region $\omega > \omega_M$, where the model of immobile holes is valid. The condition $\omega_{D1} > \omega_M$ allows one to obtain the critical value of the absorbed energy of laser radiation, below which the acoustic wave separates from the diffusion wave faster than the ambipolar diffusion begins. If the light radiation with the quantum energy $h\nu_L \cong 3eV$ is used, the absorbed energy should not exceed 3 nJ/cm^2.

ACKNOWLEDGMENTS

I am grateful to Assoc. Prof. V.E. Gusev for proposing this topical statement of the problem. This work was supported by the Belarussian Republican Foundation for Basic Research (project for young scientists no. M96-015).

REFERENCES

1. R. J. von Gutfeld and R. L. Melcher, Appl. Phys. Lett. **30** (6), 257 (1977).
2. D. A. Hutchins, R. J. Dewhurst, and S. B. Palmer, J. Acoust. Soc. Am. **70**, 1362 (1981).
3. G. C. Wetsel, Jr., Appl. Phys. Lett. **41** (6), 511 (1982).
4. A. A. Karabutov and A. V. Uvarov, Vestn. Mosk. Univ., Ser. 3: Fiz. Astron. **29** (5), 64 (1988).
5. O. Matsuda and O. B. Wright, Anal. Sci. **17** (Special Issue), s216 (2001).
6. P. A. Pyatakov, Akust. Zh. **46**, 112 (2000) [Acoust. Phys. **46**, 96 (2000)].
7. V. E. Gusev and L. N. Makarova, J. Phys. D **23** (11), 1350 (1990).
8. I. S. Grudzinskaya and P. A. Pyatakov, Akust. Zh. **35**, 616 (1989) [Sov. Phys. Acoust. **35**, 356 (1989)].
9. Yu. V. Pogorel'skiĭ, Fiz. Tverd. Tela (Leningrad) **24** (8), 2361 (1982) [Sov. Phys. Solid State **24**, 1340 (1982)].
10. V. É. Gusev and A. A. Karabutov, *Laser Photoacoustics* (Nauka, Moscow, 1991).
11. V. É. Gusev and L. N. Makarova, Akust. Zh. **37**, 670 (1991) [Sov. Phys. Acoust. **37**, 348 (1991)].
12. A. I. Kozlov and V. P. Plesskiĭ, Akust. Zh. **34**, 663 (1988) [Sov. Phys. Acoust. **34**, 381 (1988)].
13. V. É. Gusev and L. N. Makarova, Akust. Zh. **39**, 249 (1993) [Acoust. Phys. **39**, 132 (1993)].
14. V. E. Gusev and L. N. Makarova, Acustica **71** (3), 172 (1990).
15. M. K. Balakirev and I. A. Gilinskiĭ, *Waves in Piezoelectric Crystals* (Nauka, Novosibirsk, 1982).

Translated by A. Kruglov

Acoustical Physics, Vol. 49, No. 5, 2003, pp. 555–564. Translated from Akusticheskiĭ Zhurnal, Vol. 49, No. 5, 2003, pp. 656–666.

Propagation of a Short Pulse in a Medium with a Resonance Relaxation: The Exact Solution

G. A. Maksimov and V. A. Larichev

Moscow Engineering Physics Institute, Kashirskoe sh. 31, Moscow, 115409 Russia

e-mail: maximov@dpt39.mephi.ru; valar@dpt39.mephi.ru

Received December 16, 2002

Abstract—A new analytical representation is obtained for the fundamental solution (Green's function) to the problem of the propagation of a short pulse in an arbitrary medium with a single resonance relaxation process. The analytical representation is based on the generalized function of the local response of a linear medium [1] and includes the well-known Debye and Lorentz relaxation models as particular cases. The representation is used to determine the complete set of possible types of behavior for a short pulse propagating in the medium.

Much recent theoretical and experimental research has dealt with analyzing the propagation, dispersion, and attenuation of short acoustic and electromagnetic pulses in relaxing media [2–11]. The interest in this problem is caused by the additional possibilities that arise when problems of the media diagnostics are solved using pulse methods. These possibilities include the remote investigation of fast processes in a medium and the much looser requirements imposed on the experimental conditions. Previous research [5] showed that the diagnostics of the relaxation properties of a medium with low-amplitude short acoustic pulses may substantially complement the acoustic spectroscopy methods that are commonly used in such applications and even outperform them in some cases.

In the context of pulse diagnostics, the principal difficulty of the inverse problem lies in the choice of the physical model whose generality should provide an adequate description of the properties of many actual media. Such a general model can be obtained within the limits of the thermodynamic approach by Mandelshtam and Leontovich [9], who used the spectrum of relaxation times (SRT) as the fundamental parameter governing the diversity of the dissipation-dispersion properties of actual media. However, in media such as liquids with gas bubbles, resonance properties are inherent along with the relaxation properties. Therefore, these media are usually analyzed in the framework of independent models.

In our previous paper [1], we showed that the Mandelshtam–Leontovich thermodynamic approach complemented with the alternative formulation of the symmetry principle for the Onsager kinetic coefficients offers a unified description of an arbitrary linear medium with a local response. In such an approach, the models by Lorentz [13] and Debye [14, 15] are particular cases of the more general model, in which an additional parameter, namely, the sluggishness angle, is introduced. This additional parameter diversifies the dispersion behavior of a short pulse in comparison with the cases of purely relaxation (the Debye model) and purely resonance (the Lorentz model) responses of the medium.

The equation of state describing the local response of an arbitrary linear medium with a single process of resonance relaxation can be written in the form [1]

$$\sigma(t) = \rho_0 c_\infty^2 \left(\varepsilon(t) - \frac{\Delta\rho}{\tau} \int_0^t dt' \varepsilon(t-t') e^{-t/\tau} \cos(\Omega t' - \varphi) \right), \quad (1)$$

where σ is the stress, ε is the strain, ρ_0 is the density, and c_0 and c_∞ are the low- and high-frequency limits of the phase velocity in the medium. The fundamental parameters that govern the dispersion properties of the medium are the relaxation time τ, the resonance frequency Ω, and the sluggishness angle φ. Furthermore, we introduced special notations for the normalization factor $\rho = (1 + \Omega^2\tau^2)/(\cos\varphi + \Omega\tau\sin\varphi)$ and the dispersion jump of the phase velocity $\Delta = 1 - c_0^2/c_\infty^2$.

At $\Omega = 0$ and $\varphi = \pi/2$, equation of state (1) corresponds to the particular cases of purely exponential relaxation (the Debye model) and purely resonance relaxation (the Lorentz model).

Consider the wave dispersion and absorption features that follow from the equation of state (1).

In the linear approximation, the propagation of plane acoustic waves is described by the equation of motion

$$\rho_0 \frac{\partial^2 u}{\partial t^2} = \frac{\partial \sigma}{\partial x},$$

where u is the displacement; the strain is defined as the derivative $\varepsilon = \partial u/\partial x$.

In terms of the equation of state (1), the equation of motion is reduced to an equation of hereditary type:

$$\frac{1}{c_\infty^2}\frac{\partial^2 u(x,t)}{\partial t^2} = \frac{\partial^2 u(x,t)}{\partial x^2} - \frac{\Delta\rho}{\tau}\int_0^t dt' \frac{\partial^2 u(x,t-t')}{\partial x^2} e^{-t'/\tau}\cos(\Omega t' - \varphi).$$

In the frequency domain ($t \longrightarrow \omega$), this equation is equivalent to the Helmholtz equation

$$\frac{\partial^2 u(x,\omega)}{\partial x^2} + K^2(\omega)u(x,\omega) = 0,$$

where the wave number $K(\omega)$ is given by the formula

$$K(p) = \frac{p}{c_\infty}\left(1 - \Delta\rho\frac{(p\tau+1)\cos\varphi + \Omega\tau\sin\varphi}{(p\tau+1)^2 + (\Omega\tau)^2}\right)^{-1/2}. \quad (2)$$

The fundamental solution (Green's function) of the problem on the propagation of a plane pulse in an infinite medium can be represented in the form of the Laplace integral

$$I(x,t) = \frac{1}{2\pi i}\int_{\delta-i\infty}^{\delta+i\infty} dp \exp(pt - xK(p)) \quad (3)$$

with the wave number given by Eq. (2).

In the case of a small velocity dispersion ($\Delta\rho \ll 1$), the wave number $K(p)$ can be expanded in a series to the term linear in $\Delta\rho \ll 1$:

$$K(p) \approx \frac{p}{c_\infty}\left(1 + \frac{\Delta\rho}{2}\frac{(p\tau+1)\cos\varphi + \Omega\tau\cos\varphi}{(p\tau+1)^2 + (\Omega\tau)^2}\right). \quad (4)$$

From representation (4), one can obtain the following expressions for the absorption coefficient $\alpha(\omega) = \mathrm{Re}K(i\omega)$ and the phase velocity $c(\omega)$: $c^{-1}(\omega) = \mathrm{Im}K(i\omega)/\omega$:

$$\alpha(\omega) = \frac{\Delta\rho}{2c_\infty\tau}\frac{(\omega\tau)^2((\omega\tau)^2\cos\varphi + (1-(\Omega\tau)^2)\cos\varphi + 2\Omega\tau\sin\varphi)}{((\omega\tau)^2 + (1-(\Omega\tau)^2))^2 + 4(\Omega\tau)^2},$$

$$c(\omega) = c_\infty\left(1 - \frac{\Delta\rho}{2\tau}\frac{((\omega\tau)^2(\cos\varphi - \Omega\tau\sin\varphi) + (1-(\Omega\tau)^2)(\cos\varphi + \Omega\tau\sin\varphi))}{((\omega\tau)^2 + (1-(\Omega\tau)^2))^2 + 4(\Omega\tau)^2}\right).$$

The requirement that the medium be stable or dissipative, which is equivalent to the requirement that the absorption coefficient be positive, restricts the admissible values of the parameters $\Omega\tau$ and φ:

$$\Omega\tau < \tan(\varphi) + 1/\cos(\varphi) \quad \text{for} \quad -\pi/2 < \varphi < \pi/2. \quad (5)$$

The frequency-dependent phase velocity $c(\omega)$ and absorption coefficient $\alpha(\omega)$ of the medium can exhibit different features depending on the parameters $\Omega\tau$ and φ. Figures 1 and 2 show all the types of features that may appear in the phase velocity $c(\omega)$ and absorption coefficient $\alpha(\omega)$ in stable dissipative media with admissible parameters $\Omega\tau$ and φ from region (5).

As can be seen from these figures, the absorption coefficient $\alpha(\omega)$ can either monotonically increase with frequency or have a peak. The phase velocity $c(\omega)$ can also show a monotone behavior; however, it can have either a peak or a dip and even both a peak and a dip simultaneously.

The peak in the absorption coefficient $\alpha(\omega)$ exists if the following condition is satisfied:

$$\Omega\tau > -\tan(\varphi) + 1/\cos(\varphi) \quad \text{for} \quad -\pi/2 < \varphi < \pi/2. \quad (6)$$

In the phase velocity, the peak exists under the condition

$$\Omega\tau > \cot(\varphi) \quad \text{for} \quad 0 < \varphi < \pi/2, \quad (7)$$

and the dip exists under the condition

$$\Omega\tau > \tan((\varphi + \pi/2)/3) \quad \text{for} \quad -\pi/2 < \varphi < \pi/2. \quad (8)$$

Figure 3 uses the $\Omega\tau$–φ plane to show the regions in which the absorption coefficient and the phase velocity exhibit the aforementioned features. As will be shown below, a short pulse behaves differently in these regions.

Studying the pulse behavior using the representation in the form of the Laplace integral (3) is difficult. Such investigations commonly use either the asymptotic analysis based on the saddle-point technique [3, 4, 7–9] or computer simulations [10].

Below, we derive a new integral representation that is more convenient for investigating the propagation of short pulses in media with resonance relaxation.

By changing the integration variable $p\tau + 1 \longrightarrow p$, we reduce expression (3) with wave number (4) to the form

$$I(x,t) = \frac{e^{-t' - \beta\cos\varphi}}{\tau}\frac{1}{2\pi i}\int_\gamma dp \exp\left(pt' + \beta\frac{Ap + B}{p^2 + (\Omega\tau)^2}\right), \quad (9)$$

where $\beta = \Delta\rho x/2\tau c_\infty$, $t' = (t - x/c_\infty)/\tau$, and the coeffi-

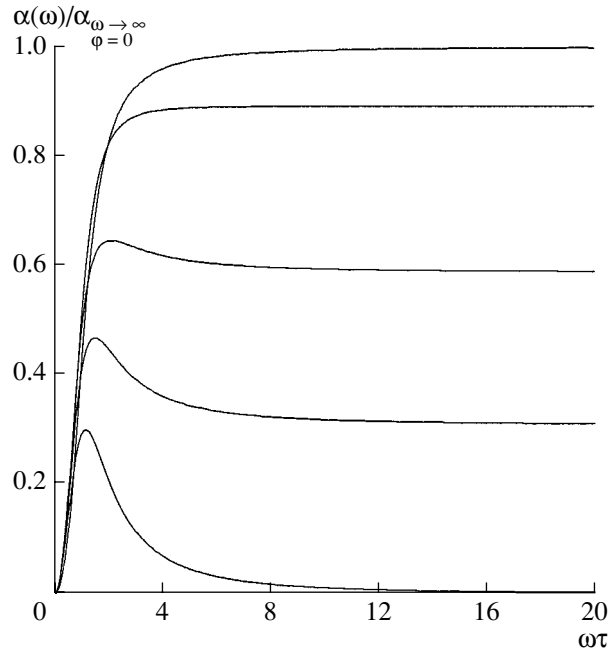

Fig. 1. Absorption coefficient versus the dimensionless frequency for different $\Omega\tau$ and φ.

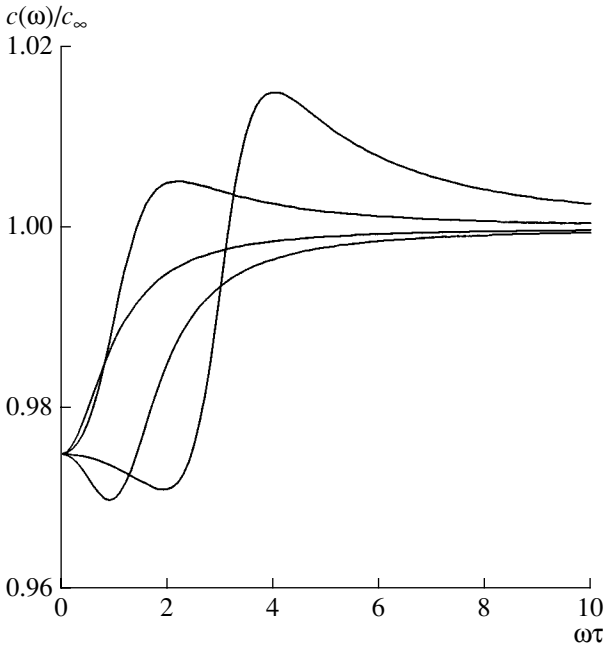

Fig. 2. Phase velocity versus the dimensionless frequency for different $\Omega\tau$ and φ.

cients A and B are determined by the formulas

$$\begin{aligned} A &= (\cos\varphi - \Omega\tau\sin\varphi), \\ B &= \Omega\tau(\sin\varphi + \Omega\tau\cos\varphi). \end{aligned} \tag{10}$$

Note that the coefficient A can take on both positive and negative values.

The integrand in Eq. (9) can be represented in the form

$$F(q(p)) = \exp\left(\beta\frac{A}{q(p)}\right), \text{ where } q = \frac{p^2 + (\Omega\tau)^2}{p + B/A}. \tag{11}$$

Then, one can use the Efros generalized convolution theorem [16] to rearrange the Laplace integral (9) into the form

$$I(x, t) = \frac{e^{-t' - \beta\cos\varphi}}{\tau}\int_0^\infty d\xi F(\xi, \beta)Q(t', \xi), \tag{12}$$

where the functions $F(\xi, \beta)$ and $Q(t', \xi)$ are, in turn, the Laplace integrals

$$F(\xi, \beta) = \frac{1}{2\pi i}\int_\gamma dp e^{p\xi}\exp\left(\frac{\beta A}{p}\right), \tag{13}$$

$$Q(t', \xi) = \frac{1}{2\pi i}\int_\gamma dp e^{pt'}\exp\left(-\xi\frac{p^2 + (\Omega\tau)^2}{p + B/A}\right). \tag{14}$$

Changing the integration variable $p \longrightarrow p + B/A$ in Eq. (14), we easily reduce it to the form

$$\begin{aligned} &Q(t', \xi) \\ &= \frac{\exp\left(-\frac{B}{A}(t' - 2\xi)\right)}{2\pi i}\int_\gamma dp\exp\left(p(t' - \xi) - \xi\frac{C}{p}\right), \end{aligned} \tag{15}$$

where C is the positive parameter:

$$C = (B/A)^2 + (\Omega\tau)^2. \tag{16}$$

Thus, the integrals in Eqs. (13) and (15) coincide in their structure. To calculate these integrals, one can, for example, expand the exponent $\exp(\beta A/p)$ in series and then perform the integration term by term:

$$\begin{aligned} F(\xi, \beta) &= \delta(\xi) + \sum_{k=1}^\infty \frac{(\beta A)^k}{k!}\frac{\xi^{k-1}}{(k-1)!}\theta(\xi) \\ &= \delta(\xi) + \sqrt{\frac{\beta A}{\xi}}\left\{\sqrt{\beta A\xi}\sum_{k=0}^\infty \frac{((2\sqrt{\beta A\xi})^2/4)^k}{k!\Gamma(1 + (k+1))!}\right\}\theta(\xi). \end{aligned} \tag{17}$$

For $A > 0$, the sum in braces is the first-order modified Bessel function $I_1(2\sqrt{\beta A\xi})$ (see [17]); for $A < 0$, it is the common Bessel function $J_1(2\sqrt{\beta|A|\xi})$ multiplied by the imaginary unit. As a result, we obtain the following representations for the functions $F(\xi, \beta)$ and

$Q(t', \xi)$:

$$F(\xi, \beta) = \delta(\xi) + \sqrt{\frac{\beta A}{\xi}} I_1(2\sqrt{\beta A \xi})\theta(\xi) \quad \text{for} \quad A > 0,$$
$$F(\xi, \beta) = \delta(\xi) - \sqrt{\frac{\beta |A|}{\xi}} J_1(2\sqrt{\beta |A| \xi})\theta(\xi) \quad \text{for} \quad A < 0, \tag{18}$$

$$Q(t', \xi) = e^{-\frac{B}{A}(t' - 2\xi)} \times \left(\delta(t' - \xi) - \sqrt{\frac{C\xi}{t' - \xi}} J_1(2\sqrt{C\xi(t' - \xi)})\theta(t' - \xi)\right). \tag{19}$$

Substituting Eqs. (18) and (19) in Eq. (12), we obtain the fundamental solution for the case of $A > 0$ in the form

$$I(x, t) = \frac{e^{-\beta\cos\varphi - \left(1 - \frac{B}{A}\right)t'}}{\tau} \times \left(\delta(t') + \sqrt{\frac{\beta A}{t'}} I_1(2\sqrt{\beta A t'})\theta(t') - \int_0^{t'} d\xi \exp\left(-2\frac{B}{A}\xi\right) \sqrt{\frac{\beta C A}{\xi}} I_1(2\sqrt{\beta A(t' - \xi)}) J_1(2\sqrt{C\xi(t' - \xi)})\right). \tag{20a}$$

In the case of $A < 0$, we obtain in a similar way

$$I(x, t) = \frac{e^{-\beta\cos\varphi - \left(1 + \frac{B}{|A|}\right)t'}}{\tau} \times \left(\delta(t') + \sqrt{\frac{\beta |A|}{t'}} J_1(2\sqrt{\beta |A| t'})\theta(t') + \int_0^{t'} d\xi e^{-2\frac{B}{|A|}\xi} \sqrt{\frac{\beta C |A|}{\xi}} J_1(2\sqrt{C\xi(t' - \xi)}) J_1(2\sqrt{\beta |A|(t' - \xi)})\right). \tag{21a}$$

The first terms in Eqs. (20a) and (21a) describe the elastic forerunner, which exponentially decays with distance according to the law $\exp(-\beta\cos\varphi)$. We note that, in the case of the Lorentz medium ($\varphi = \pi/2$), the elastic forerunner representing the contribution of the highest frequencies does not decay, which completely agrees with the high-frequency behavior of the absorption coefficient, which in this case tends to zero.

The two other terms in parentheses, i.e., the local and integral terms, determine (after multiplication by the factor before the parentheses) the body of the pulse. In the case of $A < 0$, the local term corresponds to the Sommerfeld forerunner and the integral term describes the Brillouin forerunner [4, 7–9, 18–20].

To obtain the asymptotic behavior of the pulse near the front, we note that integrals in Eqs. (20a) and (21a) have the order of magnitude $\sim t'^2$ when $t' \longrightarrow 0$; hence, the local terms govern the behavior of the pulse profile near the front. Expanding them in series in t' to the linear terms, we obtain for both $A > 0$ and $A < 0$:

$$I(x, t) \approx \exp(-\beta\cos\varphi)\delta(t') + \frac{\beta\exp(-\beta\cos\varphi)A}{\tau}\left(1 + \left(\beta A - \left(1 - \frac{B}{A}\right)\right)t' + \ldots\right). \tag{22}$$

One could obtain this near-front expansion immediately from representation (2) by expanding exponent $\exp(-xK(p))$ with wave number $K(p)$ given by Eq. (3) in series for $p \longrightarrow \infty$, thus taking into account the high-frequency pulse component that describes the front. From Eq. (22) it follows in particular that a step of magnitude $(A\beta/\tau)\exp(-\beta\cos\varphi)$ appears at the pulse front even in the general case of resonance relaxation. For dissipative media, this step is negative if the phase velocity has a dip (i.e., in the region where condition (8) is satisfied) and positive if the phase velocity has no dip; this step vanishes for points belonging to line (8) separating these regions: $\Omega\tau = \cot(\varphi)$. In addition, the near-front formula (22) shows the feature that allows one to distinguish between the media with and without the peak in the absorption coefficient from the behavior of the pulse front during the initial stage of propagation. As follows from Eq. (22), the factor $-\left(1 - \frac{B}{A}\right)$ governing the slope angle of the pulse profile for $\beta \ll |A - B|/A^2$ is positive in the regions where the absorption coefficient has a peak and negative in the regions where the absorption coefficient has no peak. The slope angle of the pulse profile at the initial stage of propagation vanishes for points belonging to line (6) $\Omega\tau = -\tan(\varphi) + 1/\cos(\varphi)$ separating these regions.

The analytical description of the Sommerfeld forerunner in the form of the local term of Eq. (21a) shows that this forerunner behaves as a packet of high-frequency oscillations that exponentially decay with time and travel together with the front of the pulse. The oscillation frequency increases proportionally to the root of distance traveled, and the oscillation amplitude varies according to the law $A\beta\exp(-\beta\cos\varphi)$. Note that,

in the particular case of the Lorentz medium ($\varphi = \pi/2$), for an extremely short initial pulse, such a behavior leads to a linear increase in the amplitude of the Sommerfeld forerunner with distance traveled by the pulse.

As regards the case $A > 0$ (Eq. (20a)), one can easily see that the integral term vanishes for $\Omega\tau = 0$ (because $C = 0$ in accordance with Eq. (16)), while other terms form the result corresponding to the pulse propagation in the medium with the Kneser (Debye) relaxation [1, 2, 5, 6]. However, for $\Omega\tau \neq 0$ and greater distances and times, the asymptotic behavior of the local term exhibits a peak at the point $t^* = \beta A/(1 - B/A)^2$ with the amplitude varying according to the law

$$\frac{1}{\tau}\frac{(1-B/A)^{3/2}}{\sqrt{4\pi\beta A}}\exp\left(\frac{\beta(\Omega\tau)^2}{A-B}\right).$$

Thus, the local term exponentially increases under the condition $A > B$, which is equivalent, in accordance with Eq. (6), to the absence of a peak in the absorption coefficient. The only possibility of obtaining a physically meaningful result that will describe the energy dissipation in the course of the pulse propagation consists in the compensation of this increasing term by a similar contribution of the integral term for $\Omega\tau \neq 0$. For this purpose, one can combine these two terms, i.e., the local and integral terms, in Eq. (20a) into one; then, Eq. (20a) for $A > 0$ can be rewritten in the form (after changing the integration variable $\xi \longrightarrow (1 - \xi)t'$)

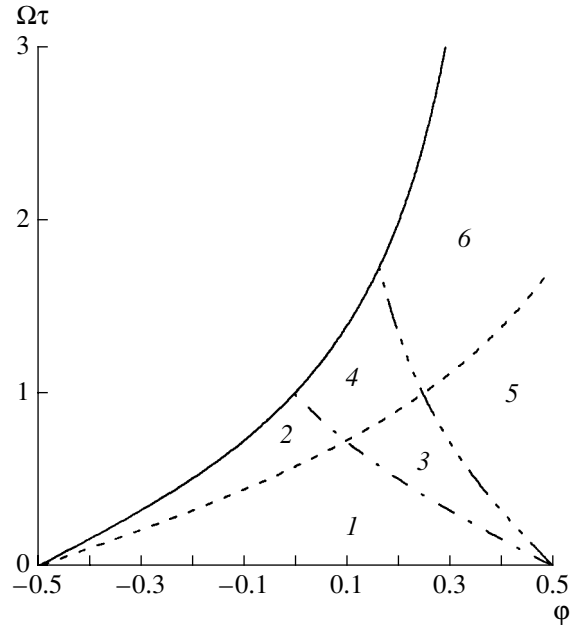

Fig. 3. Separation of the parameter plane $\Omega\tau$, φ into regions corresponding to different features in the absorption coefficient and phase velocity (the angle φ is measured in fractions of π): region *1* corresponds to monotone phase velocity and absorption coefficient; region *2* corresponds to a dip in the phase velocity and a monotone absorption coefficient; region *3* corresponds to a monotone phase velocity and a peak in the absorption coefficient; region *4* corresponds to a dip in the phase velocity and a peak in the absorption coefficient; region *5* corresponds to a peak in the phase velocity and a peak in the absorption coefficient; and region *6* corresponds to a dip and a peak in the phase velocity and a peak in the absorption coefficient. In regions *1*, *2*, *3*, and *4*, $A > 0$; in regions *5* and *6*, $A < 0$.

$$I(x,t) = \frac{\exp\left[-\beta\cos\varphi - \left(1+\frac{B}{A}\right)t'\right]}{\tau}\left(\delta(t') + \theta(t')\frac{\partial}{\partial t'}\int_0^1 d\xi e^{2\frac{B}{A}t'\xi}\sqrt{\frac{\beta A t'}{\xi}}I_1(2\sqrt{\beta A t'\xi})J_0(2\sqrt{Ct'^2\xi(1-\xi)})\right). \quad (20b)$$

An analysis shows that the vicinity of the upper limit gives the main contribution to the integral in Eq. (20b). We can use the mean value theorem to obtain an analytical estimator for this integral by factoring out of the integral the monotone function $\sqrt{\frac{\beta A t'}{\xi}}I_1(2\sqrt{\beta A t'\xi})$ at some point ξ_* in the vicinity of unity. Using the change of the integration variable $\zeta = 1 - 2\xi$, we rearrange the remaining integral into the form

$$\int_0^1 d\xi e^{2\frac{B}{A}t'\xi}J_0(2\sqrt{Ct'^2\xi(1-\xi)}) = e^{\frac{B}{A}t'}\int_0^1 d\zeta\cosh\left(\frac{B}{A}t'\zeta\right)J_0(\sqrt{Ct'(1-\zeta^2)}). \quad (23)$$

The integral in Eq. (23) allows an exact analytical calculation [21]:

$$\int_0^1 dx\cosh(\lambda x)J_0(\mu\sqrt{1-x^2}) = \frac{\sin(\sqrt{\lambda^2-\mu^2})}{\sqrt{\lambda^2-\mu^2}}. \quad (24)$$

As a result, with the use of the explicit relationships for the coefficients A, B, and C, we obtain the following analytical estimator for expression (20b):

$$I(x,t) = \frac{\exp(-\beta\cos\varphi)}{\tau}\left(\delta(t') + e^{-t'}\theta(t')\left(\frac{B}{A}+\frac{\partial}{\partial t'}\right)\left[\sqrt{\frac{\beta A t'}{\xi_*}}I_1(2\sqrt{\beta A t'\xi_*})\frac{\sin(\Omega\tau t')}{\Omega\tau t'}\right]\right). \quad (25)$$

At small distances $\sqrt{\beta|A|t'} \ll 1$, one can find the asymptotic estimator of the Green's function by

expanding the modified Bessel function in this parameter:

$$I(x,t) \approx \frac{1}{\tau}\exp(-\beta\cos\varphi)\Big[\delta(t') + 2\beta e^{-t'}\Big(\frac{B}{\Omega\tau}\sin(\Omega\tau t') + A\cos(\Omega\tau t')\Big)\Big]. \quad (26a)$$

With expressions (10) for the coefficients A and B, this estimator can be rewritten in the form

$$I(x,t) \approx \frac{1}{\tau}\exp(-\beta\cos\varphi)\{\delta(t') + \beta e^{-t'}[\cos(\Omega\tau t' - \varphi) + \Omega\tau\sin(\Omega\tau t' - \varphi)]\}. \quad (26b)$$

From Eqs. (25) and (26) it follows that the profile of the pulse body is modulated by oscillations of frequency ω if $\Omega\tau \neq 0$.

Returning to estimator (25), we can easily see that, for large times and distances $\sqrt{\beta|A|t'} \gg 1$, the amplitude of the pulse body is governed by the exponential factor

$$\exp(-\beta\cos\varphi + 2\sqrt{\beta A t'\xi_*} - t'),$$

which reaches the maximum value $\exp[-\beta(\cos\varphi - A\xi_*)]$ at the point $t' = \beta A\xi_*$. The exponent index in this expression is always negative under the condition $\xi_* < \cos\varphi/A \equiv 1/(1 - \Omega\tau\tan\phi)$, which is always satisfied for ξ_* from the interval [0, 1] where the value of ξ_* lies in accordance with the mean value theorem. Consequently, for large distances, analytical estimator (25) predicts an exponential decay of the amplitude of the pulse body.

For the case $A < 0$, representation (21a) can also be rewritten with the use of the same change of the integration variable $\xi \longrightarrow (1 - \xi)t'$:

$$I(x,t) = \frac{\exp\Big[-\beta\cos\varphi - t'\Big(1 - \frac{B}{|A|}\Big)\Big]}{\tau} \times \Bigg[\delta(t') - \sqrt{\frac{\beta|A|}{t'}}e^{-2\frac{B}{|A|}t'}J_1(2\sqrt{\beta|A|t'})\theta(t') + \theta(t')\int_0^1 d\xi e^{-2\frac{B}{|A|}t'\xi}\sqrt{\frac{\beta|A|Ct'}{1-\xi}}J_1(2\sqrt{\beta|A|t'\xi})J_1(2\sqrt{Ct'^2\xi(1-\xi)})\Bigg]. \quad (21b)$$

For short times or small distances, in which case we have $\sqrt{\beta|A|t'} \ll 1$, we can expand the Bessel functions appearing in the integral and local terms in this parameter and again obtain the same asymptotic expressions (26), which are now valid for the parameters from the region $A < 0$ (7).

The saddle point method allows a more accurate asymptotic estimator for the integrals in Eqs. (20b) and (21b) for greater times and distances; however, this investigation is beyond the scope of this work and will be described in a separate paper.

Expressions (20) and (21) form the principal result of this paper. As distinct from representation (3) in the form of the contour integral in the complex variable plane, representations (20) and (21) are real and allow one to calculate the pulse profiles for arbitrary parameters by a relatively simple integration. Another important feature of exact expressions (20) and (21) consists in the representation of the high-frequency contributions of the elastic (delta-functional) forerunner and the Sommerfeld forerunner (for $A < 0$) as separate terms.

Thus, the expressions obtained allow us to analyze the propagation of a short pulse in the whole propagation region in an arbitrary medium whose dissipation-dispersion properties can be described by a single process of resonance relaxation. In this case, two parameters, $\Omega\tau$ and φ, govern the behavior of the traveling pulse.

The asymptotic analysis of Eqs. (20) and (21) and direct simulations by these formulas provide a complete pattern of the propagation behavior of a pulse for different values of the parameters $\Omega\tau$ and φ. It appears that the features of the pulse shape variation correlate with the features of the phase velocity and absorption coefficient behavior in the regions shown in Fig. 3.

We first consider the media characterized by a positive parameter A. We will call such media the relaxation media, because the behavior of a short pulse in such a medium is similar to its behavior in the Debye model with exponential relaxation. In this case, the parameters $\Omega\tau$ and φ fall in regions *1*, *2*, *3*, and *4* (see Fig. 3).

In region *1*, both phase velocity and absorption coefficient are monotone. For this type of media, the limit for $\Omega \longrightarrow 0$ corresponds to the media with exponential relaxation [14] (which corresponds to the Debye model in electrodynamics). If $\Omega\tau > 0$, the behavior of the temporal pulse profile only slightly differs from a perfect relaxation behavior. In this more general case, the pulse body behaves, for small distances from the source, as an exponentially decaying tail, as in media with exponential relaxation. For greater distances, the pulse body is transformed into a Gaussian pulse formed by lower frequencies. However, in contrast to media with perfectly exponential relaxation, small oscillations decay-

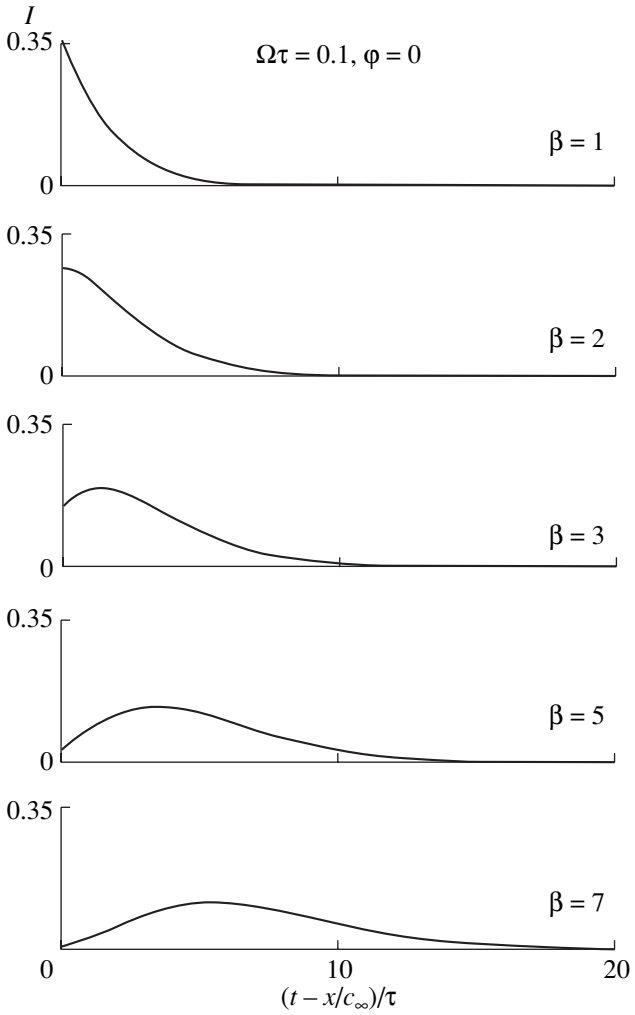

Fig. 4. Behavior of the pulse body in the medium with parameters from region *1* ($\Omega\tau = 0.1$, $\varphi = 0$) for different dimensionless distances from the interval $\beta = 0.5$–10.

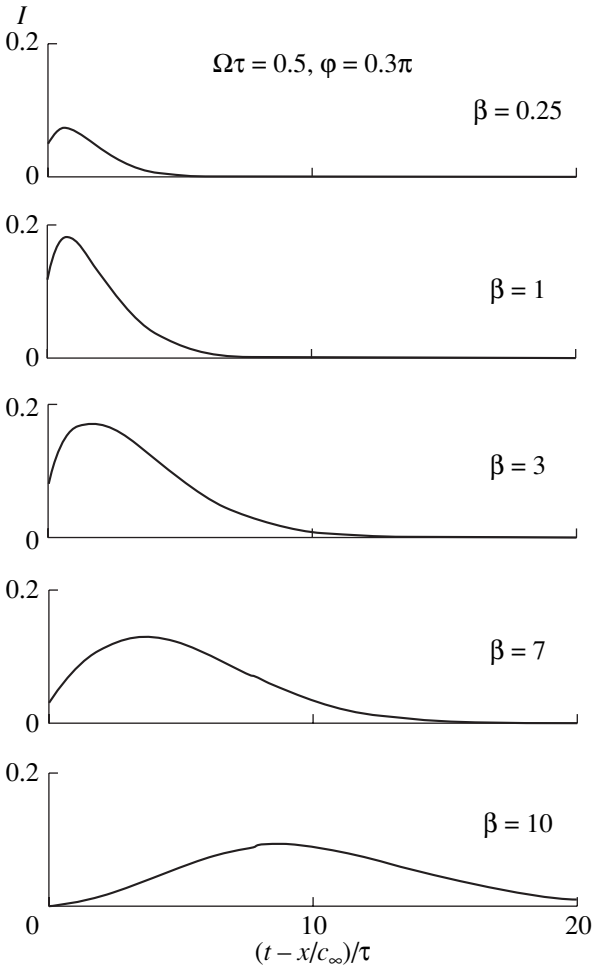

Fig. 5. Behavior of the pulse body in the medium with parameters from region *3* ($\Omega\tau = 0.5$, $\varphi = 0.3\pi$) for different dimensionless distances from the interval $\beta = 0.25$–10.

ing with the distance traveled appear on the tail of the pulse body in media with $\Omega\tau > 0$. Figures 4a and 4b show the behavior of the pulse body in the medium with parameters from region *1* ($\Omega\tau = 0.1$, $\varphi = 0$) for different dimensionless distances from the interval $\beta = 1$–7. In these figures, the small oscillations appearing on the pulse tail are indiscernible.

In region *3*, the phase velocity is monotone, while the absorption coefficient exhibits a peak. On the whole, the pulse behavior in the course of the propagation is similar to the above case excluding the fact that the pulse body appears to be dome-shaped even at the initial stage. This fact follows from the analysis of the asymptotic behavior of Eq. (22) near the front ($t' \longrightarrow 0$) for $\beta \longrightarrow 0$. In this case, the expansion coefficient in the term linear in t' is positive for $\Omega\tau$ and φ from region *3*, and, consequently, the tangent to the pulse body profile has a positive slope near the front. Figures 5a and 5b show the behavior of a short pulse in the medium with parameters from region *3* ($\Omega\tau = 0.5$, $\varphi = 0.3\pi$) for different dimensionless distances from the interval $\beta = 0.25$–25.

In region *2*, the phase velocity shows a dip, while the absorption coefficient is a monotonically increasing function. The dip in the phase velocity results in an increase in the oscillations of the pulse body as the pulse travels. Qualitatively, this fact can be explained as follows. In accordance with the saddle point method, the vicinity of the dip in the phase velocity forms a stable wave packet composed of waves with frequencies corresponding to the dip, whereas only waves with frequencies close to zero are retained in the case of a monotone behavior of the frequency-dependent absorption. Thus, two concurrent processes govern the shape of the pulse body at large distances from the source: a faster decay of higher frequencies (and, hence, the survival of the low-frequency component) and the formation of the stable group of waves with frequencies corresponding to the vicinity of the dip. The asymptotic

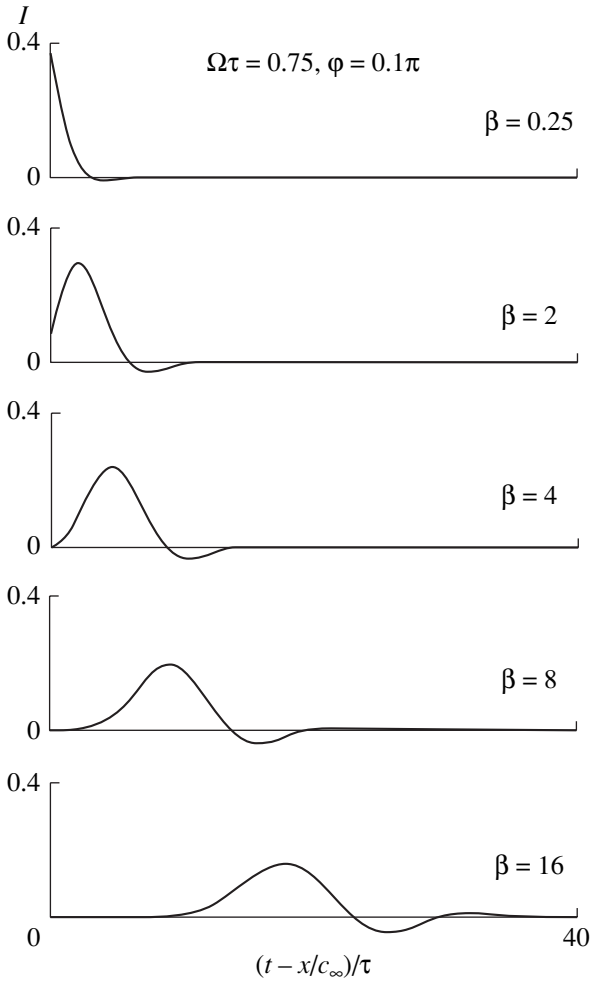

Fig. 6. Behavior of the pulse body in the medium with parameters from region *2* ($\Omega\tau = 0.75$, $\varphi = -0.1\pi$) for different dimensionless distances from the interval $\beta = 0.25$–16.

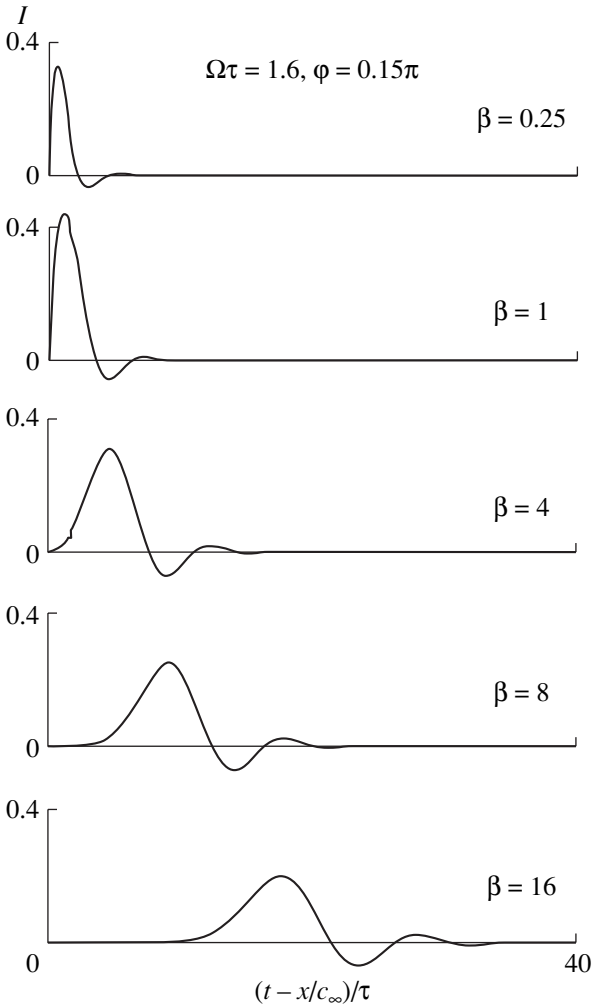

Fig. 7. Behavior of the pulse body in the medium with parameters from region *4* ($\Omega\tau = 1.6$, $\varphi = 0.15\pi$) for different dimensionless distances from the interval $\beta = 0.25$–16.

analysis shows that, at short distances from the source, the pulse body profile behaves as an exponentially decaying tail modulated by the cosine with the positive initial phase (smaller that $\pi/2$). Figures 6a and 6b show the corresponding behavior of a short pulse in the medium with parameters from region *2* ($\Omega\tau = 0.75$, $\varphi = -0.1\pi$) for different dimensionless distances from the interval $\beta = 0.25$–105.

In region *4*, the phase velocity exhibits a dip, while the absorption coefficient has a peak. As in the case of media from region *2*, oscillations of the pulse body increase as the pulse travels. The difference between the media from regions *4* and *2* is similar to the difference between the media from regions *1* and *3*: the slope of the tangent of the pulse body profile is positive near the front for small β. When β is small, the profile of the pulse body behaves as a decaying exponent modulated by the sine with a positive initial phase smaller than $\pi/2$. Figures 7a and 7b show the corresponding behavior of a pulse in the medium with parameters from region *4* ($\Omega\tau = 1.6$, $\varphi = 0.15\pi$) for different dimensionless distances from the interval $\beta = 0.25$–16.

Now, we consider the media for which the parameter A is negative. We will call such media the resonance media, because a short pulse behaves in such a medium as in the Lorentz model. In this case, the parameters $\Omega\tau$ and φ fall into regions *5* and *6* (see Fig. 3).

In these regions, the phase velocity shows a peak exceeding the high-frequency limit c_∞. In this case, near the front, the frequencies corresponding to the phase velocity exceeding the propagation velocity of the pulse front c_∞ form the pulse body portion called in electrodynamics the Sommerfeld forerunner [4, 18–20]. This portion of the pulse body is described by the second term in representation (20). Lower-frequency harmonics propagating with phase velocities smaller than c_∞ form the slowly decaying low-frequency portion of the pulse body, which is called the Brillouin forerunner [4, 18–20]. The peak in the absorption coef-

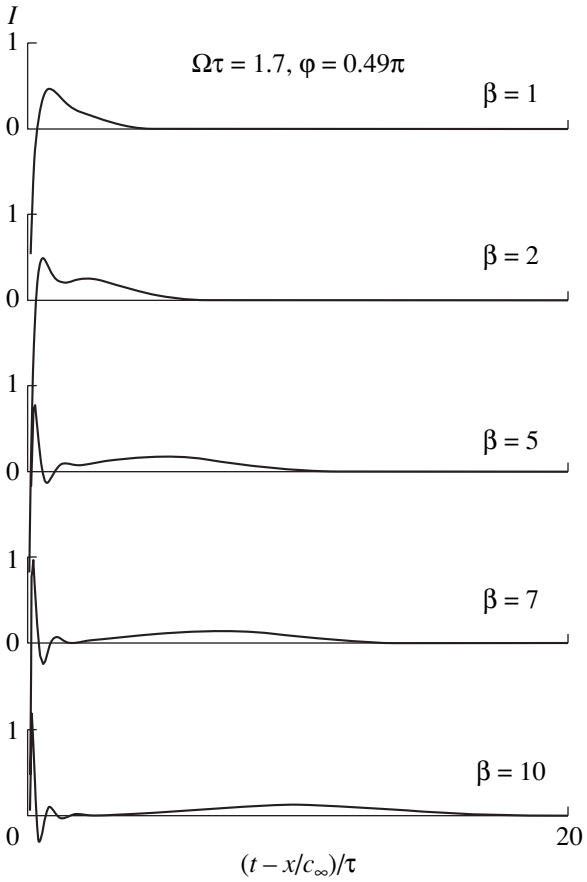

Fig. 8. Behavior of the pulse body in the medium with parameters from region *5* ($\Omega\tau = 1.7$, $\varphi = 0.49\pi$) for different dimensionless distances from the interval $\beta = 1$–16.

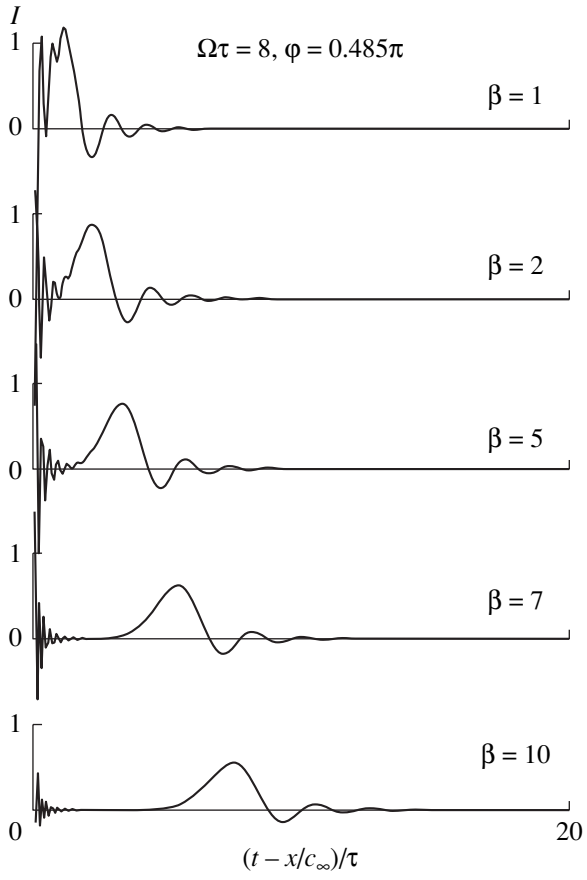

Fig. 9. Behavior of the pulse body in the medium with parameters from region *6* ($\Omega\tau = 8$, $\varphi = 0.49\pi$) for different dimensionless distances from the interval $\beta = 1$–10.

ficient causes an enhanced absorption of intermediate frequencies and results in a separate formation of the above forerunners.

In region *5*, both the absorption coefficient and the phase velocity have peaks. In the region of lower frequencies responsible for the formation of the Brillouin forerunner, the absorption coefficient and the phase velocity are monotonically increasing functions, which is similar to their behavior in regions *1* and *3* and asymptotically forms the Brillouin forerunner in the form of a Gaussian pulse. For higher frequencies responsible for the Sommerfeld forerunner, an analysis of the asymptotic behavior of the pulse body near the front ($t' \longrightarrow 0$) shows that the pulse body begins with the negative phase. As follows from Eq. (20), the amplitude of the Sommerfeld forerunner decays according to the exponential law $\exp(-\beta\cos\varphi)$ for large distances; for media close to the Lorentz model ($\varphi \longrightarrow \pi/2$), this absorption can be small in accordance with the behavior of the absorption coefficient for higher frequencies. The Sommerfeld forerunner behaves as an oscillation train with an exponential envelope. The oscillation frequency is determined by the argument of the Bessel function in the second term in Eq. (20) and increases with distance, and the total duration of the Sommerfeld forerunner is determined by the exponential function $\exp\{-t'(1 + B/|A|)\}$. Figures 8a and 8b show the corresponding behavior of a pulse in the medium with parameters from region *5* ($\Omega\tau = 1.7$, $\varphi = 0.49\pi$) for different dimensionless distances from the interval $\beta = 1$–10.

In region *6*, the absorption coefficient sows a peak, while the phase velocity shows both a peak and a low-frequency dip. In this case, the Sommerfeld forerunner behaves as in region *5*. On the contrary, the Brillouin forerunner behaves as in region *2*, where two factors affect the forerunner formation: the progressive absorption of higher-frequency components and the formation of the stable wave group near the minimum of the phase velocity. These two factors cause the Brillouin forerunner to be formed as a group of low-frequency oscillations that decay with the distance traveled by the pulse according to the power law. Figures 9a and 9b show the corresponding behavior of the pulse body in the medium with parameters from region *6* ($\Omega\tau = 8$, $\varphi = 0.49\pi$) for different dimensionless distances from the interval $\beta = 1$–10.

Thus, on the basis of the generalized equation of state of an arbitrary linear medium with a local response [1], we derived the new integral representation of the Green's function for the problem of short plane pulse propagation in a medium with a single relaxation process. The types of pulse behavior characteristic of the Debye and Lorentz media appear to be particular cases of the solution obtained. The representation derived above was used to analyze all possible types of the behavior of the short pulse profile in the course of the propagation in linear dissipative media with a local response. A correlation was revealed between the features that appear in the frequency-dependent phase velocity and the absorption coefficient of dissipative media in the plane of parameters $\Omega\tau$, φ and the behavior of the short pulse profile propagating in the medium.

ACKNOWLEDGMENTS

This work was supported by the Russian Foundation for Basic Research, project no. 00-02-16556.

REFERENCES

1. V. A. Larichev and G. A. Maksimov, Akust. Zh. **44**, 814 (1998) [Acoust. Phys. **44**, 709 (1998)].
2. L. A. Vainshteĭn, Usp. Fiz. Nauk **118** (2), 339 (1976) [Sov. Phys.–Usp. **19**, 189 (1976)].
3. M. Ya. Kel'bert and I. A. Sazonov, *Propagation of Pulses in Liquids* (Nauka, Moscow, 1991).
4. K. E. Oughstun and G. S. Sherman, *Electromagnetic Pulse Propagation in Casual Dielectrics* (Springer, Berlin, 1994).
5. G. A. Maksimov, Akust. Zh. **42**, 541 (1996) [Acoust. Phys. **42**, 478 (1996)].
6. V. A. Larichev and G. A. Maksimov, Akust. Zh. **45**, 844 (1999) [Acoust. Phys. **45**, 762 (1999)].
7. V. A. Vasil'ev, M. Ya. Kel'bert, I. A. Sazonov, and I. A. Chaban, Opt. Spektrosk. **64**, 862 (1988) [Opt. Spectrosc. **64**, 513 (1988)].
8. K. E. Oughstun and C. M. Balictsis, Phys. Rev. E **55** (2), 1910 (1997).
9. K. E. Oughstun and G. S. Sherman, J. Opt. Soc. Am. A **6**, 1394 (1989).
10. H. Xiao and K. E. Oughstun, J. Opt. Soc. Am. A **15**, 1256 (1998).
11. V. A. Larichev and G. A. Maksimov, in *Proceedings of X Session of the Russian Acoustical Society* (GEOS, Moscow, 2000), Vol. 1, p. 69.
12. L. I. Mandel'shtam and M. A. Leontovich, Zh. Éksp. Teor. Fiz. **7** (3), 438 (1937).
13. V. L. Ginzburg, *The Propagation of Electromagnetic Waves in Plasmas*, 2nd ed. (Nauka, Moscow, 1967; Pergamon Press, Oxford, 1970).
14. P. Debye, *Polar Molecules* (Dover, New York, 1929; Gostekhizdat, Moscow, 1931).
15. A. S. Nowick and B. S. Berry, *Anelastic Relaxation in Crystalline Solids* (Academic, New York, 1972; Atomizdat, Moscow, 1975).
16. M. A. Lavrent'ev and B. V. Shabat, *Methods of the Theory of Functions of a Complex Variable*, 5th ed. (Nauka, Moscow, 1987; Wissenschaften, Berlin, 1967).
17. *Handbook of Mathematical Functions*, Ed. by M. Abramowitz and I. A. Stegun, 2nd ed. (Dover, New York, 1971; Nauka, Moscow, 1979).
18. A. Sommerfeld, Ann. Phys. (Leipzig) **44**, 177 (1914).
19. L. Brillouin, Ann. Phys. (Leipzig) **44**, 203 (1914).
20. L. Brillouin, *Wave Propagation and Group Velocity* (Academic, New York, 1960).
21. A. P. Prudnikov, Yu. A. Brychkov, and O. I. Marichev, *Integrals and Series: Special Functions* (Nauka, Moscow, 1983; Gordon and Breach, New York, 1986).

Translated by A. Vinogradov

Acoustical Physics, Vol. 49, No. 5, 2003, pp. 565–573. Translated from Akusticheskiĭ Zhurnal, Vol. 49, No. 5, 2003, pp. 667–675.

Nonlinear Wave Processes in Media Containing Cracks Partially Filled with a Viscous Liquid

V. E. Nazarov and A. V. Radostin

Institute of Applied Physics, Russian Academy of Sciences, ul. Ul'yanova 46, Nizhni Novgorod, 603600 Russia

e-mail: nazarov@hydro.appl.sci-nnov.ru

Received May 15, 2002

Abstract—A nonlinear (in the cubic approximation) relaxation equation of state is derived for a rod containing cracks partially filled with an incompressible viscous liquid. The nonlinear effects of the self-action and interaction of low- and high-frequency longitudinal elastic waves propagating in such a rod are studied for the cases of identical and size-varied cracks. Linear and nonlinear acoustic parameters characterizing the self-action and interaction of elastic waves in a cracked rod are determined. *© 2003 MAIK "Nauka/Interperiodica".*

1. INTRODUCTION

Studies of nonlinear acoustic effects in microinhomogeneous media are important for developing both the general theory of nonlinear wave processes and the methods of nonlinear diagnostics of such media [1–3]. To solve these problems, it is necessary to know the equation of state of the medium, i.e., the generalized stress–strain dependence. For a particular sample of a rigid body, this dependence can be found or reconstructed (at least, in general terms) phenomenologically from detailed experimental studies of various nonlinear effects, or it can be derived theoretically from a physical model of the medium based on knowledge of its microstructure, i.e., the structural defects responsible for the acoustic nonlinearity of the medium. Naturally, knowledge of the microstructural defects of the medium implies that the equation of state of a single defect is also known, because it determines the equation of state of the medium containing a great number of such defects. The equation of state (in the cubic approximation of the perturbation theory) for a nonlinear defect of a perfect rigid body (cracks partially filled with an incompressible Newtonian liquid) was obtained in [4]. This equation has the form

$$\sigma(d) = K_0 d + \beta\dot{d} - gd^2 - \gamma d\dot{d} - qd^3 + \delta d^2\dot{d}, \quad (1)$$

where σ is the normal stress on the surface of the crack, $K_0 = K + (9\alpha\mu_0 R_0/4H^3)F_1(\theta) > 0$, $K = 3\pi E/8(1-\nu^2)R$, E and ν are the Young modulus and Poisson ratio of the rigid body, R and R_0 are the radius of the crack and the radius of a circle that bounds the liquid on the crack surface, $\mu_0 = (R_0/R)^2$ is the equilibrium concentration of the liquid in the crack, $\beta = 3\mu_0\eta R_0^2/H^3$, $g = 324\alpha\mu_0 R_0^2 F_2(\theta)/35H^5$, $\gamma = 18\mu_0\eta R_0^2/H^4$, $q = -81\alpha\mu_0 R_0^3 F_3(\theta)/8H^7$, $\delta = 72\mu_0\eta R_0^2/H^5$, H and $2d$ are the equilibrium (at $\sigma = 0$) distance between the crack surfaces and the change in this distance under the action of stress $\sigma \neq 0$ ($H \gg 2d$), α and η are the surface tension coefficient and the dynamic viscosity of the liquid, θ is the equilibrium wetting (or contact) angle, and $F_{1,2,3}(\theta)$ are functions of the contact angle.

Equation (1) was derived under the assumption that the crack surfaces outside the liquid are dry and the line of three-phase (rigid body, liquid, and gas) contact does not slide along these surfaces when the crack deformation is relatively small (due to adhesion, i.e., attachment of the viscous liquid to the rigid body). However, another situation is possible and more likely to occur in the system under consideration: the crack surfaces may be covered with a thin film of the same liquid wetting these surfaces. In this case, the line of the three-phase contact may slide over this film. In such a crack, a meniscus of the viscous liquid will behave like a meniscus of a perfect liquid (in the sense that the contact angle will be constant); however, the viscous liquid will resist the dynamic deformation of the crack. If $R_0 \gg H$ everywhere except for the region near the meniscus, the flow of the liquid in the crack will be close to the Poiseuille flow. Therefore, such a crack will exhibit a dissipation nonlinearity similar to the one described above, but its elastic nonlinearity will correspond to elasticity of a crack partially filled with a perfect liquid. Thus, the crack with the liquid film will also be described by equation of state (1), in which the elastic coefficients K_0, g, and q are defined as those for the perfect liquid [4] and the inelastic coefficients β, γ, and δ correspond to the viscous liquid:

$$K_0 = K - 8\alpha\mu_0\cos\theta/H^2,$$

$$g = -24\alpha\mu_0\cos\theta/H^3, \quad q = 64\alpha\mu_0\cos\theta/H^4,$$

$$\beta = 3\mu_0\eta R_0^2/H^3,$$

$$\gamma = 30\mu_0\eta R_0^2/H^4, \quad \delta = 180\mu_0\eta R_0^2/H^5,$$

1063-7710/03/4905-0565$24.00 © 2003 MAIK "Nauka/Interperiodica"

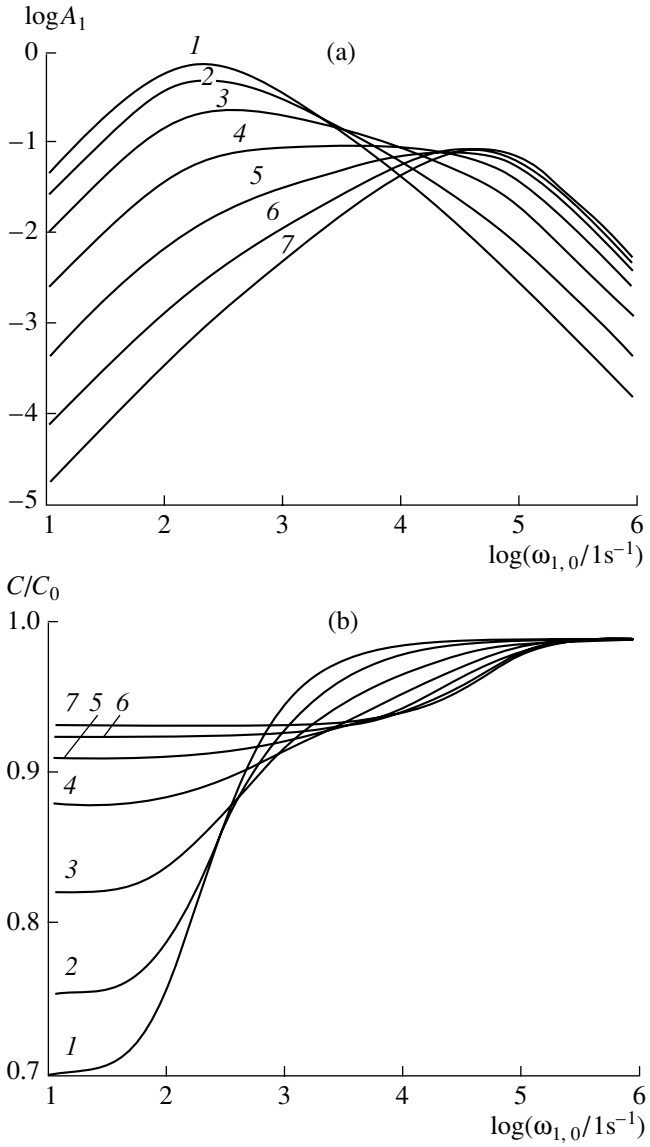

Fig. 1. (a) Linear damping decrement A_1 and (b) the relative velocity $C/C_0 = 1 - B_1$ of the pumping wave versus frequency. The numbers near the curves indicate the values of the power n in distribution function (21).

where $K_0 > 0$ when $18\alpha\mu_0\cos\theta/KD^2 < 1$, R_0 is the radius of a circle that bounds the liquid on the crack surface at $\sigma = 0$, and D is the distance between surfaces of the crack without the liquid.

As follows from Eq. (1), the acoustic nonlinearity of such cracks contains two components: elastic (or reactive) and inelastic (or dissipative), each of these components containing terms that are quadratic and cubic in d. Elastic nonlinearity is associated with the capillary pressure in the liquid; inelastic nonlinearity, with viscous pressure. It is quite natural that the rigid body with such cracks will also exhibit reactive and dissipative quadratic and cubic nonlinearity. The propagation and interaction of acoustic waves in such a medium will be accompanied by a variety of nonlinear effects. In particular, quadratic nonlinearity will produce waves at combination frequencies (the second harmonic and sum and difference frequencies) and self-rectification of the high-frequency pulses. Cubic nonlinearity will produce the third harmonic, self-action, attenuation or amplification of sound by sound, etc. In general, the latter effects may be caused not only by cubic but also by quadratic nonlinearity, because, qualitatively, third-order processes on quadratic nonlinearity may yield the same result as second-order processes on cubic nonlinearity [5, 6]. In both these processes, the amplitude behavior of the nonlinear effects is the same, but their dependences on the distance x are different. For example, the amplitude of the third harmonic generated in the medium due to cubic nonlinearity is proportional to x, while that due to quadratic nonlinearity is proportional to x^2 (because it occurs through the second harmonic) [5, 6]. It is clear that, at relatively small distances, the third harmonic will be caused mainly by cubic nonlinearity rather than by quadratic nonlinearity. Similar effects will also be observed in other nonlinear processes. The consideration of the combined effect of the quadratic and cubic nonlinearity of the medium on acoustic wave interaction and self-action processes is not so much a complex as a laborious problem; therefore, in this paper, we will limit our study to processes that are associated with cubic (reactive and dissipative) nonlinearity alone and manifest themselves at relatively short distances, where the effect of quadratic nonlinearity can be neglected. We will address the self-action of a harmonic wave, the generation of its third harmonic, and the effect of an intense low-frequency pumping wave on the propagation of a weak high-frequency wave in a medium with cracks partially filled with an incompressible viscous liquid. But, first, we will derive the equation of state for a rigid body containing a great number of such cracks.

2. EQUATION OF STATE FOR A ROD WITH A GREAT NUMBER OF CRACKS

The simplest equation of state to derive is the one for a rod with cracks oriented parallel to the rod axis and uniformly distributed throughout its volume. We assume that the concentration of cracks is sufficiently low, i.e., the distance between the cracks is much longer than their radii, so that interaction between the cracks can be ignored [7]. (We also assume that the radii of the cracks are much smaller than the cross-sectional size of the rod.) Of course, to describe the cracks in real rigid bodies, one should allow for their orientation in space and the distribution in various parameters (radii R and R_0, surface concentration μ_0 of the liquid, etc.). To simplify our calculations when deriving qualitative results, it is sufficient to address the simplest case of a rod with cracks that are uniformly distributed in it, oriented parallel to its axis, and have an identical volume liquid content. The longitudinal strain ε of such a rod under

the action of the longitudinal stress σ is described by the equations

$$\varepsilon(\sigma) = (1-b)\varepsilon_0 + \int_0^\infty V(\sigma)N(R)dR, \tag{2}$$

$$\sigma(V) = \frac{K_0}{2\pi R^2}V + \frac{\beta}{2\pi R^2}\dot{V} - \frac{q}{(2\pi R^2)^3}V^3 + \frac{\delta}{(2\pi R^2)^3}V^2\dot{V}, \tag{3}$$

where $\varepsilon_0 = \sigma/E$ is the strain of a crack-free rod, $N = N(R)$ is the crack distribution in radius, $b = \int_0^\infty V_0 N(R)dR$ is the volume crack concentration, $V_0 = \pi R^2 H$ is the equilibrium (at $\sigma = 0$) volume of a crack, and $V(\sigma) = 2\pi R^2 d$ is the crack volume as a function of stress $\sigma \neq 0$.

We solve Eq. (3) by the perturbation method, i.e., by assuming that $V(t) = V_1(t) + V_2(t)$, where $|V_2(t)| \ll |V_1(t)|$. As a result, we obtain

$$V_1(t) = \frac{2\pi R^2}{\beta}\int_{-\infty}^t \sigma(t')\exp[-\Omega(t-t')]dt',$$
$$\dot{V}_1(t) = \frac{2\pi R^2}{\beta}\left[\sigma(t) - \Omega\int_{-\infty}^t \sigma(t')\exp[-\Omega(t-t')]dt'\right], \tag{4}$$

$$V_2(t) = \frac{1}{\beta(2\pi R^2)^2} \times \int_{-\infty}^t [qV_1^3(t') - \delta\dot{V}_1(t')V_1^2(t')]\exp[-\Omega(t-t')]dt', \tag{5}$$

where $\Omega = K_0/\beta$ is the crack's relaxation frequency. By substituting these expressions for $V_1(t)$ and $V_2(t)$ into Eq. (2), we obtain (in the linear approximation in $N(R)$, i.e., at a low crack concentration, when $b \ll 1$, $\int_0^\infty N(R)V(\sigma)dR \ll 1$, and $2\pi E\int_0^\infty \frac{R^2 N(R)}{\beta}dR \ll 1$) the nonlinear equation of state for a rod with cracks partially filled with a viscous liquid:

$$\sigma(\varepsilon) = E\left[\varepsilon - 2\pi E\int_0^\infty \frac{R^2 N(R)}{\beta}D[\varepsilon(t)]dR\right] - 2\pi E^4\int_0^\infty \frac{R^2 N(R)}{\beta^4}\int_{-\infty}^t [(q+\delta\Omega)D^3[\varepsilon(t')] - \delta D^2[\varepsilon(t')]\varepsilon(t')]\exp[-\Omega(t-t')]dt'dR, \tag{6}$$

where $D[\varepsilon(t)] = \int_{-\infty}^t \varepsilon(t')\exp[-\Omega(t-t')]dt'$.

This is a relaxation equation. It contains one linear and two nonlinear (cubic with respect to the strain) relaxation terms. The linear and nonlinear relaxation of such a cracked medium is caused by the viscosity of the liquid in the cracks, the nonlinear relaxation manifesting itself twice: first, due to the linear relaxation, because nonlinear correction term (5) is determined by linear response (4) and, second, through the relaxation of nonlinear correction term (5) itself. A similar relaxation equation of state was obtained in [8] in terms of a one-dimensional rheological model of a microinhomogeneous medium consisting of a chain of linear elastic and inelastic (quadratic with respect to the strain) viscoelastic elements. In the low-frequency approximation, i.e., when $\omega \ll \Omega$ (ω is the frequency of the acoustic wave), Eq. (6) is reduced to the simpler form

$$\sigma(\varepsilon) = E\left(1 - 2\pi E\int_0^\infty \frac{R^2 N(R)}{K_0}dR\right)\varepsilon + 2\pi E^2\dot{\varepsilon}\int_0^\infty \frac{R^2 N(R)}{K_0\Omega}dR - 2\pi E^4\varepsilon^3\int_0^\infty \frac{qR^2 N(R)}{K_0^4}dR + 2\pi E^4\varepsilon^2\dot{\varepsilon}\int_0^\infty\left(\delta + \frac{6q}{\Omega}\right)\frac{R^2 N(R)}{K_0^4}dR.$$

As can be seen from this equation, a microinhomogeneous medium that contains not only the cracks considered here, but also any other defects characterized by linear absorption (or relaxation) and cubic (or other odd) reactive nonlinearity must also exhibit dissipative nonlinearity; i.e., an odd reactive nonlinearity of relaxation defects causes the medium to exhibit dissipation nonlinearity. (This statement does not refer to media with defects that possess an even reactive nonlinearity alone).

Equation of state (6) with the equation of motion $\rho U_{tt} = \sigma_x(\varepsilon, \dot{\varepsilon})$ (ρ is the density of the medium, U is the longitudinal displacement, and $\varepsilon = U_x$) and the boundary conditions define the nonlinear wave processes that occur when longitudinal elastic waves propagate and interact in such a rod. Investigations of these processes may be used in the diagnostics of the medium, i.e., to determine its parameters (concentration of the cracks, their radii, volume concentration of the liquid in the cracks, etc.). When describing the wave processes in this rod, we will assume that the nonlinearity of equation of state (6) is stronger than the geometric nonlinearity of the equation of motion and, also, that the approximation of microinhomogeneous medium [9] holds; i.e., there are many cracks per wavelength, their width H is much smaller than the wavelength, and they are uniformly distributed throughout the rod.

3. NONLINEAR PROPAGATION AND INTERACTION OF ELASTIC WAVES IN A CRACKED ROD

In this section, we study the effects of self-action and interaction of an intense low-frequency pumping wave of frequency $\omega_{1,0}$ and a weak high-frequency wave of frequency $\omega_{0,1}$ in the rod described by equation of state (6). We impose the boundary condition

$$\varepsilon(x = 0, t) = \epsilon_0 \sin\omega_{1,0} t + \varepsilon_0 \sin\omega_{0,1} t, \tag{7}$$

where $\epsilon_0 \gg \varepsilon_0$, $\omega_{1,0}/\omega_{0,1} \neq m/n$, and m and n are integers. When these conditions are satisfied, frequencies of higher order harmonics of the intense wave do not coincide with the frequency of the weak wave and the weak wave will not affect the intense wave, but the propagation velocity and attenuation of the weak wave depend on the amplitude of the intense wave. The substitution of Eq. (6) into the equation of motion yields the nonlinear wave equation for the strain:

$$\begin{aligned}\frac{\partial^2\varepsilon}{\partial t^2} - C_0^2\frac{\partial^2\varepsilon}{\partial x^2} &= -2\pi C_0^2 E\frac{\partial^2}{\partial x^2}\int_0^\infty \frac{R^2 N(R)}{\beta} D[\varepsilon(t)]\,dR \\ &- 2\pi C_0^2 E^3\frac{\partial^2}{\partial x^2}\int_0^\infty \frac{R^2 N(R)}{\beta^4}\int_{-\infty}^{t}[(q+\delta\Omega)D^3[\varepsilon(t')] \\ &- \delta D^2[\varepsilon(t')]\varepsilon(t')]\exp[-\Omega(t-t')]\,dt'\,dR,\end{aligned} \tag{8}$$

where $C_0^2 = E/\rho$. We search for a solution to this equation by the perturbation method assuming that

$$\begin{aligned}\varepsilon(x, t) &= \sum_{n,m}\hat{\varepsilon}_{n,m}(x, t) \\ &= \sum_n\sum_m \varepsilon_{n,m}(x)\sin[\omega_{n,m}t - k_{n,m}x - \varphi_{n,m}(x)],\end{aligned} \tag{9}$$

where $\omega_{n,m} = |n\Omega \pm m\omega|$, $k_{n,m} = \omega_{n,m}/C_0$, $\left|\sum_{n,m}\hat{\varepsilon}_{n\neq 1, m\neq 0}(x, t)\right| \ll |\hat{\varepsilon}_{1,0}(x, t)|$, and $\varepsilon_{n,m}(x)$ and $\varphi_{n,m}(x)$ are slowly varying functions of the x coordinate. Substituting Eq. (9) into Eq. (8) and collecting respective harmonic components on its right side, we obtain equations that describe the propagation of the intense pumping wave, the generation of its third harmonic, and the propagation of the weak wave in the presence of the intense wave:

$$\begin{aligned}\frac{d\varepsilon_{1,0}}{dx} &= -A_1\varepsilon_{1,0}k_{1,0}\left(1 + \frac{A_{1,0}\varepsilon_{1,0}^2}{4A_1}\right), \\ \frac{d\varphi_{1,0}}{dx} &= -B_1 k_{1,0}\left(1 + \frac{B_{1,0}\varepsilon_{1,0}^2}{4B_1}\right),\end{aligned} \tag{10}$$

$$\begin{aligned}\frac{d\varepsilon_{3,0}}{dx} &= -k_{3,0}\left(A_3\varepsilon_{3,0}\right. \\ &\left. - \frac{\sqrt{A_{3,0}^2 + B_{3,0}^2}}{4}\varepsilon_{1,0}^3\cos\left(3\varphi_{1,0} - \varphi_{3,0} + \arctan\frac{B_{3,0}}{A_{3,0}}\right)\right),\end{aligned} \tag{11}$$

$$\begin{aligned}\varepsilon_{3,0}\frac{d\varphi_{3,0}}{dx} &= -k_{3,0}\left(B_3\varepsilon_{3,0}\right. \\ &\left. - \frac{\sqrt{A_{3,0}^2 + B_{3,0}^2}}{4}\varepsilon_{1,0}^3\sin\left(3\varphi_{1,0} - \varphi_{3,0} + \arctan\frac{B_{3,0}}{A_{3,0}}\right)\right),\end{aligned} \tag{12}$$

$$\begin{aligned}\frac{d\varepsilon_{0,1}}{dx} &= -C_1\varepsilon_{0,1}k_{0,1}\left(1 + \frac{A_{0,1}\varepsilon_{1,0}^2}{4C_1}\right), \\ \frac{d\varphi_{0,1}}{dx} &= -D_1 k_{0,1}\left(1 + \frac{B_{0,1}\varepsilon_{1,0}^2}{4D_1}\right),\end{aligned} \tag{13}$$

where the linear and nonlinear coefficients A_1, B_1, C_1, D_1, A_3, B_3, $A_{n,m}$, and $B_{n,m}$ are defined by the expressions

$$A_1 = \pi E\int_0^\infty \frac{R^2 N(R)}{\beta}\frac{\omega_{1,0}}{\omega_{1,0}^2 + \Omega^2}dR, \quad B_1 = \pi E\int_0^\infty \frac{R^2 N(R)}{\beta}\frac{\Omega}{\omega_{1,0}^2 + \Omega^2}dR,$$

$$C_1 = \pi E\int_0^\infty \frac{R^2 N(R)}{\beta}\frac{\omega_{0,1}}{\omega_{0,1}^2 + \Omega^2}dR, \quad D_1 = \pi E\int_0^\infty \frac{R^2 N(R)}{\beta}\frac{\Omega}{\omega_{0,1}^2 + \Omega^2}dR,$$

$$A_3 = \pi E\int_0^\infty \frac{R^2 N(R)}{\beta}\frac{\omega_{3,0}}{\omega_{3,0}^2 + \Omega^2}dR, \quad B_3 = \pi E\int_0^\infty \frac{R^2 N(R)}{\beta}\frac{\Omega}{\omega_{3,0}^2 + \Omega^2}dR,$$

$$A_{1,0} = \pi E^3\int_0^\infty \frac{R^2 N(R)}{\beta^4}\frac{\omega_{1,0}[6q\Omega + \delta(\Omega^2 - \omega_{1,0}^2)]}{(\omega_{1,0}^2 + \Omega^2)^3}dR,$$

$$B_{1,0} = \pi E^3 \int_0^\infty \frac{R^2 N(R)}{\beta^4} \frac{[3q(\Omega^2 - \omega_{1,0}^2) - 2\delta\omega_{1,0}^2\Omega]}{(\omega_{1,0}^2 + \Omega^2)^3} dR, \tag{14}$$

$$A_{3,0} = \pi E^3 \int_0^\infty \frac{R^2 N(R)}{\beta^4} \frac{\omega_{3,0}\left[2q\Omega(3\Omega^2 - 5\omega_{1,0}^2) + \delta(\Omega^4 + 3\omega_{1,0}^4 - 12\omega_{1,0}^2\Omega^2)\right]}{(9\omega_{1,0}^2 + \Omega^2)(\omega_{1,0}^2 + \Omega^2)^3} dR,$$

$$B_{3,0} = \pi E^3 \int_0^\infty \frac{R^2 N(R)}{\beta^4} \frac{\left[q(\Omega^4 + 3\omega_{1,0}^4 - 12\omega_{1,0}^2\Omega^2) - 2\delta\omega_{1,0}^2\Omega(3\Omega^2 - 5\omega_{1,0}^2)\right]}{(9\omega_{1,0}^2 + \Omega^2)(\omega_{1,0}^2 + \Omega^2)^3} dR,$$

$$A_{0,1} = \pi E^3 \int_0^\infty \frac{R^2 N(R)}{\beta^4} \frac{\omega_{0,1}[6q\Omega + \delta(\Omega^2 - \omega_{0,1}^2)]}{(\omega_{1,0}^2 + \Omega^2)(\omega_{0,1}^2 + \Omega^2)^2} dR,$$

$$B_{0,1} = \pi E^3 \int_0^\infty \frac{R^2 N(R)}{\beta^4} \frac{[3q(\Omega^2 - \omega_{0,1}^2) - 2\delta\Omega\omega_{0,1}^2]}{(\omega_{1,0}^2 + \Omega^2)(\omega_{0,1}^2 + \Omega^2)^2} dR.$$

Solutions to Eqs. (10)–(13) under boundary conditions (7) with $(A_3 - A_1)k_{3,0}x \ll 1$ and $B_3 k_{3,0} x \ll 1$ have the form

$$\varepsilon_{1,0}(x) = \frac{\epsilon_0 \exp(-A_1 k_{1,0} x)}{\sqrt{1 + \frac{A_{1,0}}{4A_1}\epsilon_0^2[1 - \exp(-2A_1 k_{1,0} x)]}},$$
$$\varphi_{1,0}(x) = B_1 k_{1,0} x + \frac{B_{1,0}}{2A_{1,0}} \ln\left(1 + \frac{A_{1,0}}{4A_1}\epsilon_0^2[1 - \exp(-2A_1 k_{1,0} x)]\right), \tag{15}$$

$$\varepsilon_{3,0}(x) = \sqrt{A_{3,0}^2 + B_{3,0}^2}\frac{\epsilon_0^3 k_{3,0} x}{4},$$
$$\varphi_{3,0}(x) - 3\varphi_{1,0}(x) = -B_3 k_{3,0} x + \arctan\left(\frac{B_{3,0}}{A_{3,0}}\right) \ll \pi, \tag{16}$$

$$\varepsilon_{0,1}(x) = \frac{\varepsilon_0 \exp(-C_1 k_{0,1} x)}{\left(1 + \frac{A_{1,0}}{4A_1}\epsilon_0^2[1 - \exp(-2A_1 k_{1,0} x)]\right)^{\frac{A_{0,1}\omega_{0,1}}{2A_{1,0}\omega_{1,0}}}},$$
$$\varphi_{0,1}(x) = D_1 k_{0,1} x + \frac{2\omega_{0,1} D_1}{\omega_{1,0} A_{1,0}} \ln\left(1 + \frac{A_{1,0}}{4A_1}\epsilon_0^2[1 - \exp(-2A_1 k_{1,0} x)]\right). \tag{17}$$

4. ANALYSIS OF THE WAVE PROCESSES IN A ROD WITH IDENTICAL CRACKS

Let us analyze the solutions obtained above and underline the characteristic distinctions between the propagation of the intense and weak waves in the rod with cracks of the same radius $R = R_m$: $N(R) = N_0\delta(R - R_m)$, where $N_0 = b/\pi H R_m^2$. From expressions (15), we obtain the linear δ_{lin} and nonlinear $\delta_{\text{non}}(\varepsilon_{1,0})$ damping decrements, the relative velocity change $\Delta C(\varepsilon_{1,0})/C_0$ for the low-frequency wave, and the ratio of the nonlinear damping decrement to the relative velocity change:

$$\delta_{\text{lin}} = A_1, \quad \delta_{\text{non}}(\varepsilon_{1,0}) = A_{1,0}\varepsilon_{1,0}^2,$$
$$\frac{\Delta C(\varepsilon_{1,0})}{C_0} = B_{1,0}\varepsilon_{1,0}^2, \quad r_{1,0} = \frac{A_{1,0}}{B_{1,0}}, \tag{18}$$

where $\Delta C(\varepsilon_{1,0}) = C_0 - C_{1,0}(\varepsilon_{1,0})$ and $C_{1,0}(\varepsilon_{1,0})$ is the propagation velocity of the pumping wave.

As can be seen from these equations, when the pumping wave amplitude increases, the parameters $\delta_{\text{non}}(\varepsilon_{1,0})$ and $\Delta C(\varepsilon_{1,0})/C_0$ grow, their ratio $r_{1,0}$ remaining constant independently of $\varepsilon_{1,0}$. It is of interest to consider more closely the amplitude $\varepsilon_{1,0}$ (or of the nonlinear damping decrement) and propagation velocity of the intense pumping wave as functions of its initial amplitude ϵ_0. The effects of the elastic and inelastic nonlinearities should be studied separately, because the mechanisms of these nonlinearities are different. As follows from expressions (15), when $q \neq 0$ and $\delta = 0$, the sign of the nonlinear damping decrement is determined by the sign of the coefficient $A_{1,0}$, which in turn coincides with the sign of the parameter q. Thus, when $A_{1,0} > 0$, a nonlinear limitation of the wave amplitude will take place, while when $A_{1,0} < 0$, a self-clarification of the medium will be observed. In this case, the propagation velocity will also change, decreasing with an increase in the wave amplitude in the low-frequency range and increasing while tending to C_0 in the high-frequency range, as follows from expressions (14) for

$B_{1,0}$. In another limiting case (at $q = 0$ and $\delta > 0$), a limitation of the amplitude will take place at low frequencies ($\omega_{1,0} < \Omega_m = \Omega(R_m)$), and a self-clarification of the medium, at high frequencies ($\omega_{1,0} > \Omega_m$).

At small distances from the source, the third harmonic is synchronous with the pumping wave and is therefore generated as in a cubic dispersion-free medium: its amplitude grows in proportion with ϵ_0^3 and the distance x, the effective parameter of the cubic nonlinearity being determined by the expression

$$\sqrt{A_{3,0}^2 + B_{3,0}^2} = \frac{E^3 b}{H\beta^4}\left[\frac{q^2 + \delta^2\omega_{1,0}^2}{(\omega_{3,0}^2 + \Omega_m^2)(\omega_{1,0}^2 + \Omega_m^2)^3}\right]^{1/2}. \quad (19)$$

This expression gives the following low-frequency and high-frequency asymptotics: $\sqrt{A_{3,0}^2 + B_{3,0}^2} \cong \frac{qE^3 b}{HK^4} = \text{const}$ and $\sqrt{A_{3,0}^2 + B_{3,0}^2} \cong \frac{\delta E^3 b}{3H\beta^4\omega_{0,1}^3} \sim \omega_{1,0}^{-3}$.

Expressions (17) yield the damping decrement $\delta_{0,1}(\varepsilon_{1,0})$ and the relative velocity change $\Delta C(\varepsilon_{1,0})/C_0$ for the weak wave in the presence of the intense pumping wave and also their ratio $r_{0,1}$:

$$\delta_{0,1}(\varepsilon_{1,0}) = 2A_{0,1}\varepsilon_{1,0}^2,$$
$$\frac{\Delta C(\varepsilon_{0,1})}{C_0} = 2B_{0,1}\varepsilon_{1,0}^2, \quad r_{0,1} = \frac{A_{0,1}}{B_{0,1}}. \quad (20)$$

Here, as in Eq. (18), when the pumping wave amplitude increases, the parameters $\delta_{0,1}(\varepsilon_{1,0})$ and $\Delta C(\varepsilon_{0,1})/C_0$ vary in such a manner that their ratio $r_{0,1}$ remains constant but different from $r_{0,1}$. As follows from expressions (17), depending on the signs of the coefficients $A_{1,0}$ and $A_{0,1}$, either attenuation or amplification of sound by sound can be observed. When $A_{1,0} > 0$ and $A_{0,1} > 1$ or $A_{1,0} < 0$ and $A_{0,1} > 0$, the attenuation of sound by sound takes place, while when $A_{1,0} < 0$ and $A_{0,1} < 0$ or $A_{1,0} > 0$ and $A_{0,1} < 0$, an amplification of sound by sound takes place.

5. ANALYSIS OF THE WAVE PROCESSES IN A ROD WITH CRACKS DISTRIBUTED IN RADIUS

Let us now analyze the nonlinear wave processes in a rod with cracks distributed in radius. We describe this distribution by a power function with various integer powers n ($1 \le n \le 7$):

$$N(R) = N_0 R^{-n}, \quad R_1 \le R \le R_2, \quad (21)$$

where $N_0 = b/\pi H \int_{R_1}^{R_2} R^{2-n}\,dR$.

Figures 1a and 1b show examples of the behavior of the linear damping decrement A_1 and the relative velocity $C/C_0 = 1 - B_1$ of the pumping wave versus $\omega_{1,0}$, which were plotted for the above distribution function for $1 \le n \le 7$ with the following parameters of the cracks: $b = 10^{-4}$, $R_1 = 5.5 \times 10^{-2}$ cm, $R_2 = 5.5 \times 10^{-1}$ cm, $\Omega_1(R_1) \cong 10^5$ s^{-1}, $\Omega_2(R_2) \cong 10^2$ s^{-1}, $H = 10^{-4}$ cm, $\mu_0 = 1/2$, $E = 10^{11}$ g/cm s^2, and $\nu = 1/4$. All calculations presented here refer to cracks partially filled with water and the cracks' surfaces covered with a thin film. For such cracks, $R \ll 3\pi EH^2/64(1-\nu^2)\alpha\mu_0\cos\theta$ and their relaxation frequencies are determined by the expression

$$\Omega(R) \cong \theta[\pi EH^3/8(1-\nu^2)\eta\mu_0^2 R^3] \sim R^{-3}. \quad (22)$$

As can be seen from Fig. 1a, in the class of power functions (21), it is only at $n = 4$ that the damping decrement is almost independent of frequency in the range $\Omega_2(R_2) \le \omega_{1,0} \le \Omega_1(R_1)$. Many rocks and metals feature this property [10, 11]. At other values of the power n, the damping decrement at first goes up with frequency and then goes down, so that, at $n \ne 4$, there is no frequency range in which the damping decrement is independent of frequency. It can be seen from Fig. 1b that, when the crack distribution in radius is described by the power functions with $1 \le n \le 7$, the behavior of the velocity of the low-frequency wave is qualitatively the same; i.e., it monotonically increases with frequency $\omega_{1,0}$ tending to C_0. Formula (14) yields the expressions for the coefficients A_1 and B_1 at $n = 4$:

$$A_1 = \frac{8(1-\nu^2)bR_1R_2}{9\pi H(R_2 - R_1)}\arctan\left(\frac{\omega_{1,0}(\Omega_1 - \Omega_2)}{\omega_{1,0}^2 + \Omega_1\Omega_2}\right),$$
$$B_1 = \frac{4(1-\nu^2)bR_1R_2}{9\pi H(R_2 - R_1)}\ln\left(\frac{\omega_{1,0}^2 + \Omega_1^2}{\omega_{1,0}^2 + \Omega_2^2}\right). \quad (23)$$

(Similar expressions also determine the coefficients C_1, D_1, A_3, and B_3.) Note that, in the frequency range $\Omega_2 \le \omega_{1,0} \le \Omega_1$, the linear damping decrement A_1 is independent of $\omega_{1,0}$ and of viscosity of the liquid in the crack, being only determined by the concentration b and the dimensions H, R_1, and R_2 of the cracks:

$$A_1 \cong \frac{4(1-\nu^2)bR_1R_2}{9H(R_2 - R_1)}. \quad (24)$$

The viscosity of the liquid determines the frequency range in which the linear damping decrement is given by expression (24) [12].

Expressions for the nonlinear coefficients $A_{n,m}$ and $B_{n,m}$ are much more complex. Therefore, we only provide here examples of their behavior with frequency $\omega_{1,0}$ or $\omega_{0,1}$ (at $\omega_{1,0} = 10^3$ s^{-1}) with particular values of n (Fig. 2) with the same parameters of the crack distribution in radius and give their low-frequency asymptotics

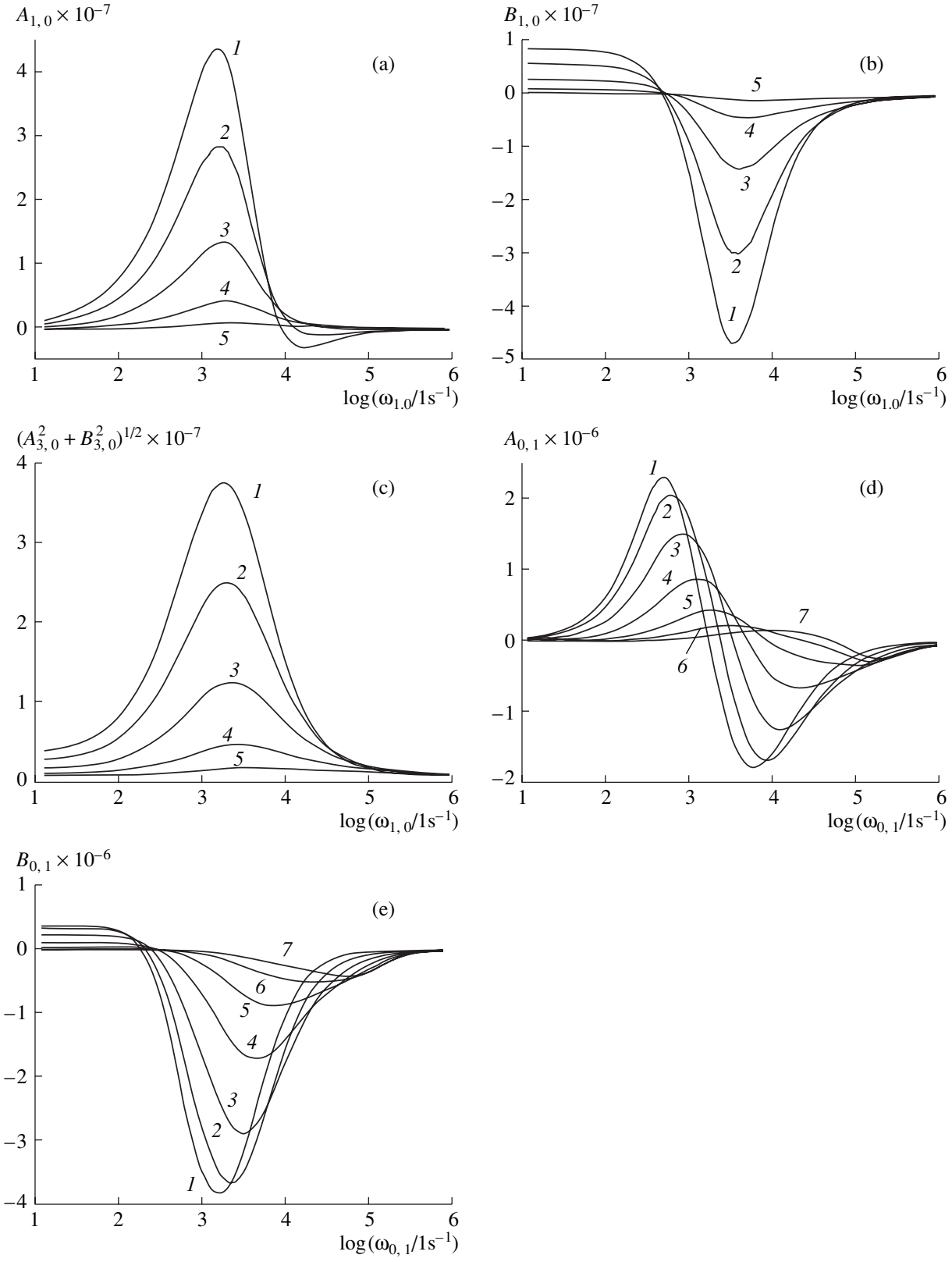

Fig. 2. Coefficients (a) $A_{1,0}$, (b) $B_{1,0}$, (c) $(A_3^2 + B_3^2)^{1/2}$, (d) $A_{0,1}$, and (e) $B_{0,1}$ versus frequency. The numbers near the curves indicate the values of the power n in distribution function (21).

(for $\omega_{1,0} \ll \Omega_2$, $\omega_{0,1} \ll \Omega_2$, and $\omega_{1,0} \ll |q/\delta|$) at $n = 4$:

$$A_{1,0} = \frac{2^{21}(1-\nu^2)^4\alpha b\eta\mu_0^2\cos\theta R_1R_2\omega_{1,0}}{81\pi^4EH^6(R_2-R_1)} \times\left[\frac{(1-\nu^2)\mu_0(R_2^6-R_1^6)}{\pi EH^2}+\frac{9(R_2^5-R_1^5)}{2^7\alpha\cos\theta}\right],$$

$$B_{1,0} = \frac{2^{18}(1-\nu^2)^4\alpha b\eta\mu_0\cos\theta R_1R_2(R_2^3-R_1^3)}{81\pi^4EH^5(R_2-R_1)} \gg A_{1,0},$$

$$\sqrt{A_{3,0}^2+B_{3,0}^2} = \frac{2^{16}(1-\nu^2)^4\alpha b\eta\mu_0\cos\theta R_1R_2(R_2^3-R_1^3)}{243\pi^4EH^5(R_2-R_1)}, \quad (25)$$

$$A_{0,1} = \frac{2^{22}(1-\nu^2)^4\alpha b\eta\mu_0^2\cos\theta R_1R_2\omega_{1,0}}{81\pi^4EH^6(R_2-R_1)} \times\left[\frac{(1-\nu^2)\mu_0(R_2^6-R_1^6)}{\pi EH^2}+\frac{9(R_2^6-R_1^6)}{2^7\alpha\cos\theta}\right],$$

$$B_{0,1} = \frac{2^{19}(1-\nu^2)^4\alpha b\eta\mu_0\cos\theta R_1R_2(R_2^3-R_1^3)}{81\pi^4EH^5(R_2-R_1)} \gg A_{0,1}.$$

As follows from these expressions, in the low-frequency range, the effects associated with the variation of the propagation velocity due to the reactive nonlinearity of the cracks manifest themselves more strongly than the effects associated with the variation of the damping decrement due to the cracks' dissipation nonlinearity. This, however, is natural, because the dissipation nonlinearity depends on $\dot{d}$, while the reactive nonlinearity does not.

As can be seen from Fig. 2, at different n, pairs of coefficients $A_{1,0}$, $A_{0,1}$ and $B_{1,0}$, $B_{0,1}$ show a similar behavior with increasing frequency. At first, the coefficients $A_{1,0}$, $A_{0,1}$ are positive, increase, and reach maximal values; subsequently, they decrease, change their sign, reach minimal values, and then tend to zero. The coefficients $B_{1,0}$, $B_{0,1}$ are initially positive, then they decrease, change their sign, reach minimal values, and finally tend to zero. The effective parameter of cubic nonlinearity, $(A_{3,0}^2 + B_{3,0}^2)^{1/2}$, at first grows with frequency and then also goes down by asymptotically tending to zero. The linear and nonlinear coefficients A_1, B_1, C_1, D_1, A_3, B_3, $A_{n,m}$, and $B_{n,m}$ decrease in the high-frequency range ($\omega_{n,m} > \Omega_1$) because of the relaxation of cracks, which increases their rigidity at high frequencies.

6. CONCLUSION

In this paper, we derived a nonlinear (in the cubic approximation) relaxation equation of state for a rod containing a great number of cracks partially filled with a viscous liquid. This equation is solved by the perturbation method with the aim of theoretically studying the nonlinear wave processes that occur when an intense low-frequency longitudinal wave and a weak high-frequency one propagate and interact in this rod. The linear damping decrement and the velocity of the acoustic wave are determined along with the nonlinearity parameters for the effects of self-action and interaction of these waves and for the generation of the third harmonic of the low-frequency pumping wave. It is shown that, when the crack distribution in radius is described by the power function (with the power $n = -4$), rather a wide frequency range exists in which the damping decrement is actually independent of frequency. It is also shown that, unlike a medium with the same (reactive or dissipative) nonlinearity but without relaxation, in which the amplitude and phase nonlinear effects are determined by the dissipative and reactive nonlinearities separately, in a nonlinear relaxation medium the amplitude and phase effects are determined by the combined effect of the dissipative and reactive nonlinearities. Although the paper addresses the simplest example of a cracked medium, namely, a rod containing cracks oriented parallel to its axis, the nonlinear wave processes in such media are sufficiently general and should be qualitatively much the same for an infinite rigid body with cracks oriented isotropically and distributed in their width and other parameters. In these cases, the equations of state will also exhibit relaxation and contain reactive and dissipative nonlinearities. The results of the study allow us to expect that a detailed and comprehensive experimental investigation (i.e., the determination of the amplitude–frequency dependences) of various nonlinear effects observed in the course of the propagation and interaction of elastic waves in such a medium will provide the necessary information for determining its equation of state, which in its turn will provide the parameters of the cracks. The nonlinear effects described above (the self-clarification of the medium or the nonlinear limitation of the wave amplitude, the attenuation or amplification of sound by sound, and the changes in the propagation velocities of the intense and weak waves) may be observed in natural cracked and granular rocks, which is confirmed, in particular, by the results of field experiments on the self-action of seismoacoustic waves in a water-saturated ground [13].

ACKNOWLEDGMENTS

This work was supported by the Russian Foundation for Basic Research, project nos. 01-05-64417, 02-02-16237, and 02-02-08021 INNO.

REFERENCES

1. V. E. Nazarov, L. A. Ostrovsky, I. A. Soustova, and A. M. Sutin, Phys. Earth Planet. Inter. **50** (1), 65 (1988).
2. R. A. Guyer and P. A. Johnson, Phys. Today **52** (4), 30 (1999).
3. L. A. Ostrovsky and P. A. Johnson, Riv. Nuovo Cimento Soc. Ital. Fis. **24** (7), 1 (2001).
4. V. E. Nazarov, J. Acoust. Soc. Am. **109**, 2642 (2001).
5. O. V. Rudenko and S. I. Soluyan, *Theoretical Foundations of Nonlinear Acoustics* (Nauka, Moscow, 1975; Consultants Bureau, New York, 1977).
6. E. M. Ballad, B. A. Korshak, V. G. Mozhaev, and I. Yu. Solodov, Vestn. Mosk. Univ., Ser. 3: Fiz. Astron., No. 6, 44 (2001).
7. R. J. O'Connel and B. Budiansky, J. Geophys. Res. **79** (35), 5412 (1974).
8. V. E. Nazarov, V. Yu. Zaitsev, and I. Y. Belyaeva, Acust. Acta Acust. **88** (1), 40 (2002).
9. M. A. Isakovich, *General Acoustics* (Nauka, Moscow, 1973).
10. K. Aki and P. Richards, *Quantitative Seismology: Theory and Methods* (Freeman, San Francisco, 1980; Mir, Moscow, 1983).
11. *Physical Acoustics: Principles and Methods*, Ed. by W. P. Mason (Academic Press, New York, 1965; Mir, Moscow, 1968), Vol. 3, Part B.
12. V. Yu. Zaĭtsev and V. E. Nazarov, Akust. Zh. **45**, 622 (1999) [Acoust. Phys. **45**, 552 (1999)].
13. V. Yu. Zaĭtsev, V. E. Nazarov, and V. I. Talanov, Akust. Zh. **45**, 799 (1999) [Acoust. Phys. **45**, 720 (1999)].

Translated by A. Khzmalyan

Acoustical Physics, Vol. 49, No. 5, 2003, pp. 574–579. Translated from Akusticheskiĭ Zhurnal, Vol. 49, No. 5, 2003, pp. 676–682.

Distribution of Elastic and Electric Fields of a Photorefractive Grating Near the Boundaries of Crystals of 4*mm* and 6*mm* Symmetry Class

K. S. Nuyaksheva, A. M. Kirillov, and S. M. Shandarov

Tomsk State University of Control Systems and Radio Electronics, pr. Lenina 40, Tomsk, Russia

e-mail: nks@svch.rk.tusur.ru

Received July 9, 2002

Abstract—A theoretical analysis of the surface structure of a photorefractive grating is carried out. The effect of the trap saturation on the electric and elastic fields that are formed near the crystal boundary by the diffusion mechanism of charge separation is taken into account. The perturbations of the crystal permittivity tensor at the light wave frequency are analyzed. The possibility of a diffraction of light with a change of polarization in the near-boundary region is revealed. *© 2003 MAIK "Nauka/Interperiodica".*

The electric and elastic fields characterizing a photorefractive grating in an electro-optical crystal may have a complex structure near the crystal boundary [1–9]. In particular, at certain conditions, a periodic surface relief can be formed at a crystal boundary. This effect has been observed in experiments [1, 6]. The surface structure of the grating may considerably affect the interaction of light waves in a planar photorefractive waveguide and, specifically, the holographic recording process, when light strongly absorbed in the crystal is used. In photorefractive crystals, one may also observe acoustoelectric phenomena, such as the acoustic wave reflection from a holographic grating [10] and the acoustic wave generation due to the interaction of modulated light with the grating [11–13]. The near-boundary structure of elastic and electric fields of a photorefractive hologram can play an important part in the acoustoelectric phenomena involving surface acoustic waves.

Barium titanate ($BaTiO_3$) and strontium barium niobate (SBN) crystals, which are widely used in photorefractive studies, are ferroelectric crystals of the 4*mm* symmetry class. The surface structure of the photorefractive grating formed in a barium titanate crystal at steady-state conditions in the absence of trap saturation is theoretically analyzed in [9]. In the present paper, we consider the effect of the trap saturation on the electric and elastic fields of a photorefractive grating that is characterized by a vector $\mathbf{K}_g$ parallel to the z axis and formed by the diffusion mechanism in a Y-cut crystal of the 4*mm* symmetry class. Note that the elastic, piezoelectric, and dielectric properties of 6*mm* crystals have the same symmetry and, hence, the model under consideration is applicable to these crystals as well.

Consider a crystal with a mechanically free boundary at $y = 0$ (Fig. 1). In this crystal, a photorefractive grating is formed as a result of a symmetric two-beam interaction of light waves with intensities I_R and I_S. The spatial period of the grating is $\Lambda = 2\pi/|\mathbf{K}_g|$. Neglecting the self-diffraction effects, we represent the distribution of the light intensity over the crystal in the form

$$I(z) = I_0[1 + m\cos(K_g z)], \qquad (1)$$

where $I_0 = I_R + I_S$ is the average intensity, $m = 2\sqrt{I_R I_S}/I_0$ is the interference contrast, and $K_g = |\mathbf{K}_g|$. The photoexcitation of charge carriers and their diffusion transport through the crystal with a subsequent recombination give rise to a space charge field $\mathbf{E}_{sc}$. To analyze these processes, we use the single-level model of zone transfer [14] for steady-state conditions under continuous irradiation with a relatively low intensity. In this case, the concentration of charge carriers satisfies the inequality $n \ll N_A$ (where N_A is the concentration of compensating acceptor centers) and, in the adiabatic approximation, has the form

$$n = SI(N_D - N_A)\tau_R \Big/ \left(1 + \frac{1}{eN_A}\operatorname{div}\mathbf{D}\right), \qquad (2)$$

where S and N_D are the photoionization cross section

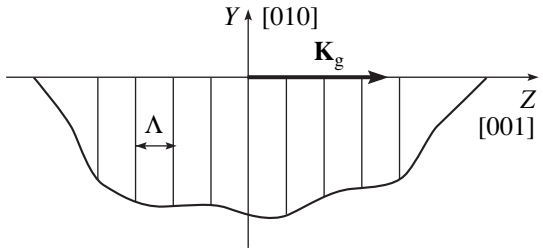

Fig. 1. Orientations of the crystal axes and the grating vector. The crystal occupies the half-space $y \le 0$.

and the concentration of donor centers in the crystal, τ_R is the recombination time of nonequilibrium charge carriers, and e is the elementary electric charge. The electric induction field **D** in a crystal without a symmetry center is determined by the sum of the electric and piezoelectric components of the polarization of the medium. To determine the two-dimensional distribution of the interrelated stationary distributions of the electric and elastic fields of the photorefractive grating, we use the continuity equation

$$\operatorname{div}[-e(\hat{\mu}\operatorname{grad}\varphi) + k_B T(\hat{\mu}\operatorname{grad} n)] = 0 \tag{3}$$

and the elastostatic equation

$$\frac{\partial T_{ij}}{\partial x_j} = 0, \tag{4}$$

where $\hat{\mu}$ is the mobility tensor of charge carriers, φ is the electric potential, k_B is the Boltzmann constant, T is the absolute temperature, and T_{ij} are the components of the elastic stress tensor. The relation between the electric and elastic fields in a piezoelectric crystal is determined by the equations of state [15]

$$T_{ij} = C^E_{ijkl}S_{kl} + e_{mij}\frac{\partial\varphi}{\partial x_m}, \tag{5}$$

$$D_n = e_{nkl}S_{kl} - \varepsilon^S_{nm}\frac{\partial\varphi}{\partial x_m}, \tag{6}$$

where C^E_{ijkl} and ε^S_{nm} are the components of the elastic modulus tensor and the dielectric permittivity tensor measured at a constant electric field and for a mechanically compressed crystal, respectively, and e_{mij} are the components of the piezoelectric constant tensor. The elastic strain tensor S_{kl} can be expressed through the components of the elastic displacement vector U_k:

$$S_{kl} = \frac{1}{2}\left(\frac{\partial U_k}{\partial x_l} + \frac{\partial U_l}{\partial x_k}\right). \tag{7}$$

The set of equations (2)–(7) determines the electric and elastic fields induced in a photorefractive crystal by its illumination. This set of equations is nonlinear. In the linear approximation with respect to the interference contrast $m \ll 1$, we can limit our consideration to analyzing only the first spatial harmonic of the photorefractive grating. Then, expression (2) for the charge carrier distribution can be represented in the form

$$n = n_0\left[1 + m\cos(K_g z) - \frac{1}{eN_A}\operatorname{div}\mathbf{D}\right], \tag{8}$$

where $n_0 = SI_0(N_D - N_A)\tau_R$ is the average concentration of nonequilibrium charge carriers.

With allowance for the crystal symmetry and the grating vector orientation, the equations for the electric potential and the components of the elastic displacement vector U_y and U_z can be derived from the set of equations (3)–(8):

$$\begin{aligned}&\frac{\partial^2\varphi}{\partial y^2} + \frac{\mu_3}{\mu_2}\frac{\partial^2\varphi}{\partial z^2} - L_{sz}^2\left\{\frac{\varepsilon_2^S}{\varepsilon_3^S}\frac{\partial^4\varphi}{\partial y^4} + \frac{\mu_3}{\mu_2}\frac{\partial^4\varphi}{\partial z^4}\right.\\ &\left.+\left(1 + \frac{\mu_3}{\mu_2}\frac{\varepsilon_2^S}{\varepsilon_3^S}\right)\frac{\partial^4\varphi}{\partial y^2\partial z^2} - \frac{e_{15}}{\varepsilon_3^S}\frac{\partial^4 U_z}{\partial y^4}\right.\\ &\left.-\frac{1}{\varepsilon_3^S}\left(e_{33} + e_{15}\frac{\mu_3}{\mu_2}\right)\frac{\partial^4 U_z}{\partial y^2\partial z^2} - \frac{e_{33}}{\varepsilon_3^S}\frac{\mu_3}{\mu_2}\frac{\partial^4 U_z}{\partial z^4}\right.\\ &\left.-\frac{(e_{15} + e_{31})}{\varepsilon_3^S}\left(\frac{\partial^4 U_y}{\partial y^3\partial z} + \frac{\mu_3}{\mu_2}\frac{\partial^4 U_y}{\partial y\partial z^3}\right)\right\}\\ &= -\frac{k_B T}{e}\frac{\mu_3}{\mu_2}mK_g^2\cos(K_g z),\end{aligned} \tag{9}$$

$$\begin{aligned}&C_{11}^E\frac{\partial^2 U_y}{\partial y^2} + C_{44}^E\frac{\partial^2 U_y}{\partial z^2} + (C_{44}^E + C_{13}^E)\frac{\partial^2 U_z}{\partial y\partial z}\\ &= -(e_{31} + e_{15})\frac{\partial^2\varphi}{\partial y\partial z},\end{aligned} \tag{10}$$

$$\begin{aligned}&(C_{44}^E + C_{13}^E)\frac{\partial^2 U_y}{\partial y\partial z} + C_{44}^E\frac{\partial^2 U_z}{\partial y^2} + C_{33}^E\frac{\partial^2 U_z}{\partial z^2}\\ &= -e_{15}\frac{\partial^2\varphi}{\partial y^2} - e_{33}\frac{\partial^2\varphi}{\partial z^2},\end{aligned} \tag{11}$$

where $L_{sz} = \sqrt{k_B T\varepsilon_3^S/e^2 N_A}$ is the Debye screening length along the polar axis of the crystal and matrix notation is used for the material tensor components.

From Eq. (9), it follows that, in the absence of trap saturation, we have $L_s = 0$, and the elastic displacements do not affect the potential distribution. For this case, the analysis of the surface structure of the photorefractive grating formed in a $BaTiO_3$ crystal was performed in [9]. To determine the distributions of the potential and the elastic displacements in the photorefractive grating for the case $L_S \neq 0$, we represent the solution to the set of equations in the form

$$\varphi(y, z) = \frac{1}{2}\left\{\varphi_0 + \sum_j \varphi_j\exp(\gamma_j K_g y)\right\}\exp(iK_g z) + \text{c.c.}, \tag{12}$$

$$U_{y,z}(y, z) = \frac{1}{2}\left\{U_{y0,z0} + \sum_j U_{yj,zj}\exp(\gamma_j K_g y)\right\}\exp(iK_g z) + \text{c.c.}, \tag{13}$$

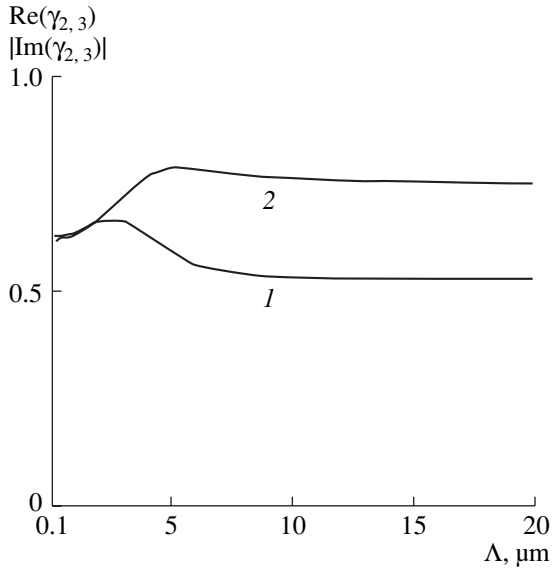

Fig. 2. Dependence of the (*1*) real and (*2*) imaginary components of the attenuation constants $\gamma_2 = \gamma_3^*$ on the spatial period of the photorefractive grating.

where φ_0, U_{y0}, and U_{z0} correspond to the bulk fields of the grating and φ_j, U_{yj}, and U_{zj} are the amplitudes of the partial components whose attenuation along the y axis is determined by the attenuation constants γ_j. Using a standard procedure, it is easy to find all four roots with positive real parts that can represent the attenuation constants. One of these roots does not depend on the external conditions of the grating formation. This root has the form

$$\gamma_1 = \sqrt{\frac{\mu_3}{\mu_2}} \tag{14}$$

and characterizes the proper solution of the electrostatic boundary-value problem in the absence of trap saturation. Two other complex-conjugate roots, γ_2 and γ_3, depend on both the material parameters of the crystal and the spatial period of the photorefractive grating. They determine the proper solution of the elastostatic boundary-value problem at $L_{sz} = 0$ (see Eqs. (10) and (11)). The fourth root is physically meaningless and should be rejected.

The bulk components of the grating fields are expressed as

$$\varphi_0 = mE_d/\left\{K_g\left[\frac{E_d}{E_{q3}}\left(1 + \frac{e_{33}^2}{C_{33}^E \varepsilon_3^S}\right) + 1\right]\right\}, \tag{15}$$

$$U_{z0} = -\frac{e_{33}}{C_{33}^E}\varphi_0, \quad U_{y0} = 0, \tag{16}$$

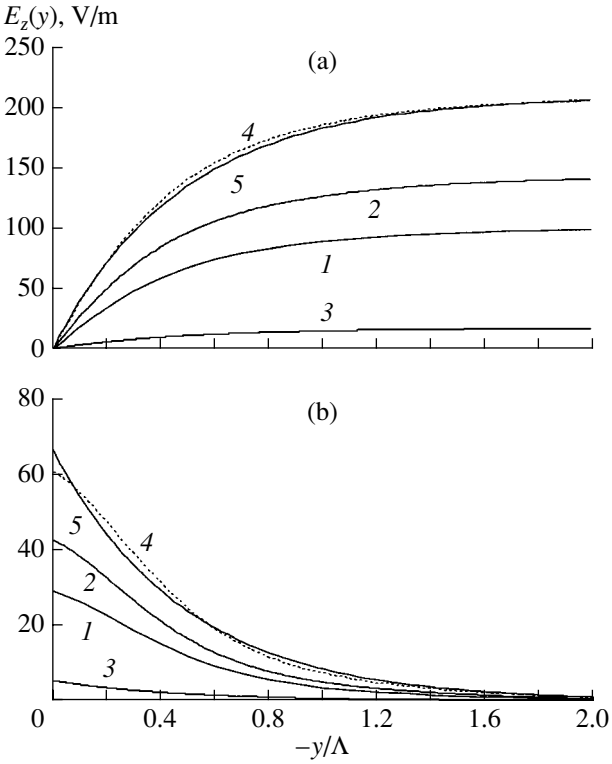

Fig. 3. Amplitude distributions $E_y(y)$ and $E_z(y)$ of the electric field components near the crystal boundary $y = 0$ for different values of the spatial period of the photorefractive grating: Λ = (*1*) 0.1, (*2*) 1, (*3*) 10, and (*4*) 0.4 μm. Curves *5* correspond to $\Lambda = 0.4$ μm in the absence of the piezoelectric effect.

where $E_d = K_g k_B T/e$ is the diffusion field and $E_{q3} = eN_A/K_g\varepsilon_3^s$ is the trap saturation field.

For the crystal under consideration with a metallized and mechanically free boundary $y = 0$, the electric and elastic fields should satisfy the boundary conditions

$$\varphi = 0 \text{ at } y = 0, \tag{17}$$

$$T_{22} = C_{11}^E\frac{\partial U_y}{\partial y} + C_{13}^E\frac{\partial U_z}{\partial z} + e_{31}\frac{\partial \varphi}{\partial z} = 0 \quad \text{at } y = 0, \tag{18}$$

$$T_{32} = C_{44}^E\frac{\partial U_y}{\partial z} + C_{44}^E\frac{\partial U_z}{\partial y} + e_{15}\frac{\partial \varphi}{\partial y} = 0 \quad \text{at } y = 0. \tag{19}$$

Applying these boundary conditions to field distributions (12) and (13) and taking into account Eqs. (14)–(16) and the roots γ_2 and γ_3 determined numerically, we determine the amplitudes of the partial components of the elastic (U_{yj} and U_{zj}) and electric (φ_j) fields of the photorefractive grating.

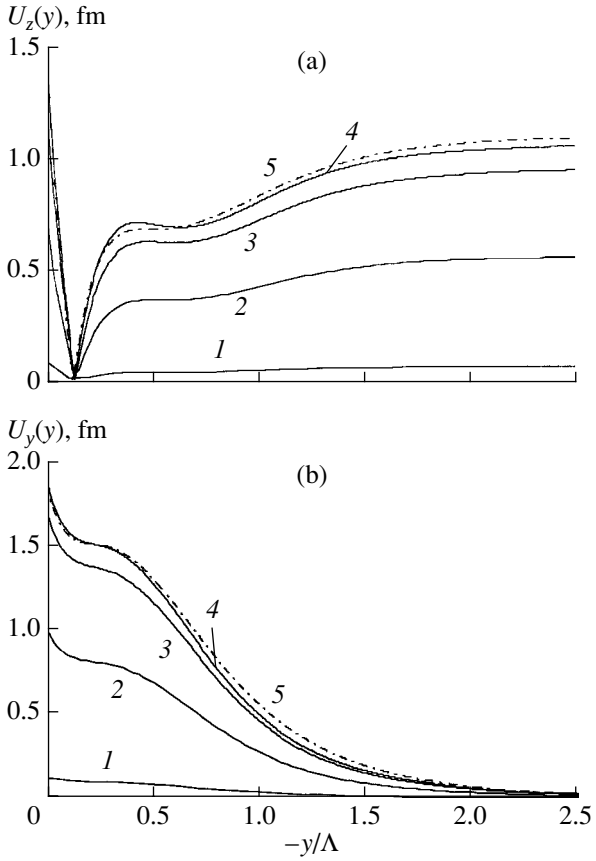

Fig. 4. Amplitudes distributions $U_y(y)$ and $U_z(y)$ of the components of the elastic displacement vector near the crystal boundary $y = 0$ for different periods of the photorefractive grating: Λ = (*1*) 0.1, (*2*) 0.4, (*3*) 1, (*4*) 2, and (*5*) 10 μm.

Because of the photoelastic and electro-optical effects, the electric and elastic fields of the photorefractive grating change the permittivity tensor [15]:

$$\Delta\varepsilon_{nm} = -\varepsilon^0_{mi}\varepsilon^0_{nj}(r^S_{ijk}E_k + p^E_{ijkl}S_{kl}), \qquad (20)$$

where ε^0_{ij} are the components of the relative permittivity tensor of the unperturbed medium at the light wave frequency, r^S_{ijk} are the electro-optical coefficients of the mechanically compressed crystal, and p^E_{ijkl} are the photoelastic constants of the electrically shortened crystal. The changes in the optical properties of the crystal near its boundary, which are fairly complicated in the case under study, may affect the interaction of light waves at the photorefractive holographic grating.

The analysis of the electric and elastic fields of the photorefractive grating and the corresponding variations of the tensor components $\Delta\varepsilon_{ij}$ at the light wave frequency was performed using Eqs. (9)–(20) by numerical methods for a barium titanate crystal. In the calculations, we used the following material parameters of the $BaTiO_3$ crystal: $\mu_3/\mu_2 = 1/9.2$ [16], $N_A = 2 \times 10^{22}$ m^{-3} [17], $C^E_{11} = 22.2 \times 10^{10}$ N/m^2, $C^E_{13} = 11.1 \times 10^{10}$ N/m^2, $C^E_{44} = 6.1 \times 10^{10}$ N/m^2, $e_{15} = 34.2$ C/m^2, $e_{31} = -0.7$ C/m^2, $e_{33} = 6.7$ C/m^2, $r^S_{13} = 10.2 \times 10^{-12}$ m/V, $r^S_{33} = 40.6 \times 10^{-12}$ m/V, $r^S_{51} = 730 \times 10^{-12}$ m/V, $\varepsilon_2 = 194.8 \times 10^{-10}$ F/m, $\varepsilon_3 = 4.958 \times 10^{-10}$ F/m, $p^E_{11} = 0.50$, $p^E_{12} = 0.106$, $p^E_{13} = 0.20$, $p^E_{31} = 0.07$, $p^E_{33} = 0.77$, $n_0 = 2.412$, $n_e = 2.360$ [18]. The interference contrast was taken to be $m = 0.001$.

The effect of trap saturation on the attenuation constants γ_2 and γ_3 is illustrated in Fig. 2. For a crystal with the compensating acceptor concentration $N_A = 2 \times 10^{22}$ m^{-3}, the Debye screening length along the polar axis is $L_{sz} = 0.06$ μm. Then, for $\Lambda > 10$ μm, the effect of trap saturation on the field of the spatial charge of the grating, which is determined by the ratio $(L_{sz}/\Lambda)^2$, is negligibly small. Noticeable changes in the attenuation constants γ_2 and γ_3 occur only for $\Lambda < 5$ μm.

The dependences of the amplitudes of the space charge field components E_y and E_z on the normalized transverse coordinate y/Λ are shown in Fig. 3 for gratings with different periods. For all periods, both field components vary monotonically in the surface layer.

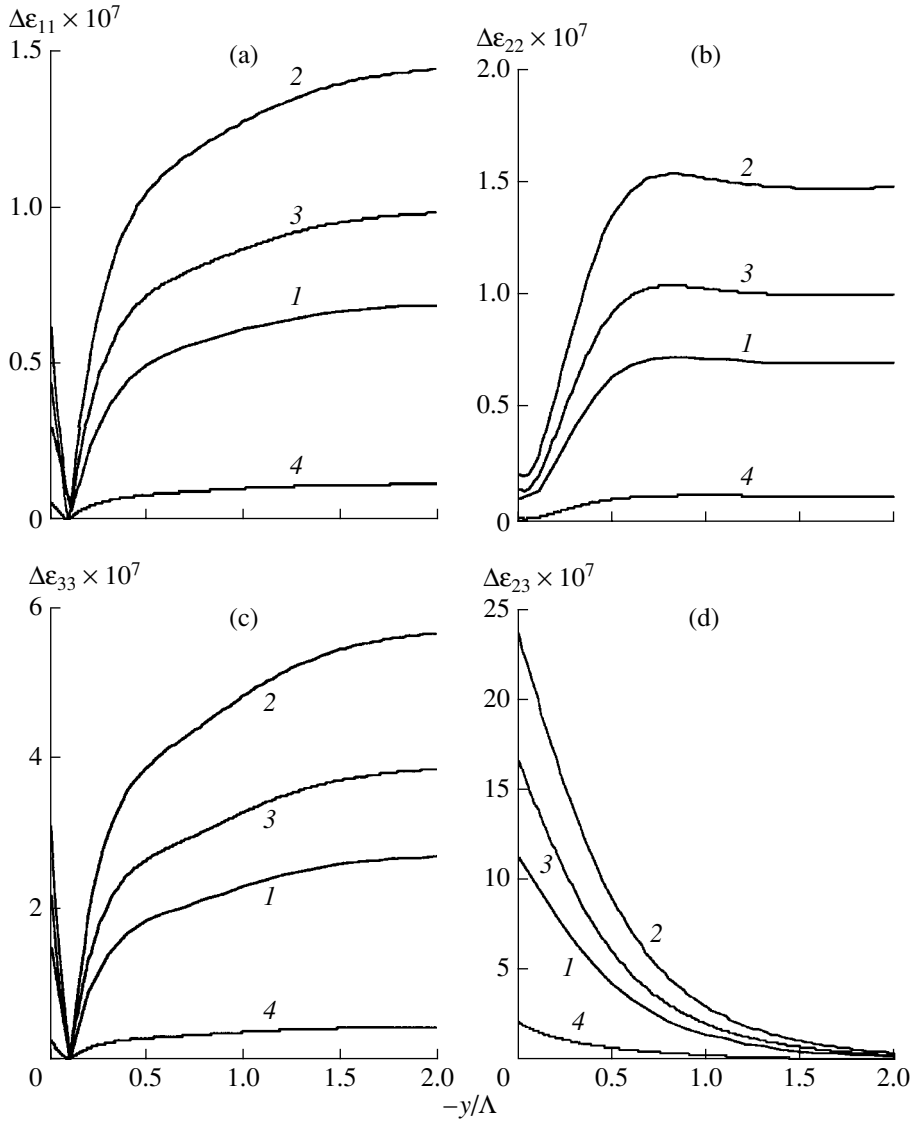

Fig. 5. Amplitude distributions of the perturbations of the permittivity tensor components, $\Delta\varepsilon_{ij}(y)$, in the near-boundary region of the crystal for different periods of the photorefractive grating: Λ = (*1*) 0.1, (*2*) 0.4, (*3*) 1, and (*4*) 10 μm.

The component E_z increases with distance from the boundary and reaches its bulk value at $y > 2\Lambda$. The component E_y that is normal to the boundary noticeably differs from zero in the surface layer of thickness $y \sim \Lambda$. Both components have maximal amplitudes when the grating period is $\Lambda \approx 0.4$ μm and the condition $K_g L_{sz} \approx 1$ is satisfied (curves *4*). Curves *5* in Fig. 3 correspond to the amplitudes of the components E_z and E_y calculated for $\Lambda = 0.4$ μm in the absence of the piezoelectric effect ($e_{31} = e_{33} = e_{15} = 0$), when the dependence of the potential on the transverse coordinate is only determined by the attenuation constant γ_1. The inverse effect of the field of elastic displacements on the distribution of the inducing space charge field is most pronounced for the component E_y: at $y = 0$, the difference in amplitudes in the presence and absence of the piezoelectric effect (Fig. 3b, curves *4* and *5*, respectively) reaches ~10%. Note that when the spatial period of the grating is $\Lambda <$ 0.2 μm or $\Lambda >$ 1 μm, this difference can be neglected.

The distributions of the elastic displacement amplitudes near the crystal boundary are shown in Fig. 4. The component U_z directed along the grating vector is maximal at the crystal boundary and changes sign at $y \sim 0.1\Lambda$; this component reaches its bulk value in the region $y > 2\Lambda$. The component U_y is normal to the boundary; at the boundary, it reaches its maximal value comparable with U_z and then monotonically decays in the direction from the boundary into the crystal depth. Curve *4* corresponding to the spatial period $\Lambda = 2$ μm little differs from curve *5* for $\Lambda = 10$ μm. For gratings with periods $\Lambda < 10$ μm, the trap saturation leads to a decrease in the elastic displacement amplitudes U_y and

U_z with decreasing Λ. This effect is most pronounced for $\Lambda < 1$ μm. At $\Lambda = 0.1$ μm, the elastic displacement amplitudes become an order of magnitude smaller than the maximal values, which occur for gratings with spatial periods exceeding 10 μm.

The distribution of the perturbation amplitudes of the permittivity tensor components $\Delta\varepsilon_{ij}$ near the crystal boundary are shown in Fig. 5 for gratings with different spatial periods. At $\Lambda = 0.4$ μm, when the condition $K_g L_{sz} \approx 1$ is satisfied (curves *2*), all components have maximal amplitudes. From this figure, one can see that all the diagonal components strongly depend on *y* near the crystal boundary and take values equal to the bulk values at the depth $y > 2\Lambda$. The diagonal components $\Delta\varepsilon_{11}$ and $\Delta\varepsilon_{33}$ have identical distributions: they change sign at a depth of about 0.1Λ, and their values at the boundary are approximately half their values in the crystal bulk. The diagonal component $\Delta\varepsilon_{22}$ exhibits a smoother dependence on *y* and takes its minimal value at $y = 0$. The nondiagonal component $\Delta\varepsilon_{23}$ exceeds all diagonal components in amplitude by an order of magnitude at the boundary, but it exists only near the boundary, in the region $y < 2\Lambda$. Note that, owing to the perturbations $\Delta\varepsilon_{23}$ near the boundary of the *Y*-cut barium titanate crystal, the diffraction of light by the holographic grating with a change in polarization (e.g., from an extraordinary wave to an ordinary one) is possible, while in the crystal bulk, this effect is absent.

Thus, in this paper we obtained the relations that allow one to analyze the space charge field and the structure of the elastic fields of a photorefractive grating near the boundary of a 4*mm* or 6*mm* crystal in the linear approximation with respect to the interference contrast with allowance for the trap saturation. We calculated the structure of the elastic and electric fields for a grating with the vector $\mathbf{K}_g$ directed along the polar axis in a *Y*-cut barium titanate crystal with an electrically shortened and mechanically free boundary. The analysis of the behavior of the perturbation amplitudes of the permittivity tensor components near the crystal boundary reveals their strong dependence on the transverse coordinate in the surface layer. We found that, near the boundary, a perturbation grating of the nondiagonal component of the permittivity tensor, $\Delta\varepsilon_{23}$, is present, while in the crystal bulk, this component is equal to zero.

REFERENCES

1. A. V. Bliznetsov, M. P. Petrov, and A. V. Khomenko, Pis'ma Zh. Tekh. Fiz. **10** (18), 1094 (1984) [Sov. Tech. Phys. Lett. **10**, 463 (1984)].
2. S. M. Shandarov, Zh. Tekh. Fiz. **56** (3), 583 (1986) [Sov. Phys. Tech. Phys. **31**, 352 (1986)].
3. S. M. Shandarov and V. M. Shandarov, Zh. Tekh. Fiz. **60** (2), 106 (1990) [Sov. Phys. Tech. Phys. **35**, 199 (1990)].
4. G. Fogarty and M. Gronin-Golomb, Opt. Lett. **20** (22), 2276 (1995).
5. S. M. Shandarov and N. I. Burimov, Izv. Vyssh. Uchebn. Zaved., Fiz., No. 9, 75 (1997).
6. S. Stepanov, N. Korneev, A. Gerwens, and K. Buse, Appl. Phys. Lett. **72** (8), 879 (1998).
7. A. M. Kirillov, S. M. Shandarov, and N. I. Burimov, Pis'ma Zh. Tekh. Fiz. **25** (17), 74 (1999) [Tech. Phys. Lett. **25**, 707 (1999)].
8. A. M. Kirillov and S. M. Shandarov, Kvantovaya Élektron. (Moscow) **26** (2), 185 (1999).
9. A. M. Kirillov and S. M. Shandarov, Proc. SPIE **3737**, 469 (1999).
10. P. A. Pyatakov and A. A. Chaban, Akust. Zh. **44**, 648 (1998) [Acoust. Phys. **44**, 561 (1998)].
11. V. N. Deev and P. A. Pyatakov, Pis'ma Zh. Tekh. Fiz. **11** (2), 76 (1985) [Sov. Tech. Phys. Lett. **11**, 30 (1985)].
12. M. P. Petrov, A. P. Paugurt, V. V. Bryskin, and V. M. Petrov, Pis'ma Zh. Tekh. Fiz. **24** (22), 11 (1998) [Tech. Phys. Lett. **24**, 873 (1998)].
13. V. E. Gusev, Electron. Lett. **25** (25), 1746 (1989).
14. N. V. Kukhtarev, V. B. Markov, S. G. Odulov, *et al.*, Ferroelectrics **22**, 949 (1979).
15. Yu. I. Sirotin and M. P. Shaskol'skaya, *Fundamentals of Crystal Physics* (Nauka, Moscow, 1975; Mir, Moscow, 1982).
16. P. Bernasconi, I. Biaggio, M. Zgonik, and P. Gunter, Phys. Rev. Lett. **78** (1), 106 (1997).
17. N. Barry and M. J. Damzen, J. Opt. Soc. Am. B **9** (8), 1488 (1992).
18. M. Zgonik, P. Bernasconi, M. Duelli, *et al.*, Phys. Rev. B **50** (9), 5941 (1994).

Translated by E. Golyamina

Acoustical Physics, Vol. 49, No. 5, 2003, pp. 580–583. Translated from Akusticheskiĭ Zhurnal, Vol. 49, No. 5, 2003, pp. 683–686.

Measurement of the Space–Time Correlation Function of Thermal Acoustic Radiation

V. I. Passechnik†, A. A. Anosov[1,2], Yu. N. Barabanenkov[1], and A. G. Sel'sky[1]

[1]ELDIS Research Center, Institute of Radio Engineering and Electronics, Russian Academy of Sciences, Starosadskii per. 8, Moscow, 101000 Russia

[2]Sechenov Medical Academy, Moscow, Russia

e-mail: selsky@tarkus.net.ru

Received September 3, 2002

Abstract—The space–time correlation function of thermal acoustic radiation pressure is measured for a stationary heated source (a narrow plasticine plate). The correlation dependence is obtained by the multiplication of two signals shifted in time with respect to each other and measured by two receivers. The dependence exhibits an oscillating behavior and changes sign when the source is displaced by half the spatial period of the correlation function. © *2003 MAIK "Nauka/Interperiodica".*

Correlation measurements of thermal acoustic radiation are much discussed in the literature in connection with the possibilities they offer for measuring the in-depth temperature distribution in biological objects [1–12]. The proposed passive noninvasive (and therefore safe and painless) method of measuring in-depth temperature is important for medical diagnostics.

Studies of the correlation properties of thermal acoustic radiation were started in our laboratory by V.I. Passechnik [2–4, 10]. We were the first to measure the space–time correlation function of thermal acoustic radiation [7, 8] and to investigate its characteristics [12]. This work was also started together with Passechnik.

In our previous studies, we measured the spatial correlation function of thermal acoustic radiation using a pair of piezoelectric transducers with a source moving in space [7, 8, 12]. The purpose of this work is to measure the space–time correlation function of thermal acoustic radiation in the case of a stationary heated source, i.e., to change in time the signals under measurement with respect to each other using two receivers.

The experimental setup (Fig. 1) included a basin with the immersion liquid (water). The source of thermal acoustic radiation was a long narrow vertical plate with the width d = 3.5 mm, a length of about 100 mm, and a thickness of 5 mm, which was made of plasticine with a large (with respect to water) coefficient of ultrasonic absorption. The plate was positioned in a cell with acoustically transparent windows, which was also filled with water. The water in the cell (and therefore, the plate) was heated to 17 K above the basin temperature.

† Deceased.

The receivers were two circular flat piezoelectric transducers (PT_1 and PT_2) with the radius a = 5 mm, and the distance between their centers was D = 18 mm. The acoustic axes of the piezoelectric transducers lay in the horizontal plane and intersected near the plate at the distance l = 200 mm from the transducers. The piezoelectric transducers (the average reception frequency was f_0 = 2.2 MHz) with a quarter-wave layer had approximately equal sensitivities. The sound pressures at PT_1 and PT_2 were transformed into electric signals, which were transmitted through preamplifiers (designed by M.A. Antonov [8]) and amplifiers (U3-29 and U3-33). The amplified signals were stored in a personal computer using an LA-n10M7PCI eight-bit card (manufactured by ZAO Rudnev–Shilyaev, Russia). The pickup frequency was 12.5 MHz. Two channels with a 256 kbyte card memory were used. The correlation function for a given signal realization was calculated according to the data obtained: the signals were shifted in time with respect to each other, and the average value of the products of signal readings was determined (note that the average values of the signals were equal to zero). The result was stored, and the measurements were repeated automatically 1000 times. Thus, we obtained a correlation function averaged over 1000 realizations.

The measurements were conducted in two modes: in the first case (the "open" state), the signal arriving at a piezoelectric transducer originated from the plate, and in the second case (the "closed" state), a duralumin reflecting plate was positioned between the piezoelectric transducer and the cell, so that the signal arriving at the transducer originated from the basin (the temperatures of the piezoelectric transducer and the basin coincided). To exclude the signal drift and possible nonacoustic correlation sources, we calculated the differ-

1063-7710/03/4905-0580$24.00 © 2003 MAIK "Nauka/Interperiodica"

ence between the averaged functions in the first and second modes.

Figure 2a shows the measured space–time correlation function $R(\tau)$ of thermal acoustic radiation, which was obtained by averaging the results of $n = 7$ measurements. The experimental points are connected by a broken line *1* for illustration. The horizontal axis represents the delay time τ of one signal with respect to the other. The standard errors ($s/\sqrt{n}$, where s is the rms deviation) for each delay value are shown in the plot.

As one can see from Fig. 2a, the maximum amplitude of the correlated signal, which is measured in units of the low-order digit (LOD), is about 3 LOD^2. Note that the average total intensity of measured signals (the average value of the squared voltage) for the piezoelectric transducers is equal to ~2000 LOD^2, and the average difference in signal intensities in the open and closed states is ~13 LOD^2. Therefore, the maximum value of the correlation coefficient (the share of the correlated signal in the total measured noise signal) is ~0.15%, and the share of the correlation component in the signal associated only with the thermal acoustic radiation from the plate is ~23%. These values are lower than those obtained in our previous measurements of the spatial correlation function (60–80%) [12], which is probably connected with the increase in the transmission band Δf of the piezoelectric transducers used in our experiments, from 0.2 [8, 12] to 0.6 MHz, and with a certain increase in the plate width.

From the experimental data, one can find that the average frequency of the correlated signal approximately coincides with the average reception frequency f_0, and the bandwidth of the correlated signal coincides with the transmission bandwidth of the piezoelectric transducer Δf. Knowing f_0, the distance l from the transducer to the source, and the distance D between the piezoelectric transducers, it is possible to determine the spatial period of the correlation function: $\Lambda = cl/Df_0 \approx 8$ mm, where $c = 1500$ m/s is the velocity of sound in water. If we shift the plate along the horizontal axis x (see Fig. 1) perpendicularly to the acoustic axis of the system by half the spatial period of the correlation function, the space–time correlation function must change its phase by π. The measured space–time correlation function of the source shifted by 4 mm is shown in Fig. 2b. Comparing Figs. 2a and 2b, one can see that the measured functions are in antiphase, which confirms the assumption. One can notice the decrease in the maximum amplitude and a somewhat greater measurement error for the second signal, which is mainly connected with the shift of the source from the center of the spread functions of the piezoelectric transducers. The analysis of the measurement errors shows that we reliably obtain 3–4 periods of the correlation function variation in the range of time delays approximately from –1.2 to 1.2 μs.

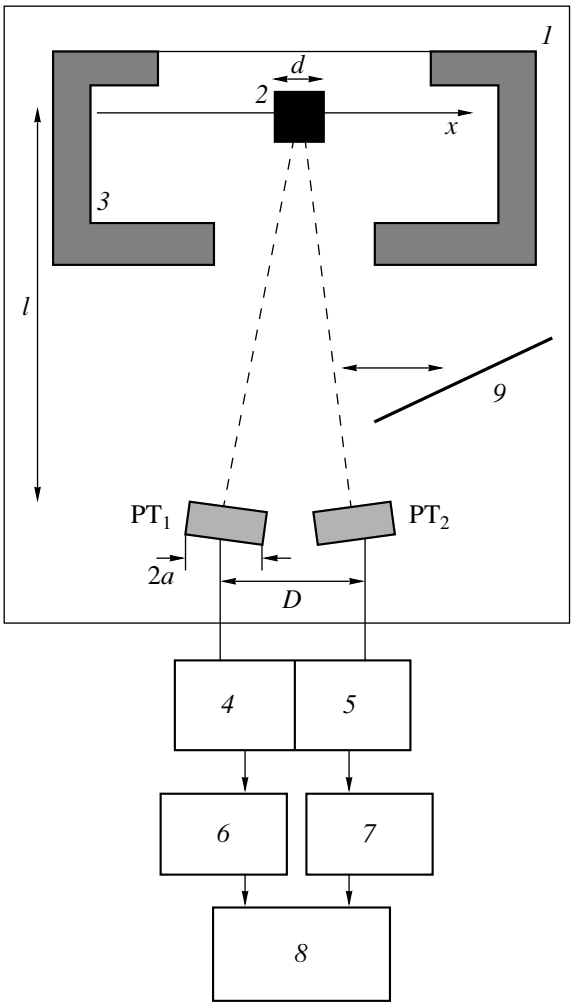

Fig. 1. Experimental setup: (*1*) a basin, (*2*) a plasticine plate with the width *d*, (*3*) a cell, (*4*, *5*) preamplifiers, (*6*, *7*) U3-29 and U3-33 amplifiers (respectively), (*8*) a personal computer, and (*9*) a reflecting plate; PT_1 and PT_2 are piezoelectric transducers with the radius a, D is the distance between their centers, and l is the distance from the x axis to the piezoelectric transducers.

The space–time correlation function $R(\tau)$ measured in our experiment can be evaluated using the following model. Let the piezoelectric transducers be infinite vertical strips with the width a and with the distance between their centers D. We assume that the transmission band of the transducers $f_0 \pm \Delta f/2$ has a rectangular form. Then, taking into account the fact that the plate size is small $\Delta\theta = d/l \ll 1$, we find that the correlation function is proportional to the expression [13]

$$R(\tau)\frac{\sin^2(\pi a\theta_0/\lambda_0)}{(\pi a\theta_0/\lambda_0)^2}\frac{\sin(\pi D\Delta\theta/\lambda_0)}{(\pi D\Delta\theta/\lambda_0)}$$
$$\times\frac{\sin[\pi\Delta f(D\theta_0/\lambda_0 - f_0\tau)/f_0]}{[\pi\Delta f(D\theta_0/\lambda_0 - f_0\tau)/f_0]}$$
$$\times\cos[2\pi(D\theta_0/\lambda_0 - f_0\tau)],$$

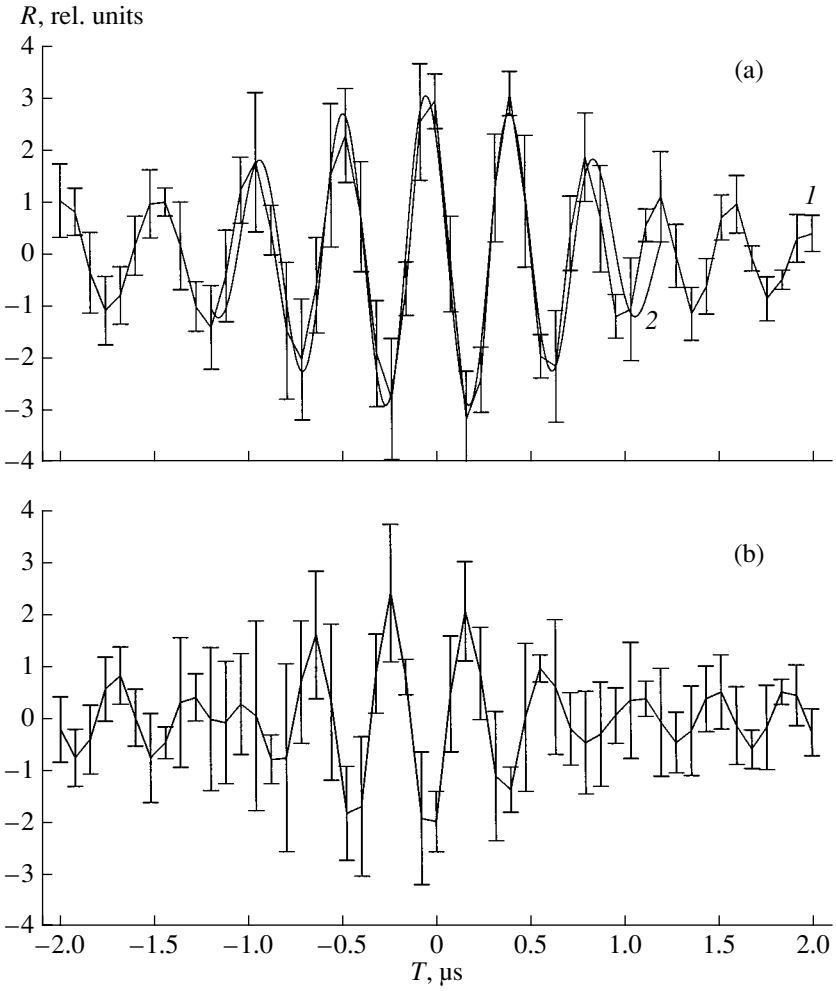

Fig. 2. (a, curve *1* and b) Measured space–time correlation functions $R(\tau)$ of thermal acoustic radiation for two positions of the plate and (a, curve *2*) the calculated dependence $R(\tau)$.

where $\theta_0 = x/l$ is the angular coordinate of the plate center. Figure 2a presents the correlation function calculated for the first position of the plate (curve *2*). In the calculation, we used the value $\theta_0 = -0.004$, which corresponds to a plate shift of 0.8 mm along the *x* axis from the acoustic axis of the system. This value specifies the plate position with respect to the intersection point of the acoustic axes of the piezoelectric transducers. As one can see, the results of calculation agree well (within the experimental error) with the results of measurements in the range of time delays from –1.2 to 1.2 μs.

Thus, we measured the space–time correlation function of thermal acoustic radiation for a stationary source by using the time delay between the signals. It should be noted that this procedure provides an opportunity to scan the region under investigation with the aim of measuring its in-depth temperature without moving the piezoelectric transducers mechanically. As a result, the scanning time is reduced, which is important for future biomedical applications of the method.

ACKNOWLEDGMENTS

This work was supported by the Russian Foundation for Basic Research, project nos. 02-02-17371 and 00-01-00361.

REFERENCES

1. R. Hessemer, T. Perper, and T. Bowen, U.S. Patent No. 4416552 (22 November 1983).
2. Yu. N. Barabanenkov and V. I. Pasechnik, Akust. Zh. **41**, 563 (1995) [Acoust. Phys. **41**, 494 (1995)].
3. V. I. Passechnick and Yu. N. Barabanenkov, J. Acoust. Soc. Am. **99**, 65 (1996).
4. V. I. Pasechnik, Akust. Zh. **43**, 563 (1997) [Acoust. Phys. **43**, 485 (1997)].
5. A. I. Chmill, V. V. Gerasimov, Yu. V. Guluaev, *et al.*, Acoust. Imaging **23**, 77 (1997).
6. R. A. Kruger, D. R. Reinecke, and G. A. Kruger, Med. Phys. **26**, 1832 (1999).

7. V. I. Pasechnik, A. A. Anosov, and K. M. Bograchev, Biomed. Radioelektron., No. 2, 3 (1999).
8. A. A. Anosov, M. A. Antonov, and V. I. Pasechnik, Akust. Zh. **46**, 28 (2000) [Acoust. Phys. **46**, 21 (2000)].
9. E. V. Krotov, A. D. Mansfel'd, A. M. Reĭman, and V. A. Vilkov, in *Speech Acoustics. Medical and Biological Acoustics: Proceedings of XI Session of the Russian Acoustic Society* (GEOS, Moscow, 2001), Vol. 3, pp. 165–169.
10. V. I. Pasechnik, Akust. Zh. **48**, 675 (2002) [Acoust. Phys. **48**, 589 (2002)].
11. V. A. Burov, P. I. Darialashvili, and O. D. Rumyantseva, Akust. Zh. **48**, 474 (2002) [Acoust. Phys. **48**, 412 (2002)].
12. A. A. Anosov and V. I. Pasechnik, Akust. Zh. **49**, 161 (2003) [Acoust. Phys. **49**, 129 (2003)].
13. N. A. Esepkina, D. V. Korol'kov, and Yu. N. Pariĭskiĭ, *Radio Telescopes and Radiometers* (Nauka, Moscow, 1973), pp. 261–268.

Translated by M. Lyamshev

Acoustical Physics, Vol. 49, No. 5, 2003, pp. 584–591. Translated from Akusticheskiĭ Zhurnal, Vol. 49, No. 5, 2003, pp. 687–695.

Estimation of Sea Bottom Parameters from the Angle–Frequency Resonances of the Reflection Coefficient

V. N. Fokin and M. S. Fokina

Institute of Applied Physics, Russian Academy of Sciences, ul. Ul'yanova 46, Nizhni Novgorod, 603950 Russia
e-mail: fokin@hydro.appl.sci.nnov.ru

Received July 9, 2002

Abstract—The resonance structure of the frequency response is used for the determination of sea bottom properties. The behavior of the resonance characteristics is investigated in the plane of two different bottom parameters for a fixed angle of incidence. The features of the behavior of the resonance structure characteristics are used to develop the procedure for evaluating the parameters of a layered sea bottom. With the proposed procedure, the parameters of a layered sea bottom are determined from model data in which an error is artificially introduced. The efficiency of the bottom parameter determination is shown to increase when several characteristics of the resonance structure are used simultaneously. © *2003 MAIK "Nauka/Interperiodica".*

1. INTRODUCTION

Fundamental characteristics of the sea bottom are parameters such as the velocities of compressional and shear waves and the densities of the sedimentary layers and underlying half-space. Knowing these characteristics is of great importance, in particular, for geophysical applications and underwater acoustics. By now, many methods for determining the sea bottom properties have been developed [1]. These methods differ in the procedure and the characteristics of the acoustic signals used to reconstruct the properties of the bottom. Pulse methods based on measuring the characteristics of acoustic pulses [2] and matched-field processing [3, 4] are used most often. For example, the method of determining the parameters of an elastic layer lying on an elastic half-space [2] is based on measuring the amplitudes and delays of a pulse signal. The parameters of the bottom are determined with the use of analytically derived expressions that allow one to sequentially determine all the parameters of an elastic layered medium from the measured quantities. Originally, the matched-field processing was used for determining the coordinates of a sound source in a waveguide. Later, it was shown that they are also appropriate for determining the parameters of the waveguide and, in particular, the bottom characteristics. Matched-field inversions are now widely used for determining the parameters of the layered bottom [3–5]. In these procedures, the determination of the bottom parameters is performed by searching for the parameters of the medium that provide the minimum of the weighting function determining the difference between the calculated and measured quantities. Different procedures exist for finding the global minimum of the weighting function. The genetic algorithm and the simulating annealing algorithm, as well as their combinations with the methods for local minima search, are used most frequently. These methods appear in many modifications and showed a high efficiency with the use of both model data and full-scale data obtained in the sea. A repeated launch of the procedure for determining the bottom parameters with different initial conditions is often used to improve the reliability of the reconstruction. The determination of bottom parameters with the use of broadband acoustic signals may also improve the reliability of the results [6]. The utmost precision of the values of bottom parameters obtained with matched-field inversions creates an illusion of a precise reconstruction, which is not necessarily the case. Errors in experimental data may give rise to a local minimum of the weighting function and cause biased estimates of the bottom parameters. The solution obtained is seldom analyzed for stability and accuracy under a small perturbation of the initial data. The situation is additionally aggravated by the fact that high-performance methods for searching the global minimum of the weighting function, which underlie the matched-field inversions, follow from formal mathematical algorithms, and this causes difficulties in the physical interpretation of the solution.

Different characteristics of acoustic signals used for determining the properties of the bottom have different sensitivities to the parameters of the sea bottom. If the acoustic characteristics used in the reconstruction show a low sensitivity to certain parameters of the sea bottom, a precise determination is hardly possible for these parameters. In this context, there is a need to search for characteristics that are sensitive to small variations of the bottom parameters and to test the corresponding methods of the bottom parameter estimation for efficiency. The characteristics of the resonance peaks of

1063-7710/03/4905-0584$24.00

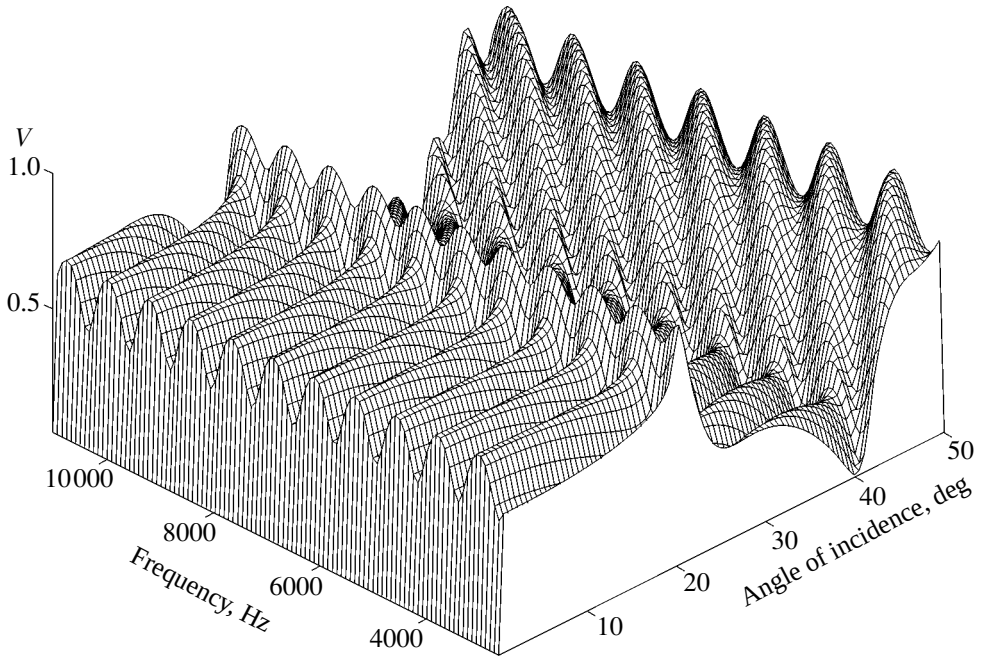

Fig. 1. Sound reflection coefficient obtained for a layered elastic bottom in the frequency–angle of incidence plane.

the sound reflection coefficient from the layered bottom can be regarded as being among these characteristics. The resonance techniques are based on measuring the characteristics of the resonance structure (the resonance frequency F_r, the resonance peak half-width $\Gamma/2$, and the peak amplitude A) and using them to reconstruct the geoacoustic parameters of the bottom [7]. Resonance phenomena experimentally observed in sound reflections from the sea bottom were described in [8]. Now, the resonance approach gains increasing popularity, which is related to the development of computer methods and progress in the theory of sound propagation [9]. In this paper, we investigate the resonance characteristics of the reflection coefficient for a two-layer model of the bottom and use these characteristics to reconstruct the bottom parameters from simulated data supplemented with an artificially introduced error. We show that the efficiency of the bottom parameter estimation is enhanced when several characteristics of the resonance structure are used simultaneously.

2. RESONANCE TECHNIQUE

Consider the resonance technique for reconstructing the bottom parameters. In the angle–frequency plane, the reflection coefficient behaves as a regular sequence of peaks and valleys that are almost parallel to the angle axis for small grazing angles 0°–21°; for grazing angles exceeding 21° (this is the critical angle for the compressional wave propagating in the lower half-space), the sequence of peaks and valleys gradually move away from the angle axis (Fig. 1). Such a behavior is evidence in favor of the description of the reflection coefficient in the vicinity of resonances as a resonance process, which makes it possible to interpret the reflection coefficient as a sequence of resonances and use the resonance formalism to determine the relationships between the resonance characteristics and the material parameters of the medium. The main feature of the resonance formalism consists in the assumption that the amplitude of the process can be described near the resonance by the Breit–Wigner curve lying on a slowly varying background. By virtue of this assumption, the reflection coefficient can be expanded in a series near the minima and then rewritten as a sum of resonance terms [7]. The sum over the resonances in this representation has only symbolic sense, because the resulting expression is valid only in the immediate vicinity of each resonance. Such types of expressions were obtained for a fluid layer between two liquids [10] and an elastic plate in liquid [11]. In papers [12, 13], we obtained the resonance expansion of the reflection coefficient expressed in terms of material parameters in the case of an elastic layer lying on an elastic half-space. The expression obtained for the reflection coefficient can be represented in the general case as a sum of resonance terms written in the Breit–Wigner variables [14]:

$$V = \sum_n \frac{P + F_1(\delta - \delta_n) + F_2(\eta - \eta_n) + iG(\Gamma_n/2)}{Q + F_3(\delta - \delta_n) + F_4(\eta - \eta_n) + i(\Gamma_n/2)}, \quad (1)$$

where $\Gamma_n/2$ is the resonance half-width measured near the local minimum of the reflection coefficient at the points where the process amplitude reaches half of its maximum value $A/2$; the index n means that this sum must be evaluated for the nth root of the characteristic

equation; δ_n and η_n specify the positions of the frequency and angular resonances relative to the compressional and shear waves; $\delta = 2\pi f d\cos(\Theta_l)/c_l$ and $\eta = 2\pi f d\cos(\Theta_t)/c_t$ are the phase terms; f is the frequency; d is the layer thickness; c_l and c_t are the velocities of the compressional and shear waves in the layer; Θ_l and Θ_t are the angles of refraction of compressional and shear waves in the layer (they are generally obtained from Snell's law for a wave incident on the layer–half-space system from the upper half-space at a fixed angle); and F_1, F_2, F_3, F_4, P, Q, and G are the coefficients dependent on the parameters of the medium interacting with the sound wave. If δ and δ_n coincide, the real part of the denominator in Eq. (1) vanishes, because $\delta = \delta_n$ is the root of the characteristic equation obtained from the condition of a zero real part of the denominator in the expression for the reflection coefficient:

$$Q + F_4(\eta - \eta_n) = 0. \quad (2)$$

Similarly, the expression

$$Q + F_3(\delta - \delta_n) = 0 \quad (3)$$

is equal to zero if $\eta = \eta_n$. The equality $\delta = \delta_n$ or $\eta = \eta_n$ can be satisfied by varying both frequency and angle of incidence of the plane wave. This fact offers the possibility of using this formula for considering both frequency and angular resonances of the reflection coefficient for compressional and shear waves in the layer. From Eq. (1), one can easily obtain analytical expressions for the resonance half-width $\Gamma_n/2$ in terms of the material parameters of the medium and the process amplitude A at resonance conditions $\delta = \delta_n$ and $\eta = \eta_n$:

$$A = 2\frac{P + i(\Gamma_n/2)(G - F)}{\Gamma_n/2 - i(\Gamma_n/2)}. \quad (4)$$

In the case of an elastic layer lying on an elastic half-space, the analytical expression for the resonance half-width written in terms of the material parameters of the medium is extremely cumbersome and is not given here. Using the relationship between the resonance characteristics and the material parameters of the medium, one can solve the inverse problem, which reduces to the solution of the system of equations relating the measured characteristics of resonances to the material parameters of the medium. However, the solution of such a system in analytical form and the investigation of the expected errors of reconstruction appear very difficult because of the cumbersome nature of the expressions obtained. Since all material parameters of the medium have an effect on every resonance characteristic, it is of great interest to investigate numerically how much separate characteristics of resonances are appropriate for reconstructing the parameters of the medium and what are the resonance characteristics that offer the possibility of reconstructing the particular parameters of the layered bottom with the highest precision. It is also of interest to determine in which cases the measurement of a single resonance characteristic is sufficient and when some combination of resonance characteristics is required for reconstructing the bottom parameters with the highest efficiency. We carried out such an investigation using our procedure of bottom parameter determination from the measured values of the reflection coefficient [15, 16].

We used the following notation for the parameters of the layered bottom: the index ∞ corresponds to the parameters characterizing the elastic half-space, and the index 0 corresponds to the water layer. For example, c_l and c_t are the longitudinal and transverse velocities of sound in the layer, ρ and d are the density and the thickness of the layer, while $c_{l\infty}$, $c_{t\infty}$, $\nu_{l\infty}$, $\nu_{t\infty}$, and ρ_∞ are the longitudinal and transverse velocities of sound, the attenuation coefficients, and the density characterizing the half-space. With the goal of investigating the sensitivity of separate resonance characteristics to the parameters of the layered bottom, we analyzed the behavior of the resonance characteristics of the reflection coefficient (location, half-width, and amplitude) in the plane of bottom parameters for a fixed angle of incidence. The analysis was carried out with the use of the expressions relating the resonance amplitude, location, and half-width to the material parameters of the medium.

To obtain the resonance characteristics as functions of an arbitrary set of parameters of the layered sea bottom and the angle of plane wave incidence, we traced the same resonance minimum in the reflection coefficient. Any variation of the bottom parameters or angle of incidence changes the quantities F_r, $\Gamma/2$, and A corresponding to the selected resonance minimum. For example, Fig. 2 shows the resonance characteristics F_r, $\Gamma/2$, and A for different parameters of the elastic layered bottom at a fixed angle of incidence; curve *1* corresponds to the following parameters of the layer and the half-space: $c_l = 2344$ m/s, $\rho = 2.2$ g/cm^3, $d = 10$ cm, $c_{l\infty} = 3495$ m/s, $c_{t\infty} = 980$ m/s, and $\rho_\infty = 2.6$ g/cm^3, while curve *2* corresponds to the bottom with higher longitudinal velocities in the layer and the half-space: $c_l = 2544$ m/s, $\rho = 2.2$ g/cm^3, $d = 10$ cm, $c_{l\infty} = 5495$ m/s, $c_{t\infty} = 980$ m/s, and $\rho_\infty = 2.6$ g/cm^3. Thus, an arbitrary combination of bottom parameters can be correlated with certain resonance characteristics. We investigated the behavior of resonances in the domain of parameters of the layered sea bottom for different planes of bottom parameters. In this paper, we used isolines to represent resonance characteristics as functions of the parameters of the layered bottom, the black and white colors corresponding to maximum and minimum values of the function under consideration, respectively. To extend the dynamic range, we presented the graphs with a gray shading scale in which each shade corresponds to two different levels of the function.

Our investigation showed that the shape of isolines for F_r, $\Gamma/2$, and A depends on both the bottom parameters and the angle of plane wave incidence on the bottom Θ_0. This fact allows one to use separate resonance characteristics for estimating the parameters of elastic media. The shapes of isolines for different resonance characteristics (F_r, $\Gamma/2$, and A) in the planes of the same parameters appear different for Θ_0 = const. This fact allows one to increase the accuracy of reconstruction of the bottom parameters using several resonance characteristics simultaneously. The features revealed in the behavior of the characteristics of the resonance structure enabled us to suggest a technique for determining the parameters of the elastic layered bottom.

Consider the essence of the suggested technique using a particular resonance characteristic (e.g., A) as an example. The bottom parameters of an arbitrary model of a layered bottom uniquely determine the resonance amplitude A. However, some specified value of amplitude A can correspond to different sets of layered bottom parameters. We will call the space whose different coordinates correspond to different bottom parameters the space of bottom parameters. In this space, many points correspond to the specified amplitude A. The coordinates of every such point form the set of bottom parameters whose combination ensures that the specified amplitude A is obtained in the calculations. The error in the measured resonance amplitude extends every point in space to a region of finite dimension. This extension follows from the fact that the points close to the initial point must be included in the region, if the difference between the measured and calculated amplitudes A for these points is smaller that the measurement error. If only a single measurement is available, all regions yielding the specified amplitude A are equivalent in the space of bottom parameters. Every measurement can be correlated with its own set of such regions in the space of bottom parameters. These sets coincide only partially. The greater the measurement error, the greater the number of common regions in these sets. If the number of independent measurements is great enough, only one common region satisfying all measurements will exist in the space of bottom parameters. This region is used for evaluating the parameters of the layered bottom. Prior information on the bottom structure can essentially reduce the range of possible combinations of bottom parameters. Similar arguments are also applicable to other resonance characteristics.

In the calculations, we described the reflection coefficient by the analytical expressions [12, 13], which were obtained by the matrix method developed in [17, 18], and the reflection coefficient of an elastic layer lying on an elastic half-space by the analytical expressions (1)–(4) written in terms of the Breit–Wigner variables. Figure 3 shows the calculated resonance amplitude A as a function of both the velocity of compressional waves in the sedimentary layer and the half-space density for two angles of incidence $\Theta_1 = 50°$ and

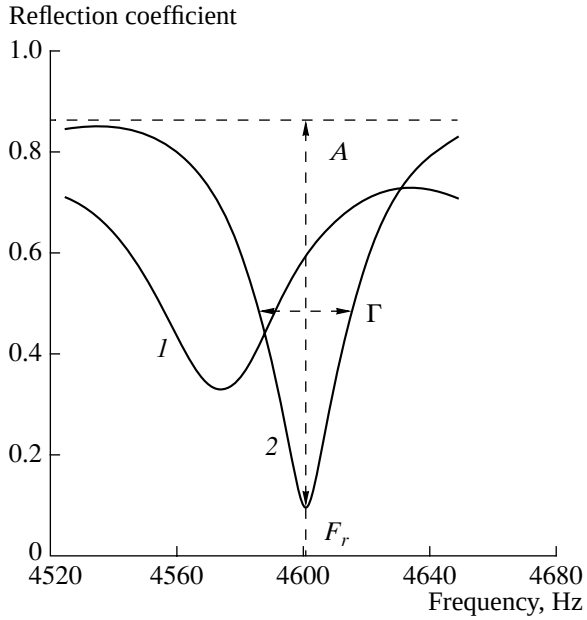

Fig. 2. Variability of a single resonance of the reflection coefficient depending on the parameters of the layered elastic bottom: curve *1* corresponds to c_l = 2344 m/s, ρ = 2.2 g/cm^3, d = 10 cm, $c_{l\infty}$ = 3495 m/s, $c_{t\infty}$ = 980 m/s, and ρ_∞ = 2.6 g/cm^3; curve *2* corresponds to c_l = 2544 m/s, ρ = 2.2 g/cm^3, d = 10 cm, $c_{l\infty}$ = 5495 m/s, $c_{t\infty}$ = 980 m/s, and ρ_∞ = 2.6 g/cm^3.

$\Theta_2 = 70°$. Other parameters of the elastic layered bottom (c_t, ν_t, ρ, $c_{l\infty}$, $\nu_{l\infty}$, $c_{t\infty}$, and $\nu_{\infty t}$) are assumed to be fixed. The combined effect of two bottom parameters on the resonance structure characteristics and the resonance structure sensitivity to different characteristics of the layered bottom can be estimated by analyzing the resonance characteristics as functions of the layered bottom parameters. For a fixed angle of incidence, the variation of acoustic characteristics of the layer and the half-space results in the variation of the parameters F_r, $\Gamma/2$, and A within certain limits. Conversely, assuming the values of resonance characteristics to be fixed, we can determine, in the plane of bottom parameters, the region in which the calculated characteristics of the resonance structure can coincide with the specified values of resonance characteristics (in Fig. 3, each shade of gray color corresponds to a certain interval of variation of the amplitude A). The narrower the interval of the possible variations of parameters F_r, $\Gamma/2$, and A because of the measurement error, the narrower the parameter region corresponding to the specified values of F_r, $\Gamma/2$, and A. Figure 3 shows that, under the assumption that the resonance amplitude A is known for two angles of incidence, which corresponds to a certain level of gray color in each graph, the bottom parameters c_l and ρ_∞ can be determined as the coordinates of the region in which isolines corresponding to the amplitudes A mea-

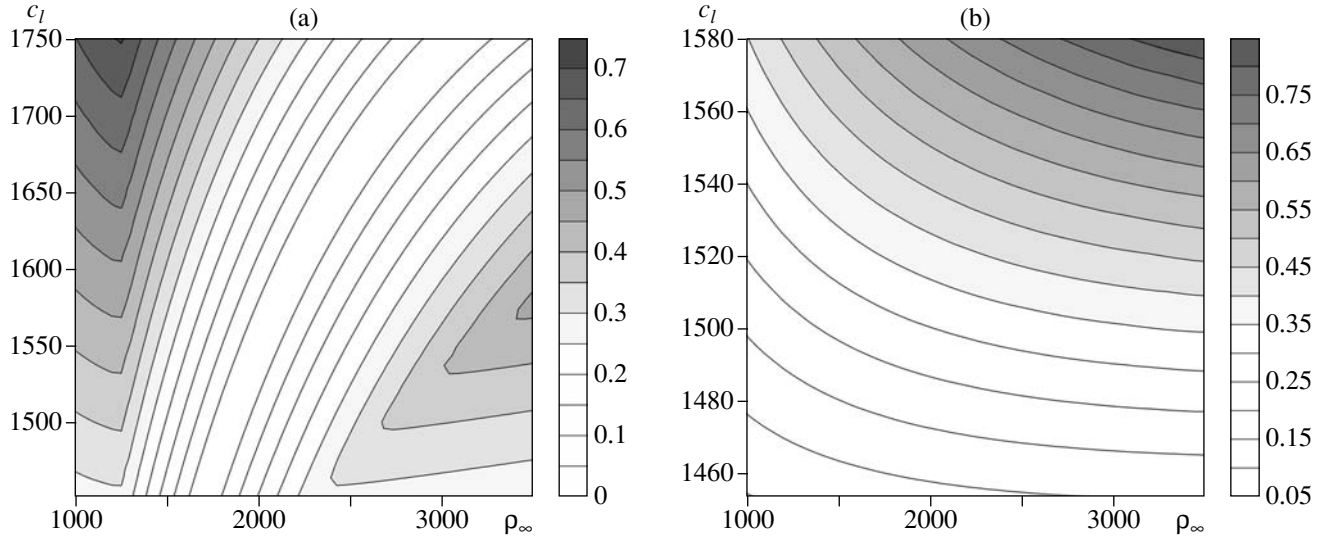

Fig. 3. Resonance amplitude as a function of the velocity of compressional waves in the sedimentary layer and the density of the half-space, $A(c_l, \rho_\infty)$, for two angles of incidence: (a) $\Theta_1 = 50°$ and (b) $\Theta_2 = 70°$.

sured for different angles of incidence intersect. To find this region, one must specify some definite value of the amplitude, which corresponds to a certain shade of gray in each graph, and superimpose the resulting regions. The intersection of these regions will qualify the quantities c_l and ρ_∞. Assume that only two parameters of the layered bottom are unknown (other parameters of the sedimentary layer are assumed to be known). For a fixed angle of incidence and definite measured parameters F_r, $\Gamma/2$, and A, one can obtain a region in the plane of bottom parameters for every characteristic of resonances. The resonance structure in these regions coincides with calculations performed under variation of the unknown parameters. Below, we describe the procedure for evaluating the bottom parameters using only one parameter of the resonance structure (A, for example). The procedure includes the following steps:

(i) the calculation of the parameter A in the selected plane of bottom parameters for a set of angles of incidence $\Theta_1, \ldots, \Theta_n$;

(ii) the determination of the region in the plane of bottom parameters, in which A varies from $(A_1 - \varepsilon)$ to $(A_1 + \varepsilon)$ for the angle of incidence Θ_1, where ε is the measurement error. Repeating this procedure for the angles of incidence $\Theta_2, \ldots, \Theta_n$ provides n different regions of parameters;

(iii) the determination of the points belonging to all regions obtained at step (ii) by superimposing all the regions in the plane of bottom parameters.

Thus, the range of bottom parameters satisfying all measurements is determined. In this range, the difference between the measured and calculated characteristics of resonances is smaller than ε. Because of the differences in the shapes of regions corresponding to different resonance characteristics, these regions will only partially intersect in the plane of bottom parameters. The parameters F_r, $\Gamma/2$, and A considered as functions of the angle of incidence testify that the regions obtained in the plane of bottom parameters for different angles of incidence will also intersect only partially. Consequently, in conditions of measurements dealing only with a single resonance characteristic, the bottom parameters can be reconstructed by superimposing the regions corresponding to different measurements and determining the region common to all measurements. If the measurements additionally deal with the half-widths and positions of resonances, the results obtained can be refined by a similar superimposition of the results obtained for F_r and $\Gamma/2$.

Because experimental data always involve measurement errors and, in addition, depend on natural noise, we consider the effect of respective errors ε_1, ε_2, and ε_3 in the quantities F_r, $\Gamma/2$, and A measured for different angles of incidence. The errors ε_1, ε_2, and ε_3 determine the range of possible variations of the calculated resonance characteristics F_r, $\Gamma/2$, and A relative to the measured quantities F_{rm}, $\Gamma_m/2$, and A_m and, consequently, the sizes of the regions in which the calculated quantities coincide with the experimental data to a desired accuracy. To formalize the reconstruction procedure, we introduce the function ϕ defined in the plane of the parameters of the medium to be reconstructed:

$$\phi = \sum_k \sum_i \vartheta_k(p_1, p_2, p_3, \ldots, p_n), \tag{5}$$

where

$$\vartheta_k(p_1, p_2, p_3, \ldots, p_n) = \begin{cases} 1, |B_c - B_m| \le \varepsilon_k \\ 0, |B_c - B_m| \ge \varepsilon_k \end{cases}; \tag{6}$$

$p_1, p_2, p_3, \ldots, p_n$ are the parameters of the layered bottom; k is the number of measured characteristics of the resonance structure; i is the number of angles of incidence used in the measurements; ε is the measurement error; and B_m and B_c are the measured and calculated values of the characteristics of the resonance structure. The parameters of the medium are determined by searching for the maximum of the function ϕ. In calculating ϑ_k, the unknown parameters of the medium are varied. To minimize the calculations required for determining several characteristics of the medium, we assume that the coordinates of the intersection region only slightly depend on the bottom characteristics, whose variation only slightly affects the reflection coefficient. With this assumption, the calculations can be performed without varying these characteristics in the process of evaluating the bottom parameters, whose variations significantly affect the reflection coefficient.

3. RESULTS

Thus, we tested the procedure proposed for reconstructing the parameters of the layered elastic bottom by using data simulated for 16 different angles of incidence and supplemented with an artificially introduced error. We consider the layer thickness d and longitudinal velocity c_l reconstructed with the use of each individual resonance characteristic (F_r, $\Gamma/2$, or A) of the reflection coefficient. The use of individual resonance characteristics for reconstructing other parameters of the layered medium is not considered here. Then, we consider the parameters d and c_l reconstructed with the simultaneous use of all three resonance characteristics and present the results of evaluating other bottom parameters with the use of all three resonance characteristics.

Figure 4 shows the results of determining the parameters d and c_l with the use of each characteristic (F_r, $\Gamma/2$, or A) of the resonance structure separately. Figure 4a shows the parameters d and c_l evaluated from the resonance amplitude A, Fig. 4b shows the parameters d and c_l evaluated from the resonance half-width $\Gamma/2$, and Fig. 4c shows the parameters d and c_l evaluated from the resonance frequency F_r. The bottom parameters are determined as coordinates of the maximum of the function ϕ. Analyzing Fig. 4a, one can infer that the thickness of the sedimentary layer only slightly affects the resonance amplitude in the (d, c_l) plane. For this reason, the peak of the function ϕ appears spread in the coordinate d. At the same time, the resonance amplitude appears highly sensitive to the sound velocity c_l in the sedimentary layer and offers a possibility for high-precision determination of the parameter c_l from the measured resonance amplitudes A for different angles of incidence. The situation drastically changes when the resonance half-width $\Gamma/2$ is used for evaluating the parameters of the sedimentary layer (Fig. 4b). The resonance half-width only slightly depends on the sound velocity in the layer, which makes the determination of the parameter c_l from this characteristic hardly possible. At the same time, Fig. 4b shows that evaluating the bottom parameters with the use of the resonance half-width allows one to determine the thickness of the sedimentary layer with an appropriate accuracy. It should be noted that the peak of the function ϕ in Figs. 4a and 4b is localized in one coordinate and spread in the other. In the case of evaluating the bottom parameters with the use of only the resonance frequencies F_r (Fig. 4c), the function ϕ has many narrow peaks slightly spread along the axis of the sound velocity c_l. Among the peaks of the function ϕ, there is a main peak; however, it exceeds the side peaks only slightly. This fact makes the selection of the main peak impracticable and indicates that the reconstruction of the desired parameters from resonance frequencies is ambiguous. Additional information on the variation range of the bottom parameters offers the possibility of high-precision determination of both thickness and sound velocity in the sedimentary layer from resonance frequencies. Analyzing the process of peak formation in the function ϕ, one may notice that each peak is a result of combining broader peaks that correspond to the functions ϑ_k and appear when the unknown bottom parameters are varied in accordance with Eq. (5). As can be seen from Fig. 4, the use of a single resonance characteristic (F_r, $\Gamma/2$, or A) is insufficient for evaluating c_l and d with appropriate accuracy in the case under consideration. However, it is quite possible that other parameters can be successfully estimated from the measurement data on a single resonance characteristic. The size and shape of peaks in the function ϕ determined from the data obtained for a single resonance characteristic depend on the coordinate plane chosen for the analysis. The coordinates that ensure the narrowest peaks of the function ϕ for the measured resonance characteristic in the plane of the bottom parameters are the most efficient choice. From Figs. 4a and 4b, one can infer that these coordinates depend on the resonance characteristic. The optimum choice of coordinates will essentially enhance the precision of the reconstruction of the bottom parameters with the simultaneous use of different resonance characteristics.

Figure 5 shows the result of evaluating the remaining parameters of the sea bottom from three resonance characteristics used simultaneously. Figure 5a shows the parameters c_l and d determined from the three resonance characteristics F_r, $\Gamma/2$, and A. Figure 5a was obtained by the summation of the functions ϕ shown in Figs. 4a–4c. The sum of functions shown in Figs. 4a and 4b forms a broad peak in the (c_l, d) plane at the intersection of mutually perpendicular peaks. This peak noticeably reduces the range of variation for the parameters of the medium and allows one to determine both c_l and d. When the function given in Fig. 4c is added to the above result, only one of the multiple peaks obtained in reconstructing the bottom parameters from

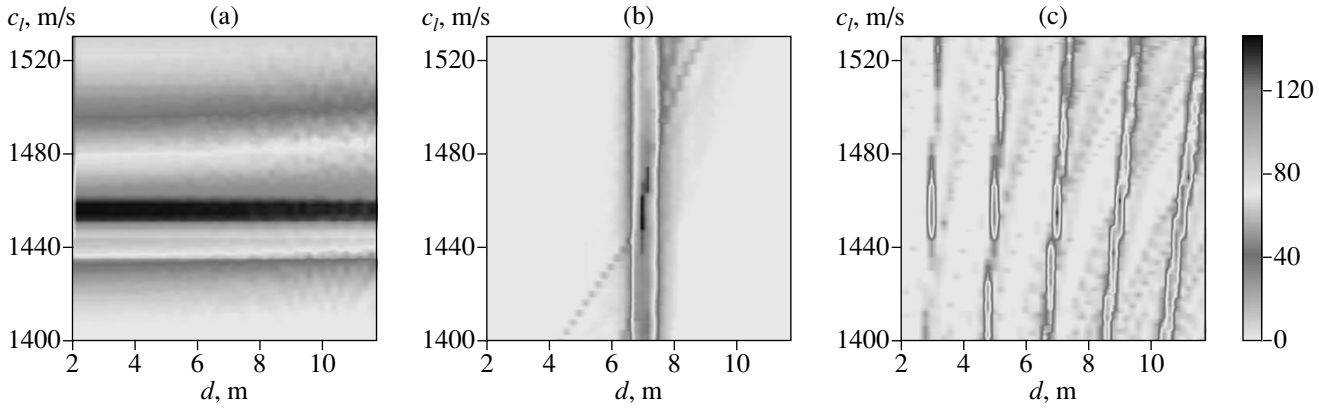

Fig. 4. Parameters c_l and ρ_∞ evaluated from different resonance characteristics: (a) the resonance amplitude A, (b) the resonance half-width $\Gamma/2$, and (c) the resonance frequency F_r.

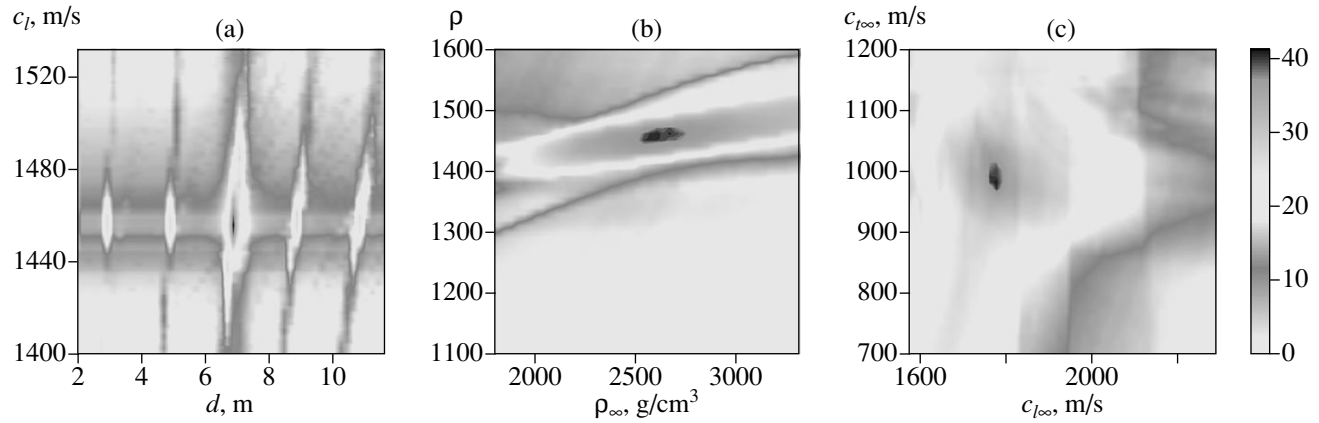

Fig. 5. Evaluation of the parameters of a layered bottom with the simultaneous use of A, $\Gamma/2$, and F_r: (a) the determination of c_l and d, (b) the determination of ρ and ρ_∞, and (c) the determination of $c_{l\infty}$ and $c_{t\infty}$.

the resonance frequencies falls within this relatively broad peak. This fact eliminates the ambiguity in the reconstruction of the bottom parameters with the use of the function ϕ given in Fig. 4c and thus ensures a high-precision determination of the bottom parameters. Figures 5a–5c clearly illustrate the advantages of the simultaneous use of several resonance characteristics for reconstructing the parameters of the bottom.

The shape of the peak of the function ϕ in Fig. 5b indicates that the effect of the half-space density on the resonance characteristics is less prominent than the effect of the density of the sedimentary layer. The size of the peak of the function ϕ along the ρ_∞ axis is several times greater than along the ρ axis. In a similar manner, one can infer from Fig. 5c that the longitudinal and transverse velocities of sound in the underlying half-space are comparable in terms of their effects on the resonance characteristics. The coordinates of the peaks of the function ϕ in Figs. 5b and 5c determine the values of the parameters of the medium. The results obtained with the proposed technique agree well with the initial data. Simulations showed that this technique is appropriate for determining the material parameters of the layer and half-space within the limits of the model used. We performed the simulations using the data typical of geoacoustic characteristics of the sea bottom. A detailed investigation of the analytical expressions for the reflection coefficient in terms of the Breit–Wigner variables and further development of the related resonance techniques for evaluating the parameters of layered elastic media is the subject of future research.

Thus, in this paper we studied the resonance characteristics of the reflection coefficient of a plane wave reflected from a layered elastic bottom. We proposed a procedure for evaluating the parameters of the layered elastic bottom from the resonance characteristics. The procedure was used to evaluate the parameters of the layered elastic bottom from the resonance characteristics of the reflection coefficient with the use of simulated data with artificially introduced errors. It was shown that individual resonance characteristics can be successfully used for evaluating the bottom characteristics. However, a simultaneous use of several resonance

characteristics considerably improves the precision of the reconstruction.

ACKNOWLEDGMENTS

This work was supported by the Russian Foundation for Basic Research, project no. 00-05-64956.

REFERENCES

1. A. Tolstoy and N. R. Chapman, in *Proceedings of the 4th European Conference on Underwater Acoustics* (1998), Vol. 1, p. 347.
2. P. J. Papadakis and G. S. Piperakis, in *Proceedings of the 3rd European Conference on Underwater Acoustics* (1996), Vol. 2, p. 619.
3. M. Siderius and P. L. Nielsen, in *Proceedings of the 5th European Conference on Underwater Acoustics* (2000), Vol. 1, p. 197.
4. S. E. Dosso and M. J. Wilmut, in *Proceedings of the 5th European Conference on Underwater Acoustics* (2000), Vol. 1, p. 185.
5. R. M. Dizaji, N. R. Chapman, and R. L. Kirlin, J. Acoust. Soc. Am. **111**, 800 (2002).
6. M. Snellen and D. G. Simons, in *Proceedings of the 5th European Conference on Underwater Acoustics* (2000), Vol. 1, p. 209.
7. A. Nagl, H. Überall, and W. R. Hoover, IEEE Trans. Geosci. Remote Sens. **20** (3), 332 (1982).
8. V. I. Volovov, *Sound Reflection from an Oceanic Bottom* (Nauka, Moscow, 1993).
9. D. M. F. Chapman and O. A. Godin, J. Acoust. Soc. Am. **110**, 1908 (2001).
10. R. Fiorito, W. Madigosky, and H. Überall, J. Acoust. Soc. Am. **69**, 897 (1981).
11. R. Fiorito, W. Madigosky, and H. Überall, J. Acoust. Soc. Am. **66**, 1857 (1979).
12. M. S. Fokina and V. N. Fokin, J. Comput. Acoust. **9** (3), 1079 (2001).
13. M. S. Fokina and V. N. Fokin, Akust. Zh. **46**, 690 (2000) [Acoust. Phys. **46**, 605 (2000)].
14. G. Breit and E. P. Wigner, Phys. Rev. **49**, 519 (1936).
15. V. N. Fokin and M. S. Fokina, J. Comput. Acoust. **9** (4), 1475 (2001).
16. V. N. Fokin and M. S. Fokina, Akust. Zh. **44**, 676 (1998) [Acoust. Phys. **44**, 585 (1998)].
17. L. A. Molotkov, *Matrix Method in the Theory of Wave Propagation in Elastic and Fluid Layered Media* (Nauka, Leningrad, 1984).
18. L. M. Brekhovskikh and O. A. Godin, *Acoustics of Layered Media*, 2nd ed. (Nauka, Moscow, 1989; Springer, Berlin, 1999).

Translated by A. Vinogradov

Acoustical Physics, Vol. 49, No. 5, 2003, pp. 592–594. Translated from Akusticheskiĭ Zhurnal, Vol. 49, No. 5, 2003, pp. 696–699.

Acoustic Properties of a Dielectric with Cavities in a Polarizing Electric Field

N. S. Shevyakhov

Institute of Radio Engineering and Electronics, Ul'yanovsk Branch, Russian Academy of Sciences, ul. Goncharova 48, Ul'yanovsk, 432011 Russia

e-mail: ufire@mv.ru

Received January 29, 2002

Abstract—The effect of an external polarizing electric field on the shear wave propagation in a centrosymmetric crystal with electrostriction, whose body is penetrated with parallel cylindrical cavities (pores), is considered. The cavities are distributed throughout the crystal at random and with a low density. The waves are assumed to be polarized along the cavity generatrices, and the wave propagation occurs in the elastic isotropy plane, which is orthogonal to the cavity axes. The external field is assumed to be axial. Possibility of controlling the propagation of shear waves by the polarizing field is demonstrated for the case of metallized cavity surfaces.

The well-known method of controlling the acoustic channels of solid-state acoustoelectronic devices is based on the use of electrostriction. Specifically, with a static polarizing field one can noticeably change the propagation velocity of bulk [1] and surface [2] acoustic waves in centrosymmetric crystals with a high dielectric permittivity. Using microwave radiation, one can cause the generation of surface acoustic waves (SAW) [3, 4] or parametrically excite acoustic vibrations of dielectric resonators [5]. It was also shown [6] that, owing to the "piezoelectric effect" induced and, hence, controlled by the external field [7, 8], electrostriction allows one to affect the scattering of acoustic waves by single inhomogeneities in $BaTiO_3$-type centrosymmetric crystals. The possibility of controlling the sound scattering in this way seems to be promising for the development of artificial (composite) media, whose effective acoustic properties can be predetermined by controlling the scattering of acoustic waves from the inhomogeneities of the material with the use of the external polarizing field.

In recent years, the effective properties of heterophase piezoelectric media attracted much attention [9, 10]. However, it still remains unclear how efficient and in what way the acoustic scattering controlled through the induced piezoelectric effect affects the characteristics of an artificial material with electrostriction. In this paper, the scalar theory of multiple scattering [11] and the results of the previous study [6] are used to describe the properties of an artificial medium in the form of a dielectric crystal containing parallel cavities of a single radius R. As in the cited paper [6], the cavity axes are assumed to coincide with the direction of one of the crystallographic symmetry axes of the paraelectric under study, which is assumed to belong to the cubic system. An external polarizing field $\mathbf{E}_0$ is applied along the cavity axes. The propagation of a shear wave with an axial particle displacement $\mathbf{u} \parallel \mathbf{E}_0$ occurs in the plane in which the elastic properties of the crystal are isotropic, this plane being orthogonal to the cavity axes.

The propagation geometry described above retains the type of the wave after its scattering from each cavity. This property is a necessary condition for the application of the scalar theory of multiple scattering [11]. Another requirement, which implies the relative weakness of the rescattering of acoustic waves from the cavities and the possibility of using the approximation of scattering with low multiplicity, is the limitation $kd \gg 1$, where k is the shear wave number in the homogeneous dielectric and d is the average distance between the cavities. The same condition allows one, in considering the scattering, to neglect the mutual induction effect of piezoelectric polarization charges arising at the cavity boundaries.[1] Specifically, from the asymptotics of a single-scattered field in the far wave zone [6], it follows that this field decreases as $1/\sqrt{kr}$, while the electric field potential of the piezoelectric polarization charges decreases as $1/kr$ (even for the dipole term characterized by the slowest decrease), where $kr \gg 1$ according to the aforementioned condition and r is the distance from the cavity axis.

From the point of view of controlling the characteristics of the medium through the scattering, the adopted random distribution of the cavities most widely differs from the optimal one because of the absence of the

[1] The case of $k\bar{d} \sim 1$, when the mutual effect of piezoelectric polarization charges is considerable, qualitatively corresponds to the weak localization of the wave by random inhomogeneities in nonconducting piezoelectrics [12].

1063-7710/03/4905-0592$24.00 © 2003 MAIK "Nauka/Interperiodica"

coherent component in the phases of the combined oscillations of the rescattered fields. Hence, the loss introduced by the scattering, which reduces the quality of the material, is highest in this case. This means that the corresponding estimate is the estimate "from below," and the loss should be reduced if the distribution of cavities is ordered to a certain extent.

When the scattering of a shear wave by the cavities is characterized by a low multiplicity, the effective wave number K of this wave propagating in the artificial medium is expressed as [11]

$$K \simeq k\sqrt{\left[1 + 2\frac{q}{\xi^2} f_s(0)\right]^2 - 4\frac{q^2}{\xi^4} f_s^2(\pi)}, \qquad (1)$$

where $\xi = kR$ is the wave size of a cavity, $q = \pi R^2 n_0$ is the specific volume of cavities, and n_0 is the concentration of cavities. Formula (1) also contains the values of the scattering function

$$f_s(\theta) = a_0 + 2\sum_{m=1}^{\infty} a_m \cos(m\theta) \qquad (2)$$

for the polar angles $\theta = 0$ and π, which correspond to the forward and backward scattering, respectively. The amplitude coefficients a_m of the partial scattered waves are determined by the expression [6]

$$a_m = -\frac{\xi J_m'(\xi) + m\mathcal{K}^2(1 + \varepsilon_2/\varepsilon_1)^{-1} J_m(\xi)}{\xi H_m^{(1)'}(\xi) + m\mathcal{K}^2(1 + \varepsilon_2/\varepsilon_1)^{-1} H_m^{(1)}(\xi)}. \qquad (3)$$

Here, standard notations are used for cylindrical functions and their derivatives; $\mathcal{K}^2 = a^2 E_0^2/16\pi\varepsilon_2\mu^*$ is the square of the electromechanical coupling coefficient, where $\mu^* = \mu + a^2 E_0^2/16\pi\varepsilon_2$; μ is the shear modulus of the dielectric; $a \approx \varepsilon_2^2/3$ is the electrostriction coefficient [7, 8]; and ε_2 and ε_1 are the permittivities of the dielectric and the gaseous medium filling the cavities, respectively.

Along with the relation $\xi = \xi_0(1 - \mathcal{K}^2)^{1/2}$ (ξ_0 is the wave size of a cavity in the absence of the polarizing field), expressions (1)–(3) allow one to determine the effective acoustic parameters of the artificial medium: the phase velocity of shear waves $V = \omega/\mathrm{Re}(K)$, where ω is the cyclic frequency, and the absorption coefficient for these waves $\alpha = \mathrm{Im}(K)$. At fixed q and ξ_0 and with a given permittivity ratio $\varepsilon_2/\varepsilon_1$, it is possible to obtain the dependences $V = V(E_0)$ and $\alpha = \alpha(E_0)$ and to estimate the efficiency of the control effect of the polarizing field. The calculations were performed for $BaTiO_3$ with the following parameters: $\mu = 2 \times 10^{11}$ dyn/cm^2, $\varepsilon_2 = 5000$, and $c_t = 2 \times 10^5$ cm/s (c_t is the shear wave velocity in the absence of the polarizing field); $q \ll 1$ was set according to the condition $kd \gg 1$. In combination with the limitation $\xi_0 < 1$, this condition provided the required smallness of the single scattering of a shear wave from the cavities located (on average) in the Fresnel zones with respect to each other.

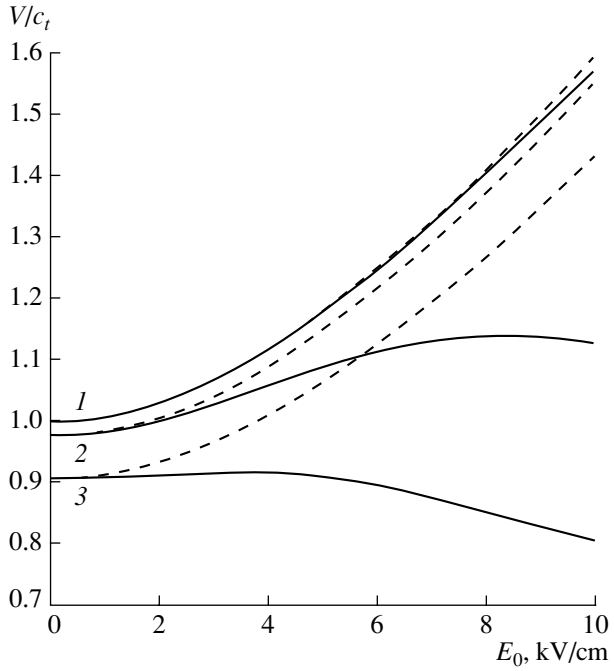

Fig. 1. Phase velocity of shear waves in a medium with cavities versus the polarizing field: q = (*1*) 0.01, (*2*) 0.05, and (*3*) 0.1.

Figure 1 shows the typical dependences of the shear wave phase velocity in the medium with cavities on the applied polarizing field below the breakdown field strength for the material. The density and radius of the cavities were chosen so as to retain the value $\xi_0 = 0.25$. The solid curves correspond to the case of metallized ($\varepsilon_1 \longrightarrow \infty$) cavities; the dashed curves, to cavities with vacuum or strongly rarefied gas ($\varepsilon_1 = 1$).

The difference in the behavior of the dependences $V(E_0)$ (Fig. 1) for media with metallized and nonmetallized cavities reflects the duality of the polarizing field manifestation in the scattering events, which was mentioned in [6]. First, the polarizing field causes an increase in the shear modulus up to the value μ^* and, hence, leads to a decrease in the wave size ξ of the cavities. Second, the possible response to the near-boundary electric oscillations excited at $E_0 \neq 0$ leads to qualitative changes in the wave scattering by the cavities. These changes are described by the second terms in the numerator and denominator of formula (3) and are considerable for metallized cavities and minor for nonmetallized cavities because of the very small value of the quantity $\mathcal{K}^2(1 + \varepsilon_2/\varepsilon_1)^{-1}$.

When the quantity q is very small, the role of the scattering is insignificant and the difference between the properties of media with metallized and nonmetallized cavities vanishes. Therefore, curves *1* in Fig. 1 almost completely reproduce the parabolic dependence

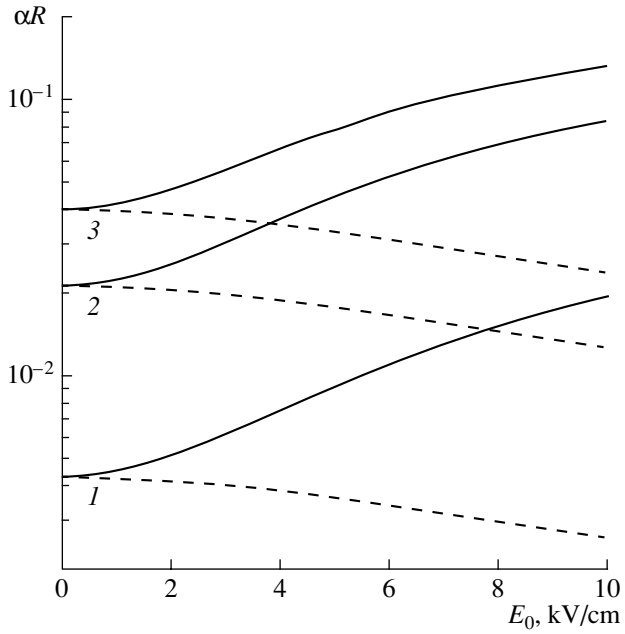

Fig. 2. Attenuation coefficient for shear waves in a medium with cavities versus the polarizing field: q = (*1*) 0.01, (*2*) 0.05, and (*3*) 0.1.

$V(E_0)$ characteristic of waves propagating in a homogeneous electrostrictive material [7, 8]. From the total shift of curves *2* and *3* in Fig. 1 in the downward direction, it follows that the role of the porosity of the paraelectric without metallization of the cavity surfaces consists in the "softening" of the medium due to the perforation. In this sense, a dielectric with an induced piezoelectric effect does not differ from a common nonpiezoelectric material. This result agrees well with the notion that the manifestation of the piezoelectric effect in the wave scattering from a nonmetallized cavity is rather weak. The fact that the growth of V with increasing E_0 is retained can be explained in this case by the seeming decrease in the porosity of the material because of the renormalization of ξ.

In the case of metallized cavities, the effect of the near-boundary electric oscillations on the scattering is noticeable and manifests itself as an increase in the scattering cross section of the cavities [13]. Therefore, the behavior of the solid curves in Fig. 1 represents the result of the combined action of opposite factors: the growth of V with increasing E_0 because of the decrease in scattering due to the renormalization of ξ and the decrease in V in stronger polarizing fields because of the enhancement of scattering under the effect of the near-boundary electric oscillations. If q is very small, the effect of the second factor, which reduces the value of V, manifests itself only in strong polarizing fields as a slight decrease in the rate of growth of the dependence $V(E_0)$: the solid curve *1* lies somewhat below the dashed curve *1* in the region of strong polarizing fields. When the concentration of metallized cavities is relatively high, such a decrease in the growth rate of the dependence $V(E_0)$ with its subsequent drop is possible even in moderate (curve *2*) or weak (curve *3*) fields E_0. In the latter case, it is precisely the effect of the qualitative change in the wave scattering by the cavities that governs the formation of the effective properties of the artificial microinhomogeneous medium.

Figure 2 presents the dependences of the absorption coefficient on the polarizing field for shear waves propagating in a medium with cavities (the curves in Fig. 2 correspond to those in Fig. 1). One can see that, in the cases under consideration, the attenuation due to the wave scattering proves to be fairly weak: $\alpha R < 0.1$. A characteristic feature of the curves $\alpha(E_0)$ is their separation according to the factors that govern the scattering. Namely, for metallized cavities, because of the enhancement of their scattering properties due to the excitation of near-boundary electric oscillations, the dependences $\alpha(E_0)$ represented by the solid lines exhibit a steady growth. The dashed curves $\alpha(E_0)$, which correspond to nonmetallized cavities, decrease because of the predominance of the renormalization of ξ under the effect of the polarizing field, which reduces the scattering and, hence, reduces the scattering loss.

REFERENCES

1. A. A. Demidenko, A. P. Zdebskiĭ, V. N. Piskovoĭ, and N. S. Chernaya, Ukr. Fiz. Zh. **27** (11), 1737 (1982).
2. Yu. V. Gulyaev, A. V. Ermolenko, B. D. Zaĭtsev, *et al.*, Akust. Zh. **35**, 154 (1989) [Sov. Phys. Acoust. **35**, 93 (1989)].
3. E. V. Balashova and A. V. Sherman, Pis'ma Zh. Tekh. Fiz. **9** (2), 108 (1983) [Sov. Tech. Phys. Lett. **9**, 48 (1983)].
4. G. N. Burlak and T. N. Pustyl'nik, Akust. Zh. **27**, 307 (1981) [Sov. Phys. Acoust. **27**, 168 (1981)].
5. G. V. Belokopytov, V. N. Semenenko, and V. A. Chistyaev, Izv. Vyssh. Uchebn. Zaved., Radiofiz. **33** (4), 417 (1990).
6. N. S. Shevyakhov, Akust. Zh. **32**, 136 (1986) [Sov. Phys. Acoust. **32**, 84 (1986)].
7. S. I. Pekar, Zh. Éksp. Teor. Fiz. **49** (2), 621 (1965) [Sov. Phys. JETP **22**, 431 (1966)].
8. Yu. V. Gulyaev, Fiz. Tverd. Tela (Leningrad) **9** (6), 1816 (1967) [Sov. Phys. Solid State **9**, 1425 (1967)].
9. Ce-Wen Nan and Fu-Sheng Jin, Phys. Rev. B **48** (12), 8578 (1993).
10. O. Lacour and M. Lagier, J. Acoust. Soc. Am. **96**, 3548 (1994).
11. R. Truell, C. Elbaum, and B. B. Chick, *Ultrasonic Methods in Solid State Physics* (Academic, New York, 1969; Mir, Moscow, 1972).
12. M. B. Gitis, Yu. V. Gulyaev, and I. A. Chaĭkovskiĭ, Dokl. Akad. Nauk SSSR **301** (6), 1370 (1988) [Sov. Phys. Dokl. **33**, 617 (1988)].
13. N. S. Shevyakhov, Akust. Zh. **44**, 855 (1998) [Acoust. Phys. **44**, 747 (1998)].

Translated by E. Golyamina

Acoustical Physics, Vol. 49, No. 5, 2003, pp. 595–604. Translated in Akusticheskiĭ Zhurnal, Vol. 49, No. 5, 2003, pp. 700–710.

Effect of Thermal Conductivity on Ultrasonic Attenuation in Praseodymium Monochalcogenides

Raja Ram Yadav and Devraj Singh

Department of Physics, University of Allahabad, Allahabad –211 002 (INDIA)

e-mail: rryadav1@rediffmail.com;
devraj2001@rediffmail.com

Received June 17, 2002

Abstract—The ultrasonic attenuation in intermetallic praseodymium monochalcogenides are evaluated in the temperature interval 100–500 K along the crystallographic directions ⟨100⟩, ⟨110⟩, and ⟨111⟩ for longitudinal and shear waves. A comparison has been made with lanthanum monochalcogenides and other similar materials. Ultrasonic attenuation at different temperatures is mainly affected by the lattice thermal conductivity values of the materials at these temperatures. Thermoelastic loss is very small in comparison to the attenuation due to phonon–phonon interaction mechanism at higher temperatures. *© 2003 MAIK "Nauka/Interperiodica".*

INTRODUCTION

Anomalous physical properties in rare-earth monochalcogenides RX (R = La, Ce, Pr, Sm, …; X = S, Se, and Te) were given considerable attention during the 1960s–1970s [1–3] because they are typical low carrier, strongly correlated systems with a simple NaCl-type structure. Intermetallic praseodymium monochalcogenides are widely used as a core material for carbon arcs used by the motion picture industry for studio lighting projection [3, 4]. Ultrasonics offers the possibility to detect and characterize microstructural properties, as well as flaws in materials, controlling material behavior on the basis of a physical mechanism that predicts future performance of the materials. Structural inhomogenities, elastic parameters, precipitates, dislocations, grain, phase transformation, porosity, cracks, electrical resistivity, thermal conductivity, etc., are well connected with the frequency or temperature dependence of ultrasonic attenuation and evaluations of velocity. In the present paper, some characteristic microstructural thermophysical parameters that make a considerable contribution to the temperature dependence of ultrasonic attenuation in PrS, PrSe, and PrTe along the ⟨100⟩, ⟨110⟩, and ⟨111⟩ orientations are discussed. For this analysis, we have evaluated ultrasonic attenuation with other associated parameters, as well as second- and third-order elastic constants (SOEC and TOEC), as a function of higher temperatures.

THEORY OF PRESENT EVALUATION

In evaluating ultrasonic absorption, second- and third-order elastic constants (SOEC and TOEC) play an important role. We calculated SOEC and TOEC following Brugger's definition of elastic constants at absolute zero (C_{IJ}^0 and C_{IJK}^0) [5, 6]. The SOEC and TOEC at various higher temperatures are obtained by the method developed by Leibfried and Haln, Ludwig, and Hiki and Ghate [7–11] for NaCl-type crystals, since praseodymium monochalcogenides have well-developed crystal structures of the NaCl type. Our lattice parameters were very close to others in the literature [3, 12–14]. The praseodymium monochalcogenides are compounds with ionic-metallic type bonding [3]. Here, it is assumed that $\phi_{\mu\nu}(r)$ is the interaction potential equal to the sum of the Coulomb potential and the Born–Mayer short-range repulsive potential, i.e.,

$$\phi_{\mu\nu}(r) = \pm (e^2/r) + A\exp(-r/b).$$

Here, e is the electronic charge, r is the nearest neighbor distance, the ± signs apply to like and unlike charges, and A and b are the parameters. We further assume that A and b are the same for interactions between like (positive or negative) and unlike ions [9–11]. All the formulations used in the calculation of SOEC and TOEC of PrS, PrSe, and PrTe are the same as those in our previous paper [15].

The second part of our present investigation was to establish a theory for the evaluation of ultrasonic attenuation in PrS, PrSe, and PrTe describing some characteristic features of these materials. The Mason and Bateman theory [16, 17] is still being widely used to study ultrasonic attenuation at higher temperatures (≅300 K) in praseodymium monochalcogenides. It is a more reliable theory for studying the anharmonicity of crystals as it directly involves elastic constants through the nonlinearity parameter D in the evaluation of ultrasonic absorption coefficient (α).

1063-7710/03/4905-0595$24.00

Table 1. Second and third-order elastic constants (SOEC & TOEC) [10^{11} dyn/cm^2] of PrS in the temperature range of 100–500 K

Temp (K)	100	200	300	400	500
C_{11}	4.757	4.905	5.069	5.237	5.409
C_{12}	1.352	1.279	1.205	1.132	1.058
C_{44}	1.432	1.438	1.433	1.450	1.456
C_{111}	−75.576	−76.191	−76.972	−77.800	−78.686
C_{112}	−5.543	−5.272	−4.999	−4.726	−4.453
C_{123}	1.936	1.515	1.095	0.675	0.255
C_{144}	2.374	2.392	2.411	2.429	2.447
C_{166}	−5.849	−5.871	−5.896	−5.922	−5.949
C_{456}	2.355	2.355	2.355	2.355	2.355

Table 2. Second- and third-order elastic constants (SOEC & TOEC) [10^{11} dyn/cm^2] of PrSe in the temperature range of 100–500 K

Temp (K)	100	200	300	400	500
C_{11}	4.550	4.651	4.741	4.945	5.104
C_{12}	1.142	1.074	1.001	0.931	0.859
C_{44}	1.224	1.228	1.231	1.237	1.242
C_{111}	−73.102	−73.331	−73.375	−74.639	−75.418
C_{112}	−4.639	−4.396	−4.118	−3.848	−3.572
C_{123}	1.609	1.185	0.758	0.332	0.095
C_{144}	2.056	2.071	2.087	2.103	2.119
C_{166}	−4.990	−5.002	−5.013	−5.042	−5.064
C_{456}	2.039	2.039	2.039	2.039	2.039

The thermal relaxation time [16, 17] for a longitudinal wave is twice that of a shear wave,

$$\tau_{th} = \tau_{sh} = \frac{1}{2}\tau_{long} = \frac{3K}{C_V \bar{V}^2}, \quad (1)$$

where K is thermal conductivity, C_V is the specific heat per unit volume, and $\bar{V}$ is the Debye average velocity of ultrasonic wave as

$$\frac{3}{\bar{V}^3} = \frac{1}{V_1^3} + \frac{2}{V_S^2}. \quad (2)$$

Thermoelastic loss [16, 17] is obtained by

$$(\alpha/f^2)_{th} = \frac{4\pi^2 \langle \gamma_i^j \rangle^2 KT}{2\rho V_{long}^5}, \quad (3)$$

where $\langle \gamma_i^j \rangle$ is the average Gruneisen numbers, j is the direction of propagation, and i is the mode of propagation. $\langle \gamma_i^j \rangle$ is related to SOEC and TOEC [16]. ρ is the density of the material, and T is the temperature in Kelvins.

The ultrasonic absorption coefficient over frequency squared $(\alpha/f^2)_{Akh}$ (Akhieser type loss) is given by $(\omega\tau \le 1)$ [15–17]

$$(\alpha/f^2)_{Akh} = \frac{E_0 (D/3) 4\pi^2 \tau}{2\rho V^3}, \quad (4)$$

where

$$D = 9\langle (\gamma_i^j)^2 \rangle - (3\langle \gamma_i^j \rangle^2 C_V T)/E_0. \quad (5)$$

Here, D is the nonlinearity parameters for a longitudinal and shear wave, and E_0 is the thermal energy density evaluated from values of C_V from physical constant tables.

RESULTS AND DISCUSSIONS

The first parts of SOEC and TOEC (C_{IJ} and C_{IJK}) at different temperatures are evaluated from the nearest neighbor distance (short-range parameter) [3–12] r_0 = 2.855 Å, 2.96 Å, and 3.14 Å, for PrS, PrSe, and PrTe, respectively, and the Born parameter (hardness parameter) b = 0.315 Å in all three. The Born parameter was determined as in a previous paper [15].

All the computed values of SOEC and TOEC of PrS, PrSe, and PrTe at 100–500 K are presented in Tables 1, 2, and 3, respectively.

SOEC and TOEC of PrS, PrSe, and PrTe are slightly higher than those of like compounds LaS, LaSe, and LaTe, respectively, at all temperatures [15]. Thus, the theory for the calculation of SOEC and TOEC at different temperatures is well established, this is also discussed in our previous paper [15]. There are no experimental values for elastic constants; therefore, comparison with experimental data was not possible.

However, taking full account of many interactions, including van der Waals interactions between ions, as well as considering the nonlinearity of the materials up to a certain point, may further improve the calculated results of TOEC [18].

The values of ultrasonic velocities (V_l and V_S) evaluated with the values of second-order elastic constants, the Debye average velocity ($\bar{V}$), the thermal relaxation time (τ_{th}) and thermal conductivity (K), the specific heat

Table 3. Second- and third-order elastic constants (SOEC & TOEC) [10^{11} dyn/cm^2] of PrTe in the temperature range of 100–500 K

Temp (K)	100	200	300	400	500
C_{11}	4.002	4.120	4.263	4.413	4.567
C_{12}	0.870	0.803	0.734	0.666	0.597
C_{44}	0.944	0.947	0.951	0.955	0.959
C_{111}	−66.779	−67.205	−67.897	−68.67	−69.484
C_{112}	3.499	−3.232	−2.954	−2.674	−2.395
C_{123}	1.173	0.737	0.300	0.136	−0.573
C_{144}	1.623	1.635	1.648	1.661	1.673
C_{166}	−3.816	−3.829	−3.846	−3.863	−3.880
C_{456}	1.610	1.610	1.610	1.610	1.610

Table 4. Density (ρ) in g/cm^3, thermal conductivity (K) in 10^5 erg/cm s K, specific heat (C_V) in 10^8 erg/cm^3 deg, internal energy (E_0) in 10^8 erg/cm^3, longitudinal and shear velocities (V_l and V_S) in 10^5 cm/s, Debye average velocity ($\bar{V}$) in 10^5 cm/s, and thermal relaxation time (τ_{th})in 10^{-11} s of PrS in the temperature range of 100–500 K

Temp. (K)	100	200	300	400	500
ρ	6.225	6.201	6.173	6.160	6.154
K	8.400	11.574	13.813	15.400	15.464
C_V	7.300	8.430	8.710	8.770	8.670
E_0	3.800	11.850	20.397	29.101	37.888
V_l	2.764	2.813	2.866	2.916	2.965
V_S	1.517	1.523	1.529	1.534	1.538
	1.671	1.769	1.689	1.695	1.701
τ_{th}	1.237	1.444	1.671	1.834	1.849

Table 5. Density (ρ) in g/cm^3, thermal conductivity (K) in 10^5 erg/cm s K, specific heat (C_V) in 10^8 erg/cm^3 deg, internal energy (E_0) in 10^8 erg/cm^3, longitudinal and shear velocities (V_l and V_S) in 10^5 cm/s, Debye average velocity ($\bar{V}$) in 10^5 cm/s, and thermal relaxation time (τ_{th})in 10^{-11} s of PrSe at the temperature range 100–500 K

Temp (K)	100	200	300	400	500
ρ	7.205	7.102	7.042	6.932	6.812
K	5.413	7.280	8.960	9.520	9.927
C_V	7.010	7.760	7.871	7.812	7.573
E_0	3.942	11.357	19.055	26.546	33.799
V_l	2.513	2.559	2.595	2.671	2.737
V_S	1.303	1.315	1.322	1.336	1.350
$\bar{V}$	1.442	1.455	1.464	1.481	1.498
τ_{th}	1.115	1.329	1.594	1.668	1.753

Table 6. Density (ρ) in g/cm^3, thermal conductivity (K) in 10^5 erg/cm s K, specific heat (C_V) in 10^8 erg/cm^3 deg, internal energy (E_0) in 10^8 erg/cm^3, longitudinal and shear velocities (V_l and V_S) in 10^5 cm/s, Debye average velocity ($\bar{V}$) in 10^5 cm/s, and thermal relaxation time (τ_{th}) in 10^{-11} s of PrTe in the temperature range of 100–500 K

Temp (K)	100	200	300	400	500
ρ	7.40	7.305	7.204	7.101	7.015
K	4.667	6.347	7.653	8.400	8.973
C_V	6.191	6.624	6.631	6.583	6.500
E_0	3.777	10.162	16.608	22.925	29.199
V_l	2.324	2.375	2.433	2.493	2.552
V_S	1.129	1.139	1.152	1.160	1.169
$\bar{V}$	1.254	1.265	1.280	1.291	1.302
τ_{th}	1.440	1.800	2.113	2.299	2.443

per unit volume (C_V), and thermal energy density (E_0) are presented in Tables 4, 5, and 6.

All the calculated values of the average Gruneisen number $\langle \gamma_i^j \rangle$, average square Gruneisen number $\langle (\gamma_i^j)^2 \rangle$, and nonlinearity parameter (D) along ⟨100⟩, ⟨110⟩, and ⟨111⟩ directions are presented in Tables 7, 8, and 9. All of the calculated values of the temperature dependence of $(\alpha/f^2)_{th}$, $(\alpha/f^2)_{Akh.long}$, and $(\alpha/f^2)_{Akh.shear}$ are presented in Tables 10, 11, and 12. The evaluated values (α) at 900 MHz and room temperature in dB/μs of PrS, PrSe, and PrTe compared with those of LaS, LaSe, and LaTe, as well as with the experimental of LiF, are shown in Table 13.

The temperature dependence of nonlinearity parameters (D) is shown in Figs. 1–7. The temperature dependences of the ultrasonic attenuation coefficient over the frequency squared (α/f^2) for PrS, PrSe, and PrTe along all three crystallographic orientations are shown in Figs. 8–17.

Second-order elastic constants, thermal relaxation time, nonlinearity parameters, and thermal conductivity make considerable contributions to the ultrasonic absorption in PrS, PrSe and PrTe.

Because all second- and third-order elastic constants (SOEC and TOEC) of PrS, PrSe, and PrTe at 100–500 K are slightly larger than those of LaS, LaSe, and LaTe at 100–500 K [15]. Therefore, the values of ultrasonic velocities (V_l, V_S, and $\bar{V}$) will be larger than those

Table 7. Average of ultrasonic Gruneisen parameters ($\langle \gamma_i^j \rangle_l$ for longitudinal wave), average of square ultrasonic Gruneisen parameters ($\langle (\gamma_i^j)^2 \rangle_{long}$ for longitudinal wave and $\langle (\gamma_i^j)^2 \rangle_{Shear}$ for shear wave) and acoustic coupling constants (D_l for longitudinal wave and D_S for shear wave) of PrS, PrSe, and PrTe in the temperature range of 100–500 K along the ⟨100⟩ crystallographic direction

Material	Temp (K)	$\langle (\gamma_i^j)^2 \rangle$	$\langle (\gamma_i^j)^2 \rangle_l$	$\langle (\gamma_i^j)^2 \rangle_S$	D_l	D_S
PrS	100	0.519	2.064	0.142	17.024	1.278
	200	0.501	1.942	0.140	16.394	1.260
	300	0.483	1.833	0.138	15.600	1.242
	400	0.462	1.740	0.137	14.888	1.233
	500	0.452	1.648	0.134	14.131	1.206
PrSe	100	0.511	2.094	0.136	17.453	1.224
	200	0.496	1.992	0.135	16.919	1.215
	300	0.482	1.900	0.134	16.236	1.206
	400	0.464	1.790	0.132	15.349	1.188
	500	0.448	1.703	0.131	14.650	1.178
PrTe	100	0.514	2.260	0.133	19.041	1.197
	200	0.496	2.135	0.132	18.253	1.188
	300	0.478	2.014	0.130	17.305	1.170
	400	0.461	1.909	0.129	16.449	1.161
	500	0.446	1.815	0.128	15.674	1.152

of lanthanum monochalcogenides, and the values of (α/f^2) will be smaller in comparison to the values of (α/f^2) in lanthanum monochalcogenides.

The thermal relaxation time (τ_{th}) for praseodymium monochalcogenides is smaller than that for lanthanum monochalcogenides.

Now, if we compare the values of the nonlinearity constant D between praseodymium and lanthanum monochalcogenides, the following features are seen:

(i) If we consider D_1, D_{S1}, and D_{S2}; the nonlinearity parameters along the ⟨110⟩ direction for a longitudinal wave, along ⟨110⟩ shear wave polarized along ⟨001⟩ and along ⟨110⟩ shear wave polarized along $\langle 1\bar{1}0 \rangle$.

(ii) The values of D_l for praseodymium monochalcogenides are smaller than those for lanthanum monochalcogenides.

(iii) The values of D_{S1} for praseodymium monochalcogenides are larger than those for lanthanum monochalcogenides.

(iv) The values of D_{S2} for praseodymium monochalcogenides are smaller than those for lanthanum monochalcogenides.

It is obvious from Tables 4, 5, and 6 and [15] that the values of thermal conductivity of PrS, PrSe, and PrTe are smaller than those of LaS, LaSe, and LaTe.

Thus, all of the parameters for PrS, PrSe, and PrTe at different temperatures contribute less towards the

Table 8. Average of ultrasonic Gruneisen parameters ($\langle (\gamma_i^j)^2 \rangle_l$ for longitudinal wave), average of square ultrasonic Gruneisen parameters ($\langle (\gamma_i^j)^2 \rangle_{long}$ for longitudinal wave, $\langle (\gamma_i^j)^2 \rangle_{Shear1}$ for shear wave polarized along the ⟨001⟩ direction, and $\langle (\gamma_i^j)^2 \rangle_{Shear2}$ for shear wave polarized along the $\langle 1\bar{1}0 \rangle$ direction), and acoustic coupling constants (D_l for longitudinal wave, D_{S1} for shear wave polarized along the ⟨001⟩ direction, and D_{S2} for shear wave polarized along the $\langle 1\bar{1}0 \rangle$ direction) for PrS, PrSe, and PrTe in the temperature range of 100–500 K range along the ⟨110⟩ crystallographic direction

Material	Temp (K)	$\langle (\gamma_i^j)^2 \rangle$	$\langle (\gamma_i^j)^2 \rangle_l$	$\langle (\gamma_i^j)^2 \rangle_{S1}$	$\langle (\gamma_i^j)^2 \rangle_{S2}$	D_l	D_{S1}	D_{S2}
PrS	100	−0.788	2.262	0.319	3.081	17.367	4.365	26.757
	200	−0.755	2.082	0.286	2.970	16.575	3.699	25.578
	300	−0.725	1.921	0.260	2.870	15.252	3.168	24.471
	400	−0.686	1.721	0.225	2.737	14.104	2.961	23.886
	500	−0.655	1.604	0.203	2.633	12.963	2.421	22.158
PrSe	100	−0.788	2.262	0.319	3.018	17.045	2.871	27.729
	200	−0.755	2.082	0.286	2.970	16.401	2.574	26.730
	300	−0.725	1.921	0.260	2.870	15.335	2.340	25.830
	400	−0.686	1.742	0.225	2.737	14.017	2.025	24.633
	500	−0.655	1.604	0.203	2.633	13.438	1.287	26.001
PrTe	100	−0.783	2.338	0.215	3.403	18.028	1.935	30.627
	200	−0.744	2.134	0.193	3.264	17.043	1.737	29.376
	300	−0.706	1.944	0.173	3.124	15.705	1.577	28.116
	400	−0.670	1.783	0.156	3.001	14.501	1.404	27.009
	500	−0.638	1.645	0.143	2.889	13.446	1.289	26.011

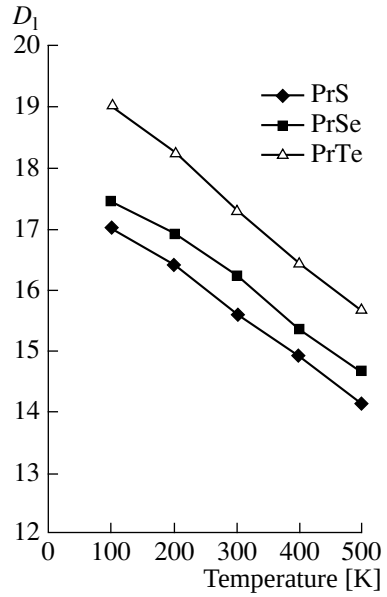

Fig. 1. D_l vs. temperature along the ⟨100⟩ direction.

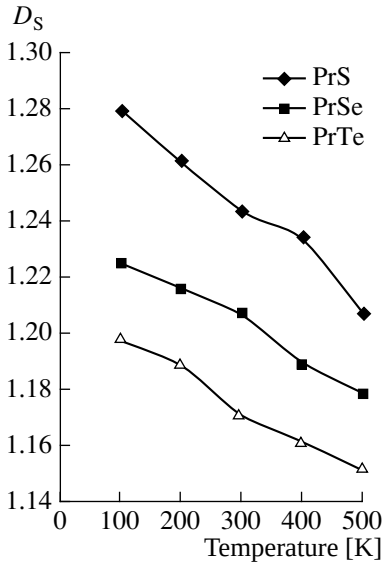

Fig. 2. D_S vs. temperature along the ⟨100⟩ direction.

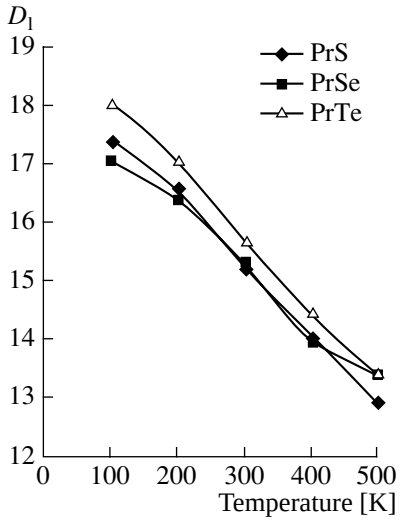

Fig. 3. D_l vs. temperature along the ⟨110⟩ direction.

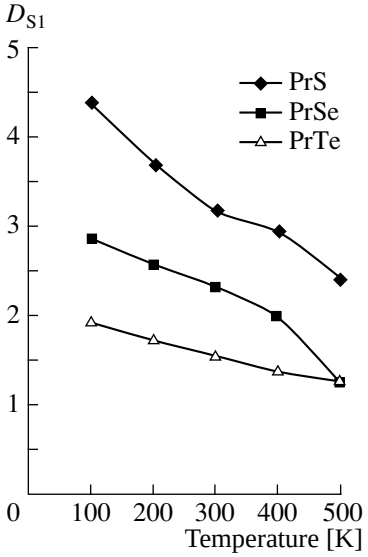

Fig. 4. D_{S1} vs. temperature along the ⟨110⟩ direction; shear wave polarized along the ⟨001⟩ direction.

ultrasonic absorption coefficients—$(\alpha/f^2)_{th}$, $(\alpha/f^2)_L$, and $(\alpha/f^2)_S$—in comparison with the case of LaS, LaSe, and LaTe, except for the nonlinearity parameter D_{S1}.

Therefore, as a result, it can be seen from Table 11 and [15] that the ultrasonic absorption coefficients in PrS, PrSe, and PrTe at 100–500 K along the ⟨110⟩ direction for a longitudinal wave and the ⟨110⟩ direction for a shear wave polarized along the $\langle 1\bar{1}0 \rangle$ are smaller than those values in LaS, LaSe, and LaTe, except along the ⟨110⟩ direction for a shear wave polarized along the ⟨001⟩ direction, where the values are larger.

It is also obvious from Fig. 4 in the present paper and Fig. 2 in [15] that D_{S1} is almost constant with temperature in the case of lanthanum monochalcogenides, while, in the case of praseodymium monochalcogenides, D_{S1} decreases with temperature and affects the temperature dependence of ultrasonic absorption along the ⟨110⟩ direction for a shear wave polarized along the ⟨001⟩ direction.

Table 9. Average of ultrasonic Gruneisen parameters ($\langle(\gamma_i^j)^2\rangle_l$ for longitudinal wave), average of square ultrasonic Gruneisen parameters ($\langle(\gamma_i^j)^2\rangle_{long}$ for longitudinal wave and $\langle(\gamma_i^j)^2\rangle_{Shear}$ for shear wave), and acoustic coupling constants (D_l for longitudinal wave and D_S for shear wave) PrS, PrSe, and PrTe in the temperature range of 100–500 K along the $\langle 111\rangle$ crystallographic direction. (* shear wave polarized along $\langle \bar{1}10\rangle$)

Material	Temp (K)	$\langle(\gamma_i^j)^2\rangle$	$\langle(\gamma_i^j)^2\rangle_l$	$\langle(\gamma_i^j)^2\rangle_S$	D_l	D_S
PrS	100	−0.630	1.883	2.005	14.659	18.045
	200	−0.603	1.723	1.918	13.955	17.262
	300	−0.578	1.581	1.837	12.945	16.533
	400	−0.549	1.463	1.796	12.077	16.164
	500	−0.533	1.348	1.695	11.157	15.255
PrSe	100	−0.625	1.848	2.080	14.548	18.720
	200	−0.602	1.713	2.007	13.931	18.063
	300	−0.581	1.592	1.942	13.073	17.478
	400	−0.555	1.455	1.855	12.008	16.695
	500	−0.533	1.348	1.787	11.174	16.083
PrTe	100	−0.639	2.452	2.300	20.061	20.700
	200	−0.612	1.768	2.210	14.448	19.890
	300	−0.585	1.616	2.118	13.314	19.062
	400	−0.560	1.486	2.038	12.264	18.342
	500	−0.538	1.372	1.965	11.382	17.685

Table 10. Ultrasonic attenuation due to phonon–phonon interaction [$(\alpha/f^2)_{Akh.long}$ for longitudinal wave and $(\alpha/f^2)_{Akh.shear}$ for shear wave] and due to thermoelastic loss $(\alpha/f^2)_{th}$ for PrS, PrSe, and PrTe in the temperature range of 100–500 K along $\langle 100\rangle$ in 10^{-18} Np s^2/cm

Crystal	Temp (K)	$(\alpha/f^2)_{th}$	$(\alpha/f^2)_{Akh.long}$	$(\alpha/f_2)_{Akh.shear}$
PrS	100	0.035	7.301	1.659
	200	0.096	24.400	5.907
	300	0.146	43.917	11.510
	400	0.186	62.411	17.744
	500	0.202	74.095	22.640
PrSe	100	0.035	8.048	2.023
	200	0.083	25.747	6.814
	300	0.136	48.096	13.501
	400	0.157	61.742	19.097
	500	0.172	74.562	24.996
PrTe	100	0.044	13.360	3.665
	200	0.102	40.873	12.069
	300	0.154	70.256	22.399
	400	0.188	94.565	33.150
	500	0.211	115.151	44.006

Table 11. Ultrasonic attenuation due to phonon–phonon interaction [$(\alpha/f^2)_{Akh.long}$ for longitudinal wave and $(\alpha/f^2)_{Akh.shear}$ for shear wave] and due to thermoelastic loss $(\alpha/f^2)_{th}$ PrS, PrSe, and PrTe in the temperature range of 100–500 K along $\langle 110\rangle$ in 10^{-18} Np s^2/cm

Crystal	Temp (K)	$(\alpha/f^2)_{th}$	$(\alpha/f^2)_{Akh.long}$	$(\alpha/f^2)^*_{Akh.shear_1}$	$(\alpha/f^2)^{\#}_{Akh.shear_2}$
PrS	100	0.0100	7.448	5.667	34.736
	200	0.228	24.961	17.547	121.335
	300	0.339	42.937	29.359	226.738
	400	0.408	59.125	42.611	343.738
	500	0.443	68.049	45.451	442.725
PrSe	100	0.084	7.860	4.744	45.820
	200	0.192	24.959	14.436	149.912
	300	0.307	45.426	26.195	289.965
	400	0.342	56.379	32.551	395.965
	500	0.347	68.394	27.285	551.239
PrTe	100	0.103	12.646	5.925	93.787
	200	0.229	38.161	17.647	298.451
	300	0.336	64.015	30.116	543.829
	400	0.397	83.647	40.089	771.194
	500	0.433	98.783	49.163	993.222

Note: * Shear wave polarized along the $\langle 001\rangle$ direction.

Shear wave polarized along the $\langle 1\bar{1}0\rangle$ direction.

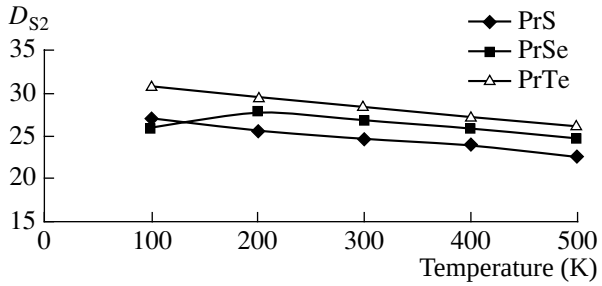

Fig. 5. D_{S2} vs. temperature along ⟨110⟩ the direction; shear wave polarized along the $\langle 1\bar{1}0\rangle$ direction.

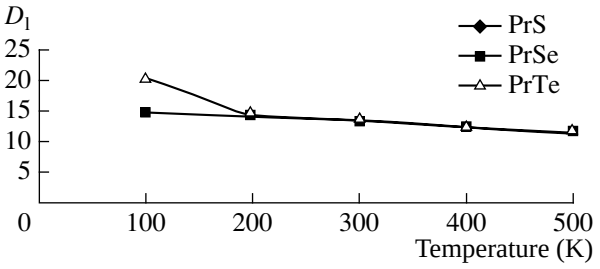

Fig. 6. D_l vs. temperature along the ⟨111⟩ direction.

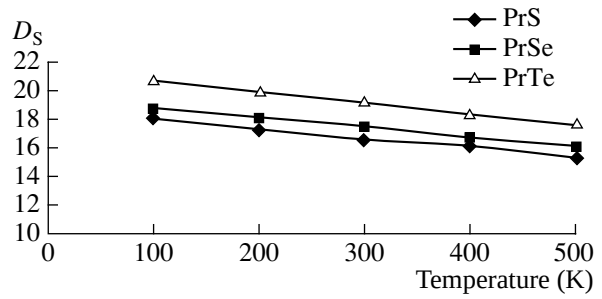

Fig. 7. D_S vs. temperature along the ⟨100⟩ direction.

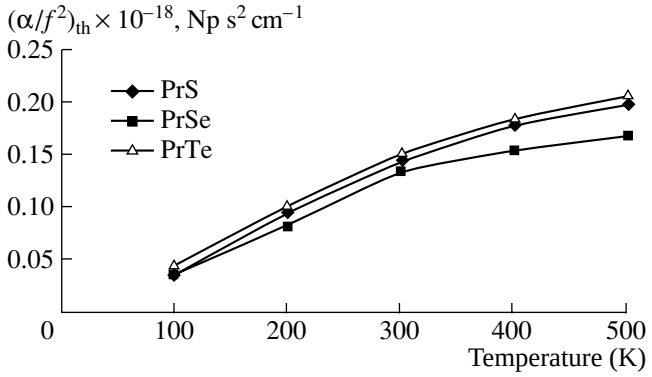

Fig. 8. $(\alpha/f^2)_{th}$ temperature along the ⟨100⟩ direction.

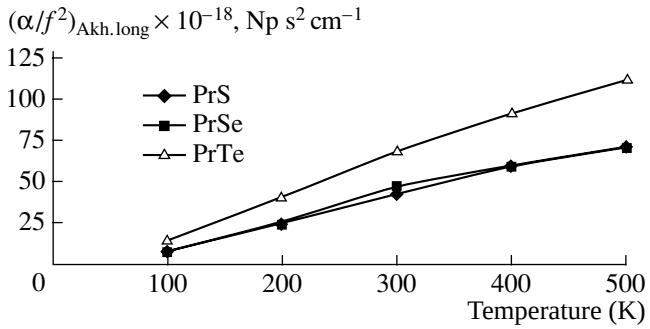

Fig. 9. $(\alpha/f^2)_{Akh.long}$ vs. temperature along the ⟨100⟩ direction.

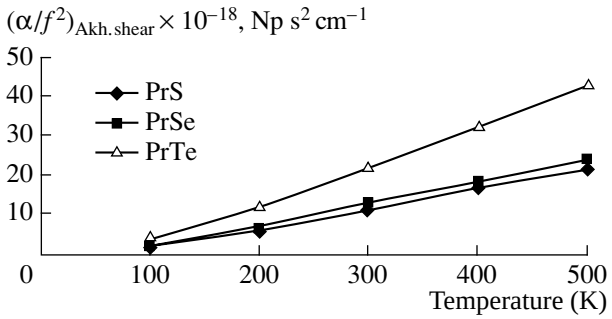

Fig. 10. $(\alpha/f^2)_{Akh.shear}$ vs. temperature along the ⟨100⟩ direction.

Also a comparison of α in dB/μs of PrS, PrSe, and PrTe with LiF (experimental) and LaS, LaSe, and LaTe for other orientations at room temperature at 900 MHz [19–21] is shown in Table 13.

In general, it is obvious from Tables 8–17 that the effect of higher temperature on the ultrasonic attenuation in PrS, PrSe, and PrTe is greater than that of LaS, LaSe, and LaTe.

It is obvious from Tables 5–7 that nonlinearity parameters *D* for all three substances decrease by very small values with temperature along all orientations. Therefore it contributes much less to the temperature dependence of absorption in PrS, PrSe, and PrTe.

Although experimental data of ultrasonic attenuation in PrS, PrSe, and PrTe are not available in the literature for comparison, comparison has been made with those values for LaS, LaSe, and LaTe, and can be made with other like substance with an NaCl structure. The experimental value [22] for ultrasonic attenuation in NaCl at room temperature and 100 MHz for a longitudinal wave is 0.2 dB/μs. In our calculations for the materials the ultrasonic attenuation values at 300 K become 0.10 dB/μs. Similarly, for a longitudinal wave along the ⟨110⟩ crystallographic direction, our calculated values for PrS, PrSe, and PrTe become 0.06 dB/μs at 100 MHz, and the experimental value for NaCl at

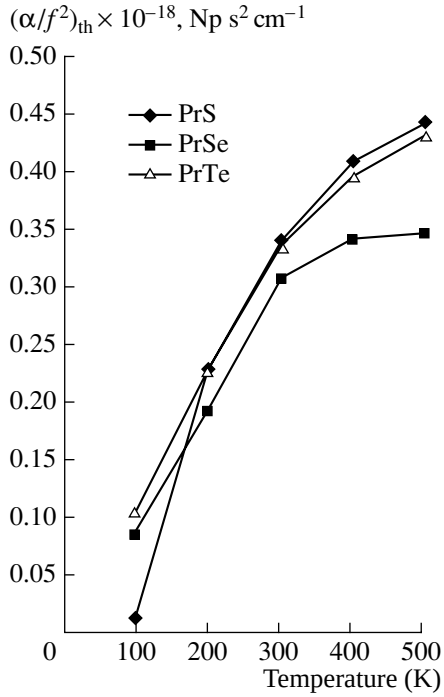

Fig. 11. $(\alpha/f^2)_{th}$ vs. temperature along the ⟨110⟩ direction.

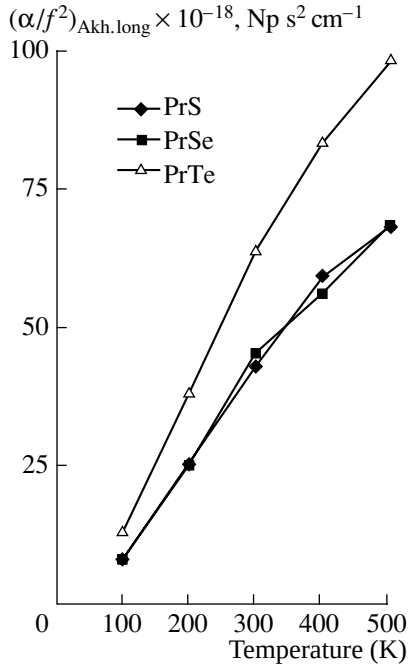

Fig. 12. $(\alpha/f^2)_{Akh.long}$ vs. temperature along the ⟨110⟩ direction.

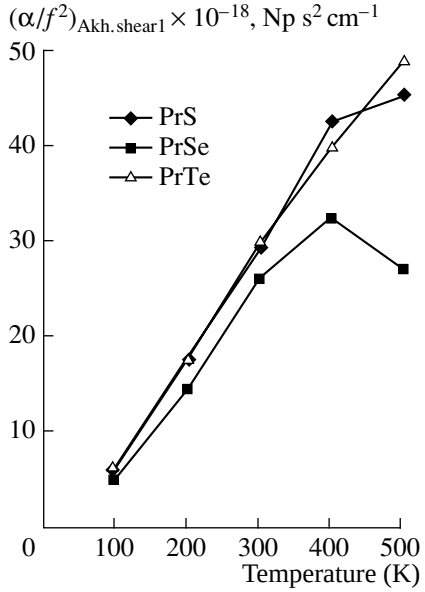

Fig. 13. $(\alpha/f^2)_{Akh.shear1}$ vs. temperature along the ⟨110⟩ direction polarized along ⟨001⟩ direction.

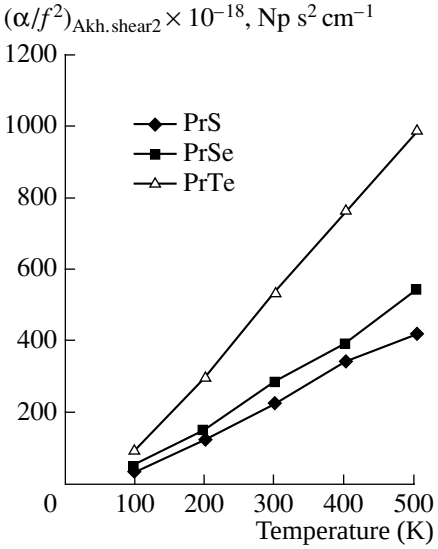

Fig. 14. $(\alpha/f^2)_{Akh.shear2}$ vs. temperature along the ⟨110⟩ direction and polarized along $\langle 1\bar{1}0\rangle$.

100 MHz is 0.1 dB/μs. However, due to the lack of experimental values for the entire temperature region, comparison is not possible for different temperatures. None the less, the variation of attenuation clearly supports the present approach for ultrasonic attenuation, which is directly connected to our evaluations of SOEC and TOEC based on only two basic parameters.

As discussed, the nonlinearity parameter D (acoustic coupling constant) does not contribute greatly to the temperature dependence of the attenuation in Praseodymium monochalcogenides. The quantization behavior of the temperature dependence of $(\alpha/f^2)_{Akh}$ and $(\alpha/f^2)_{th}$ is the same as the variation in the total thermal conductivity of these compounds from 100 to 500 K [3]. A dis-

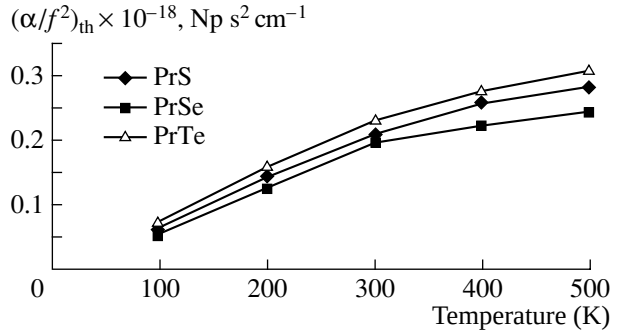

Fig. 15. $(\alpha/f^2)_{th}$ vs. temperature along the ⟨111⟩ direction.

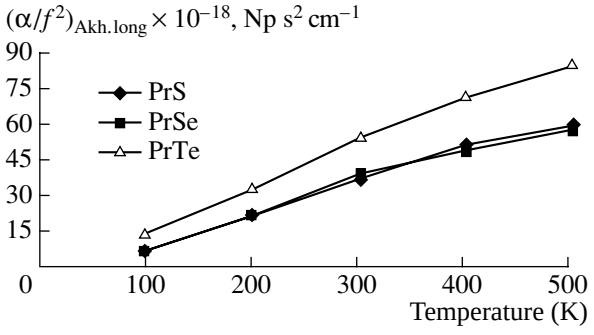

Fig. 16. $(\alpha/f^2)_{Akh.long}$ vs. temperature along the ⟨111⟩ direction.

tinctive peculiarity of rare-earth metallic compounds is their lower electronic thermal conductivity with an anomalous temperature dependence. The electronic thermal conductivity of these compounds decreases with temperature from 100 to 500 K [3]. Therefore, the attenuation in those compounds is mainly due to the lattice part of the thermal conductivity and it directly affects the temperature dependence of the attenuation. As expected, thermoelastic loss is negligible due to low values of thermal conductivity.

It was confirmed by measurements that, for temperatures below 500 K, the attenuation is independent of the dislocation count and, thus, it is not considered here [23]. It has been well established by many experimental and theoretical studies that phonon–phonon interaction is the dominating cause for attenuation in solids at higher temperatures (room temperature) and electron–phonon interaction is the main cause where free electrons are available. In the theory employing phonon–phonon interactions, several approximations are made that are valid at higher temperatures [24].

Thus, on the basis of the above analysis which compares the values of attenuation with other like substances at 100–500 K along different crystallographic directions, our theoretical approach to the temperature dependence of ultrasonic attenuation, which allows one

Table 12. Ultrasonic attenuation due to phonon–phonon interaction [$(\alpha/f^2)_{Akh.long}$ for longitudinal wave and $(\alpha/f^2)_{Akh.shear}$ for shear wave] and due to thermoelastic loss $(\alpha/f^2)_{th}$ PrS, PrSe, and PrTe in the temperature range of 100–500 K along ⟨111⟩ in 10^{-17} Np s^2/cm

Crystal	Temp. (K)	$(\alpha/f^2)_{th}$	$(\alpha/f^2)_{Akh.long}$	$(\alpha/f^2)^*_{Akh.shear}$
PrS	100	0.060	6.287	23.427
	200	0.139	21.016	81.886
	300	0.209	36.442	153.216
	400	0.257	50.627	232.612
	500	0.281	58.502	286.378
PrSe	100	0.053	6.708	30.933
	200	0.112	21.200	101.304
	300	0.197	38.726	195.658
	400	0.224	48.298	268.365
	500	0.243	56.873	340.971
PrTe	100	0.068	14.075	63.388
	200	0.155	32.352	202.076
	300	0.231	54.270	368.703
	400	0.277	70.677	523.722
	500	0.308	83.617	675.556

Notes: * Shear wave polarized along the ⟨$\bar{1}$ 10⟩ direction.

Table 13. Comparison of ultasonic absorption coefficient (α) in dB/μsec of intermetallics with LiF at room temperature and 900 MHz

Material	$\langle 100\rangle_1$	$\langle 100\rangle_S$	$\langle 110\rangle_1$	$\langle 110\rangle_{S1}$	$\langle 110\rangle_{S2}$	$\langle 111\rangle_1$	$\langle 111\rangle_{S3}$
LiF (exp.)	3.5	0.8	1.3	0.8	10.0	0.8	5.0
LaS	1.3	0.2	1.5	0.2	4.5	0.1	0.3
LaSe	1.5	0.3	2.0	0.1	6.0	0.1	0.4
LaTe	2.6	0.4	3.3	0.1	10.0	0.2	0.8
PrS	0.9	0.1	0.9	0.3	2.5	0.7	1.7
PrSe	0.9	0.1	0.8	0.3	2.7	0.7	1.8
PrTe	1.2	0.2	1.0	0.3	4.4	1.5	3.0

Subscripts have the following meaning:
l stands for longitudinal wave,
S stands for shear wave,
S1 stands for shear wave polarized along the ⟨001⟩ direction,
S2 stands for shear wave polarized along the ⟨1$\bar{1}$ 0⟩ direction,
S3 stands for shear wave polarized along the ⟨$\bar{1}$ 10⟩ direction.

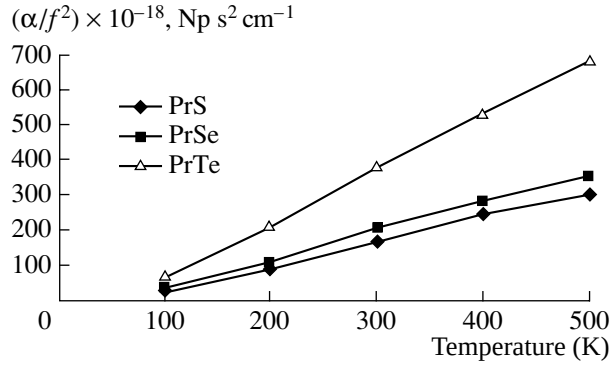

Fig. 17. $(\alpha/f^2)_{\text{Akh.shear}}$ vs. temperature along the $\langle 111 \rangle$ direction and polarized along the $\langle \bar{1}10 \rangle$ direction.

to observe the effect of lattice thermal conductivity and some important characteristic features closely connected to ultrasonic parameters, is justified.

REFERENCES

1. A. V. Golubkov, E. D. Debyatkova, V. P. Zhuze, *et al.*, Fiz. Tverd. Tela (Leningrad) **8**, 1761 (1966) [Sov. Phys. Solid State **8**, 1403 (1966)].
2. V. P. Zhuze, A. V. Golubkov, E. V. Goncharova, and V. M. Sergeeva, Fiz. Tverd. Tela (Leningrad) **6**, 257 (1964) [Sov. Phys. Solid State **6**, 205 (1964)].
3. E. D. Debyatkova, V. P. Zhuze, A. V. Golubkov, *et al.*, Fiz. Tverd. Tela (Leningrad) **6**, 430 (1964) [Sov. Phys. Solid State **6**, 343 (1964)].
4. *CRC Handbook of Chemistry and Physics*, Ed. by R. C. Weast, 79th ed. (CRC Press, Ohio, 1998), pp. 4–23.
5. M. Born and J. E. Mayer, Z. Phys. **75**, 1 (1931).
6. K. Brugger, Phys. Rev. **133** (6), A1611 (1964).
7. G. Liibfried and H. Haln, Z. Phys. **150**, 497 (1958).
8. G. Leibfried and W. Ludwig, Solid State Phys. **12**, 275 (1964).
9. Y. Hiki, Annu. Rev. Mater. Sci. **11** (1981).
10. P. B. Chate, Phys. Rev. **139** (5), A1666 (1965).
11. S. Mori and Y. Hiki, J. Phys. Soc. Jpn. **45** (5), 1449 (1978).
12. *Crystal Structures*, Ed. by R. W. G. Wychoff (Interscience, New York, 1963), p. 89.
13. A. Chatterjee, A. K. Singh, and A. Jayaraman, Phys. Rev. B **6** (6), 2285 (1975).
14. E. Bucher, K. Andres, F. J. di Salvo, *et al.*, Phys. Rev. B **11** (1), 500 (1975).
15. R. R. Yadav and D. Singh, J. Phys. Soc. Jpn. **70** (6), 1825 (2001).
16. *Physical Acoustics*, Ed. by W. P. Mason (Academic, New York, 1965; Mir, Moscow, 1968), Vol. 3, Part B, pp. 237–285.
17. W. P. Mason and T. B. Batemann, J. Acoust. Soc. Am. **40**, 852 (1966).
18. D. S. Puri and M. P. Verma, Solid State Commun. **18**, 1295 (1976).
19. R. C. Hanson, J. Phys. Chem. Solids **28**, 475 (1967).
20. R. R. Yadav and D. Singh, J. Acoust. Soc. India **30** (1–2), 55 (2002).
21. D. Singh, R. R. Yadav, and A. K. Tiwari, Indian J. Pure Appl. Phys. **40** (12), 845 (2002).
22. S. K. Kor and R. P. Khare, Acustica **56**, 280 (1984).
23. E. R. Dobbs, B. B. Chick, and R. Trull, Phys. Rev. Lett. **3** (7), 332 (1959).
24. S. D. Lambade, G. G. Sahasrabudhe, and S. Rajgopalan, Phys. Rev. B **51** (22), 15861 (1995).

Acoustical Physics, Vol. 49, No. 5, 2003, pp. 605–607. Translated from Akusticheskiĭ Zhurnal, Vol. 49, No. 5, 2003, pp. 711–713.

SHORT COMMUNICATIONS

Modulation of Ultrasonic Pulses by a Magnetized Magnetic Colloid

A. V. Karelin and V. M. Polunin

Kursk State Technical University, ul. 50 let Oktyabrya 94, Kursk, 305040 Russia

e-mail: Polunin_VM@hotbox.ru

Received July 17, 2002

Abstract—The dependence of the shape of an ultrasonic pulse transmitted through a magnetized magnetic colloid on the angle between the wave vector and the magnetic induction vector is investigated. © *2003 MAIK "Nauka/Interperiodica".*

In the literature, a certain interest has been expressed in studying elastic systems with active elements consisting of magnetorheological fluids [1–6].

In this paper, we investigate the relative amplitude and shape of an ultrasonic pulse transmitted through an acoustic cell filled with a magnetic fluid (MF) under a prolonged exposure to magnetic field.

The carrier frequency and pulse repetition frequency were 6 MHz and 4 kHz, respectively. Video pulses taken from the receiver output were fed to an oscilloscope. For subsequent computer processing, the resulting oscillograms were photographed by a digital video camera. A permanent magnet mounted on a rotating platform served as a source of magnetic field. The acoustic cell had the form of a parallelepiped with a base of 2×2 cm and height of 7 cm.

To avoid the penetration of air bubbles into the MF at the stage of sample preparation for measurements, the following provisions were made: the cell was filled with MF several hours prior to placing it in magnetic field; to prevent the penetration of air cavities into the projected zone because of the instability of the open surface of MF in magnetic field, the cell was filled with the fluid practically up to the brim and then was placed in the magnet gap by moving the cell in a downward direction.

The samples under investigation were magnetic colloids prepared on the basis of kerosene. The disperse phase was Fe_3O_4 magnetite, and the stabilizer was oleic acid. The table shows the main physical parameters of the MF samples used in the experiment.

The experiment was carried out at a temperature of 290 ± 1 K. The magnetic field strength in the magnet gap was 122 kA/m, and the initial angle between the magnetic vector $\bar{H}$ and the wave vector $\bar{k}$ was $\vartheta = 90°$.

The increment of the absorption coefficient was calculated by the formula

$$\Delta\alpha_i = \frac{1}{l}\ln\frac{U_{\max}}{U_i},$$

where l is the path length of ultrasound in the magnetic fluid, $U_{\max}$ is the maximum amplitude, and U_i is the signal amplitude at the instant t_i.

The results of the first part of the experiment (prior to the change of the video pulse shape) are given in Fig. 1. The triangles represent the results of measuring the relative amplitude of the video pulse $U/U_{\max}$, and the squares show the increment of the absorption coefficient $\Delta\alpha$. In the experiment, a considerable decrease in the amplitude of the ultrasonic pulse was observed within $t \approx 30$–35 h for MF-1 and 70–75 h for MF-2. The

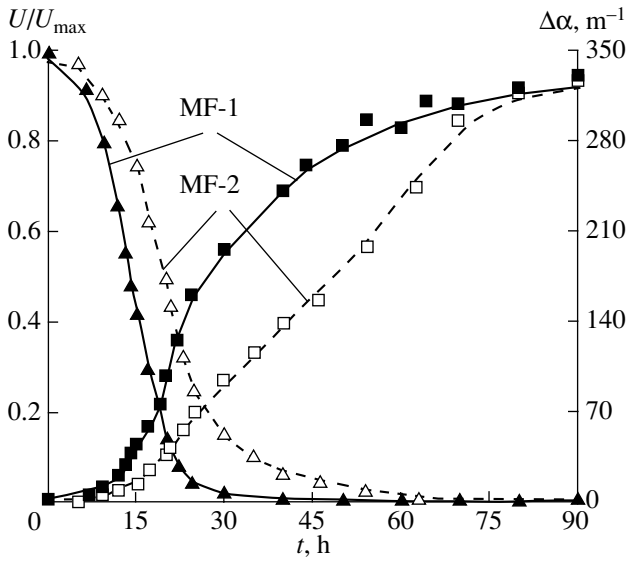

Fig. 1. Dependences of the relative amplitude of the video pulse $U/U_{\max}$ and the increment of the absorption coefficient $\Delta\alpha$ on time t.

1063-7710/03/4905-0605$24.00 © 2003 MAIK "Nauka/Interperiodica"

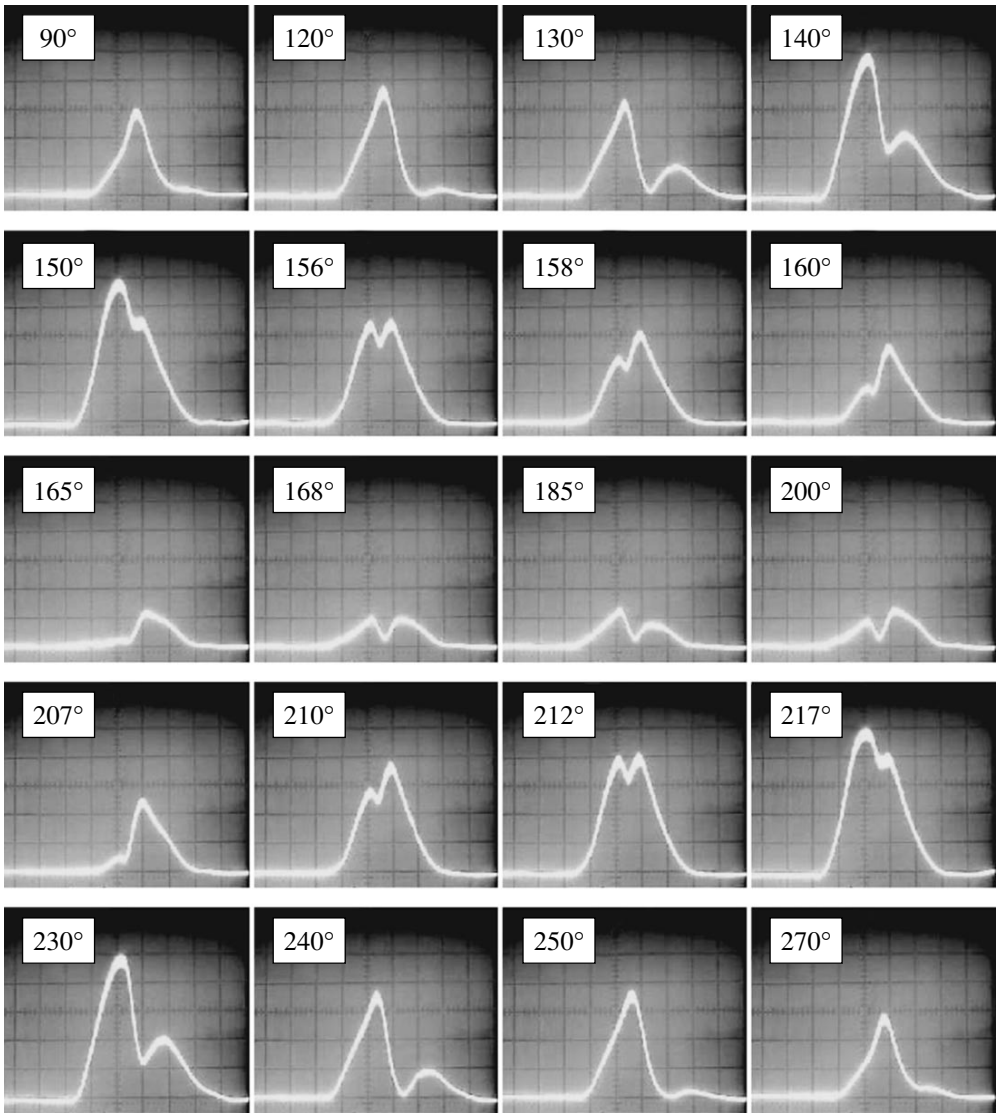

Fig. 2. Oscillograms of the ultrasonic pulse transmitted through MF-2 for different values of the angle ϑ (indicated in the plots).

nonmonotone character of the angular dependence of $\Delta\alpha$ observed in the experiment mainly agrees with the data reported in [3].

The additional absorption of ultrasound is connected with the change in the structure of the MF [1, 2]. Under the effect of magnetic field, chain aggregates are formed from ferroparticles. The sound wave transmitted through the disperse system is partially absorbed and scattered by the aggregates. The fact that $\Delta\alpha$ approaches its equilibrium value within several days testifies that the process of structure formation is relatively slow.

A change in the shape of the video pulse is distinctly visible at certain angles ϑ after a time interval $t \approx 50$ h for MF-1 and 150 h for MF-2 measured from the beginning of the experiment, when additional signal amplification in the receiver is applied by means of the input attenuator adjustment. In other papers concerned with the same subject (e.g., [1–6]), such an effect was never mentioned.

Figure 2 shows the oscillograms of an ultrasonic pulse transmitted through MF-2 for the indicated values of ϑ. The value of the scale division along the y axis is 0.5 V/div, and along the x axis, it is 5 μs/div. The oscillograms obtained for MF-1 are of a similar character.

With the rotation of magnetic field, the shape of the video pulse changes; i.e., a controlled modulation of the ultrasonic pulse takes place. At angles of 130°–160°, a dip appears in the middle part of the video pulse. The dip is observed again at angles of 210°–240°. However, in the first case the dip moves from right to left, while in the second case it moves in the opposite direction.

Table

Sample	ρ, kg/m^3	φ, %	M_s, kA/m
MF-1	1350	12.8	54 ± 1
MF-2	1300	11.7	50 ± 1

Here: ρ is the density of the magnetic colloid, φ is the volume concentration of the solid phase, and M_s is the saturation magnetization.

We note some features of the effect reveled in our experiment: if the amplitude of the transmitted pulse is reduced several times, the amplitude of the received video pulse also decreases while its shape is retained. The amplification of the signal in the receiver is accompanied by the appearance of a probing pulse (a stray signal) at the beginning of the sweep and by an increase in the received video pulse. However, the video pulse begins to change its shape as it reaches beyond the dynamic range. When the cell is removed from the magnetic field, the dip disappears and the pulse amplitude rises, although it does not reach the initial level. A multiple (20–30 times) rotation of the magnetic field leads to the recovery of the pulse shape close to the initial one and to a certain increase in the pulse amplitude. However, within several days, the dip reappears. The recovery of the initial shape and amplitude of the ultrasonic pulse is achieved by a careful mechanical stirring of the MF.

These facts allow us to reject the possible "instrumental" origin of the signal modulation observed in our experiment.

One may assume that the change in the shape of the ultrasonic pulse observed in the experiment is a consequence of the self-modulation of the wave in the course of its propagation through a medium with nonlinearity and dispersion [7]. In this case, the dispersion could be related to the appearance of aggregates consisting of fine ferroparticles in the magnetic colloid, which exhibit resonance properties in magnetic field in the megahertz frequency band. The processes of structure formation due to the dipole–dipole interaction proceed in a certain sequence: the structures consisting of the largest particles with great magnetic moments are formed first, and the particles with small magnetic moments form aggregates later on. Aggregates consisting of small particles are less stable and are easily destroyed in a rotating magnetic field [8, 9].

REFERENCES

1. V. M. Polunin, Magn. Gidrodin., No. 3, 137 (1986).
2. V. V. Gogosov, S. I. Martynov, S. N. Tsurikov, and G. A. Shaposhnikova, Magn. Gidrodin., No. 3, 15 (1987).
3. B. I. Kuzin and V. V. Sokolov, Akust. Zh. **40**, 689 (1994) [Acoust. Phys. **40**, 611 (1994)].
4. L. I. Roslyakova, A. A. Chernyshova, and T. I. Aksenova, in *Ultrasound and Thermodynamic Properties of Matter* (Kursk. Gos. Pedagog. Inst., Kursk, 1994), pp. 77–78.
5. V. V. Nadvoretskiĭ and V. V. Sokolov, Magn. Gidrodin. **33**, 36 (1997).
6. B. R. Mace, R. W. Jones, and N. R. Harland, J. Acoust. Soc. Am. **109**, 1417 (2001).
7. M. I. Rabinovich and D. I. Trubetskov, *Introduction to the Oscillation and Wave Theory* (NITs Regulyarn. Khaot. Din., Moscow, 2000).
8. S. S. Kantorovich, in *Proceedings of 10th Anniversary International Pless Conference on Magnetic Liquids* (IGÉU, Ivanovo, 2002), p. 51.
9. E. E. Bibik and V. E. Skobochkin, Inzh.–Fiz. Zh. **22** (4), 687 (1972).

Translated by A. Svechnikov

Acoustical Physics, Vol. 49, No. 5, 2003, pp. 608–611. Translated from Akusticheskiĭ Zhurnal, Vol. 49, No. 5, 2003, pp. 714–718.

CHRONICLE

Research Projects in Acoustics and Related Fields of Physics—Recipients of Grants from the Russian Foundation for Basic Research

The list of research projects that received grants from the Russian Foundation for Basic Research as a result of the competitions run in the last few years is presented below. The list includes only the projects concerned with acoustics. Evidently, the choice below cannot be absolutely exact, because some projects that could be of interest to specialists in acoustics were submitted by the authors to other sections of the physics department (e.g., to the sections of plasma physics, condensed state, or theoretical physics) and even to other departments (mathematics, mechanics, and information science; Earth science; etc.). It was especially difficult to select projects from those submitted by authors to departments other than physics. Possibly, if the list were made by other compilers, some of its items would be different. Therefore, the list presented below is organized as follows: it includes projects that were submitted to the physics department and supported in the last three years, i.e., projects that received financial support starting from 2000, 2001, and 2002; it also includes projects concerned with acoustics and submitted to other departments of natural sciences but only those supported in 2002. To obtain more information, one should refer to the *Information Bulletin of the Russian Foundation for Basic Research* No. 10 (Nauchnyi Mir, Moscow, 2002) or to other similar publications of the past few years.

The title of each project is preceded by the name of the principle researcher; the name of the corresponding institute is indicated after the title. Hopefully, the information on the areas of basic research in acoustics and related sciences and the research groups and organizations that received support from the Foundation after being approved by independent experts will be of interest to many acousticians.

PHYSICS, 2000

1. G. M. Shalashov, *Acoustic Studies of Nonlinear Local Elastic Parameters of Real Media*, Radiophysical Research Institute, Nizhni Novgorod.

2. V. I. Turchin, *Emission, Reception, and Processing of Broadband Electromagnetic and Acoustic Signals in Conditions of Propagation through Complex Media*, Institute of Applied Physics, Russian Academy of Sciences, Nizhni Novgorod.

3. A. I. Potapov, *Nonlinear Acoustic Waves in Media with Complex Structure: Theoretical and Experimental Studies*, Institute of Mechanical Engineering, Nizhni Novgorod Branch.

4. A. M. Reĭman, *Optical–Acoustic Tomography of Biological Tissues through Centimeter Depths*, Institute of Applied Physics, Russian Academy of Sciences, Nizhni Novgorod.

5. V. A. Bulanov, *Acoustic Characteristics of Microstructured Liquids and Solutions and Their Measurement at the Transition to Nanostructures in the Presence of Phase Transformations*, Institute of Marine Technology Problems, Far East Division of the Russian Academy of Sciences, Vladivostok.

6. O. V. Abramov, *Effect of the Properties and Motion Features of a Liquid on the Development of an Ultrasonic Cavitation in the Frequency Band within 200–400 kHz in Different Vibration Excitation Conditions*, Institute of General and Inorganic Chemistry, Russian Academy of Sciences, Moscow.

7. V. I. Erofeev, *Nonlinear Acoustic Waves in Solids with Dislocations*, Institute of Mechanical Engineering, Nizhni Novgorod Branch.

8. A. P. Lavrov, *Acoustooptic Spectropolarimeter with a High Temporal Resolution for Studying Pulsar Radio Emission*, St. Petersburg State University of Telecommunications.

9. A. L. Virovlyanskiĭ, *Study of Wave Chaos in Range-Dependent Waveguides*, Institute of Applied Physics, Russian Academy of Sciences, Nizhni Novgorod.

10. A. M. Dykhne, *Acoustics of Supercritical Media*, Advanced Laser Technology Department of the Institute of Laser and Information Technology Problems, Troitsk, Moscow oblast.

11. O. P. Galkin, *Sound Fields in Regular and Irregular Waveguides*, Acoustics Institute, Moscow.

12. O. A. Kapustina, *Study of the Mechanism Governing the Formation of Two-Dimensional Domains in Cholesteric Liquid Crystals under the Effect of Ultrasound*, Acoustics Institute, Moscow.

13. L. R. Gavrilov, *Physical Foundations of the Dynamic Focusing of Intense Ultrasound in Inhomogeneous Viscoelastic Media*, Acoustics Institute, Moscow.

14. A. G. Semenov, *Sound Propagation in the Vicinity of Moving Bodies and Moving Inhomogeneities of a Medium*, Acoustics Institute, Moscow.

1063-7710/03/4905-0608$24.00

15. V. S. Teslenko, *Mechanisms of Glow in a Liquid Medium in the Cavitation Conditions and the Role of the Bubble Collapse Dynamics in the Activation of Physical–Chemical Processes*, Hydrodynamics Institute, Siberian Division of the Russian Academy of Sciences, Novosibirsk.

16. V. K. Kedrinskiĭ, *Experimental and Theoretical Modeling of the Process of Sound Generation by Bubble Systems with Phase Transitions and Chemical Reactions*, Hydrodynamics Institute, Siberian Division of the Russian Academy of Sciences, Novosibirsk.

PHYSICS, 2001

1. S. A. Makhortykh, *Inverse Problem of the Acoustic Tomography of Ground and the Problem of Environmental Predictions near the Sources of Intense Sound and Vibration*, Institute of Mathematical Problems in Biology, Russian Academy of Sciences, Pushchino, Moscow oblast.

2. V. I. Al'shits, *A Series of Works on the Theory of Elastic Waves in Anisotropic and Inhomogeneous Media*, Institute of Crystallography, Russian Academy of Sciences, Moscow.

3. B. D. Zaĭtsev, *Theoretical and Experimental Studies of Surface Acoustic Waves in Piezoelectric Structures with Conducting Layers*, Saratov Branch of the Institute of Radio Engineering and Electronics, Russian Academy of Sciences.

4. V. A. Burov, *Investigation of Theoretical and Experimental Methods of Solving Inverse Scattering Problems in Acoustics and Their Application to Medical Diagnostics and Ocean Tomography*, Faculty of Physics, Moscow State University.

5. A. V. Golenishchev-Kutuzov, *Propagation, Generation, and Transformation of Acoustic Waves in Transition Metal Oxides Containing Periodic Structures*, Kazan State Power University.

6. Yu. N. Cherkashin, *Study of Acoustic Gravity Waves in Ionosphere at the Maximal Applicable Frequency with the Use of a Multichannel Automated Receiving System*, Institute of Terrestrial Magnetism and Radio Wave Propagation, Russian Academy of Sciences, Troitsk, Moscow oblast.

7. V. G. Andreev, *Optical-Acoustic Tomography of Light Absorbing Inhomogeneities in Scattering Media*, Faculty of Physics, Moscow State University.

8. V. L. Preobrazhenskiĭ, *Self-Focusing of Finite-Amplitude Sound Beams in the Parametric Wave Conjugation*, Wave Research Center of the General Physics Institute, Russian Academy of Sciences, Moscow.

9. N. V. Studenichnik, *Studies of the Sound Field Structures in Layered and Inhomogeneous Underwater Waveguides in the Audio and Infrasonic Frequency Bands*, Acoustics Institute, Moscow.

10. Yu. N. Makov, *A Complex Study of the Ultrasonic and Acoustomechanical Effects on the Functional Activity of the Heart and Its Tissues: Physical Principles and Medical-Biological Applications*, Faculty of Physics, Moscow State University.

11. N. A. Mityakov, *Study of Convective, Turbulent, and Wave Processes in Troposphere and Stratosphere by a Unique System of Decameter Radioacoustic Sounding*, Radiophysical Research Institute, Nizhni Novgorod.

12. I. N. Didenkulov, *Study and Development of Methods of Nonlinear Acoustic Imaging*, Institute of Applied Physics, Russian Academy of Sciences, Nizhni Novgorod.

13. N. I. Pushkina, *Study of the Main Laws of Nonlinear Acoustic Wave Propagation in Multiphase Media*, Computational Research Center of Moscow State University.

14. A. V. Osetrov, *Theory of the Acoustic Tomography of Two-Dimensional Inhomogeneities*, St. Petersburg State University of Electrical Engineering.

15. V. A. Vdovin, *Study of the Interaction of Intense Microwave Pulses with Solids by Thermal Acoustic Diagnostics*, Institute of Radio Engineering, Russian Academy of Sciences, Moscow.

16. V. V. Mityugov, *Study of the Physical Characteristics of Spatial and Temporal Acoustic Holography in Underwater Channels*, Institute of Applied Physics, Russian Academy of Sciences, Nizhni Novgorod.

17. V. V. Chernov, *Study of the Acoustic and Physical Properties of Ice at the Phase Transition*, Institute of Applied Physics, Russian Academy of Sciences, Nizhni Novgorod.

18. P. L. Soustov, *Study of the Laboratory and Atmospheric Turbulence by Means of Remote Acoustic Diagnostics*, Institute of Applied Physics, Russian Academy of Sciences, Nizhni Novgorod.

19. Yu. V. Ilisavskiĭ, *Acoustic and Acoustoelectronic Phenomena in Rare Earth Manganite Films*, Physical-Technical Institute, St. Petersburg.

20. A. D. Mansfel'd, *Theoretical and Experimental Study of Acoustic Infrared Imaging of the Internal Temperature of Biological Objects by Focused Antennas*, Institute of Applied Physics, Russian Academy of Sciences, Nizhni Novgorod.

21. N. V. Pronchatov-Rubtsov, *Study of the Nonlinear Dynamics of Gas Bubbles and the Resonance Interaction of Intense Acoustic Waves*, Nizhni Novgorod State University.

22. A. V. Klyuchnik, *Phonon Laser, Generation of Coherent Phonons, and Near-Field Acoustic Microscopy*, Institute of Laser Technology and Materials Science of the General Physics Institute, Russian Academy of Sciences, Moscow.

PHYSICS, 2002

1. A. L. Sobisevich, *Nonlinear Resonant Structures: Quality Factor, Spectral Characteristics, and Acoustic Diagnostics*, Joint Institute of Earth Physics, Russian Academy of Sciences, Moscow.

2. A. I. Korobov, *Experimental Studies of the Characteristic Features of Acoustic Wave Propagation in Metals in the Region of Elastoplastic Deformations*, Faculty of Physics, Moscow State University.

3. V. Yu. Zaitsev, *Study of the Structure-Induced Acoustic Nonlinearity of Solids*, Institute of Applied Physics, Russian Academy of Sciences, Nizhni Novgorod.

4. I. Yu. Solodov and B. A. Korshak, *Parametric Instability, Chaotization, and "Memory" in the Nonlinear Interaction of Acoustic Waves with Defects in Solids*, Faculty of Physics, Moscow State University.

5. I. B. Esipov, *Nonlinear Acoustic Processes in a Non-Newtonian Fluid*, Acoustics Institute, Moscow.

6. V. G. Petnikov, *Sound Wave Propagation in a Randomly Inhomogeneous Channel and Acoustic Monitoring by Low-Intensity Signals*, Wave Research Center of the General Physics Institute, Russian Academy of Sciences, Moscow.

7. L. M. Lyamshev, *Fractals and Wavelets in Acoustics*, Institute of Radio Engineering and Electronics, Russian Academy of Sciences, Moscow.

8. F. V. Bunkin, *Ultrasonic Fields in Inhomogeneous and Nonlinear Media at a Parametric Wave Conjugation*, Wave Research Center of the General Physics Institute, Russian Academy of Sciences, Moscow.

9. O. A. Sapozhnikov, *Dynamics of Cavitation Fields and the Mechanisms of Cavitation Damage Due to the Propagation of Intense Ultrasound and Weak Shock Waves*, Faculty of Physics, Moscow State University.

10. V. A. Zverev, *Study of the Physical Limitations and Limiting Abilities of the Acoustic Methods Used for the Observation of Underwater Inhomogeneities*, Institute of Applied Physics, Russian Academy of Sciences, Nizhni Novgorod.

11. V. I. Talanov, *Sounding of Inhomogeneities of the Earth Medium and Remote Seismic Monitoring by Means of Coherent Acoustics*, Institute of Applied Physics, Russian Academy of Sciences, Nizhni Novgorod.

12. S. A. Rybak, *Theoretical and Experimental Study of Wave Processes in Inhomogeneous and Multiphase Media*, Acoustics Institute, Moscow.

13. V. B. Bychkov, *Acoustic Diagnostics of Radiation Effects in Physics of High-Energy Particles*, Institute of Theoretical and Experimental Physics, Moscow.

14. N. I. Polzikova, *Acoustoelectronic and Acoustomagnetic Parametric Interactions in Multilayer Resonant Acoustic Structures*, Institute of Radio Engineering and Electronics, Russian Academy of Sciences, Moscow.

15. O. M. Gradov, *New Nonlinear Methods for the Acoustic Analysis of the Physical-Mechanical Properties and Structural Changes of Parameters of a Material with a Fully Developed Defect Structure*, Institute of General and Inorganic Chemistry, Russian Academy of Sciences, Moscow.

16. A. N. Serebryanyĭ, *Acoustic Effects Induced by Internal Solitons in the Sea*, Acoustics Institute, Moscow.

17. A. A. Anosov, *Physical Foundations of Reconstructing the Spatial Distributions of the Temperature and the Absorption Coefficient from the Measured Characteristics of Thermal Acoustic Radiation*, ELDIS Research Center of Electronic Diagnostic Systems, Moscow.

18. S. N. Gurbatov, *Theoretical and Experimental Study of the Evolution of Strongly Nonlinear Wave Fields and Structures and Its Dynamical and Statistical Description*, Nizhni Novgorod State University.

19. V. D. Kiselev, *Experimental Studies of the Mechanisms of Energy Transformation from Laser Radiation to Sound at an Optical Breakdown in Liquid*, Pacific Oceanological Institute, Far East Division of the Russian Academy of Sciences, Vladivostok.

20. V. A. Khokhlova, *Effects of Nonlinear Focusing and Heat on Liquids and Biological Tissues in Super-High-Intensity Acoustic Fields*, Faculty of Physics, Moscow State University.

MATHEMATICS, INFORMATION SCIENCE, AND MECHANICS, 2002

1. V. E. Antsiperov, *Synthesis of Neuron-Like Information Systems for the Tasks of Speech Signal Discrimination on the Basis of a Sequential Selective Identification*, Institute of Radio Engineering and Electronics, Russian Academy of Sciences, Moscow.

2. A. A. Arsen'ev, *Resonant Scattering in Quantum and Acoustic Waveguides*, Faculty of Physics, Moscow State University.

3. V. M. Babich, *Study of the Mathematical Aspects of the Current Problems of the Theory of Wave Phenomena (Direct and Inverse Problems)*, St. Petersburg Branch of the Mathematical Institute.

4. Z. M. Benenson, *Theory and Experimental Study of the New Method of Processing Ultrasonic Signals of Linear Phased Arrays to Provide a Quick Survey of a Three-Dimensional Space with a Superhigh Resolution*, Scientific Council on the Complex Problem of Cybernetics, Russian Academy of Sciences, Moscow.

5. S. A. Gaponov, *Theoretical and Experimental Study of the Acoustic Susceptibility of a Supersonic Boundary Layer on a Rough Surface*, Institute of Theoretical and Applied Mechanics, Siberian Division of the Russian Academy of Sciences, Novosibirsk.

6. A. G. Gorshkov, *Development of Numerical-Analytical Methods for Solving the Problems of Aerohydroelasticity and Aeroacoustics*, Moscow Aviation Institute.

7. I. É. Ivanov, *Numerical Study of Nonstationary Processes in a Hartmann Gas-Dynamic Jet Resonator*, Moscow Aviation Institute.

8. Yu. S. Kolesov, *Method of Quasi-Normal Forms and the Attractors of Nonlinear Wave Equations in Plane Regions*, Yaroslavl State University.

9. V. F. Kop'ev, *Mechanism of Aerodynamic Sound Generation and Its Application for Contactless Diagnostics of Turbulence*, Central Aerohydrodynamics Institute, Moscow.

10. A. G. Kulikovskiĭ, *Study of Large-Scale Phenomena Associated with Wave Propagation in Continuous Media*, Mathematical Institute, Russian Academy of Sciences, Moscow.

11. A. V. Faminskiĭ, *Study of the Solutions to the Boundary-Value Problems for Quasi-Linear Equations Describing the Propagation of Waves and the Motion of Solids in a Fluid*, Russian University of People's Friendship, Moscow.

12. V. Ya. Chuchupal, *Study and Development of the Methods of Adaptation of the Speech Discrimination System to an External Medium*, Computational Center of the Russian Academy of Sciences, Moscow.

CHEMISTRY, 2002

1. A. I. Aleksandrov, *Solid-Phase Mechanochemical Synthesis of Cluster Polymers under the Effect of Elastic Wave Pulses*, Institute of Synthetic Polymer Materials, Russian Academy of Sciences, Moscow.

2. A. G. Istratov, *Theoretical and Experimental Study of the Parameters of Pressure Waves Generated by Self-Accelerated Turbulent Gas Flames*, Institute of Chemical Physics, Russian Academy of Sciences, Moscow.

BIOLOGY AND MEDICAL SCIENCE, 2002

1. L. M. Kotelenko, *Reflection of the Speed of Sound in the Auditory Cortex*, Institute of Physiology, Russian Academy of Sciences, St. Petersburg.

2. D. N. Lapshin, *Frequency Tuning of the Auditory System of Moths (Lepidoptera, Noctuidae)*, Institute of Information Transfer Problems, Russian Academy of Sciences, Moscow.

3. A. Ya. Supin, *Effect of Noise on the Spectral Resolution of Hearing*, Institute of Ecology and Evolution Problems, Russian Academy of Sciences, Moscow.

EARTH SCIENCE, 2002

1. V. V. Bakhanov, *Theoretical and Experimental Study of the Transformation of Nonlinear Surface Waves to a Field of Three-Dimensional Inhomogeneous Streaming*, Institute of Applied Physics, Russian Academy of Sciences, Nizhni Novgorod.

2. A. N. Gavrilov, *Acoustic Monitoring of Large-Scale Variations in the Water Temperature and Salinity in the Arctic Ocean*, Oceanology Institute, Russian Academy of Sciences, Moscow.

3. S. A. Ermakov, *Experimental and Theoretical Study of the Nonlinear Dynamics of Small-Scale Wind Waves in Slicks in Application to the Development of the Principles of Remote Diagnostics of Organic Films on the Sea Surface*, Institute of Applied Physics, Russian Academy of Sciences, Nizhni Novgorod.

4. B. F. Kur'yanov, *Theoretical and Experimental Studies of Digital Acoustic Methods for Controlling Oceanographical Instruments and Communicating with Them in Shallow and Deep Seas*, Oceanology Institute, Russian Academy of Sciences, Moscow.

5. A. G. Luchinin, *Statistical Problems of the Theory of Image Transfer through a Wavy Surface*, Institute of Applied Physics, Russian Academy of Sciences, Nizhni Novgorod.

6. A. V. Nikolaev, *Changes in the Fine Structure of Seismic Emission as an Indicator of Slow Deformations of the Earth Crust and the Processes Preceding Earthquakes*, Institute of Earth Physics, Russian Academy of Sciences, Moscow.

7. E. N. Pelinovskiĭ, *Killer Waves: Physical Mechanisms and Modeling*, Institute of Applied Physics, Russian Academy of Sciences, Nizhni Novgorod.

8. V. F. Pisarenko, *New Parametrization Scheme for the Seismic Regime and the Problem of Evaluating Seismic Danger*, International Institute of the Theory of Earthquake Prediction and Mathematical Geophysics, Russian Academy of Sciences, Moscow.

9. M. V. Rodkin, *Modeling of the Seismic Process in the Framework of the Fluidometamorphogenic Model of Earthquake Genesis*, Geophysics Center of the Russian Academy of Sciences, Moscow.

10. A. A. Rozhnoi, *Study of the Characteristic Features of Super-Long-Wave Signal Propagation with a View to Predicting Intense Earthquakes*, Institute of Earth Physics, Russian Academy of Sciences, Moscow.

11. V. B. Smirnov, *Physical Parameters of the Seismic Regime*, Faculty of Physics, Moscow State University.

12. B. K. Tkachenko, *Dynamics of Wave Processes and the Formation of Hydraulic Jumps in the Coastal Zone*, Moscow Institute of Physics and Technology.

13. V. N. Troyan, *Study of Wave Processes in Complex-Structured Media by Solving Direct and Inverse Geophysical Problems*, Physics Research Institute of St. Petersburg State University.

14. P. A. Chernous, *Theoretical and Experimental Modeling of the Effect of Seismicity on the Mechanical Stability of Snow on a Slope*, Apatity Branch of the Murmansk State Technical University, Apatity.

15. R. F. Shvachko, *Computer Simulation of the Sound Propagation in the Ocean with a Fine-Structure Stratification in Terms of the Wave Approach*, Acoustics Institute, Moscow.

N.I. Drobysheva

Translated by E. Golyamina

Acoustical Physics, Vol. 49, No. 5, 2003, pp. 612–613. Translated from Akusticheskiĭ Zhurnal, Vol. 49, No. 5, 2003, pp. 719–720.

CHRONICLE

Information on the Activities of the St. Petersburg Seminar on Computational and Theoretical Acoustics of the Scientific Council on Acoustics of the Russian Academy of Sciences in 2002

In 2002, the St. Petersburg Seminar on Computational and Theoretical Acoustics proceeded with its regular activities. Seventeen meetings were held. Several papers were devoted to acoustic processes in media, and some of them also considered wave processes of different physical nature.

B.P. Sharfarets examined acoustic fields of directional sources in oceanic waveguides. He used an approach based on representing the solution in the form of a geometric-optics expansion. With this approach, he managed to solve the direct problem of directional radiation for volumetric and surface sources in regular and irregular waveguides on a unified basis.

S.P. Kshevetskiĭ's paper was devoted to the theory of the propagation of long acoustic-gravity waves in the atmosphere. The author concentrated on the propagation of weakly-nonlinear internal gravity waves, which were described by a system of linked Korteweg–de Vries equations. The paper presented analytical and numerical results of studying the soliton-type decay of internal waves and the formation of turbulence.

V.A. Pavlov described the role of acoustic processes in wave propagation in plasma. He studied both analytically and numerically the structure of a plasma formation (a precursor) before the front of a shock wave. It was noted that, when the velocity of a shock wave exceeded the velocity of ionic sound, a specific nonlinear phenomenon arose that was analogous to the hydrodynamic effect in narrow channels, the latter being known as "the effect of Houston's horse."

The transmission of acoustic waves through elastic barriers in regular waveguides with rigid walls was studied on the basis of exact analytical representations in a joint paper by O.A. Al-Arji (Jordan), Yu.A. Lavrov, and V.D. Luk'yanov. They considered two models. In the first of them, the waveguide cross section was assumed to be rectangular. Two opposite sides of the barrier (a thin elastic plate) were assumed to be rigidly fixed, while a sliding contact occurred on two other sides. The second model consisted of a cylindrical waveguide with a channel that was baffled by two transverse plates. The dependence of sound insulation on the mechanical and geometric parameters of the system was investigated.

A.P. Tanchenko used the Wiener–Hopf method to obtain an exact analytical solution to a specific boundary-value problem of the diffraction theory for an infinite circular helix positioned on an infinite-sheeted Riemann surface. At the helix, a generalized impedance boundary condition was set with a discontinuity at a certain point. At this point, contact boundary conditions were set. The source of the field was a cylindrical wave. The final objective of the consideration was the determination of the form of an asymptotic ray expansion (initial object) for the problem of the field diffraction by an arbitrary convex curvilinear contour at which a discontinuity in the generalized impedance boundary condition takes place.

A.I. Makarov considered resonance acoustic oscillations for various rigid structures located in channels with rectangular and circular cross sections. These oscillations were excited by a gas flow in a channel, the resonance being determined by the coincidence of the frequency of the vortex separation in a gas flow with the fundamental frequency of the acoustic mode of the cell. The fundamental frequencies and natural modes of cells were calculated, and the characteristic fields of velocities and pressures were studied for individual modes.

A series of papers was devoted to structural acoustics, i.e., to elastic wave processes in solids.

Vertical vibrations of a circular stamp moving with a sub-Rayleigh speed along the surface of an elastic half-space were investigated by S.N. Gavrilov. He considered the problem in three dimensions under the assumption that the stamp movement is slow (the characteristic time scale of the oscillation process was assumed to be greater than the travel time of elastic waves from the stamp center to the edge). It was demonstrated that the vertical movement of a stamp can be described in the first approximation by the equation of the dynamics of a system with one degree of freedom with viscous friction.

E.A. Ivanova presented the derivation (according to P.A. Zhilin) of the basic equations of the theory of plates and shells that take into account rotary inertia and the shear deformation. This derivation was performed by a direct method on the basis of the fundamental laws of mechanics. In another paper, E.A. Ivanova considered the oscillations of a ring-shaped plate rigidly fixed along the outer rim. A rapidly rotating solid (a fast centrifuge) rested on the inner edge of the rim.

1063-7710/03/4905-0612$24.00

S.A. Nazarov's paper was devoted to the relations between a three-dimensional model and a conventional two-dimensional (Kirchhof) description of the processes in an elastic plate. He demonstrated that, contrary to traditional concepts, the first eigenfrequency of oscillations of a three-dimensional plate can exceed the first eigenfrequency of the plate considered on the basis of a two-dimensional model.

In K.M. Ovsyannikov's paper, a thin elastic plate bounded a layer of an acoustic medium while its other surface was assumed to be rigid. The wave motion of the plate was caused by a force uniformly distributed along a circle. The effect of a ring-shaped inclusion concentric with the source, which had a preset mass, rigidity, and damping coefficient, on the wave processes in the system was studied.

I.V. Andronov demonstrated that the problem of the diffraction of a flexural wave propagating in a thin plate by a circular impedance barrier can also be solved in the case when in the barrier vicinity an intrinsic process is possible that does not produce any radiation into the plate (a so-called trap form). The possibility of the existence of such a process was proved earlier (*Acoustical Physics*, **47**, 3 (2001)).

E.V. Shishkina compared the frequencies and forms of vibrations of a coil rod of finite length, whose behavior is described by a set of Kirchhof–Klebsch equations, with the rod equations for a spring, which are conventionally used in engineering, to specify the limits of applicability of the latter.

The papers by A.V. Porubov and A.V. Karpenko were devoted to nonlinear wave processes in solids.

A.V. Porubov considered the propagation of long nonlinear waves in rods and elastic media. He focused mainly on waves that retain their shape in the process of propagation, primarily, bell-shaped solitary waves. Possible practical applications of solitary strain waves in nondestructive testing and in testing the strength of structural materials were discussed.

Two papers by A.V. Karpenko described the methods and results of numerical calculations with the help of finite-difference schemes of deformation development (including the case of plastic deformation) in heavily loaded layered shell structures. Collisions of a structure with plane rigid barriers and explosions were considered as the sources of such deformations.

More detailed author's abstracts of papers and other information on the seminar can be obtained on the web site of our seminar:

http://mph.phys.spbu.ru/~george/seminar.html

Applications for papers can be forwarded by e-mail (kouzov@alfa.ipme.ru or george@GF4663.spb.edu) or by phone to the seminar head D.P. Kouzov (812) 312-3530 or the seminar secretary G.V. Filippenko (812) 143-2323.

D.P. Kouzov

Translated by M. Lyamshev